UNIVERSITÀ DI PARMA

UNIVERSITA' DEGLI STUDI DI PARMA

DOTTORATO DI RICERCA IN

"SCIENZA E TECNOLOGIA DEI MATERIALI"

CICLO XXXIV

NANO - PHOTOCATALYSTS: DESIGN, UP - SCALE AND CHARACTERISATION MODELS

Coordinatore:

Chiar.mo Prof. Enrico Dalcanale

Tutore:

Dott.ssa Anna Luisa Costa

Dott.ssa Simona Ortelli

Dottoranda: Lara Faccani

Anni Accademici 2018/2019 – 2020/2021

“Only those who dare to fail greatly can ever achieve greatly.”

“Solo chi osa fallire molto può ottenere grandi risultati.”

(Robert Kennedy)

Summary

Abstract (ENG)

Two extremes in a current world are present: the deficiency of drinking water in underdeveloped countries and the growing amount of emerging pollutants in highly industrialized areas. Two opposite scenarios but the solution could be unique: nanotechnologies for water purification. If on the one hand the aim is to make drinkable water contaminated mainly by bacteria, organic substances and dyes, on the other hand the industrialization and the advancement of technology have introduced hormones, microbes and viruses, pharmaceutical products, detergents and microplastics on the list of wastewater contaminants.

Emerging pollutants are not removed by current waste water treatment common to most urban waste water treatment plants, therefore there is a need to investigate new technologies, such as nanotechnologies, capable to remove potentially toxic contaminants from water.

This thesis proposes four main solutions, as key points of innovation.

Development of nano – photocatalysts used in AOPs for removing (bio-) organic pollutants. (Chapter 1).

Four different nano-photocatalysts have been developed and characterized:

1. Commercial titanium dioxide nanosol (TAC);

2. Thermally synthesized carbon nitride powder (g-C_3N_4);

3. Heterocoagulated titanium dioxide nanosol with silica dioxide (TiO_2:SiO_2);

4. Titanium dioxide powder supported on graphene oxide, obtained with sonochemical method (TGO).

The structural, colloidal and optoelectronic properties were measured, and correlated to the functional ones, using the Rhodamine B dye as an organic pollutant model and UV lamp or solar simulator as an irradiation source. The functional performance was coupled by cost and environmental sustainability profiles evaluated with Life Cycle Assessment and Life Cycle Costing models, applied to the materials use phase. The union of the three

aspects made it possible to identify decision-making intervals relating to the variables: type of material, source and time of irradiation, which guaranteed maximum functionality, while keeping costs and environmental impact to a minimum. The study showed that the TAC material and the composite formulated by it (TiO_2:SiO_2) guarantee greater decision areas, favouring their use, compared to other materials, which suffer from the high consumption of energy necessary for preparation (TGO) or of the lowest photocatalytic efficiency (g-C_3N_4).

Semi-pilot plant study for the photodegradation of water pollutants. (Chapter 2).

In response to the need to transfer knowledge and technologies developed on a laboratory scale to a scale of industrial interest, the nano-photocatalysts were immobilized on fabric supports and inserted as active matrices in a pre-pilot plant capable to treat approximately 6L of recirculated water continuously. From a multi-variable optimization (type of irradiation, working temperature, type of fabric, type of coating), based on the functionality of the nano-photocatalysts, the application of a TiO_2:SiO_2 coating on cotton at a working temperature of 25 °C, emerged as a winning strategy.

Experimental evaluation of the reactivity of nano-photocatalysts and assessment of their potential (eco-) toxicity. (Chapter 3).

In response to the increasingly felt need to have fast and simple methods available to evaluate the indicators, associated with the surface reactivity of nanomaterials, predictive of their functional and biological reactivity, experimental models have been developed and investigated for the evaluation of the oxidative power of nano-photocatalysts, mediated by the production of reactive oxygen species (ROS). The consumption of the two redox pairs GHS / GSSG and Cysteine / Cystine, at the forefront of cellular defence from oxidizing agents, as well as the •OH mediated oxidation of p-nitroaniline (RNO) was evaluated. It was found that the material that most requires chemicals in its synthesis, TGO, has a high oxidative power while the coupling of SiO_2 with TiO_2 allows to increase the photocatalytic efficiency, in spite of a decreased ROS production, thus doing of the TiO_2:SiO_2 material an excellent candidate in terms of Safe and sustainable by design (SSbD). As a predictive tool, a computational model based on machine learning was also used, which identifies the characteristics of the nanoparticles and the exposure conditions

and correlates them with the consumption of antioxidants and the generation of ROS, providing indications on which parameters are most they influence the oxidizing power, with a view to optimizing the nano-photocatalyst, according to the SSbD approach.

Identification and characterization of new class of pollutants: micro – nano plastics (MNPs). (Chapter 4).

In response to the growing interest in managing an emerging class of pollutants, namely micro-nano plastics and evaluating the impact that may derive from exposure to both humans and the environment, some major plastics have been characterized (PE, PS and PET) and studied the methods of dispersion in environmental matrices, exploiting approaches and protocols developed from the study of nanoparticles. Thanks to the participation in the European project PlasticsFate (Plastic fate and effects in the human body - GA: 965367), we had access to a repository of representative MNPs, different by type of polymer, origin, size and use scenarios. The study showed that by simply measuring the zeta potential and the isoelectric point, it is possible to identify whether synthetic additives are present and how they influence the state of dispersion. In response to the need to optimize dispersion protocols, two dispersants of different nature were tested to ensure reproducibility of the physico - chemical and biological characterizations: Bovine Serum Albumin (BSA) and Sodium Surfactin. In particular, the latter will be analysed for its biocompatibility and considered by the project as a valid alternative to the use of BSA (dispersant of choice for nanoparticle dispersion protocols in the nano-safety field), since it has a very high degree of efficiency.

Abstract (ITA)

La carenza di acqua potabile nei paesi sotto sviluppati e la crescente quantità di inquinanti emergenti nelle zone fortemente industrializzate rappresentano due criticità estreme dell'attuale quadro globale. Se da una parte l'esigenza è quella di rendere potabile l'acqua contaminata principalmente da batteri, sostanze organiche e coloranti, dall'altra parte l'industrializzazione e l'avanzare della tecnologia hanno introdotto nuove categorie di inquinanti come ormoni, microbi e virus, prodotti farmaceutici, detergenti e microplastiche nella lista di contaminanti delle acque reflue.

Gli inquinanti emergenti non vengono rimossi dalle attuali tecniche di purificazione delle acque comuni alla maggior parte degli impianti urbani di purificazione, da cui la necessità di indagare nuove tecnologie, come le nanotecnologie, in grado di sottrarre all'acqua contaminanti potenzialmente tossici.

Questa tesi propone quattro soluzioni principali, come punti chiave di innovazione.

Sviluppo di nano-fotocatalizzatori utilizzati in trattamenti AOP per rimuovere inquinanti (bio-) organici. (Capitolo 1).

Sono stati sviluppati e caratterizzati quattro diversi nano-fotocatalizzatori:

1. nanosol di biossido di titanio (TAC) di origine commerciale;
2. polvere di nitruro di carbonio sintetizzato termicamente (g-C_3N_4);
3. nanosol di biossido di titanio etero-coagulato con biossido di silice (TiO_2:SiO_2);
4. polvere di biossido di titanio supportata su grafene ossido, ottenuta con metodo sonochimico (TGO).

Le proprietà strutturali, colloidali e optoelettroniche, sono state misurate, e correlate a quelle funzionali, utilizzando come modello di inquinante organico il colorante Rodamina B e come fonte di irraggiamento lampada UV o simulatore solare. Alle prestazioni funzionali sono stati affiancati profili di costo e sostenibilità ambientale valutati con modelli di Life Cycle Assessment e Life Cycle Costing, applicati alla fase di utilizzo dei materiali. L'unione dei tre aspetti ha permesso di individuare intervalli decisionali relativi alle variabili: tipo di materiale, fonte e tempo di irraggiamento, che garantissero la massima funzionalità, mantenendo costi e impatto ambientale al minimo. Dallo studio è emerso che il materiale TAC e il composito da esso formulato (TiO_2:SiO_2) garantiscono aree di decisione maggiori, favorendo il loro impiego, rispetto agli altri materiali, i quali soffrono dell'alto consumo di energia necessario alla preparazione (TGO) o della più bassa efficienza fotocatalitica (g-C_3N_4).

Studio di un impianto semi pilota per la foto-degradazione di inquinanti acquatici. (Capitolo 2).

In risposta alla necessità, oggi primaria, di trasferire conoscenze e tecnologie messe a punto su scala di laboratorio ad una scala di interessa industriale, i nano-fotocatalizzatori sono stati immobilizzati su supporti tessili ed inseriti come matrici attive in un impianto

pre-pilota in grado di trattare in continuo circa 6L di acqua a ricircolo. Da una ottimizzazione multi-variabile (tipo di irraggiamento, temperatura di lavoro, tipo di tessuto, tipo di rivestimento), sulla base della funzionalità dei nano-fotocatalizzatori, è emersa come strategia vincente l'applicazione di un rivestimento di TiO_2:SiO_2 su cotone, ad una temperatura di lavoro di 25 °C.

Valutazione sperimentale della reattività dei nano-fotocatalizzatori e della loro potenziale (eco-) tossicità. (Capitolo 3).

In risposta alla necessità sempre più sentita di avere a disposizione metodi veloci e semplici per valutare gli indicatori, associati alla reattività superficiale dei nanomateriali, predittivi di una loro reattività funzionale e biologica, sono stati sviluppati e investigati modelli sperimentali per la valutazione del potere ossidativo dei nano-fotocatalizzatori, mediato dalla produzione di specie radicaliche ad ossigeno (ROS). È stato valutato il consumo delle due coppie redox GHS / GSSG e Cisteina / Cistina, in prima linea nella difesa cellulare da agenti ossidanti, così come la ossidazione mediata da •OH della p-nitroanilina (RNO). Si è evinto che il materiale che maggiormente richiede chimici nella sua sintesi, il TGO, ha un elevato potere ossidativo mentre l'accoppiamento della SiO_2 con il TiO_2 permette di aumentare l'efficienza fotocatalitica, a dispetto di una diminuita produzione di ROS, facendo così del materiale TiO_2:SiO_2 un ottimo candidato in un'ottica di SSbD. Come strumento predittivo, è stato anche utilizzato un modello computazionale basato sul *machine learning*, che identifica le caratteristiche delle nanoparticelle e le condizioni di esposizione e le correla con il consumo di antiossidanti e la generazione di ROS, fornendo indicazioni su quali sono i parametri che maggiormente influenzano il potere ossidante, in un'ottica di ottimizzazione del nano-fotocatalizzatore, secondo l'approccio SSbD.

Identificazione e caratterizzazione di una nuova classe di inquinanti: micro-nano plastiche (MNPs). (Capitolo 4).

In risposta al crescente interesse per gestire una classe emergente di inquinanti, ovvero le micro-nano plastiche e valutare quale impatto possa derivare dall'esposizione sia dell'uomo che dell'ambiente sono state caratterizzate alcune plastiche di maggiore rilievo (PE, PS e PET) e studiati i metodi di dispersione in matrici ambientali, sfruttando approcci

e protocolli messi a punto dallo studio delle nanoparticelle. Grazie alla partecipazione al progetto europeo PlasticsFate EU (Plastic fate and effects in the human body – GA: 965367), abbiamo avuto accesso ad un repository di MNPs rappresentative, differenti per tipologia di polimero, origine, dimensioni e scenari di utilizzo. Dallo studio è emerso che attraverso la semplice misura del potenziale zeta e del punto isoelettrico è possibile individuare se sono presenti additivi di sintesi e come influenzano lo stato di dispersione. In risposta all'esigenza di ottimizzare i protocolli di dispersione, per garantire riproducibilità alle caratterizzazioni chimico-fisiche e biologiche sono stati testati due disperdenti di diversa natura: Bovine Serum Albumin (BSA) e Sodium Surfactin (SS). In particolare quest'ultimo verrà analizzato per la sua biocompatibilità e considerato dal progetto come valida alternativa all'utilizzo del BSA (disperdente di elezione per i protocolli di dispersione delle nanoparticelle in ambito nano-safety), poiché presenta un grado di efficienza molto elevato.

Chapter 1:

Introduction

1.1. Concept and objectives

"We ourselves are made of water. Human beings are the way that water has found to go around even away from rivers." Anonymous

Clean water is essential for life, and ensuring the availability and sustainable management of water and sanitation became in 2015 one of the 17 Sustainable Development Goals (SDGs) which world leaders agreed upon to achieve a better world in 2030[1]. The World Health Organization (WHO) and the United Nations International Children's Emergency Fund (UNICEF) declared that in 2019 one in three people had no access to clean water. Consequently, 2.2 billion residents are unable to reach clean water, 4.2 billion have not lavatory and 3 billion cannot wash their hands[2], especially in underdeveloped countries.

On December 14 of 2019 the European (EU) Green Deal was presented to EU Commission. The aim of the political initiatives set is to achieve climate neutrality by 2050. The objectives envisaged various sectors of concern such as construction industry, food, energy, transport, recycling and biodiversity[3]. In the latter field the objective is environment preservation to ensure seas, oceans and other environments are able to support humanity. The priorities of Green Deal are:

- Protection of biodiversity and ecosystems
- Air, water and soil pollution reduction, especially from pharmaceuticals and microplastics pollution, harmful and persistent
- Fostering the circular economy
- Improved waste management
- Ensuring sustainability of the blue economy and the fisheries sectors[4].

Evidently the water quality of aquatic environments is deteriorating and this is attributed to pollutants such as dyes, metals, persistent organic pollutants (POPs) etc…[5]. Additionally, there are new generation pollutants i.e., Emerging Contaminants (EC), including Pharmaceuticals and Personal Care Products (PPCPs)[6], antimicrobials, animal and human hormones[7], micro - nano plastics (MNPs)[8] and detergents. The

contaminants are derived from different sources, i.e. effluent discharges from wastewater treatment plants, industrial wastewater, agricultural practices and urban rainwater runoff. This underscores the growing calls for all stakeholders to accept responsibility and reduce their environmental impacts in order to ensure future sustainability.

The need for alternatives for the water treatment and pollutant remediation methods to complement or replace existing technologies is clear[9]. Nanomaterials have the potential to act like effective adsorbents, filters, disinfectants and reactive agents[10–12].

This great potential comes from the properties of nanomaterials which show:

- high surface area
- absorbent properties
- antibacterial and antiviral properties
- high reactivity
- photosensitive.

In this thesis we took the advantage of nanotechnologies to provide more effective responses to water challenges. In details:

1. The photocatalysis ability to degrade organic pollutants was investigated as a green alternative to Advanced Oxidation Processes (AOPs) in wastewater treatment.
2. In addition to the organic contaminants, the MNPs were also examined.
3. Finally, the challenging objectives of developing models for the prediction of nano-photocatalysts functionality and their hazardous potential were also addressed.

The vision that inspired this thesis is to support the water challenge “Improving water quality and ecosystems”, by providing solutions for the implementation of the Sustainable Development Goal “6” dedicated to water[13].

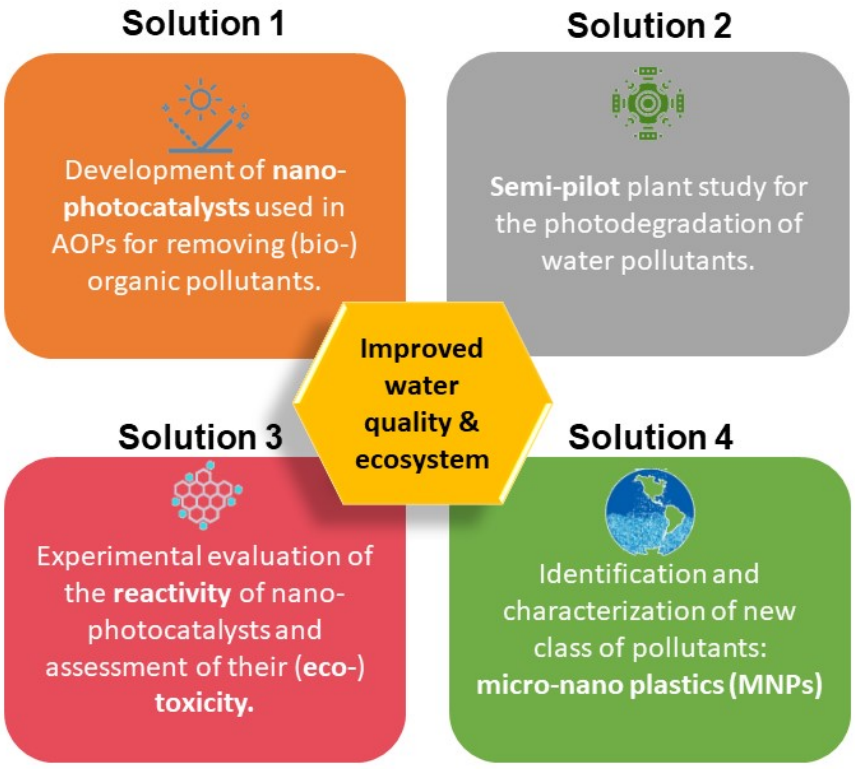

Figure 1.1. Key points of innovation researched and developed in this thesis.

As seen in Fig. 1.1, this thesis proposes four main solutions as key points of innovation.

1. Development of nano–photocatalysts for sustainable purposes (See chapter 2).
2. Semi – pilot scale up (See chapter 3).
3. For each solution, experimental models for the characterization of physico - chemical properties and performances attributes were used and optimized (See chapter 4). Data were exploited to derive information on the safety and sustainability profiles of the proposed nano–photocatalysts.
4. New class of pollutant (MNPs) are characterized (See chapter 5).

1.2. From vision to action

1.2.1. Solution 1: Development of nano–photocatalysts used in AOPs for removing (bio-) organic pollutants

Four different nano-photocatalyst (NM) were developed and characterized:

1. commercial source titanium dioxide nanosol (TAC);

2. thermal synthesised graphitic carbon nitride powder (g-C_3N_4);
3. heterocoagulated nanosol of titanium dioxide coupled with silica dioxide (TiO_2:SiO_2);
4. titanium dioxide-graphene oxide powder obtained by sonochemical method (TGO).

The aim was to compare the photocatalytic activity of the samples by varying their chemical composition while applying diverse irradiation sources. In particular we investigate the reactivity under visible light irradiation, as a more sustainable alternative to UV, since most of the water remediation plants are already placing natural light environments that can exploit sun's rays to activate the photocatalysts[14,15].

- The composite material TiO_2:SiO_2 represents the best strategy in terms of photocatalytic efficiency normalized for the quantity of active phase present.
- No particular differences were found between the tests conducted under UV light and the tests conducted under visible light, supporting the fact that few photons present in the solar spectrum are sufficient to obtain good results of degradation of pollutants[16].
- The result follows the Safe and Sustainable by Design (SSbD) concept and allow the usage of less expensive, safer and environmental friendlier techniques.

1.2.2. Solution 2: Semi - pilot plant study for the photodegradation of water pollutants

After testing the four NMs in beaker at the laboratory scale, two of the materials (TAC and TiO_2:SiO_2) were deposited on fabric substrates by dip-pad curing process and integrated in a semi-pilot 6 litres plant, designed to simulate a system suitable for wastewater treatment, in real application. The aim of this study was to optimise the design of the investigated system that *per se* presents many advantages:

1. immobilisation of nano-photocatalyst to eliminate any type of post-purification treatment,
2. usage of low weight, low cost supports with great geometries flexibility already tested for their capacity to form stable and washing resistant coatings with TiO_2[17],

3. integrate irradiation system that can be switched between UV and Visible light.

We have found that:

- 100% biodegradable cotton fabric irradiated by visible LEDs is the best solution.
- The very low intensity of UV radiation fabrics activation under visible LED expands the applicability of the technology to sunlight, since the measured intensity of the UV radiation component, in the visible LED, is much less than the annual solar average.
- Results of multivariable optimization study are translated into updated recommendations for the design and technical application of these efficient and cost-effective TiO2-based photocatalysts, suitable for the development of a range of technologies aimed at protecting the environment.

The design options proposed in solutions 1 and 2 were evaluated also in terms of sustainability and safety profiles. In particular, Life Cycle Assessment (LCA) and Technical Economic Assessment (TEA) models were applied to assess cost / effectiveness and environmental impacts, whilst experimental models described in solution 3, provided indications on material functionality, photo-oxidation mechanism and safety potential.

1.2.3. Solution 3: Experimental evaluation of the reactivity of nano-photocatalysts and assessment of their (eco-) toxicity

Different experimental models were adapted to the investigated systems at the aim to predict different performance attributes, such as the capacity to decompose an organic dye, the capacity to decompose the •OH radicals mediated photooxidation and, the oxidative potential against cell natural antioxidant defences using:

1. rhodamine B dye discoloration under UV or Visible light irradiation, as a model of organic pollutants degradation (RhB model);
2. p-nitrosodimethylaniline assay, specific for the assessment of •OH radical reactivity (RNO model);
3. thiol group assay (Ellman reagent) to evaluate the oxidation of Glutathione (GSH) and Cysteine (Cys) as probes of cell oxidative stress (GSH / Cys model).

- The difference between the found reactivity trends were discussed and mechanistic hypothesis, extremely useful for implementing a safe-and-sustainable-design, were formulated.
- Part of these results contributed to support the alternative tests for the assessment of NPs hazard potential and exposure / fate behaviours (participation to EU project PATROLS – Physiologically Anchored Tools for Realistic Nanomaterial hazard assessment - GA: 760713 and ASINA - Anticipating Safety Issues at the Design Stage of Nano Product Development - GA: 862444).
- Part of these results contributed provided descriptors to computational models that correlate physico - chemical properties to hazard and exposure related effects (participation to EU project NanoInformaTIX - Development and implementation of a Sustainable Modelling Platform for Nanoinformatics - GA: 814426).

1.2.4. Solution 4: Identification and characterization of new class of pollutants: micro – nano plastics (MNPs)

Finally, the characterization of micro – nano plastics (MNPs) to support the evaluation of potential risk to human health and environment was performed.

- Thanks to the collaboration and involvement in the PlasticsFate EU project (Plastic fate and effects in the human body – GA: 965367), we had access to a repository of representative MNPs, differing for polymer type, source / size and use scenarios was provided.
- Contribution to MNPs basic characterisation, in order to:
  - define their physico - chemical identity (morphology, surface chemistry)
  - study dispersibility in order to provide a dispersion protocol
  - support the characterisation environmental matrices and human compartments simulant fluids.

With this study it was possible to identify two dispersing media that allow to obtain stable suspensions of MPs. Furthermore, from the studies conducted in the simulant media, a change in the colloidal behaviour was noted, in particular it seemed that the MPs covered themselves with negative charges by shifting their Z-potential / pH and $pH_{i.e.p.}$ towards acid pH.

1.3. Core concept

In this thesis work I set out to develop nanotechnology based safe-and-sustainable-by-design solutions, as water remediation strategies, by implementing a data-driven methodology molded on industrial six sigma practice[18,19], whose steps are identified by the capital letter of the selected model DMADV: Definition, Measure, Analysis, Design and Verification. I report in the following paragraphs the state of the art and the proposed solutions advance beyond it, for each step of the addressed methodology.

1.3.1. Definition

Solution 1 proposed in this thesis work aims to develop and test nano-photocatalysts for water purification with the safe and sustainable by design strategy. This requires a definition phase to understand the advantages / disadvantages of the most used material up to now: TiO_2; as well as the advantages in the development and use of new materials that can respond to the limitations of the reference material. The Define phase includes a series of actions such as the definition of the problem and the identification of requirements for new materials with the aim of advancing the current state of the art.

The following materials have been chosen for developing the proposed nano-photocatalysts:

- benchmark material: titanium dioxide (TiO_2).
- synthesized materials: graphitic carbon nitrides (g-C_3N_4).
- composite materials: titanium dioxide – graphene oxide (TGO), titanium dioxide – silicon dioxide (TiO_2 – SiO_2).

Titanium Dioxide (TiO_2)

Titanium dioxide exists in three different crystal structures (Fig. 1.2): rutile, anatase, brookite and in the amorphous phase. The brookite consists of an orthorhombic structure, the other two forms instead have a tetragonal structure containing three distorted octahedra, specifically the one relating to rutile contains two molecules of TiO_2 per primitive cell. The forms that are most widespread in nature are those of rutile and anatase. The TiO_6 octahedra represent the basic structural unit in the various polymorphic

structures, in which the greatest differences between the different morphologies are in the number of shared octahedra, in particular two in the rutile, three in the brookite and four in the anatase. Rutile is the most thermodynamically stable form and is the most used industrially while anatase is metastable. Of the three forms, however, this is the most active in photocatalysis and therefore the most used technologically (however, both are still used as photocatalysts)[20].

The synthesis of TiO_2 occurs mostly hydrothermal in steel pressure vessels called autoclaves by precipitating a precursor in aqueous solution. The control of temperature and internal pressure are the factors that determine the size of the particles or nanorods. Another synthesis method is the solvothermal method where the solvent is non-aqueous. This method allows for better control of particle size and particle size distribution. Then there is the sol-gel method, a very versatile process used in the ceramic field. In this method the precursors form a sol by polymerization and hydrolysis thanks to the alkaloid metals. TiO_2 nanostructures can also be synthesized by direct oxidation of a titanium metal using oxidants or under anodization. With this method, TiO_2 nanorods, planes or nanotubes are mainly produced. Other methods can be electrodeposition, sonochemical method or microwave method, all less used methods[21,22].

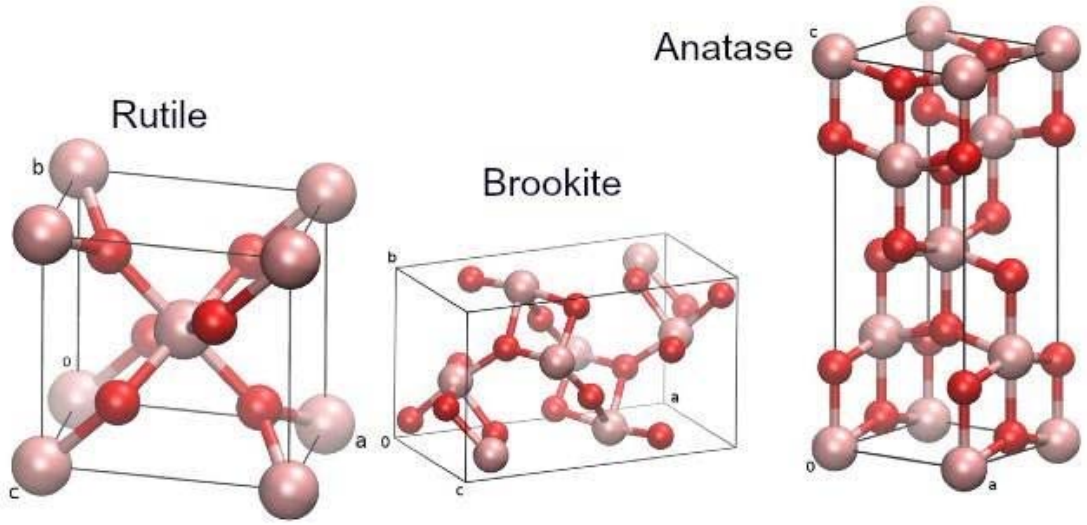

Figure 1.2. TiO_2 crystal structure.

Titanium dioxide has been the most investigated semiconductor material used in photocatalysis for the purification of water (Fig. 1.3)[23]. TiO_2 is a NM with a high chemical and photochemical stability, declared safe, non-toxic and not subject to photo-degradation. Moreover, TiO_2 is widely produced industrially, so it is now a low-cost material, easy to extract and synthesize. TiO_2 is a versatile material: rutile form is used in paints. It can be used as a screen in sun creams, it is used for electrochemistry, as a capacitor or in solar cells, one field of application is as a colouring agent in food. The anatase form is mostly used as a photocatalyst due to its high photocatalytic activity, high specific area, photochemically stability[24].

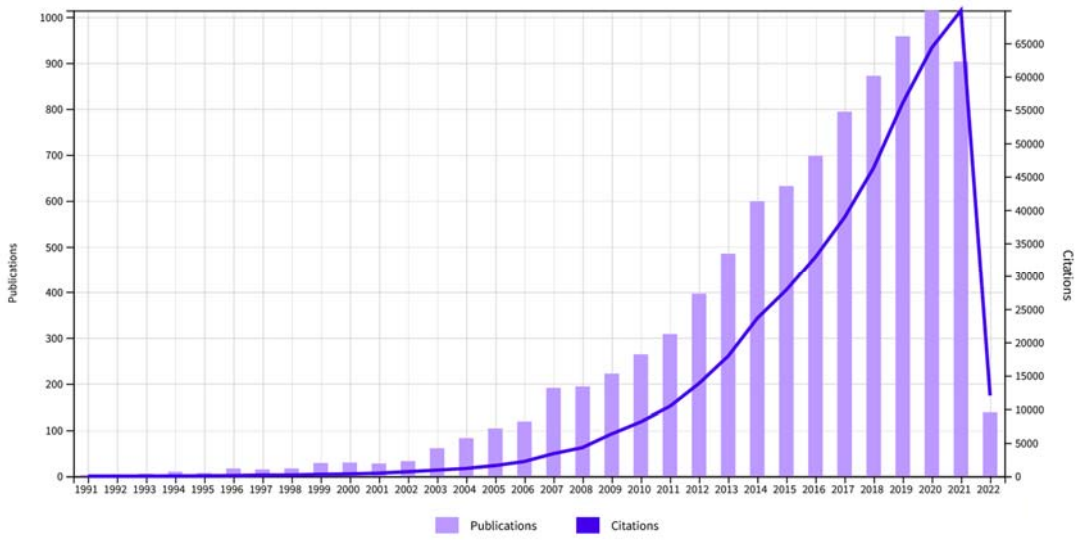

Figure 1.3. Publication and citation of TiO_2 used as photocatalyst in water to remove pollutants. 9234 result from Web of Science Core Collection for: TiO_2 photocatalysts water.

The photocatalytic activity of TiO_2 can be divided into various steps. First, the photoreduction phase: the TiO_2 electrons need enough energy to pass to the valence band. It is known that the band gap of TiO_2 is 3.2 eV, therefore the energy of the photon able to excite the e^- of TiO_2 corresponds to 380 nm and therefore to UV light[20]. When the electrons are excited, they pass from the valence band to the conduction band with formation of holes (h^+). The electrons and holes thus generated emerge on the surface of titania and react with the adsorbed species. The photo-generated electrons react with the adsorbed oxygen to form hydroxyl radicals (•OH) and superoxide ($O_2•^-$), highly reactive and main intermediates of the oxidation of organic pollutants. Then there is the photo-

oxidation phase, in which the positive gaps previously formed in the conduction band oxidize the hydroxyl radicals and the adsorbed water molecules. The •OH radicals produced contribute to the process of degradation. Eventually, the organic materials decompose into carbon dioxide and water (mineralization process)[12-13]. The following are the main reactions involved in the photodegradation mechanism:

$$TiO_2 + hv \rightarrow TiO_2^* (e^- + h^+)$$

$$H_2O + h^+ \rightarrow \bullet OH + H^+$$

$$e^- + O_2 \rightarrow O_2\bullet^-$$

$$O_2\bullet^- + H^+ \rightarrow HO_2\bullet$$

$$H^+ + O_2\bullet^- + HO\bullet \rightarrow H_2O_2 + O_2$$

$$H_2O_2 + hv \rightarrow 2\ \bullet OH$$

The greatest disadvantages that nanometric TiO_2 brings with it are partly due to its intrinsic characteristics such as the band gap that makes it active only under UV light, and partly due to its nanometric shape. TiO_2 nanoparticles in aqueous suspension form aggregates making active sites unavailable that could be involved in photocatalyst reactions. Furthermore, due to the nanometric size, recovery from the suspension is difficult. Finally, despite having a large surface area, compared to other materials such as coal, it does not have a high capacity to absorb pollutants[27]. In the perspective of the Green Deal and green chemistry, the goal of the scientific committee is to find a method to obtain the reactivity of TiO_2 under the irradiation of visible light to efficiently use the abundant natural resource that is sunlight. A number of strategies can be used such as adding metallic / non-metallic elements as doping or coupling with other materials. These strategies allow a reduction of the band gap resulting in the need for an energy closer to the wavelength of the visible spectrum to excite the electrons of the semiconductor[28].

Graphitic carbon nitrides (g-C_3N_4)

g-C_3N_4 is a light-yellow compound belonging to the carbon nitride family. It has an angular planar phase similar to graphite, with one difference: that it has nitrogen bonds coordinated at three and at two and each carbon atom is bonded with three nitrogen

atoms. This material exhibits good chemical stability, low cost preparation and specificity in composition[29]. g-C_3N_4 is a n-type semiconductor with advantages as non-toxic, metal-free and offers a large-scale commercial application. The material has a "graphite-like" structure as the name also indicates, that is, it is made up of nano-sheets of tris-triazine units repeated in two-dimensional space and these sheets, in turn, are stacked and held together by secondary interactions such as Van der Waals ties[30]. The band gap of g-C_3N_4 is 2.7 eV and the wavelength corresponding to the absorption edge of the solar spectrum is 460 nm[31]. Is a promising organic alternative, active under visible light, to TiO_2.

There are several mechanisms for preparing this compound, but the most effective ones for the production of a crystallographic phase free of contamination involve a thermal polymerization mechanism starting from an organic substrate containing nitrogen atoms in structure, such as urea, melamine or amide-type. It is therefore preferable to start from melamine, a bulk that comes from renewable and harmless raw materials[32]. By subjecting the melamine to a heat treatment at 550 °C for 4h (Fig. 1.4) a g-C_3N_4 is obtained.

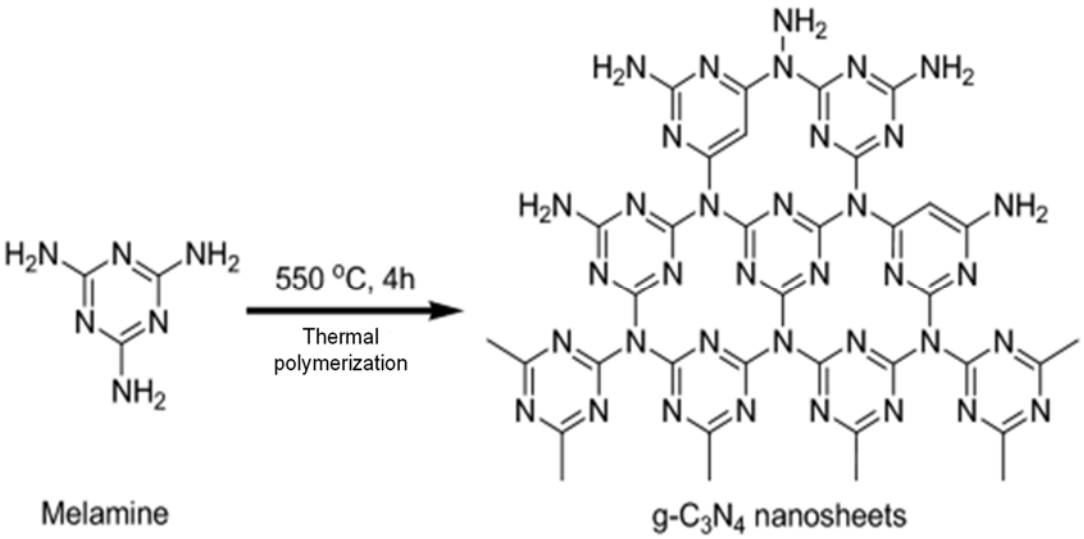

Figure 1.4. g-C_3N_4 nanosheets synthesis.

Due to the rapid recombination of the photogenerated electron-hole pairs, several new strategies are being investigated by manipulating the polymeric structure (nanorods,

nanosheets, nanospheres and porous structures) of g-C_3N_4 because morphology and structure are parameters that influence optical properties[31,33]. Heterogeneous photocatalysis by g-C_3N_4 can be divided into successive stages:

- capture of visible light strongly influenced by the surface morphology and the structure of the photocatalysts, therefore the smooth surface of 2D g-C_3N_4 is a disadvantage that can be avoided by building a hierarchy of microporous or mesoporous architectures.
- excitation charge and e^- / h^+ generation;
- separation and migration of photogenerated electron pairs. the rapid recombination of electron-hole pairs in the mass and on the surface of a photocatalyst is considered the main deciding factor in the realization of the maximum photocatalytic activity, which is one of the most challenging e problematic scientific problems in the heterogeneous photocatalytic process
- reactions occurring on the surface of the catalysts.

The electron-hole photoexcitation of g-C_3N_4 is listed in Eq. (1). The VB and CB potentials of g-C_3N_4 are approximately a 1.30 and 1.40 eV, respectively. The standard redox potential of O_2 / O_2 (0.13 eV vs. NHE) is much higher so the g-C_3N_4 reacts with the O_2 adsorbed on the surface to produce radicals (Eq. (2)). The redox potential of OH / OH (1.99 eV vs. NHE) is also higher than that of g-C_3N_4, and some •OH radicals can be produced (Eq. (3)).

$$g\text{-}C_3N_4 + h\nu \rightarrow g\text{-}C_3N_4 - h^+ + g\text{-}C_3N_4 - e^- \quad (1)$$

$$g\text{-}C_3N_4 - e^- + O_2 \rightarrow g\text{-}C_3N_4 + O_2^{\bullet -} \quad (2)$$

$$O_2 + 2H^+ + 3g\text{-}C_3N_4 - e^- \rightarrow OH^- + \bullet OH + g\text{-}C_3N_4 \quad (3)$$

Doping with suitable elements on the surface of g-C_3N_4 could simultaneously improve these restrictive disadvantages through the acceleration of the separation of the charges and the promotion of the catalytic reaction[34].

Titanium dioxide – Graphene oxide (TGO)

Recently as a carbonaceous doping material, graphene oxide (GO) has attracted the attention of the scientific community, unique for its properties as it has a high surface area, a structure consisting of flexible sheets, excellent electrical conductivity and thermal and excellent mobility of charge carriers. It has a high electrical conductivity due to the very high mobility of electrons, it is also one of the most resistant materials in nature, with an elastic modulus of 1 TPa, higher than that of diamond. Pure graphene is insoluble and chemically not very reactive, while functionalized graphene can be made soluble in various solvents, and thanks to the presence of surface hydroxyl groups it can better adsorb organic particles, for example those of pollutants[35]. The crystalline structure of graphene consists of layers of carbon atoms arranged on hexagonal cells. It is a two-dimensional material in which the carbon atoms are sp^2 hybridized, in which three of the four valence electrons participate in the bond with the first neighbours (σ bond), while the fourth is delocalized in an electron orbital oriented perpendicular to the plane (π bond). The VB and CB of graphene consist of two types of bonding orbitals, π and antibonding π* orbitals, which produce a single sheet of semiconductor graphene with zero band gap. It is a material that has a non-stoichiometric atomic composition, therefore, there is no precise relationship between the carbon, oxygen and hydrogen atoms that form it. They are stacked structures of GO monolayers held together by hydrogen bonds, moreover, compared to graphite, the spacing between the planes is larger, from 6 to 12 Å (depending on the quality of the material and humidity) against 3.35 Å of graphite[36].

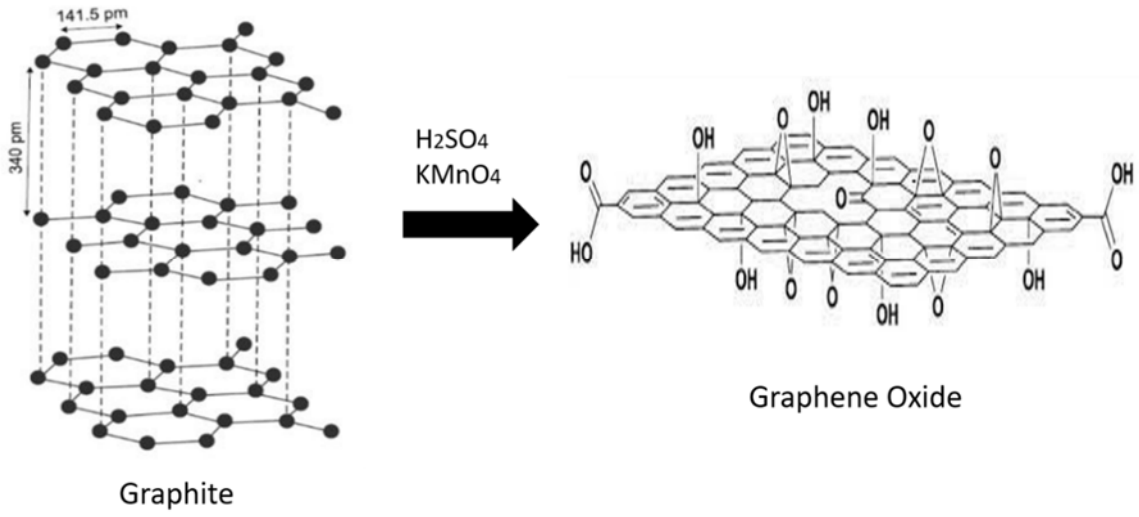

Figure 1.5. graphite - graphene oxide transformation.

One of the most commonly used synthesis techniques for the production of GO is the modified Hummer method, which consists in the exfoliation and oxidation of graphite. In this method, sulfuric acid (H_2SO_4) and sodium nitrate ($NaNO_3$) act as intercalation reagents in the carbonaceous structure, and potassium permanganate ($KMnO_4$) oxidizes the acid-intercalated graphite to GO (Fig. 1.5). A brown paste in suspension is obtained, which is then diluted with water and H_2O_2 to increase the degree of oxidation and remove excess of manganese from the dispersion, followed by washing with hydrochloric acid (HCl) and water.

What we are trying to study in the laboratory is the synthesis of a composite material consisting of titanium dioxide and graphene oxide, which is an excellent support as it contains, on the surface, numerous reactive oxygen functional groups (hydroxyl, epoxide, ketone and carboxyl)[29,37]. Once the graphene oxide powder has dried, the TiO_2 / GO (TGO) composite can be formed. One of the methods mainly used is the use of an ultrasound probe[38].

The heterojunction between graphene and TiO_2 promotes the separation of the hole / electron pair in TiO_2, hindering its recombination. Also, the formation of the Ti – O - C bond using carbon as a dopant of TiO_2 allows to extend at visible wavelength range the activation of TiO_2[39]. The photocatalytic process is promoted by GO, which absorbs visible photons. The photoexcited electrons in the high-energy GO states are then delocalized (with kinetics in the range 0.1 – 0.2 ps) onto the TiO_2 structure. In the presence of dyes, two different mechanisms activated by visible light must be considered: in the case of a pure TiO_2 catalyst the adsorbed dyes can inject photo-excited electrons on the surface of the Titania; in the presence of the TGO composite this mechanism can couple with an alternative: the dyes with photo-excited electrons are adsorbed by the GO and delocalize the charges. In both cases oxidized dye molecules can independently evolve towards transients or stable by-products and consequently towards the degradation of the substrate. The mechanism is complex and it can be concluded that GO operates as a sensitizer to visible light of TiO_2, but in the presence of species that absorb the visible the degradation process can be dominated by direct auto-oxidation of the species that absorb the visible[40].

Titanium dioxide – Silicon dioxide (TiO_2:SiO_2)

Despite having numerous positive characteristics, titanium dioxide still has a high band gap (E_g), which limits the application of photocatalysis, in the UV range, as only 4% of the solar energy that the Earth receives is made up of radiation. UV (capable of activating TiO_2), while 45% of the energy falls within the visible light range. It is therefore necessary to reduce the band gap of this semiconductor and consequently improve the absorption in the visible region. At the same time, it is necessary to work following the Safe-by-design approach with the aim of minimizing the toxicity and potential risk of nanoparticles, both those used in the human and terrestrial environment, throughout its life, even while it is used in industries where products containing nanoparticles are made. TiO_2 is known to induce changes in cell growth[41]. A silica coating can be a modification strategy thanks to its chemical inertness, biocompatibility and low reactivity, therefore the low ability to produce ROS[42].

The introduction of SiO_2 allows to reduce the hole / electron recombination speed[43], the radical being available for a longer time and it is able to attack and degrade more organic molecules[23] increasing the photocatalytic efficiency. Moreover, SiO_2 added to TiO_2 could act as dispersant increasing the homogeneity in the particle size distribution with the consequent increase of surface area and thus photocatalytic activity[14,44]. The composite material is synthesized starting from commercial TiO_2 and SiO_2 suspensions through heterocoagulation method, an electrostatic interaction between negatively charged silica nanoparticles and positively charged titania nanoparticles (Fig. 1.6). Heterocoagulation involves the adsorption of particles of a dissimilar nature in the event of a collision as a result of their individual Brownian movement. The adsorption of nanoparticles to the surface of other nanoparticles is mainly governed by a variety of forces, such as electrostatic interactions, hydrophobic interactions, and secondary molecular interactions. With electrostatic attractions, a given charged nanoparticle can adhere to an opposite charged nanoparticle. Therefore pH, surface charge (electrostatic interactions) and magnetic agitation (Brownian motions) are the main factors that influence the adhesion between nanoparticles of different nature and the formation of the composite material[45].

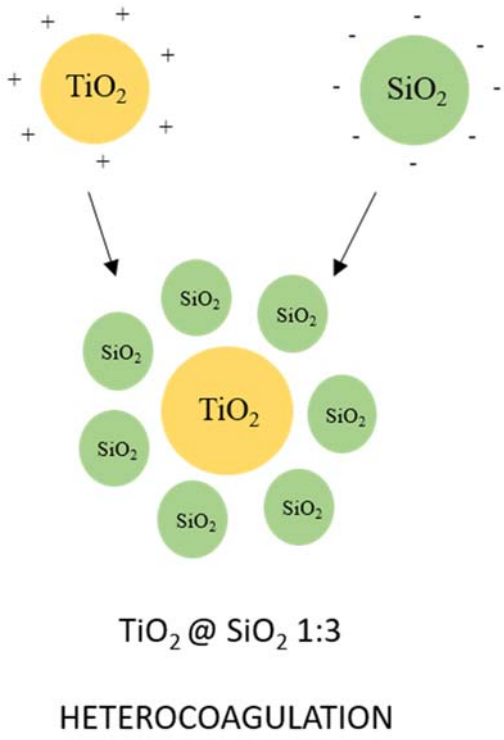

Figure 1.6. Heterocoagulation processes.

1.3.2. Measure

The functionality of nano-photocatalysts is evaluated through pollutant models, usually organic dyes, such as rhodamine B; a parameter called Photocatalytic efficiency (%) is provided which allows to know in a certain time the percentage of degraded dye. Secondly, it is important to evaluate the production of radicals, especially ROS (reactive oxygen species), intermediaries in the degradation of pollutants in photocatalysis. For this purpose, many experimental models have been proposed, in general they require a lot of time, a lot of economic resource and a lot of experience on the part of the operator who conducts the tests. Thirdly, it is necessary to evaluate the oxidative stress that nano-photocatalysts can induce when they are inserted in the context of use (waters with living beings). For this purpose, it becomes important to be able to more truthfully replicate the final conditions, then study how the NPs disperse in aqueous environment and simulate the waters where they will be used, such as river or sea waters rich in mineral salts and free ions. In this paragraph the state of the art of each aspect to be considered will be discussed.

Dye model to evaluate photocatalytic efficiency

The use of dyes to test the photocatalytic efficiency is an easy and versatile tool to demonstrate the technological benefits of photocatalysis[46]. Dyes were originally used to study water purification techniques from the textile industry where dyes are used on a large scale. Over time they have become laboratory scale models thanks to the many advantages they present: easy to find, easy to monitor with spectroscopic techniques, many dyes are low cost and very available. The dye that have the greatest attraction among the scientific community is rhodamine B (RhB)[47].

Rhodamine B ($C_{28}H_{31}ClN_2O_3$ – structure in Fig. 1.7a) is an indicator and a dye (red in water – green in powder) widely used in various fields, such as histology as biomarker and the study of degradation kinetics for water purification. It belongs to the group of fluorescent dyes and has a molecular structure composed of xanthene-core, amine and imine groups. Rhodamine B exists in two forms in equilibrium, a fluorescent one which dominates in an acid environment and a non-coloured one which dominates in a basic environment[48]. It is soluble in water and has a well-defined absorbance peak at 554 nm (Fig. 1.7b).

RhB is used more and more as an organic pollutant model, thanks to its traceability with a spectrophotometer. It is possible to evaluate the degradation kinetics at different experiment times and RhB concentrations. The possibility of a secondary mechanism, such as de-ethylation, and sensitization decrease the generality required for a contaminant model used to test a new photocatalytic material.

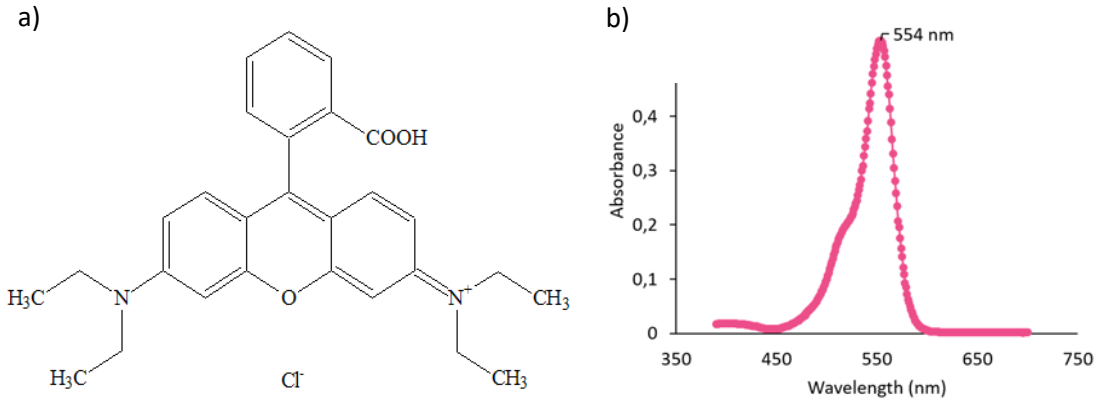

Figure 1.7. (a) Rhodamine B structure. (b) Emission spectra of rhodamine B.

ROS and oxidative stress assessment

ROS (reactive oxygen species) are highly reactive chemical species originating from oxygen. Include peroxides (H_2O_2), superoxide ($\bullet O_2^-$), hydroxyl radicals (•OH - ROS more reactive), singlet oxygen ($^1O_2$). In photocatalysis, ROS are primary intermediates of photocatalytic reactions, the identification, the quantification and the kinetic evaluation of ROS are important in terms of understanding photodegradation mechanisms, improving the efficiency of degradation and using the various technologies developed for practical applications[49]. In the biological field ROS cause oxidative stress, the term Oxidative Stress indicates the set of alterations that occurs in biological tissues, cells and macromolecules are exposed to an excess of oxidizing agents. The effect consists of metabolic damage and cell death. Any disturbances in normal redox state can have toxic effects for the production of peroxides and free radicals that damage all components of the cell, including proteins, lipids and DNA. Oxidizing species and free radicals play very important physiological roles, such as defence against bacteria, transmission of biochemical signals between cells, blood pressure control etc... It is only their excess, generally referred to one or more classes of oxidants, that is implicated in oxidative stress, now considered to be associated with over one hundred human pathologies[50,51].

The common methods to ROS detection are different[52]:

- fluorescent methods: Fluorescent probes are often sensitive to oxidants and only become fluorescent when oxidized by a ROS. there are cell-permeable probes that allow to identify the oxidative state of the cell and non-cell-permeable probes. Most probes are oxidized by a free radical mechanism to one electron, which produces an intermediate probe radical and the products are fluorescent. some compounds produce by-products which are not sufficient to quantify each radical[53].
- Chemiluminescence methods: Chemiluminescence analysis is generally used in superoxide detection. chemiluminescent probes are sensitive to radicals and easy to use. The probes may react with $O_2^{\bullet -}$ to form a photon, which is captured by a photometer or scintillation counter without the requirement of a light source of excitation. The above reaction also involves the radical steps and intermediates of

the probe play a pivotal role during this mechanism, hence the limits of the luminescent the probes are also similar to those of fluorescent probes, including not complete selectivity of the radicals, the probes can spontaneously generate radicals by overestimating the measurement[54].

- Chromatography methods: Chromatography methods are used in the separation and identification of the hydroxyl radical. The •OH reacts with specific reactants to generate stable compounds detectable by chromatographic assays, of which liquid chromatography and its combination with mass spectrometry is often used. The reagents generally used for the stabilization of free radicals are benzoic acid, salicylic acid and DMSO (ESR technique). The chromatography methods are fast, efficient and sensitive in the detection of hydroxyl radicals, while the reaction process and products are complicated and the treatment of the pre-detection is complex, which makes it less popular than other methods. Considering the non-specificity of fluorescent probes and luminescent probes towards hydroxyl radicals, the chromatographic assay could be used as a means of verifying the existence of •OH[55].
- Spectrophotometry methods: are well-established means of detection of ROS. They work based on the reaction between radicals and redox substances and the difference in absorbance at different wavelengths between substrates and products makes it possible to semi-quantify free radicals. the probes used in these methods are not very sensitive and specific[56].
- Electrochemical biosensor: biosensors work based on the following mechanism: superoxide could reduce some proteins, while these proteins are re-oxidized by the electrode with a suitable one potential; during this process there is an electric current signal generated and then captured by the sensor, and considering the proportional relationship between the strength of the electric signal and superoxide, the concentration of the latter could be determined. The main drawback of this method is the limited types of proteins that could be coated on the surface of the electrodes. biosensors may not be suitable for the production of commercial probes because, due to their instability and uncertainty in the number of layers for different proteins, the composition of their electrodes must be designed on the basis of certain experiments[57].

In general, the methods developed up to now for ROS detection are able to permeate cells, give real-time information and do not kill cells. In the other hand the methods are not very specific and not very sensitive, intermediates are produced which can invalidate the measurement. All measurement techniques require expensive instruments and probes and require a great deal of experience on the part of the operator[52]. Using tests that must be a cell culture means having time, experience and financial resources. Being able to test the large number of new nanomaterials produced every day becomes difficult, very consumed and expensive. Therefore, the need for low-cost, fast tests that do not require cells is increasing[58,59]. During my thesis work I optimised a fast, acellular method, which does not require particular experiences and tools. The method is based on the oxidation of a specific probe molecule for the •OH radicals, N, N – dimethyl - 4 - nitrosoaniline (RNO – $C_8H_{10}N_2O$).

The oxidative power cannot be simply quantified as the degree of ROS generation but it is necessary to evaluate the alteration of the antioxidant capacity. In this regard the consumption of glutathione (GSH) is precisely the key step to be able to evaluate the oxidative power of nanoparticles in the laboratory. GSH is a molecule capable of oxidizing and reducing easily, thus protecting proteins and other cellular materials from the action of free radicals in the body[60]. Cysteine (Cys) is an amino acid constituent of proteins and precursor of GSH with -S termination and its consumption can be interpreted in terms of oxidation, and therefore damage, of the proteins that expose the -S group[61]. Both of these compounds in the reduced form (GSH and Cys) when mixed with Ellman's reagent (2-2 'dinitro 5-5' diphthiobenzoic acid) have a yellow colour (λ = 412nm) which allows them to be analysed using spectrophotometric techniques[62]. Ellman's reagent is used for the analysis of thiols that react with the compound by breaking the disulphide bridge, producing an ion that is yellow in neutral pH water.

The set of GSH - Cys - RNO and RhB models allows to provide indication on the mechanism by which nano-photocatalysts degrade RhB, whether by direct oxidation or by the production of •OH radicals. Moreover, we can predict if the investigated materials have the ability to induce oxidative stress in cells.

Nanomaterials properties affecting their exposure and fate

Nanoparticles are particles formed by atomic or molecular aggregates with a diameter between approximately 1 and 100 nm (according to the EU recommendation 2011 / 696 / EU). They generally occur in the form of powder and are subsequently inserted into aqueous matrices. When this happens, various phenomena can occur[63]:

- Agglomeration: when the particles are inserted into aqueous matrices, forces are established which tend to attract the particles to each other, thus forming an aggregate. This phenomenon is more or less intensified by the chemical nature of the nanoparticle, by its intrinsic properties and by the presence of dispersants, which prevent the aggregation of the nanoparticles[64].
- Diffusion and sedimentation: it can be instantaneous and occurs when the nanoparticles are not stable in suspension and tend to precipitate: it can be lasting over time, in this case a deposit will be seen only after time which can go from hours to days or months[65].
- Dissolution and ion release: for soluble particles, which therefore have the ability to release ions in solution, such as ZnO or Ag[66]. The degree of dissolution of the nanoparticles is another fundamental parameter to understand the availability of ion in solution. For example, the metallic nanoparticles once dissolved increase the availability of ion in the aqueous environment or MNPs can release ion absorbed before. These ions can become a source of risk, a cause of oxidative stress[59].

Understanding these phenomena is necessary to evaluate the effective dose of nanoparticles and ions that can reach the cells, in in-vitro tests or in a broader view in the case of nanoparticles placed in an aqueous environment such as the cellular environment in case of ingestion or inhalation of nanoparticles or nanoparticles dispersed in rivers, lakes or seas. To limit the time and resources required for in vitro or in vivo studies, the European Commission has funded numerous projects (PATROLS – ASINA – NanoInformaTIX) that aim to develop in silico tools that allow predicting the risk and calculating the effective dose of nanoparticles[63,67,68].

The behaviour of nanoparticles that are composed of metal oxides or polymers depends on the very nature of the nanoparticle and its intrinsic properties. With the aim of

providing information from every point of view, an important step is to characterize the nanoparticles at the physical - chemical level[69]. Both metal oxide nanoparticles and MNPs were physical - chemical characterized through different techniques, that give information about morphology, chemical composition, surface area and chemistry etc…

At the same time, it is essential standardize and harmonize dispersion protocol for each type of nanoparticle that allows to obtain stable suspensions (at least for the time of the measurement), reproducible and quality data, minimize test artefacts. The most widespread protocol for metal oxide nanoparticles was developed during a European project NANoREG and is called the 'Nanogenotox dispersion protocol'[70]. This methodology requires the addition of a specific quantity of Bovine Serum Albumin (BSA). BSA is a protein derived from cows. BSA has numerous biochemical applications, it is a small, stable and moderately non - reactive protein. BSA is used for its ability to boost signal in tests, its lack of effect in many biochemical reactions, and its low cost, as large quantities can be readily purified from bovine blood, a by - product of the livestock industry. It is a very popular molecule in the field of nanoparticles because it is biocompatible and does not interfere with in vitro toxicology studies, it also has a remarkable dispersing property, preventing the aggregation of the nanoparticles.

If there is a well - defined and widely used protocol for nanoparticles, the first studies are underway for MNPs. The scientific community expert in nanoparticles proposes the same path carried out in the last decades for the metal oxide NPs, i.e. the first step is to create a dispersion protocol then we move on to a chemical - physical characterization of reference material (another critical point of the study of MNPs). Then the knowledge will be transferred to real MNPs, coming from sampling in soil, sea water etc ... at the same time another key point is the study of the phenomena mentioned above, sedimentation, agglomeration, diffusion in simulating matrices. We try to replicate in the laboratory the real conditions in which the nanoparticles are found, both biological and environmental conditions can be simulated: in the first case, simultaneous body fluids are recreated, therefore salivary, pulmonary, gastrointestinal and other fluids; in the second case it is possible to recreate the saline, chemical and physical conditions of rivers and lakes by studying the behaviour of the nanoparticles at the same temperature as real water, under current or in stagnation conditions.

1.3.3. Analysis

The nano-photocatalysts developed / investigated during the thesis work are evaluated on:

- the basis of the functionality
- the oxidative stress they can induce
- and on cost and environmental sustainability profiles.

The data collected on oxidative stress are used to develop a model, based on the concept of machine learning, which can be predictive of oxidative stress in order to reduce the complexity, albeit minimal, of laboratory tests and allow a first screening and subdivision of photocatalysts according to the same oxidative they can generate. To our knowledge there is neither an explicit mechanistic interpretation nor a predictive model specific to outcomes that relate to oxidative stress. In order to study and examine the usage of machine learning application in this thesis, we used a machine learning algorithm that is able to predict the oxidative stress potentials of the nanomaterial's studies while providing knowledge to be used in a SSbD approach.

An innovative aspect is the consideration of process parameters and general LCA performance criteria as well as the characteristics of nanomaterials for the selection of the best SSbD solution. So, in this section I will describe the four criteria considered to evaluate the photocatalysts investigated during my thesis project. I followed the four main criteria used in industries for the decision of the best material:

1- Functional performance(s) of the addressed solution (Design for Performance): the aim is to provide chemical - physical descriptors of the photocatalytic functionality that compare the experiment parameters, such as the photocatalyst used, the type of irradiation used, the working temperature, the photocatalyst and pollutant concentrations etc… the first question to ask is 'Did I make a good catalyst, or not?'. A good and complete characterization of the material under examination, carried out by combining different techniques, is able to answer the question. However, it is necessary to combine the characterization of reproducibility studies where the material is taken from different synthesis batches and is tested at least 3 times. After carrying out the tests, the descriptors have to be built, a part where the

different knowledge and different techniques must come together to define a scale of goodness of the material[71]. In the case of photocatalysis, the most used descriptor is the photocatalytic efficiency calculated as the ratio between the absorbance at time t and the absorbance at point 0. But this parameter does not consider another important factor involved. So, the focus shifted to the descriptor called Turn Over Frequency (TOF), that considers moles of catalyst, time in second of experiment and efficiency of reaction, as derived by the measured absorbance. A parameter is the kinetic constant k calculated from a pseudo first order equation that superimposes the data in the time graph as abscissa axis, natural logarithm of the absorbance ratio at time t and absorbance at time 0 as the coordinate axis. Finally, it is important to evaluate the quantity of hydroxyl radicals that are produced during the photocatalysis reaction. This is possible with photoluminescence techniques or by incubating photocatalysts with an •OH scavenger such as nitroaniline.

2- Regulation: over the years a lot of information has been collected on the toxicity of nanoparticles for the environment and health and these partly raise the concerns of regulatory and government bodies about the harmful effects of nanoparticles. It is important to ensure that the health and environmental potential impacts of nanoparticles are well under control[72]. Nanotechnologies are being used more and more in various environments, new materials of nanometric dimensions are created every day and like any new material used in industries, whether medical or environmental, nanomaterials must also be tested and evaluated from the point of view of safety. Before being placed on the market, all materials must be tested to verify that they comply with the requirements of government regulations. But first of all, these regulations must exist. When the class of nanomaterials was born there were no guidelines that would allow the establishment of limits and evaluation criteria, scientific projects were funded all over the world, by associations such as EPA (Environmental Protection Agency) and FDA (food and Drug administration) (in the united states) or the commission European Union, designed to define the limits and criteria for evaluation together with governments[73,74]. Community education, engagement and consultation

tend to occur "downstream" once there is at least a moderate level of awareness, often during the process of disseminating and adapting technologies. Upstream engagement, on the other hand, occurs much earlier in the innovation cycle and involves: dialogue and debate on options and pathways of future technology, bringing often expert - led, horizon - exploring approaches to technology forecasting and to a scenario that plans to involve a wider field of perspectives and inputs. It is precisely this latter way of thinking that has developed the safe by design approach which takes into account safety and compliance with regulations from the very first steps of designing a product or material[75].

3- Environmental (& social) sustainability of process and product through its life cycle (Design for Environmental): The Life Cycle Assessment (LCA) is an analytical and systematic methodology that evaluates the environmental footprint of a product or service, throughout its life cycle. It starts from the extraction phases of the raw materials making up the product and then passes in sequence to assess the environmental impact in the phases of production, use and disposal of the product or service[76]. Usually we speak of CO_2 emissions into the atmosphere generated by the consumption of energy and material for each step in the life of the product or service. The quantity of CO_2 emitted is a fact that helps to understand the impact generated on the environment by the product. The purpose of this study allows to identify the product or service or the methods with which they are produced with the least environmental footprint and to choose the most eco - sustainable strategy. LCA studies are regulated by ISO 14040 standards[77].

LCA studies include four phases:

- Definition of the objective and field of application: the motivation, the context and the type of public to which the product or service is intended are defined. Impact categories and impact assessment methods are also defined, as well as quality requirements.
- Life Cycle Inventory (LCI): in this phase the data are collected and the modelling of the system in question is defined. Data of necessary resources and emissions are acquired as well as the waste flow[78].

- Life Cycle Impact Assessment (LCIA): in this phase the potential dangers for human health and the environment are assessed, combined with the data on the consumption of resources and energy and in accordance with the ISO standards, the damage is classified and characterized by providing indicators real impact. In this phase it is possible on a case – by - case basis to normalize or group the impacts and provide each of them with a different weight.
- Interpretation: it is the phase of correlation of all data to propose recommendations in accordance with the objectives of the study. In this phase the critical points are identified to then improve the modelling and obtain more robust conclusions[79].

4- Cost (Design for Costing): to evaluate the cost of a product, the TEA (technical economic analysis) software models are used, which allow the calculation of capital costs, operating costs and revenues based on technical and financial input parameters. It is increasingly used in the chemical, oil, bioprocess and energy sectors to study new technologies or optimize existing ones. You can evaluate the economic feasibility and anticipate if a process will be profitable enough, so it can help companies to avoid bad investments. TEAs can help the research and development phase to steer researchers towards the most promising path. TEA models combine elements of cost design and modelling with process or tool sizing, estimate capital costs and operating costs[80].

The criteria just described can be defined in a 4 - dimensional space, difficult to represent. Then the functionality and cost criteria are merged. Therefore, it is possible to define the Safe by Design strategy in an easily representable 3 - dimensional space and evaluate which material is actually good for the application in question, taking all aspects into account.

1.3.4. Design

In Table 1.1 the design cases of this thesis have been listed. As far as nano-photocatalysts are concerned, they have been studied at laboratory level and in semi - pilot plants using rhodamine B as a model of pollutant. At the laboratory level four materials have been

studied: TAC, TiO_2:SiO_2 1:3, TGO and g-C_3N_4. While in the semi - pilot plant TAC and TiO_2:SiO_2 1:3. For both cases the main end point is the functionality of the photocatalysts expressed as photocatalytic efficiency and TOF. The final effects coming from the different type of material, from the radiating light (UV and visible) were studied, in the semi - pilot plant the effects of the working temperature and the type of support for the nano-photocatalysts were investigated.

The third case study aims to evaluate the tendency to produce •OH radicals (RNO model) and the oxidative stress induced by photocatalysts (GSH / Cys model). The study was conducted in dark and UV light conditions for all four materials investigated in the thesis.

A regard the MNPs, the most relevant materials such as PE (polyethylene), PU (polyurethane) and PET (polyethylene terephthalate) were chosen and they were characterized at the chemical - physical level and in relevant matrices such as river and sea water, at different exposure times.

Table 1.1. Design cases of thesis.

DESIGN CASES	Case study	Model	Material	End point	Parameters
Nano - photocatalysts	Lab scale	RhB	TAC TiO_2:SiO_2 1:3 TGO g-C_3N_4	Photocatalytic efficiency TOF	Materials light
	Semi – pilot plant	RhB	TAC TiO_2:SiO_2 1:3	Photocatalytic efficiency TOF	Materials Light Fabrics temperature
	ROS productin & Oxidative stress	GSH – Cys - RNO	TAC TiO_2:SiO_2 1:3 TGO g-C_3N_4	Moles of MODEL consumed / m^2	Materials light
Micro – nano Plastics	P – chem characterization	-	PE – PU - PET	Dimension Shape Chemical surface Colloidal information	Materials
	Behaviour in relevant matrices	Simulant fluid	PE – PU - PET	Dimension Shape Chemical surface Colloidal information	Materials Time of exposure

1.3.5. Verify

In the context of experimental research, test beds (semi - pilot plants) play an important role in enabling the development of new products and processes, providing a range of services that help designers create the experimental environment, collect data on it and

produce samples for quality and performance evaluation. Furthermore, pilot plants are necessary for the scale - up and validation of production processes, for technical - economic purposes, also helping to define the safe operating environment within which the plant must operate, to ensure compliance with safety codes and regulations.

The pilot plant allows to obtain representative data of an industrial plant, to study the physical effects on the chemical reaction, the long - term effects on the material components, the encrustation phenomena of equipment and the corrosion phenomena. In addition, the pilot can be used to produce representative quantities of the product for the control of quality[81,82]. A plant design phase is required, following the guidelines of standard plants used in urban areas. All the parameters analysed in a real plant such as the water flow rate, the dimensional proportions and the pollutant concentrations are all to be evaluated and engineered in the pilot plant with the aim of replicating the real conditions in the best possible way. It is important to evaluate in the mass production of a material or its use in the field before using a large amount of time and construction of a plant, in the changes to be made to adapt to a new or a new production. Understanding at this level the problems that can occur during a scale - up allows a quick and inexpensive resolution. On the other hand, however, it is necessary to guarantee the same quality and performance of the material found on a laboratory scale. This step is used to:

- Define the physical spaces required and the arrangement of the different parts of the system.
- Evaluate, validate and finalize all process and control parameters.
- Define and validate the operations to be carried out and in what order.
- Focus on all the critical steps that need to be monitored.
- Evaluate production and costs[83,84].

There may be many aspects to be assessed on a case – by - case basis, based on the objective to be achieved. In the case of photocatalysts intended to be used for the purification of water from pollutants, different aspects must be evaluated such as the best working temperature which maximizes the photocatalytic efficiency but which does not require further steps. The ideal case is that the greatest efficiency occurs at the temperature at which the water to be purified is already found[85,86]. Also, the type of light used to irradiate the photocatalysts is an important aspect, because as already

mentioned above, the UV radiations in the solar spectrum are a minimum quantity, perhaps not necessary to make the material express the photocatalytic activity. Inserting UV lamps in an urban installation may not be so simple, due to the costs of electricity, the individual protections that workers should adopt etc ...[14,15]. Another fundamental aspect to be evaluated is the release of nanoparticles into the environment. It is therefore an obligation to ensure that the material is not dispersed by immobilizing the nanoparticles on a support that could be a fabric. Fabrics, especially natural ones, show hydrophilic behaviour and a high affinity to metal oxides, such as TiO_2, which can be firmly bonded to fabric fibres.

I want to thank Massimo Perucca (Managing Director of Project - Project Hub 360) and Irini Furxhi (Postdoctoral researcher) for their support during the development of the sustainability profiles and the machine learning tool, respectively. Moreover, thanks go to the Witek company (Italy) for the realization of the lamps used in the semi - pilot plant.

Finally, I want to thank for the opportunity to have been involved in the EU project PATROLS (GA: 760813), ASINA (GA: 862444), NanoInformaTIX (GA: 814426) and PlasticsFate (GA: 965367).

Reference

1. Organizzazione delle Nazioni Unite Trasformare il nostro mondo: l'Agenda 2030 per lo Sviluppo Sostenibile (Agenda2030). *Risoluzione adottata dall'Assemblea Gen. 25 settembre 2015* **2015**, 1.
2. Pirozzi, G. Progress on household drinking water, sanitation and hygiene I 2000-2017 Progress on household drinking water, sanitation and hygiene I 2000-2017 Progress on household drinking water, sanitation and hygiene 2000-2017: Special focus on inequalities. **2016**.
3. Patto, I.N.; Europeo, V. Il Nuovo Patto. **2020**, 1–16.
4. European Commission Eliminating pollution - The European Green Deal. **2019**.
5. Clarke, R.M.; Cummins, E. Evaluation of "Classic" and Emerging Contaminants Resulting from the Application of Biosolids to Agricultural Lands: A Review. *Hum. Ecol. Risk Assess.* **2015**, *21*, 492–513, doi:10.1080/10807039.2014.930295.
6. Nikolaou, A. Pharmaceuticals and related compounds as emerging pollutants in water: Analytical aspects. *Glob. Nest J.* **2013**, *15*, 1–12, doi:10.30955/gnj.000969.

7. Azizi-Lalabadi, M.; Pirsaheb, M. Investigation of steroid hormone residues in fish: A systematic review. *Process Saf. Environ. Prot.* **2021**, *152*, 14–24, doi:10.1016/j.psep.2021.05.020.
8. Ingham, H.R.; Sisson, P.; Selkon, J.B. Interactions between micro-organisms and metronidazole. *J. Antimicrob. Chemother.* **1982**, *10*, 84–87, doi:10.1093/jac/10.2.84.
9. Adeleye, A.S.; Conway, J.R.; Garner, K.; Huang, Y.; Su, Y.; Keller, A.A. Engineered nanomaterials for water treatment and remediation: Costs, benefits, and applicability. *Chem. Eng. J.* **2016**, *286*, 640–662, doi:10.1016/j.cej.2015.10.105.
10. Ghasemzadeh, G.; Momenpour, M.; Omidi, F.; Hosseini, M.R.; Ahani, M.; Barzegari, A. Applications of nanomaterials in water treatment and environmental remediation. *Front. Environ. Sci. Eng.* **2014**, *8*, 471–482, doi:10.1007/s11783-014-0654-0.
11. Lu, F.; Astruc, D. Nanocatalysts and other nanomaterials for water remediation from organic pollutants. *Coord. Chem. Rev.* **2020**, *408*, 213180, doi:10.1016/j.ccr.2020.213180.
12. Khin, M.M.; Nair, A.S.; Babu, V.J.; Murugan, R.; Ramakrishna, S. A review on nanomaterials for environmental remediation. *Energy Environ. Sci.* **2012**, *5*, 8075–8109, doi:10.1039/c2ee21818f.
13. UN Water Water and Sustainable Development From vision to action: Means and tools for Implementation and the role of different actors. *UN-Water Zaragoza Conf.* **2016**, 68.
14. Mahanta, U.; Khandelwal, M.; Suresh Deshpande, A. TiO2@SiO2 nanoparticles for methylene blue removal and photocatalytic degradation under natural sunlight and low-power UV light. *Appl. Surf. Sci.* **2021**, *576*, 151745, doi:10.1016/j.apsusc.2021.151745.
15. Basavarajappa, P.S.; Patil, S.B.; Ganganagappa, N.; Reddy, K.R.; Raghu, A. V.; Reddy, C.V. Recent progress in metal-doped TiO2, non-metal doped/codoped TiO2 and TiO2 nanostructured hybrids for enhanced photocatalysis. *Int. J. Hydrogen Energy* **2020**, *45*, 7764–7778, doi:10.1016/j.ijhydene.2019.07.241.
16. Chong, M.N.; Jin, B.; Chow, C.W.K.; Saint, C. Recent developments in photocatalytic water treatment technology: A review. *Water Res.* **2010**, *44*, 2997–3027, doi:10.1016/j.watres.2010.02.039.
17. Ortelli, S.; Costa, A.L.; Dondi, M. TiO2 nanosols applied directly on textiles using different purification treatments. *Materials (Basel).* **2015**, *8*, 7988–7996, doi:10.3390/ma8115437.
18. Circle, S.J.; Bay, G. System Dynamics in Six Sigma Practice Strategic Six Sigma Roles for SD. **2002**, 1–28.
19. Cronemyr, P. DMAIC and DMADV – differences , similarities and synergies. **2007**, *3*.
20. Fujishima, A.; Zhang, X.; Tryk, D.A. TiO2 photocatalysis and related surface phenomena. *Surf. Sci. Rep.* **2008**, *63*, 515–582, doi:10.1016/j.surfrep.2008.10.001.
21. Auta, H.S.; Emenike, C.U.; Fauziah, S.H. Distribution and importance of microplastics in the marine environmentA review of the sources, fate, effects, and potential solutions. *Environ. Int.* **2017**, *102*, 165–176, doi:10.1016/j.envint.2017.02.013.
22. Liebezeit, G.; Liebezeit, E. Synthetic particles as contaminants in German beers. *Food Addit. Contam. - Part A Chem. Anal. Control. Expo. Risk Assess.* **2014**, *31*, 1574–1578, doi:10.1080/19440049.2014.945099.
23. Lee, S.Y.; Park, S.J. TiO2 photocatalyst for water treatment applications. *J. Ind. Eng. Chem.* **2013**, *19*, 1761–1769, doi:10.1016/j.jiec.2013.07.012.

24. Malekshahi Byranvand, M.; Nemati Kharat, A.; Fatholahi, L.; Malekshahi Beiranvand, Z. A Review on Synthesis of Nano-TiO2 via Different Methods. *J. Nanostructures* **2013**, *3*, 1–9, doi:10.7508/jns.2013.01.001.
25. Bhatkhande, D.S.; Pangarkar, V.G.; Beenackers, A.A.C.M. Photocatalytic degradation for environmental applications - A review. *J. Chem. Technol. Biotechnol.* **2002**, *77*, 102–116, doi:10.1002/jctb.532.
26. Ortelli, S.; Costa, A.L.; Matteucci, P.; Miller, M.R.; Blosi, M.; Gardini, D.; Tofail, S.A.M.; Tran, L.; Tonelli, D.; Poland, C.A. Silica modification of titania nanoparticles enhances photocatalytic production of reactive oxygen species without increasing toxicity potential in vitro. *RSC Adv.* **2018**, *8*, 40369–40377, doi:10.1039/C8RA07374K.
27. Dong, H.; Zeng, G.; Tang, L.; Fan, C. ScienceDirect An overview on limitations of TiO 2 -based particles for photocatalytic degradation of organic pollutants and the corresponding countermeasures. *Water Res.* **2015**, *79*, 128–146, doi:10.1016/j.watres.2015.04.038.
28. Chen, J.; Qiu, F.; Xu, W.; Cao, S.; Zhu, H. Applied Catalysis A : General Recent progress in enhancing photocatalytic efficiency of TiO 2 -based materials. *"Applied Catal. A, Gen.* **2015**, *495*, 131–140, doi:10.1016/j.apcata.2015.02.013.
29. Wu, Y.; Wang, T.; Zhang, Y.; Xin, S.; He, X.; Zhang, D.; Shui, J. Electrocatalytic performances of g-C 3 N 4 -LaNiO 3 composite as bi-functional catalysts for lithium-oxygen batteries. *Sci. Rep.* **2016**, *6*, 4–11, doi:10.1038/srep24314.
30. Inagaki, M.; Tsumura, T.; Kinumoto, T.; Toyoda, M. Graphitic carbon nitrides (g-C3N4) with comparative discussion to carbon materials. *Carbon N. Y.* **2019**, *141*, 580–607, doi:10.1016/j.carbon.2018.09.082.
31. Wen, J.; Xie, J.; Chen, X.; Li, X. A review on g-C 3 N 4 -based photocatalysts. *Appl. Surf. Sci.* **2017**, *391*, 72–123, doi:10.1016/j.apsusc.2016.07.030.
32. Chen, Z.; Zhang, S.; Liu, Y.; Alharbi, N.S.; Rabah, S.O.; Wang, S.; Wang, X. Synthesis and fabrication of g-C3N4-based materials and their application in elimination of pollutants. *Sci. Total Environ.* **2020**, *731*, 139054, doi:10.1016/j.scitotenv.2020.139054.
33. Liang, J.; Yang, X.; Wang, Y.; He, P.; Fu, H.; Zhao, Y.; Zou, Q.; An, X. A review on g-C3N4incorporated with organics for enhanced photocatalytic water splitting. *J. Mater. Chem. A* **2021**, *9*, 12898–12922, doi:10.1039/d1ta00890k.
34. Liu, X.; Ma, R.; Zhuang, L.; Hu, B.; Chen, J.; Liu, X. Technology Recent developments of doped g-C 3 N 4 photocatalysts for the degradation of organic pollutants. *Crit. Rev. Environ. Sci. Technol.* **2021**, *51*, 751–790, doi:10.1080/10643389.2020.1734433.
35. Soldano, C.; Mahmood, A.; Dujardin, E. Production, properties and potential of graphene. *Carbon N. Y.* **2010**, *48*, 2127–2150, doi:10.1016/j.carbon.2010.01.058.
36. Dai, L.; Xue, Y.; Qu, L.; Choi, H.J.; Baek, J.B. Metal-Free Catalysts for Oxygen Reduction Reaction. *Chem. Rev.* **2015**, *115*, 4823–4892, doi:10.1021/cr5003563.
37. SIEGEL, R.W.; HAHN, H.; RAMASAMY, S.; ZONGQUAN, L.; TING, L.; GRONSKY, R. STRUCTURE AND PROPERTIES OF NANOPHASE TiO 2 . *Le J. Phys. Colloq.* **1988**, *49*, C5-681-C5-686, doi:10.1051/jphyscol:1988589.
38. Adly, M.S.; El-Dafrawy, S.M.; El-Hakam, S.A. Application of nanostructured graphene oxide/titanium dioxide composites for photocatalytic degradation of rhodamine B and acid green 25 dyes. *J. Mater. Res. Technol.* **2019**, *8*, 5610–5622, doi:10.1016/j.jmrt.2019.09.029.

39. Pan, X.; Zhao, Y.; Liu, S.; Korzeniewski, C.L.; Wang, S.; Fan, Z. Comparing graphene-TiO 2 nanowire and graphene-TiO 2 nanoparticle composite photocatalysts. *ACS Appl. Mater. Interfaces* **2012**, *4*, 3944–3950, doi:10.1021/am300772t.
40. Minella, M.; Sordello, F.; Minero, C. Photocatalytic process in TiO2/graphene hybrid materials. Evidence of charge separation by electron transfer from reduced graphene oxide to TiO2. *Catal. Today* **2016**, doi:10.1016/j.cattod.2016.03.040.
41. Materials, E.A. *Medical Devices: Priority medical devices*; ISBN 9781783269860.
42. Ortelli, S.; Poland, C.A.; Baldi, G.; Costa, A.L. Silica matrix encapsulation as a strategy to control ROS production while preserving photoreactivity in nano-TiO2. *Environ. Sci. Nano* **2016**, *3*, 602–610, doi:10.1039/c6en00009f.
43. Chen, F.; Zhao, J.; Hidaka, H. Highly selective deethylation of Rhodamine B: Adsorption and photooxidation pathways of the dye on the TiO2/SiO2 composite photocatalyst. *Int. J. Photoenergy* **2003**, *5*, 209–217, doi:10.1155/S1110662X03000345.
44. Wang, G.; Xu, L.; Zhang, J.; Yin, T.; Han, D. Enhanced photocatalytic activity of TiO 2 powders (P25) via calcination treatment. *Int. J. Photoenergy* **2012**, *2012*, doi:10.1155/2012/265760.
45. Friedmann, D.; Mendive, C.; Bahnemann, D. TiO2 for water treatment: Parameters affecting the kinetics and mechanisms of photocatalysis. *Appl. Catal. B Environ.* **2010**, *99*, 398–406, doi:10.1016/j.apcatb.2010.05.014.
46. Rochkind, M.; Pasternak, S.; Paz, Y. Using dyes for evaluating photocatalytic properties: A critical review. *Molecules* **2015**, *20*, 88–110, doi:10.3390/molecules20010088.
47. Anwer, H.; Mahmood, A.; Lee, J.; Kim, K.H.; Park, J.W.; Yip, A.C.K. Photocatalysts for degradation of dyes in industrial effluents: Opportunities and challenges. *Nano Res.* **2019**, *12*, 955–972, doi:10.1007/s12274-019-2287-0.
48. Arbeloa, I.L.; Ojeda, P.R. Molecular forms of rhodamine B. *Chem. Phys. Lett.* **1981**, *79*, 347–350, doi:10.1016/0009-2614(81)80219-9.
49. Ma, H.Y.; Zhao, L.; Guo, L.H.; Zhang, H.; Chen, F.J.; Yu, W.C. Roles of reactive oxygen species (ROS) in the photocatalytic degradation of pentachlorophenol and its main toxic intermediates by TiO2/UV. *J. Hazard. Mater.* **2019**, *369*, 719–726, doi:10.1016/j.jhazmat.2019.02.080.
50. Picardo, M.; Dell'Anna, M.L. Oxidative stress. *Vitiligo* **2010**, 231–237, doi:10.1007/978-3-540-69361-1_27.
51. Liebert, M.A.; Jones, D.P. Clinical Measures of the Balance. **2006**, *8*.
52. Zhang, Y.; Dai, M.; Yuan, Z. Methods for the detection of reactive oxygen species. *Anal. Methods* **2018**, *10*, 4625–4638, doi:10.1039/c8ay01339j.
53. Gomes, A.; Fernandes, E.; Lima, J.L.F.C. Fluorescence probes used for detection of reactive oxygen species. *J. Biochem. Biophys. Methods* **2005**, *65*, 45–80, doi:10.1016/j.jbbm.2005.10.003.
54. Yu, W.; Zhao, L. Chemiluminescence detection of reactive oxygen species generation and potential environmental applications. *TrAC - Trends Anal. Chem.* **2021**, *136*, 116197, doi:10.1016/j.trac.2021.116197.
55. Niederländer, H.A.G.; van Beek, T.A.; Bartasiute, A.; Koleva, I.I. Antioxidant activity assays on-line with liquid chromatography. *J. Chromatogr. A* **2008**, *1210*, 121–134, doi:10.1016/j.chroma.2008.09.061.

56. Herman, J.; Zhang, Y.; Castranova, V.; Neal, S.L. Emerging technologies for optical spectral detection of reactive oxygen species. *Anal. Bioanal. Chem.* **2018**, *410*, 6079–6095, doi:10.1007/s00216-018-1233-1.
57. Calas-Blanchard, C.; Catanante, G.; Noguer, T. Electrochemical Sensor and Biosensor Strategies for ROS/RNS Detection in Biological Systems. *Electroanalysis* **2014**, *26*, 1277–1286, doi:10.1002/elan.201400083.
58. Sauvain, J.J.; Rossi, M.J.; Riediker, M. Comparison of three acellular tests for assessing the oxidation potential of nanomaterials. *Aerosol Sci. Technol.* **2013**, *47*, 218–227, doi:10.1080/02786826.2012.742951.
59. Simeone, F.C.; Costa, A.L. Assessment of cytotoxicity of metal oxide nanoparticles on the basis of fundamental physical-chemical parameters: A robust approach to grouping. *Environ. Sci. Nano* **2019**, *6*, 3102–3112, doi:10.1039/c9en00785g.
60. Meister, A.; Anderson, M.E. Further 1983.52:711--60. **1983**.
61. Kredich, N.M. Biosynthesis of Cysteine. *EcoSal Plus* **2008**, *3*, doi:10.1128/ecosalplus.3.6.1.11.
62. Ellman, G.L. Tissue Su ~ yd ~ l Groups. **1959**, 70–77.
63. Thomas, D.G.; Smith, J.N.; Thrall, B.D.; Baer, D.R.; Jolley, H.; Munusamy, P.; Kodali, V.; Demokritou, P.; Cohen, J.; Teeguarden, J.G. ISD3: A particokinetic model for predicting the combined effects of particle sedimentation, diffusion and dissolution on cellular dosimetry for in vitro systems. *Part. Fibre Toxicol.* **2018**, *15*, 1–22, doi:10.1186/s12989-018-0243-7.
64. Ashraf, M.A.; Peng, W.; Zare, Y.; Rhee, K.Y. Effects of Size and Aggregation/Agglomeration of Nanoparticles on the Interfacial/Interphase Properties and Tensile Strength of Polymer Nanocomposites. *Nanoscale Res. Lett.* **2018**, *13*, doi:10.1186/s11671-018-2624-0.
65. Cho, E.C.; Zhang, Q.; Xia, Y. The effect of sedimentation and diffusion on cellular uptake of gold nanoparticles. *Nat. Nanotechnol.* **2011**, *6*, 385–391, doi:10.1038/nnano.2011.58.
66. Misra, S.K.; Dybowska, A.; Berhanu, D.; Luoma, S.N.; Valsami-Jones, E. The complexity of nanoparticle dissolution and its importance in nanotoxicological studies. *Sci. Total Environ.* **2012**, *438*, 225–232, doi:10.1016/j.scitotenv.2012.08.066.
67. DeLoid, G.M.; Cohen, J.M.; Pyrgiotakis, G.; Pirela, S. V.; Pal, A.; Liu, J.; Srebric, J.; Demokritou, P. Advanced computational modeling for in vitro nanomaterial dosimetry. *Part. Fibre Toxicol.* **2015**, *12*, 1–20, doi:10.1186/s12989-015-0109-1.
68. Keller, J.G.; Quevedo, D.F.; Faccani, L.; Costa, A.L.; Landsiedel, R.; Werle, K.; Wohlleben, W. Dosimetry in vitro–exploring the sensitivity of deposited dose predictions vs. affinity, polydispersity, freeze-thawing, and analytical methods. *Nanotoxicology* **2021**, *15*, 21–34, doi:10.1080/17435390.2020.1836281.
69. Cerasa, M.; Teodori, S.; Pietrelli, L. Searching nanoplastics: From sampling to sample processing. *Polymers (Basel).* **2021**, *13*, 1–26, doi:10.3390/polym13213658.
70. Hartmann, N.B.; Jensen, K.A.; Baun, A.; Rasmussen, K.; Rauscher, H.; Tantra, R.; Cupi, D.; Gilliland, D.; Pianella, F.; Riego Sintes, J.M. Techniques and Protocols for Dispersing Nanoparticle Powders in Aqueous Media - Is there a Rationale for Harmonization? *J. Toxicol. Environ. Heal. - Part B Crit. Rev.* **2015**, *18*, 299–326, doi:10.1080/10937404.2015.1074969.
71. Melchionna, M.; Fornasiero, P. Updates on the Roadmap for Photocatalysis. *ACS Catal.* **2020**, *10*, 5493–5501, doi:10.1021/acscatal.0c01204.

72. [Dhawan,_Alok;_Kumar,_Ashutosh;_Shanker,_Rishi;_Si(b-ok.xyz).pdf.
73. Omann, I.; Kowalski, K.; Bohunovsky, L.; Madlener, R.; Stagl, S. The Influence of Social Preferences on Multi-Criteria Evaluation of Energy Scenarios. *SSRN Electron. J.* **2012**, 1–25, doi:10.2139/ssrn.1620466.
74. Marchant, G.E.; Sylvester, D.J. Transnational models for regulation of nanotechnology. *J. Law, Med. Ethics* **2006**, *34*, 714–725, doi:10.1111/j.1748-720X.2006.00091.x.
75. Leach, M.; Scoones, I. The Slow Race: Making Technology Work For The Poor. *Demos* **2006**, 7–73.
76. Klöpffer, W. Life Cycle Assessment: From the beginning to the current state. *Environ. Sci. Pollut. Res.* **1997**, *4*, 223–228, doi:10.1007/BF02986351.
77. International council of chemical associations An Executive Guide: How to Know If and When it's Time to Commission a Life Cycle Assessment An Executive Guide. **2010**, 4.
78. Simonen, K. Life cycle assessment. *Life Cycle Assess.* **2014**, *45*, 1–159, doi:10.4324/9781315778730.
79. Azapagic, A.; Solberg-Johansen, B. Life cycle assessment. *Eng.* **1998**, *239*, 26, doi:10.1002/0471238961.lifeguin.a01.pub2.
80. Medina, J.A. 22 . Economic Analysis and Environmental Assessment.
81. Stitt, E.H.; Simmons, M.J.H. Scale-Up of Chemical Reactions. **2011**.
82. Alert, T.S.; Web, C. A Checklist for Inherently Safer Chemical Reaction Process Design and Operation Introduction Œ Chemical reaction hazard identification • Reaction process design considerations Ž Where to get more help. **2004**.
83. Khodadadian, F.; de Boer, M.W.; Poursaeidesfahani, A.; van Ommen, J.R.; Stankiewicz, A.I.; Lakerveld, R. Design, characterization and model validation of a LED-based photocatalytic reactor for gas phase applications. *Chem. Eng. J.* **2018**, *333*, 456–466, doi:10.1016/j.cej.2017.09.108.
84. Li, R.; Li, T.; Zhou, Q. *Impact of titanium dioxide (TiO2) modification on its application to pollution treatment—a review*; 2020; Vol. 10; ISBN 2223501117.
85. Meng, Y.; Xia, S.; Pan, G.; Xue, J.; Jiang, J.; Ni, Z. Preparation and photocatalytic activity of composite metal oxides derived from Salen-Cu(II) intercalated layered double hydroxides. *Korean J. Chem. Eng.* **2017**, *34*, 2331–2341, doi:10.1007/s11814-017-0135-9.
86. Meng, F.; Liu, Y.; Wang, J.; Tan, X.; Sun, H.; Liu, S.; Wang, S. Temperature dependent photocatalysis of g-C3N4, TiO2 and ZnO: Differences in photoactive mechanism. *J. Colloid Interface Sci.* **2018**, *532*, 321–330, doi:10.1016/j.jcis.2018.07.131.

Chapter 2: Development of nano – photocatalysts used in AOPs for removing (bio-) organic pollutants – SOLUTION 1

2.1. Introduction

In urban areas, water is purified through Wastewater Treatment Plants (WWTPs). These allow for the introduction of wastewater from agricultural processes, industries and household waste, back into the system as drinking water, at best, or as irrigation water. Wastewater management in combination with sanitation and hygiene offers the best cost - effective alternative to reap multiple benefits in terms of health improvements, food security, increased production and income and new job opportunities. The traditional water purification treatments aim to reduce undesired chemical compounds, organic and inorganic materials, and biological contaminants below certain limits, established in Europe by the EU Water Framework Directive (WFD), in compliance with more specific legislation, such as the Drinking or Bathing Water Directive, the Floods Directive and the Marine Strategy Framework Directive, as well as by international agreements[1].

Water remediation treatments can be divided based on detected contaminants in:

- Physic: sedimentable and non - sedimentable suspended solids are eliminated.
- Physical - chemical: the non - sedimentable residues are completely removed and the chemical characteristics are corrected (iron removal, desilication, fluorination).
- Purification: the organoleptic characteristics of the water are improved with absorption on activated carbon and demineralization.
- Disinfection: the presence of microorganisms is eliminated (chlorination, ozonation)[2].

All post - treatment problems use resources and costs. If the plant includes an anaerobic phase, there is also the biogas to be disposed. Scientific research efforts are put to solve the following problem: extensive use of chemicals such as chlorine which allows disinfection but at the same time produces by - products that can be dangerous (disinfection – by - product). In the disinfection step, bacteria, viruses and other pathogens are killed thanks to hydroxyl radicals. However, traditional disinfection does not allow to eliminate persistent organic pollutants (POPs) and pharmaceuticals and personal care products (PPCPs)[3,4]. This is why Advanced Oxidation Processes (AOPs) are introduced

as a set of chemical treatments designed with the aim of eliminating recalcitrant contaminants through the use of hydroxyl radicals generated with non - hazardous chemical elements[5,6]. In AOPs three main phases are involved:

1. •OH production.
2. initial attack of the target molecules by •OH and partial breakdown of the molecules;
3. sequential attack of the •OH to complete mineralization (contaminants are turned into CO_2 and H_2O).

Photocatalysis is referred to as the acceleration of a photoreaction by the presence of a semiconductor catalyst. For this reason, photocatalysis can be considered as an effective AOP. Semiconductor materials are used for photocatalysis due to their band structure: in a semiconductor the valence (lower energy band) and conduction (higher energy band) bands are separated by a band gap. When the semiconductor is irradiated with sufficiently energy light, equal to or greater than the amount of the band gap, an electron in the valence band can absorb the energy of the photon and pass into the conduction band, leaving a gap in the valence band. The electrons that are promoted to the conduction band are able to move through the semiconductor generating hole (h^+) / electron (e^-) ion pairs. The h^+ / e^- recombination process is very favoured and in the order of nanoseconds, however this time is sufficient to allow the charge transfer to species adsorbed on the surface of the semiconductor. The released electrons are able to react with water and oxygen molecules on the surface to form free radicals (Reactive Oxygen Species – ROS). These radicals are very reactive species that are able to decompose most organic compounds as well as biological contaminants present in aqueous media[7–9].

Nanomaterials (NMs) are the suitable candidates as photocatalysts in AOPs because of their small size (10 – 100 nm) and therefore high surface areas. The photocatalysis reaction occurs at the surface of the catalysts and therefore increases their efficiency necessary to maximize the surface / volume ratio of the catalysts. Furthermore, nano-photocatalysts having the crystal lattice in a state of almost perfection, electrons and holes migrate to the surface in a very short time with a maximization of a photoactivity

[10]. NMs also have high absorbency and reactivity, antimicrobial properties for disinfection and biofouling control[2,10].

The main catalysts used are metal oxide compounds such as TiO_2, ZnO and CeO_2[12], but it all presented the big disadvantage of being active only under UV light. In recent years, the scientific community is moving in the direction of active photocatalysts under the irradiation of sunlight, a unique natural resource that is abundant, inexpensive and risk - free. Replacing UV rays with solar rays also allows for greener chemistry, to respect the Green Deal mentioned above, without however renouncing the photocatalytic efficiency for the degradation of pollutants[13,14]. The requirements to define a material as a good catalyst are: (i) photoactive (ii) activated by visible irradiation (iii) chemically and biologically inert (iv) stable (not subject to photo - corrosion) (v) economical (vi) non - toxic[15].

To overcome the disadvantages, two main ways are possible:

1. doping TiO_2: the oxygen vacancies can be easily created in the grain boundaries of the polycrystalline samples which form a grain boundary defect state in the band gap of TiO_2. Oxygen vacancies are active electron traps. Since the oxygen defect states lie close to the CB of TiO_2, the electrons captured by oxygen defects can be promoted to the surface by visible light absorption where they engage in degradation of pollutants[16]. The metals used to doping TiO_2 are N[17], S[18], B[19], Fe[20], Mo[21] and C[19].
2. Surface sensitization: facilitates electron transfer between the dye molecules and the host semiconductor. The insertion of noble metals such as Au or Ag allow to exploit the concept of plasmon resonance. When the electric field of light interacts with the unbound electron in metal nanostructures, a powerful evanescent electromagnetic wave is generated on the surface of these nanostructures. This can increase absorption and photocurrent[22].

During my thesis research, different TiO_2 - based photocatalysts were synthesized and characterized: TiO_2:SiO_2 1:3 obtained by heterocoagulation and TiO_2 - graphene oxide (TGO) obtained by sonochemical method. The introduction of SiO_2 allows the reduction of the hole / electron recombination speed[23], the increase of the radicals' availability

and the increased ability to onset and degrade more organic molecules[24]. Thus, it is supposed that the introduction of SiO_2 in TiO_2 allows an improvement of the photocatalytic efficiency. In TGO composite, the heterojunction between graphene and TiO_2 promotes the separation of the h^+ / e^- pairs in TiO_2, hindering its recombination. Also, the formation of the Ti – O - C bond in TGO composite allows to extend at visible wavelength range the activation of TiO_2[25]. Both composite materials were synthesized in our laboratory starting from commercial TiO_2 (nanosol in TiO_2:SiO_2 1:3 and powder in TGO), in particular for the TGO material, the synthesis of graphene oxide was performed through the modified Hummer method starting from graphite powder[26].

Following the way of shifting the activation of the photocatalyst into the visible light range, we investigated a novel material graphitic carbon nitride (g-C_3N_4) selected due to its visible light sensitive material with an adequate band gap (2.7 eV).

In this work, we focused on the development of a laboratory - scale photocatalysts by investigating their quantum efficiency when irradiated by UV and visible light, using a solar simulator. Photodegradation of rhodamine B (RhB) was used as a reaction model. The photocatalytic efficiency, the Turn over Frequency (TOF) and Chemical Oxygen Demand (COD) values were the endpoints of interest. In addition, sustainability and cost studies (during the use phase) were identified as evaluation criteria to select the best trade - off material and define the better strategy by following a Safe – by - Design paradigm.

2.2. Materials & Methods

2.2.1. Materials

TiO_2 nanosol (NAMA41, 6 wt%), called TAC and SiO_2 nanosol 40 wt% (Ludox® HS - 40) were purchased from Colorobbia (Italy) and Grace Davison (USA), respectively. TiO_2 nano-powder DT - 51 was purchased from CristalACTiV™, melamine 99%, rhodamine B (dye content ≈95%) target dye, ion exchanger Dowex® 50 W x 4 acidic cation exchanger resin, hydrogen peroxide - H_2O_2 (30%), hydrochloric acid - HCl (37 %), sodium nitrate – NaOH (> 99 %), potassium permanganate - $KMnO_4$ (99.5 %) and absolute ethanol (> 99.8 %) were purchased from Sigma Aldrich (Italy). Graphite GS25E powder was purchased from Magaldi (Italy). Sulphuric acid - H_2SO_4 (96 %) was purchased from Titolchimica (Italy).

2.2.2. Photocatalyst preparation

2.2.2.1. TiO_2:SiO_2

Acid TiO_2 nanosol (TAC, pH = 1.5) was used as benchmark material and precursor to TiO_2:SiO_2 suspension. TAC was obtained diluting at the 3 wt% concentration with distilled water (DI) water. SiO_2 nanosol 40 wt% (Ludox® HS - 40) was diluted at the concentration 3 wt% with DI water and treated with ion exchange Dowex® 50 W X 4 acidic cationic exchanger resin in order to decrease the pH from 10 to 4 (SiO_2-R). TiO_2:SiO_2 composite was prepared by the heterocoagulation method. TAC suspension was dropped into SiO_2-R suspension and the TiO_2:SiO_2 sample was obtained through electrostatic interactions between negatively charged silica nanoparticles and positively charged titania nanoparticles. The electrostatic interactions between SiO_2 and TiO_2 surfaces were promoted by mixing the sols in well - defined ratios (TiO_2:SiO_2 1:3) and by ball milling for 24h with zirconia spheres (diameter 5 mm) as grinding media.

2.2.2.2 TGO

The graphene oxide used was synthesized from graphite powder using the modified Hummer method as described by Adly and co - workers[26]. 2 g of $NaNO_3$ and 25 mL of concentrated H_2SO_4 were added to a synthesis flask, when the sodium nitrate is completely dissolved 2 g of graphite powder were added for exfoliation. The compound was kept under mechanical stirring for 2 h with an ice bath. Making sure that the temperature was < 20 °C, 4 g of $KMnO_4$ were slowly added and left under mechanical stirring for 24 hours, a colour changes of the mixture from black to dark green was noted and a progressive thickening until a smooth and homogeneous paste was obtained. After 24 h, while maintaining mechanical stirring, 100 mL of deionized H_2O were added to the paste. In this phase $KMnO_4$ oxidizes and causes a violent increase in temperature and brown gas emissions. The temperature was kept constant at 98 °C for 15 minutes then 200 mL of hot deionized water were added. When the temperature dropped below 60 °C, H_2O_2 (30 mL – 30%) was added to eliminate $KMnO_4$ residues. Gold - coloured bubbles formed on the surface. The obtained sample was washed with HCl (10%) for three times and one with deionized water to eliminate the residues of H_2SO_4. Finally, the suspension

was dried in a vacuum oven at 80 °C for 24h to obtain the GO sheets. After that the powder was hand-ground and sieved (mesh 80 μm).

TGO composite was obtained mixing 0.1 g synthetized GO and 0.5 TiO_2 DT-51 (ratio TiO_2 - GO 5:1) nano - powder through sonochemical route. In the specific, TiO_2 DT - 51 powder was dispersed in 20 mL of absolute ethanol and then graphene oxide was added. The composite was subjected to 1 hour of ultrasound probe (Bandelin sonoplus), maintaining an ice bath which prevents overheating of the suspension. After the suspension was dried in an oven at 120 °C until complete evaporation of the solvent [24].

2.2.2.3 g-C_3N_4

g-C_3N_4 was synthesized starting from Melamine. By subjecting this powder to a heat treatment at 550 °C for 4h with a thermal gradient of 2 °C / min, a yellow powder was obtained. Also, in this case the powder was hand - ground and sieved (mesh 80 μm).

2.2.3. Physico - chemical characterization methods

To facilitate understanding, the codes of the various samples characterized and used were reported in Table 2.1.

Table 2.1. Code and description of each analysed sample.

Sample CODE	**Description**
TAC	Commercial TiO_2 (supplier Colorobbia) acid suspension 3 wt%
TAC SFD	SPRAY FREEZE DRIED commercial TiO_2 acid suspension 3 wt%
SiO_2	Commercial SiO_2 Ludox HS - 40 (supplier Colorobbia) suspension 3 wt%
SiO_2-R	Commercial SiO_2 Ludox HS - 40 (supplier Colorobbia) suspension 3 wt% treated with ionic exchange resin to pH=4.
TiO_2:SiO_2 1:3	Composite material obtained by heterocoagulation based TAC and SiO_2

TiO_2:SiO_2 1:3 SFD	SPRAY FREEZE DRIED composite material obtained by TiO_2:SiO_2 1:3 suspension
TiO_2 DT51	Commercial TiO_2 powder (supplier CristalACTiV™)
TiO_2 DT51 - US	TiO_2 DT51 after 1h of ultrasounds
G	Commercial graphite powder (supplier Magaldi industry)
GO	Graphene oxide synthetized by Hummer modify method
GO – US	GO after 1h of ultrasounds
TGO	Composite material based on GO and TiO_2 DT51
g-C_3N_4	Material obtained from melamine through heating treatment

Dynamic Light scattering (DLS) / Electrophoretic Light scattering (ELS)

The hydrodynamic diameters distribution, zeta potential and $pH_{i.e.p.}$ of TAC, SiO_2, TiO_2:SiO_2 1:3, TiO_2 DT51 - US, GO, TGO and g-C_3N_4 suspensions, dispersed at 0.3 wt% in DI water, were evaluated by using a Zetasizer instrument (Malvern Instruments, Zetasizer Nano - ZS, Malvern, UK) based on the dynamic light scattering (DLS) and electrophoretic light scattering (ELS) techniques. For particle size distribution evaluation, about 1 mL of the sample was measured consecutively three times at 25 °C. The size distribution (nm) was reported as the intensity - weighted mean diameter derived from the cumulant analysis (Z - average) and was the average of three independent measurements. The reliability of the measurements was controlled by using the automatic attenuator (kept between 6 and 8) and the intercept autocorrelation function (< 0.9) as quality criteria[27]. The zeta potential was measured on 700 µL of the sample at 25 °C, setting the measurement time, the attenuator position, and the applied voltage to automatic. After a 2 min temperature equilibration step, the samples were measured three times, and the data were obtained

by averaging the three measurements. The data of zeta potential (mV) were derived by electrophoretic mobility using Smoluchowski's formula. The reliability of the measurements was controlled by check the phase plot graph. The same instrument coupled with an automating titrating system was used to create zeta potential vs. pH curve to identify the pH at which the zeta potential sets to zero, namely the isoelectric point ($pH_{i.e.p.}$). The titrants used were 0.1M KOH solution and 0.1M HCl solution.

X - Ray Diffraction (XRD) Analysis

The analysis was conducted on powder samples: TiO_2 DT51 - US, G, GO, TGO and g-C_3N_4. TAC and TiO_2:SiO_2 1:3 obtained by Spray Freeze Drying (SFD) technique[28].

The X - Ray diffraction spectra were obtained with a Bruker D8 Advance X - ray diffractometer, using CuKα monochromatic radiation (1.5406 Å). The instrument was equipped with a particular fast detection system (Accelerator), capable of providing spectra with a better signal / noise ratio than normal detectors in a few seconds of acquisition. The samples were analysed in the 2Θ range 5° - 80°.

Brunauer – Emmett – Teller (BET) Analysis

BET measurements on powder sample: TiO_2 DT51 - US, G, GO, TGO and g-C_3N_4 were carried out to calculate the specific area (m^2 / g) on powder samples using N_2 as adsorptive gas, Sorpty 1750 CE instruments and each sample were pre - treated under vacuum at 120 °C (Mode Sonos 351 - Mazzali).

Fourier Transform Infrared Spectroscopy – Attenuated Total reflectance (FTIR-ATR)

This analysis was carried out using the Nicolet iS5 instrument (Thermofischer, Italy), with the measurement parameters: 24 scans, 0.1 cm^{-1} resolution, spectrum measured from 100 to 800 nm wavelength. The powder sample does not require pre - treatments. The analysis was conducted on powder samples: TAC SFD and TiO_2:SiO_2 1:3 SFD, GO, TGO and g-C_3N_4.

Thermo Gravimetric Analysis (TGA)

A Netzsch Jupiter® F3 instrument was used to carried out TG analysis. The powder samples (TAC SFD and TiO_2:SiO_2 1:3 SFD, TGO and g-C_3N_4) were heated up to 800 °C, in air flux, at

a rate of 10 °C / min. The weight of the sample was recorded as a function of temperature. This technique allows to know the degradation kinetics of a material. The powder sample does not require pre - treatments. The instrument also allows to obtain the DSC (differential scanning calorimetry) graph, which measures the difference in flow between a sample under examination and a reference sample, obtaining intrinsic information of the material under examination which is not dependent on the working environment.

Scanning Electron Microscope (SEM)

The morphology and dimensions of the nanoparticles and the degree of integration of the composites were observed using the Field Emission Scanning Electron Microscope (FESEM ZEISS Sigma HV). The powder samples: TiO_2 DT51, G, GO, TGO and g-C_3N_4 were attached onto an aluminium holder using carbon tape. All samples were gold - coated (thickness = 5 nm) (Spatter Quorum Q150T ES) to increase the conductivity and obtain well - defined images.

Transmission Electron Microscope (TEM)

A thorough morphological analysis on TAC and TiO_2:SiO_2 1:3 was performed by transmission electron microscopy (TEM). One drop of NM diluted in DI water (30 µg / mL) was deposited on a film - coated copper grid and then air dried. The samples were examined by FEI titan TEM operating at an acceleration voltage of 300 kV[29].

Band Gap Measurements

The measurement of the band gap of a semiconductor involved the use of optical diffuse reflectance spectroscopy. The powder samples (TAC SFD, TiO_2:SiO_2 1:3 SFD, TiO_2 DT51 – US, TGO and g-C_3N_4) were characterized by a LAMBDA 750 UV / VIS / NIR spectrophotometer (Perkin Elmer) equipped with a 150 mm integrating sphere. The powder sample was placed inside the sample holder, pressed and inserted inside the sphere. The spectrum was recorded by relating the %reflectance (R) to the wavelength (nm). The data was then processed through the Kubelka - Munk equation (F(R) remission fraction):

$$F(R) = \frac{(1-R)^2}{2R}$$

Tauc plot was obtained from the equation:

$$\alpha h\nu = A(h\nu - E_g)^n$$

Where α was the absorption coefficient and was proportional to F(R) and specific for the material, h was a Plank's constant, ν was the frequency of the incident radiation, A was a constant and n indicates the electronic transition, in this case n = 2. Finally, it was possible to achieved the E_g (band gap) value by graphical method.

2.2.4. Degradation tests

The photodegradation tests were carried out using Rhodamine B (RhB) as a model of organic trace pollutant. RhB is a synthetic dye that is commonly use in water remediation due to the easy detection of small concentrations by UV - Vis absorption analysis using a single beam spectrophotometer Hach Lange, DR3900. RhB imparts a deep magenta hue to its water solutions and displays a well - defined absorbance peak at 554 nm (Fig. 2.1).

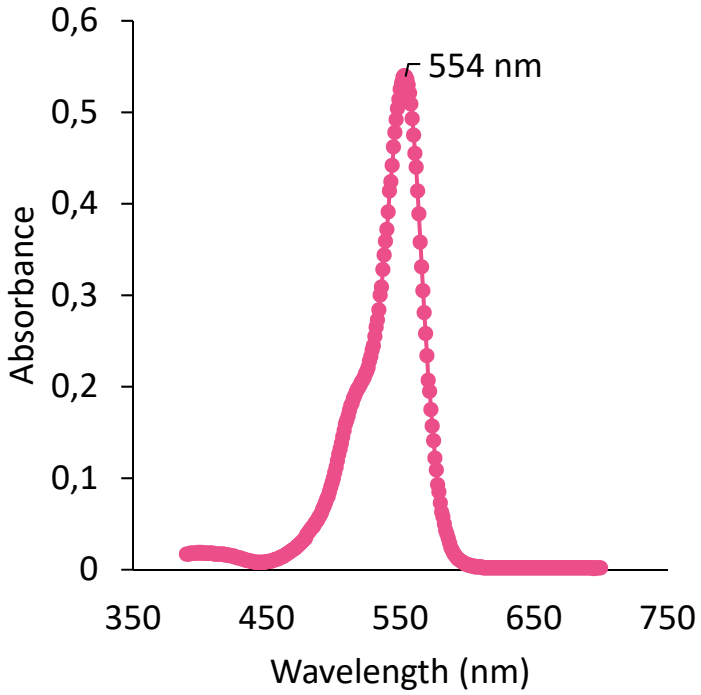

Figure 2.1. RhB absorbance spectra.

In our experiment, we used 150 mL f 7 ppm RhB solution. The lamp was switched on 60 min before starting the test in order to stabilize the power of emission; simultaneously,

the catalyst in 0.1 g / L concentration was introduced in RhB solution to reach the adsorption–desorption equilibrium. For the composite materials, photocatalytic tests were also carried out for the SiO_2 and GO samples as negative control. The aim was to demonstrate that by themselves they are not active, but once coupled to TiO_2 they increase its photocatalytic activity. Another control test was carried out by subjecting the RhB solution only to light sources to ensure that the dye molecules did not undergo photolysis.

In order to evaluate the degradation kinetics, an aliquot of 5 mL was withdrawn, centrifuged for 8 min at 8000 rpm (Digicen 21R – Orto alresg) and analysed at time 15, 30, 60, 90 and 120 minute (A_x) through UV - Vis analysis in the range of 350 – 700 nm. The A_x was measured in correspondence to the maximum of the absorbance peak detected. Before starting the degradation tests, after 60 min of absorption, the initial absorbance (A_0) was determined. The order of photocatalytic degradation reactions was ascertained from the pseudo first - order kinetic model:

$$\ln\left(\frac{A_0}{A_x}\right) = k * t$$

The photocatalytic efficiency was calculated at t = 120 min. It indicates the ratio between the amount of reagent consumed and the amount of reagent initially present in the reaction environment, and it was determined by the following formula:

$$\text{Photocatalytic efficiency } (\%) = \left(1 - \frac{\mathrm{A_x}}{\mathrm{A_0}}\right) * 100$$

where A_x was the peak value at time t and A_0 is the peak value at time 0. In order to facilitate the comparison between the different photocatalysts, normalizing for the amount of active phase the turn over frequency (TOF) parameter was calculated. The TOF parameter was calculated by following equation:

$$\mathrm{TOF} = \frac{\left(\frac{\text{mol of product}}{\mathrm{t\ (s)}}\right)}{\text{mol of active phase}}$$

where mol of product was calculated as the initial concentration of reagent per efficiency reached at the time t (in second), mol of active phase (only TiO_2 in composite cases) were the moles of the active phase arriving in the RhB solution.

The photocatalytic tests were carried out using two different light sources:

- OSRAM ultra - vitalux 300 W lamp was used as the UV light source, mounted on a lamp holder 20 cm from the bottom of the beaker (UV - A 60 W / m^2), arranged in the dark room so that only the photons emitted from the lamp irradiate the suspension of RhB and photocatalyst. The latter was maintained under magnetic stirring at 600 rpm and the temperature during the test was kept constant at 28 °C by a flow of water around the beaker (600 mL / min). The emission spectrum of UV light is shown in Fig. 2.2.

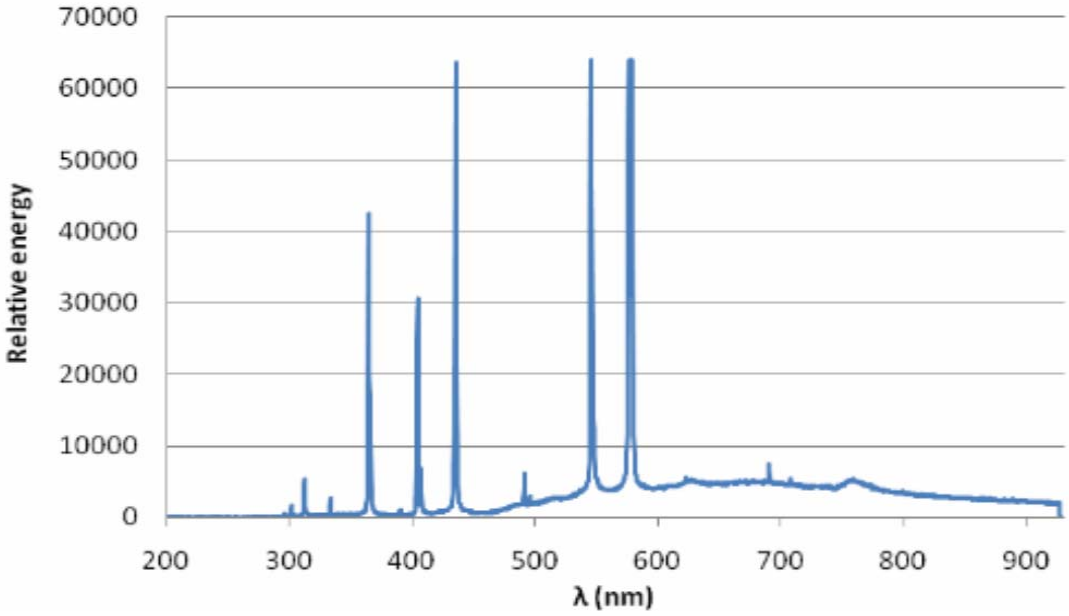

Figure 2.2. Emission spectrum of UV lamp[30].

- SUN2000 solar simulator (ABET technologies) was used as the visible light source, which uses a 150 W Xenon lamp (Fig. 2.3 spectra light). The light beam illuminates an area of 10 x 10 cm with an irradiance of 1000 W / m^2 (UV - A 40 W / m^2). In this case it was not necessary to control the temperature because it did not vary during the test. As in the previous case, the suspension was kept under magnetic stirring at 600 rpm so that the entire suspension was irradiated with light.

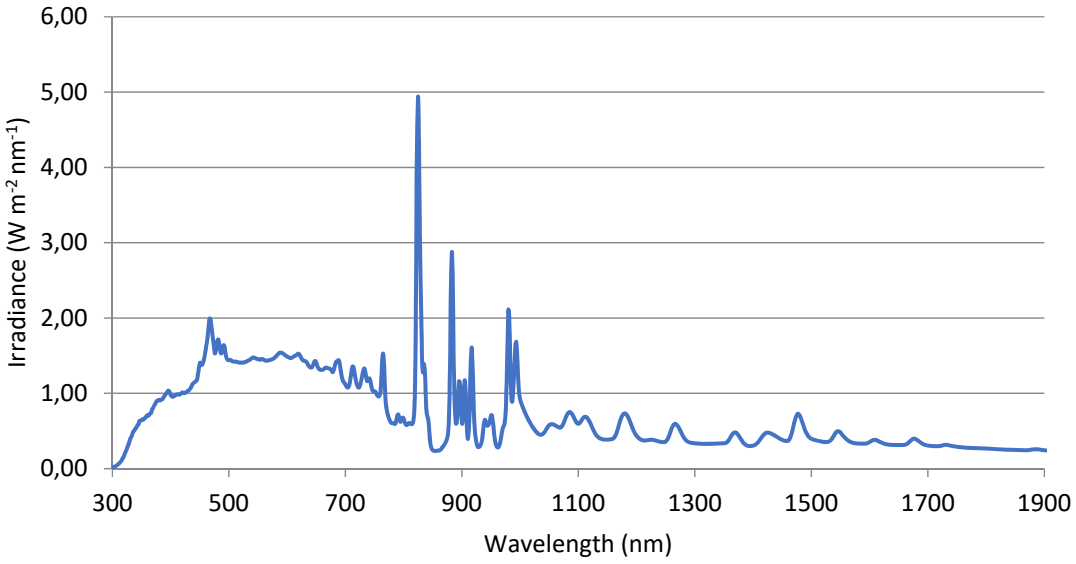

Figure 2.3. Visible spectrum light.

2.2.5. Chemical Oxygen Demand (COD)

COD is an indicator of water pollution and represents the quantity in mg of oxygen necessary to chemically oxidize both organic and inorganic pollutants present in a litre of water. It is a standardized parameter that allows to evaluate the efficiency of the remediation treatment for natural or waste water. By now the tools that allow to calculate the COD are very small and fast, this also allows to carry out measurements in the field. As an oxidizing agent, potassium dichromate with a bright orange colour is mainly used, capable of oxidizing 95 - 100% of the organic matter present in the sample to be analysed[31]. The COD test was performed with the standard procedure: after mixing the reagent tube (LCK 514 100 - 2000 mg / L O_2) for 15 seconds, add 2 mL of sample. Mix for 15 seconds and wait 15 minutes. The test tube was placed in the thermo-digester (Langer LT 200) for 2 hours at 148 °C. When the temperature had dropped to room temperature, the measurements using UV - Vis spectrophotometer Hach Lange, DR3900 was performed. The RhB solutions after 120 min of irradiation by both UV and visible light (photocatalytic test) using TiO_2:SiO_2 1:3, TiO_2 DT51 – US, TGO and g-C_3N_4 as photocatalysts were analysed by COD test. For TAC sample the COD test was carried out on RhB solution after 60 min of irradiation because a total RhB degradation was obtained already in this time. Positive (7 ppm RhB solution – after 120 min irradiation) and negative (tap water and distilled water) controls were also measured and considered.

2.2.6. Functional, Sustainability and Cost model

Considering the main purpose of the Green deal of obtaining climate neutrality also through the rules of green chemistry, it is necessary to know the level of environmental sustainability for the proposed materials, to know if they do not impact too much on the amount of electricity spent for their production. Furthermore, for the development of materials, considering the final use in large - scale plants, the economic factor also plays a significant role. Therefore, in this thesis work we evaluated the photocatalysts studied on the basis of the functional properties (photocatalytic efficiency parameter), the environmental sustainability and the cost (for their production and use) employing a multi - criteria analysis. To do this, we applied a Life Cycle Assessment (LCA) analysis to identified the optimal photocatalyst. For the environmental sustainability and the cost, the phases of synthesis and use of the photocatalysts were evaluated, according to the gross energy requirement (GER). In particular, the following energy inputs were considered:

- synthesis process of the TiO_2:SiO_2 1:3 sample: through 24h of ball milling;
- US process and subsequent drying in an oven for the TiO_2 DT51 - US sample;
- US process and subsequent drying in an oven for the TGO sample;
- energy consumption of UV and visible lamps.

The Italian energy mix with low voltage power supply was used for the analysis. The environmental impact data were obtained with the Ecoinvent v.3.7 database and with the Open LCA software. The method of use remained the CLM 2001 and the CO_2 emissions in Kg - equivalents per KWh of electricity were equal to 0.41615 Kg CO_2 - eq / KWh.

As regards energy costs, a value of 0.13 € / KWh was considered (updated to the year 2021).

In the specific, the multi-criteria optimization algorithm was applied to the functionality data (photocatalytic efficiency) and cost (Kg CO_2 - eq / kWh), which allowed to define the materials and the relative conditions of optimal use in the photocatalytic process that now respond to the maximum functional performance, minimum environmental impact and minimum cost of production. The multi - criteria analysis does not offer solutions of maximum or absolute minimum but allows the decision maker (designer, end user) to restrict the field of choice (of materials and operating conditions) in line with the

requirements of the optimization problem by making a choice between those proposals that best meet specific needs according to a hierarchy that the decision maker can choose a priori or posteriori.

In our study the variable "cost" was chosen as the control function (f - c). The dependent variables "photocatalytic efficiency" (f - 1) and "CO_2 emissions" (f - 2) were the variables of the performance space. It followed that in the decision space the variables were:

- continuous variable x - 1 = time of exposure to bright light
- variable interruption x - 2 = type of user material.

The algorithm has been implemented on an IT platform that allows to tackle the problem in three phases:

1) interpolating the response functions (performance variables) as a function of the values of the decision space
2) solving the MOOP (Multi - Objective Optimization Problem) to maximize photocatalytic performance and minimize environmental impacts by identifying a subset of the decision-making space that meets these criteria
3) reducing the subset of the decision space into a maximum acceptable cost for the identified solution.

2.3. Results & Discussion

2.3.1. Physico - chemical characterization

Colloidal characterization

Table 2.2 shows the hydrodynamic diameter, Z - potential and $pH_{i.e.p.}$ values of pristine materials and composite materials.

Table 2.2. Hydrodynamic diameter (d_{DLS}), Z - potential (mV), and $pH_{i.e.p.}$ of pristine and composite materials used as photocatalysts.

Sample	d_{DLS} (nm)	Z Potential (mV)	pH	$pH_{i.e.p.}$
TAC	27	+36	1.5	7.7

SiO_2	30	-45	7	<1.5
TiO_2:SiO_2 1:3	317	+38	4	5.2
TiO_2 DT51 - US	1304	-31	7.5	3.4
GO	5203	-28	5	n.a.
TGO	2211	-22	5.5	5.2
g-C_3N_4	> 6000	-22	5	2.2

As regards the sample TiO_2: SiO_2 1:3, a significant increase in the hydrodynamic diameter was observed compared to the pristine materials TAC and SiO_2. The increase was due by both the steric hindrance of SiO_2-R heterocoagulated on the TAC surface[32] and the consequent electrostatic destabilization due to progressive neutralization of the TAC surface charge with the increase in negatively charged SiO_2-R content. This was further demonstrated by the shift of the $pH_{i.e.,p.}$ toward acidic pH (from 7.7 to 5.2). The TiO_2:SiO_2 1:3 sample was obtained by the self - assembled heterocoagulation process between TAC and SiO_2-R, which exhibit, at the working pH = 4, potentials opposite in sign and high enough to preserve colloidal stabilization (Fig. 2.4). Therefore, TAC and SiO_2-R were able to promote the heterocoagulation between positive TAC and negative SiO_2 nanosurfaces.

The sample TiO_2 DT51 - US had a negative zeta potential (-31 mV – pH = 7.5) depending on the sites with Bronstead acidity due to H_2SO_4 residues of the material synthesis[33] and acidic $pH_{i.e.p.}$ = 3.4, different from the typical $pH_{i.e.p.}$ of TiO_2. The Z - potential of a TGO sample refers to the surface groups, the GO having on the surface epoxide, carboxyl and hydroxyl groups shows a strongly acidic behaviour showing a $pH_{i.e.p.}$ < 1.7[34]. Compared to TiO_2 DT51 – US and GO, the TGO composite showed a more basic isoelectric point (from 3.4 (TiO_2 DT51 – US), 1.7 (GO) to 5.2).

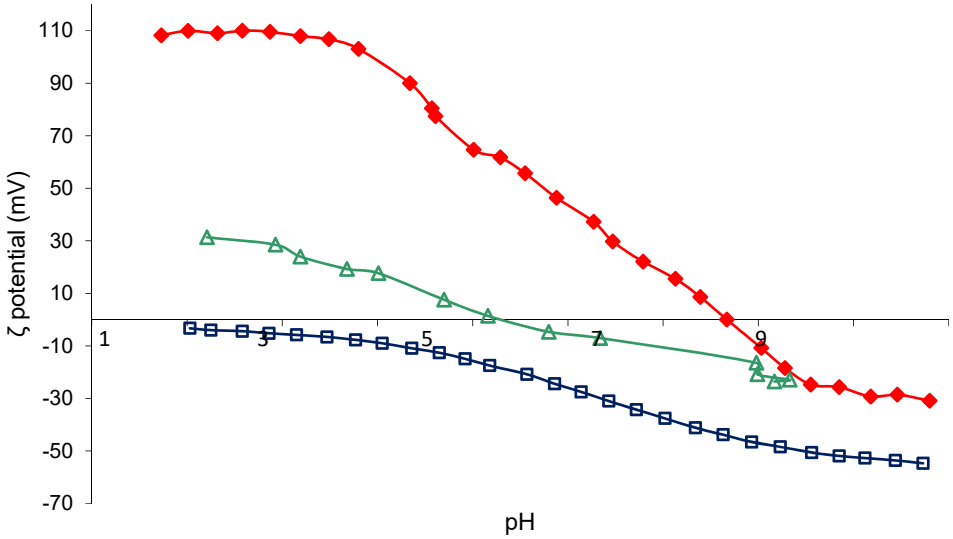

Figure 2.4. Z - potential vs. pH curves of TAC (red), SiO_2 (blue), and TiO_2:SiO_2 1:3 (green) nanosuspension.

Morphology and superficial area characterization

Fig. 2.5 show TEM images of TAC and TiO_2:SiO_2 1:3[29]. The micrograph of the TAC sample (Fig. 2.5a) showed a very fine primary structure, but organized in the form of scattered aggregates, as the DLS data confirmed (Table 2.2). The diameter of the primary NPs was about 5 nm, corresponding to the crystal lattice. In TiO_2:SiO_2 1:3 sampleTiO_2 nanoparticles were randomly distributed in a silica matrix (Fig. 2.5b).

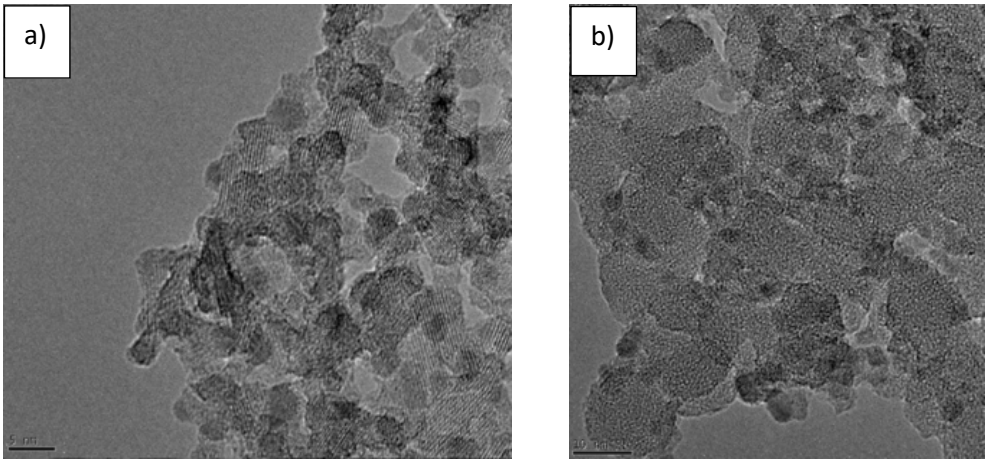

Figure 2.5. TEM image of a) TAC b) TiO_2:SiO_2 1:3 [30].

TiO_2 DT51 – US sample appears aggregated with micrometric size (Fig. 2.6a), as also demonstrated by hydrodynamic diameter (d_{DLS} = 1304 nm -Table 2.2). On the other hand, a nanometric structure was observed in a higher magnification imagine (Figure 2.6b), confirming the presence of 20 nm primary particles, as declared in literature[31, 32].

Table 2.3. Specific surface area (s.s.a.) determined by BET analysis.

Sample	**s.s.a. (m^2 / g)**
TiO_2 DT51 - US	91
G	21
GO	23
TGO	76
g-C_3N_4	11

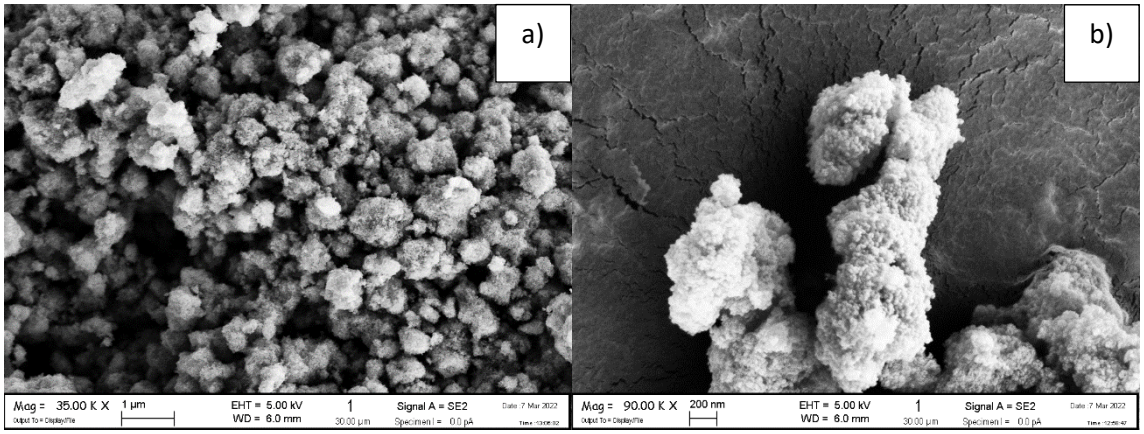

Figure 2.6. SEM image of TiO_2 DT51 powder at different magnitude.

SEM images (Fig. 2.7) on GO - US showed the typical layered - sheet morphology of graphene - based samples[37]. This founding confirmed the successful exfoliation during GO synthesis.

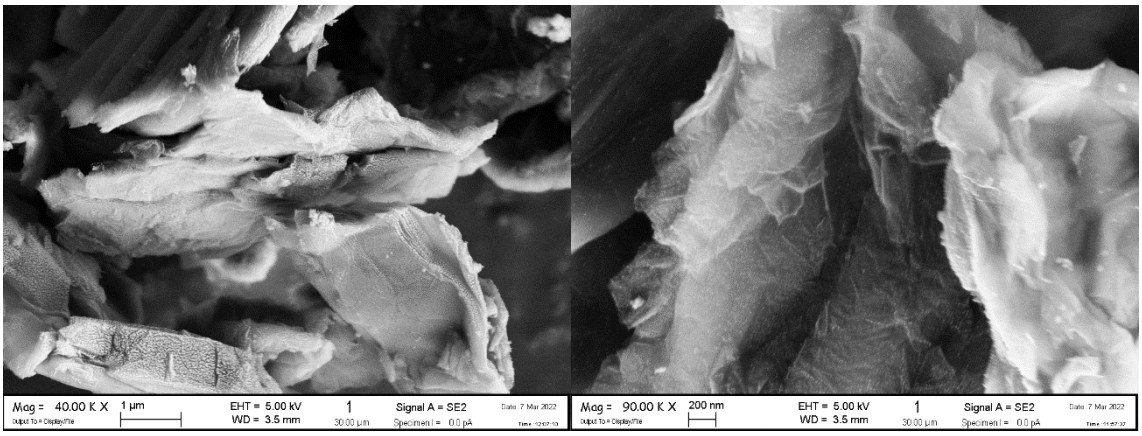

Figure 2.7. SEM images of GO – US sample at different magnitude.

The SEM images of the TGO composite (Fig. 2.8) showed the presence of both phases interconnected with each other. A structure based on graphene oxide sheets surrounded by TiO_2 nanoparticles was recognized. The distribution of TiO_2 NPs on graphene oxide sheets was homogeneous.

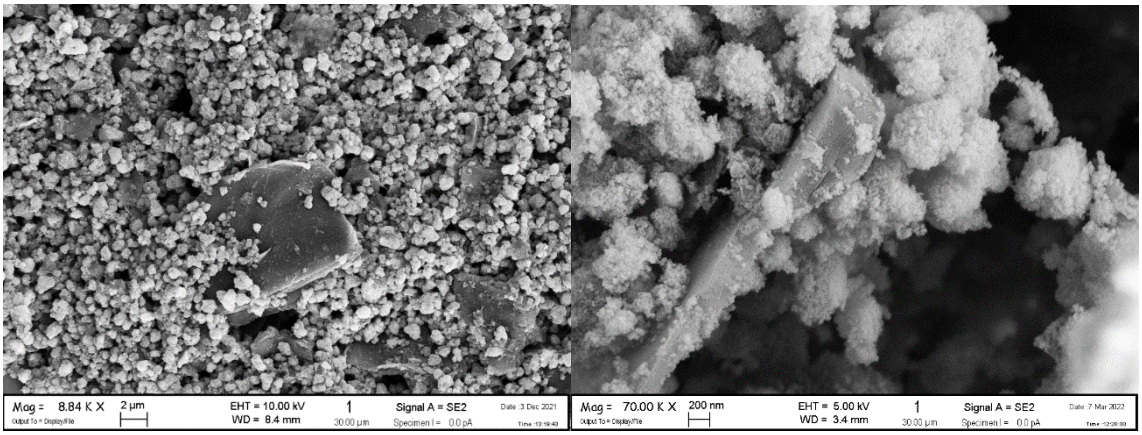

Figure 2.8. SEM image of TGO at different magnitude.

The SEM image (Fig. 2.9) of the g-C_3N_4 sample showed a disordered structure characterized by heterogeneously distributed layers and agglomerated structures. This was confirmed by the hydrodynamic diameter data (> 6000 nm), consistent with SEM image. The observed morphology had repercussions on low surface area, as demonstrated by BET value (11.07 m^2 / g – Table 2.3).

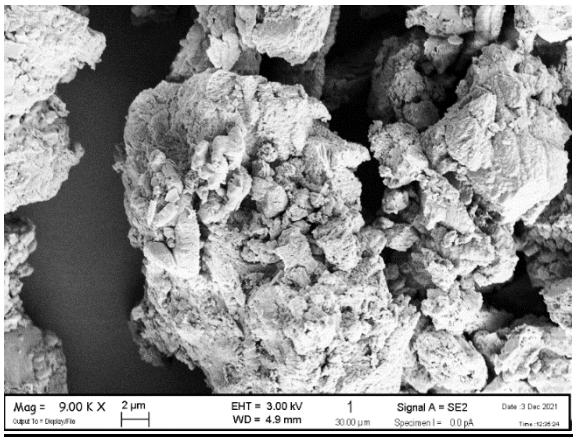

Figure 2.9. SEM image of g-C_3N_4.

Crystallographic characterization

XRD analysis was used to identify the crystalline phases of photocatalysis studied.

Fig. 2.10 shows XRD patterns for TAC SFD (black) and TiO_2: SiO_2 1:3 SFD (red). Anatase A (JCPDS 21–1272) was predominant in the commercial TAC sample and there were small amounts of brookite B (JCPDS 29–1360 / 2Θ = 30.81) and rutile R (JCPDS 65–0190 / 2Θ = 27.44). In the silica - modified samples, there was a wide band centred at 2θ = 22°, the characteristic peak for amorphous SiO_2 (JCPDS 29–0085)[38]. The presence of silica also induced a decrease in the crystallinity of the TAC peaks consistent with the electrostatic interactions that occur between TAC and SiO_2[39].

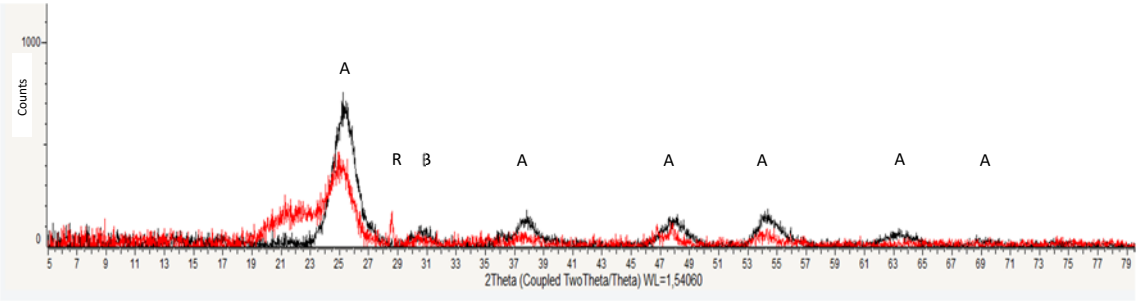

Figure 2.10. XRD diffractograms of TAC SFD (black) and TiO_2:SiO_2 1:3 SFD (red); A= anatase B=brookite R=rutile.

Fig. 2.11a shows XRD patterns for G and GO samples. Graphite G (in red) had an intense characteristic peak at 2Θ = 26.4°. During the oxidation of the graphite powder, oxygen atoms were introduced as different functional groups: OH, COOH and epoxy groups, these stick to the graphite surface. The GO spectrum shows a wide band at 2Θ = 10.7°, which

corresponds to the crystalline plane (200) of the GO sheets. In Fig. 2.11b the characteristic graphite peaks were recognized in the GO sample demonstrating an incomplete oxidation of G to GO[26]. However, the low intensity of the peaks confirmed that only a small amount of graphite was not - oxidized.

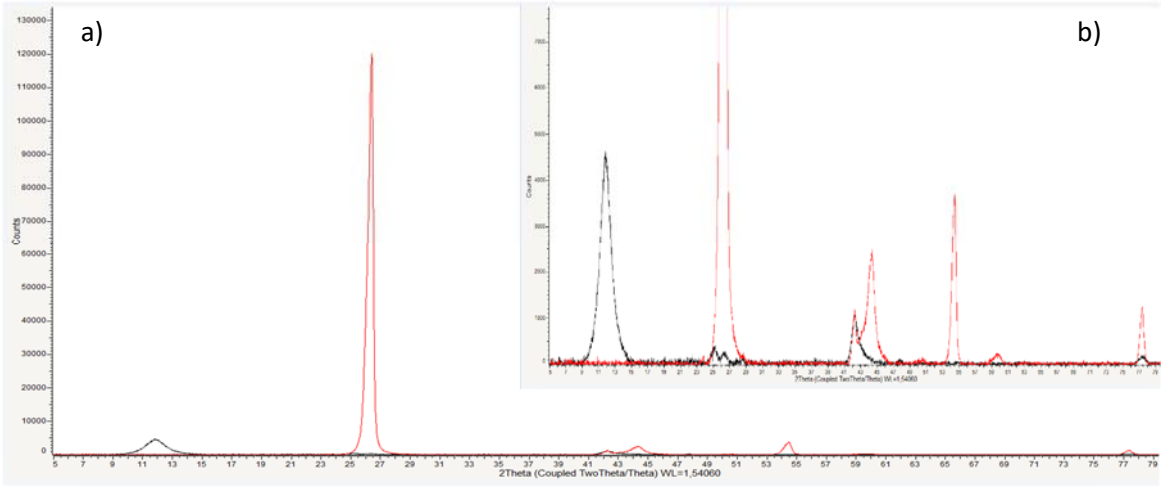

Figure 2.11. XRD diffractograms of G (red) and GO (black); a) full spectrum b) zoom from 0 to 7500 counts (y axis).

XRD patterns for TiO_2 DT51 - US, GO and TGO samples are shown in Fig. 2.12a. The sample based on TiO_2 DT51 - US consisted entirely of the anatase crystalline phase as declared by supplier. The TGO composite showed a polycrystalline structure with peaks of anatase TiO_2 at 2θ = 25.37 °, 37.07 °, 37.89 °, 38.58 °, 48.07 °, 53.97 °,55.1 °, 62.71 °, 68.78 °, 70.41 °, 75.08 ° corresponding to diffraction planes (1 0 1), (1 0 3), (0 0 4), (1 1 2), (2 0 0), (1 0 5), (2 1 1), (2 0 4), (1 1 6), (2 2 0), (2 1 5) respectively (JCPDS 21–1272). The peaks of the GO sample were appreciated in the diffraction pattern of the composite TGO (Fig. 2.12b).

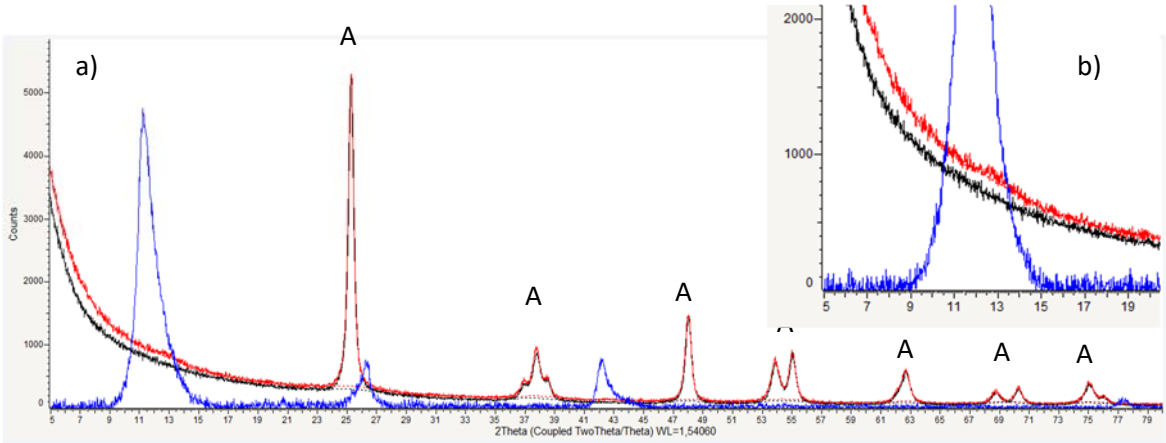

Figure 2.12. a) XRD diffractograms of TiO_2 DT51 - US (black) A: anatase, graphene oxide (blue) and composite TGO (red).

The Fig. 2.13 shows the XRD model for g-C_3N_4 and it was possible to see two characteristic peaks at 13° and 27° (JCPDS Card No. 46 - 1088). The small peak at 13° represented the (100) facet. The intensity of this peak detected the presence of imperfections in the structure, usually dependent on the synthesis temperature[40]. The peak of intensity greater than 27° represented the (002) facet characteristic of graphitic materials due to the interaction of the interlayer with the conjugated aromatic system[41,42].

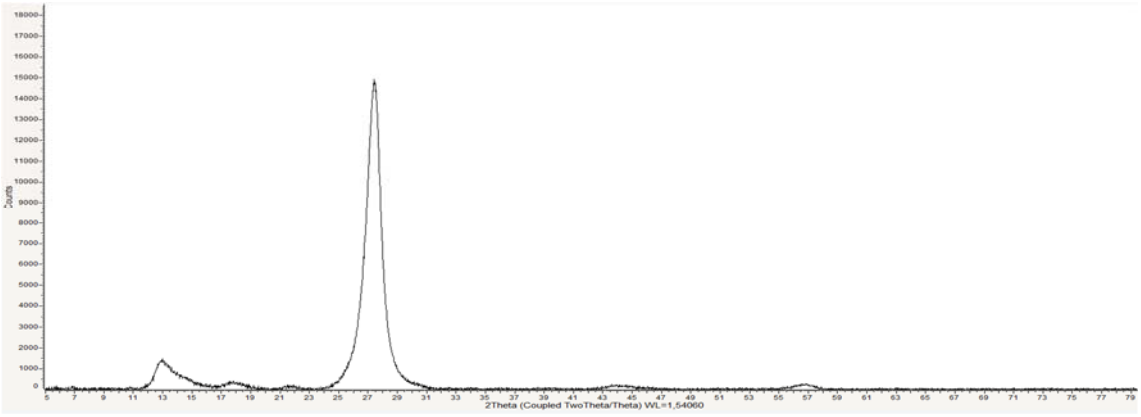

Figure 2.13. XRD diffractogram of g-C_3N_4.

FTIR-ATR

Fig. 2.14a shows the FT-IT ATR spectra of the TAC SFD and TiO_2: SiO_2 1:3 SFD samples. For the TAC sample the broad peak at 3200 and at 1650 cm^{-1} corresponded to surface adsorbed water and hydroxyl groups, respectively. The main peak at 500 – 700 cm^{-1} was attributed to Ti - O stretching and Ti – O - Ti bridging stretching modes. As regards the TiO_2:SiO_2 1:3 SFD sample, it was possible to attribute to the silica the peak around 1100 cm^{-1} due to the vibrations of the symmetrical Si – O - Si stretching, of the Si - OH stretching and of the asymmetric Si - O - Si stretching. The characteristic absorption bands of the stretching vibrations of Si - OH and OH bound to hydrogen of physiosorbed water molecules were integrated into a large peak at 3400 cm^{-1}[43,44].

FT-IR ATR spectrum of the GO and TGO samples are reported in Fig. 2.14b. GO sample showed a peak around 1600 cm^{-1} attributable to the skeletal vibration of the graphene oxide planes. In case of TGO sample the broadening of the spectra below 1000 cm^{-1} has been attributed to the formation of Ti − O − C bonds. The existence of Ti − O − C bonds confirmed that chemical bonds were firmly constructed between graphene and TiO_2

nanostructures. For both samples the wide absorption from 2900 to 3700 cm^{-1} was consistent with the OH stretching vibration of the surface hydroxyl groups[25,26,45].

a)

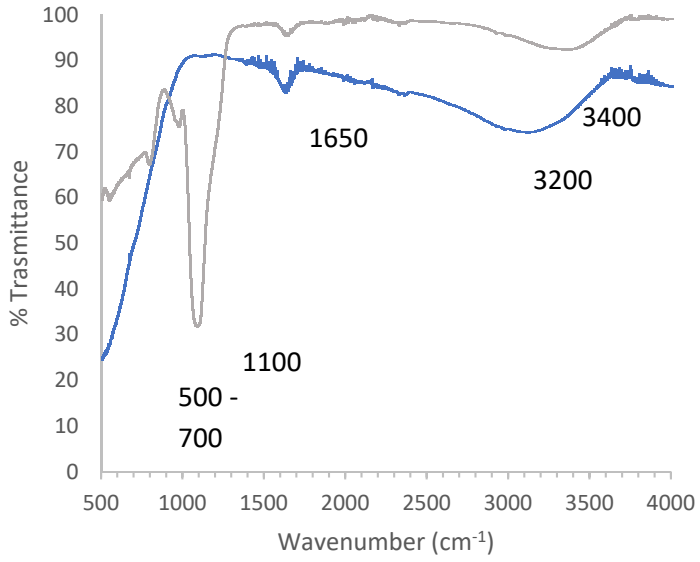

b)

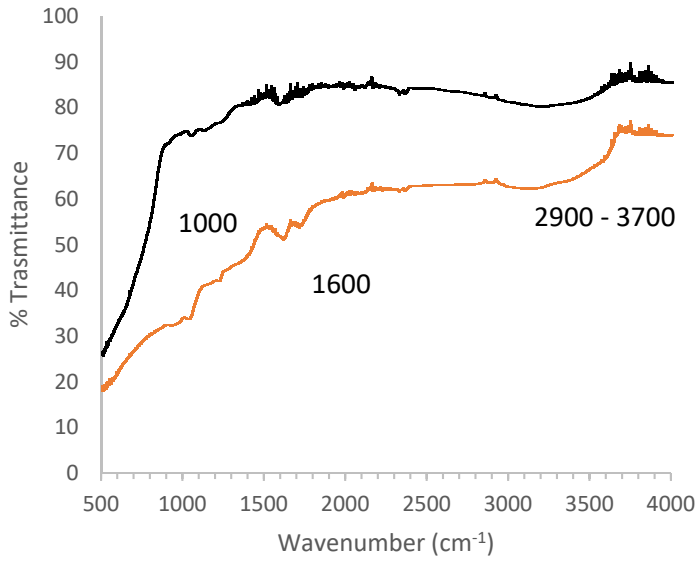

c)

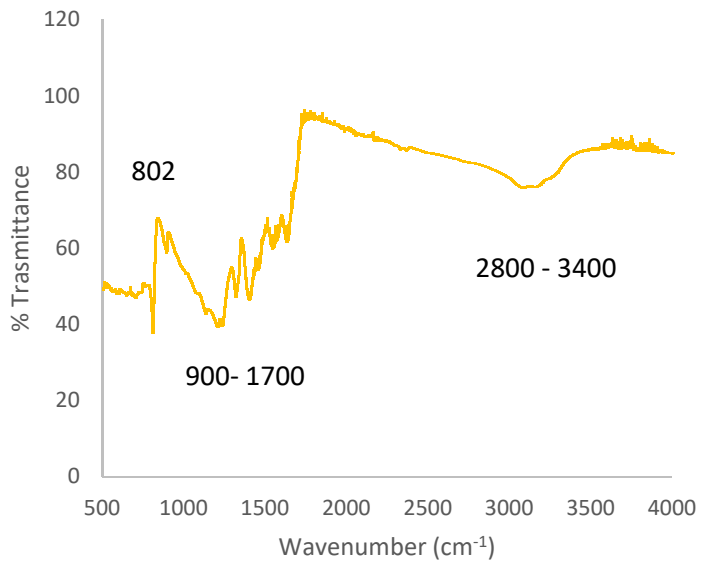

Figure 2.14. FT-IR ATR spectrum of nano-photocatalysts: (a) TAC SFD (blue) and TiO_2:SiO_2 1:3 SFD (grey) (b) GO (orange) and TGO (black) (c) g-C_3N_4.

Regarding g-C_3N_4 FT-IR ATR spectrum (Fig. 2.14c), the multiple peaks in the wavenumber range 920 – 1700 cm^{-1} were recognized though the stretching vibrations of the conjugated CN rings could be seen. The acute absorption peak at 802 cm^{-1} referred to the breathing mode of the triazine units. The broad absorptions at 2800 – 3400 cm^{-1} were assigned to the N – H and O – H stretching vibration modes[42,46].

TG / DSC analysis results

The TGA curve of TAC SFD sample (Fig. 2.15a) show a total weight loss in air of 9% until to 800 °C[47]. A mild endothermic effect was observed at from 260 °C to 400 °C, probably caused by the desorption of CO_2 and the water and organic compounds degradation. The exothermic signal was detected from 400 °C to 800 °C to which was possible to assign the anatase - rutile polymorphic phase transition[47,48].

The TiO_2:SiO_2 1:3 SFD sample (Fig. 2.15b) shows a weight loss of 3%, the presence of SiO_2 seemed to thermally stabilize TiO_2 phase. The DSC curve indicated a prominent endothermic peak below 100 °C due to free absorption water and an exothermic peak at 500 °C which corresponded to the crystallization of the anatase phase in the brookite or rutile phase of TiO_2[49,50].

The weight loss curve of TGO sample (Fig. 2.15c) shows the typical behaviour of GO[51]. The weight losses were separated into unique events namely loss of adsorbed water, loss of oxygen moieties, and finally combustion at 30 – 100 °C, 100 – 300 °C and 300 – 700 °C respectively. The decomposition of functional groups was confirmed by the endothermic peak of the DSC curve.

Fig. 2.15d shows the TG and DSC graphs of g-C_3N_4 sample. Two phases were distinguished: during heating from 25 °C to 540 °C the g-C_3N_4 absorbed heat slowly (as demonstrated by DSC). When the temperature was increased from 540 to 720 °C, a drastic mass loss of g-C_3N_4 was noted which reaches about 95% with a strong exothermic peak at about 720 °C[41,52].

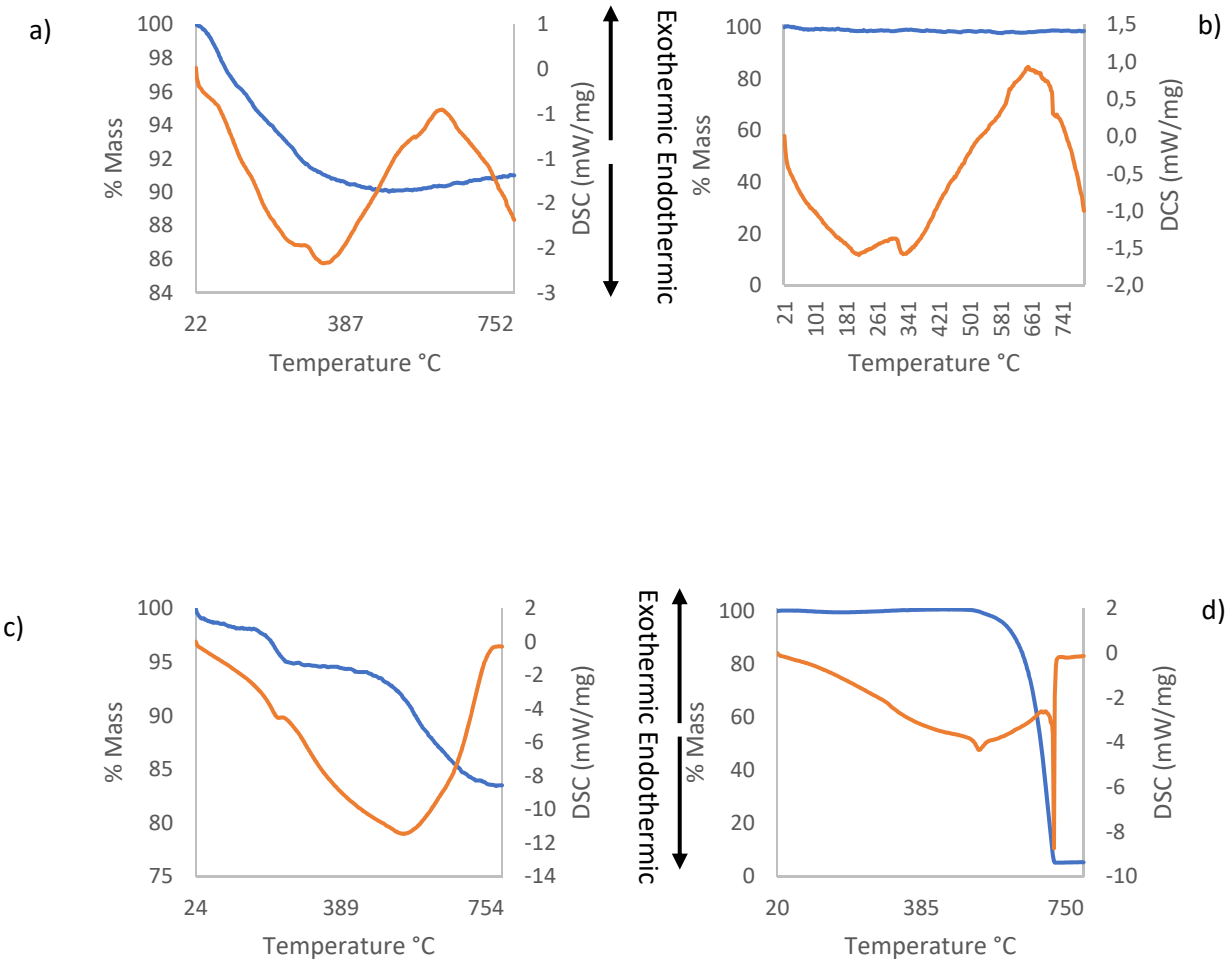

Figure 2.15. TG (blue) and DSC (orange) analysis results of a) TAC SFD b) TiO_2:SiO_2 1:3 SFD c) TGO d) g-C_3N_4.

Band Gap

The light energy necessary to activate (therefore to bring an electron from the valence band to the conduction band) a semiconductor with band gap about 3 eV falls within the UV range[13]. Therefore, the photocatalysis processes using (unmodified) TiO_2 exploit UV irradiation. It is known that the band gap value of TiO_2 can range from 3.0 for the rutile form to 3.3 for the anatase form. TiO_2 based materials that are made up of a mix of the two forms have intermediate band gaps in this range[53]. In fact, the TiO_2 DT51 - US sample, declared by the supplier 100% anatase, showed a band gap of 3.3 eV (Table 2.4).

Table 2.4. Band Gap value of nano-photocatalysts.

Sample	**E_g (eV)**
TAC SFD	3.1
TiO_2:SiO_2 1:3 SFD	3.2
TiO_2 DT51 - US	3.3
TGO	3.2
g-C_3N_4	2.7

While the TAC SFD which was a mix of anatase (84%) and rutile (16%)[54], as also highlighted by the XRD spectrum (Fig. 2.10), had a band gap of 3.1 eV. The presence of SiO_2 and GO led to a slight decrease of TiO_2 band gap. It has been assumed that this slight decrease is not sufficient to shift photocatalytic activity into the visible range. On the other hand, the g-C_3N_4 showed a band gap of 2.7 eV resulting the most promising sample as photocatalysts with visible light applications.

2.3.2. Photocatalysts tests

To evaluate the photocatalytic efficiency, we used a Rhodamine B as organic pollutant model. This molecule has a well - defined absorbance peak at 554 nm and we verified that it was not photodegraded by UV light (photolysis phenomenon - Fig. 2.16a). On the other hand, in presence of photocatalyst based on TiO_2 under irradiation the RhB molecules were photodegraded with an attendant decreasing of absorbance peak at 554 nm (Fig.

2.16b). In fact, Rhodamine B is a common used model in laboratory water remediation studies[55].

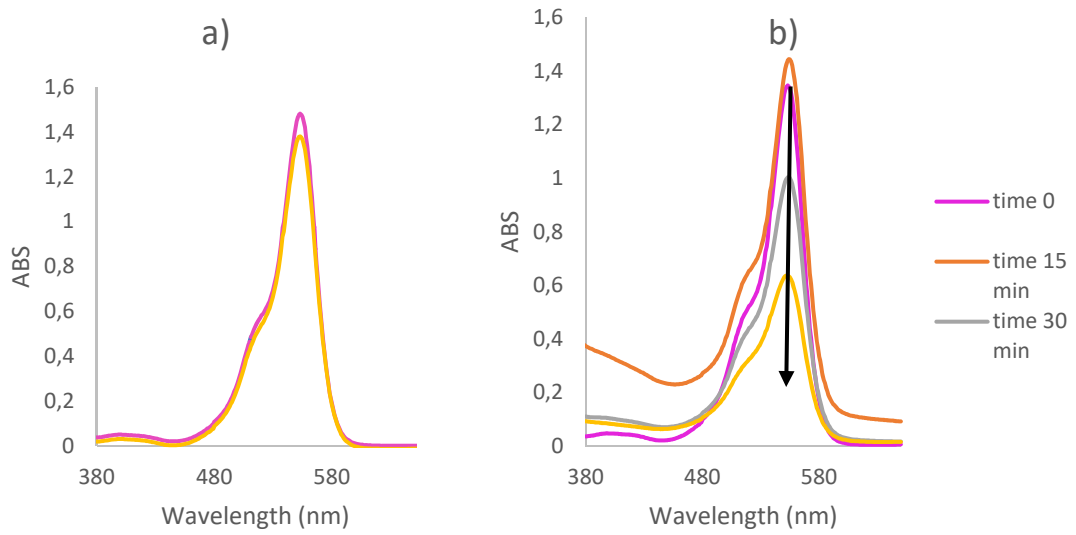

Figure 2.16. RhB absorbance spectra at different time (0, 15, 30 and 60 min) (a) without photocatalyst (b) with photocatalyst (TiO_2:SiO_2 1:3) under UV light.

The results of the photocatalytic tests, expressed as photocatalytic efficiency, under UV and visible illumination are shown in Fig. 2.17a and b respectively.

The TAC and TiO_2 DT51 – US samples were used as benchmark materials. Under UV light, TAC showed a photocatalytic efficiency of 100% while the TiO_2 DT51 – US of about 63% (Fig. 2.17a). The same trend was found under visible light, but the efficiencies were lower than UV light (Fig. 2.17b). This was explained by the values BET (Table 2.3) and DLS (Table 2.2). The TiO_2 DT51 – US showed a lower BET value and a higher DLS than the TAC. The more aggregated TiO_2 DT51 – US and the lower surface area available led to have fewer sites where radicals can be produced and that are involved in the photodegradation of the RhB[56]. Furthermore, from literature[57] was known that the anatase / rutile mix, as showed in TAC sample by XRD diffractogram (Fig. 2.10) exhibited greater photocatalytic activity. This was because the charge carriers are displaced between the two crystallographic phases and as soon as a charge carrier flows in one direction or the other, the holes move in the opposite direction and inhibit electron / hole recombination.

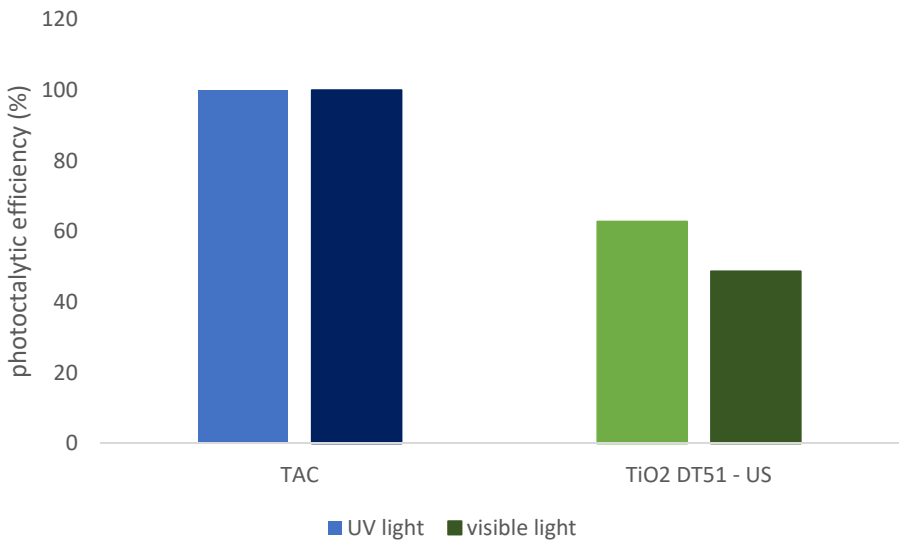

Figure 2.17. Photocatalytic efficiency of TAC and TiO_2 DT51 - US under UV light (blue) and visible light (green) after 120 min of photocatalysts test.

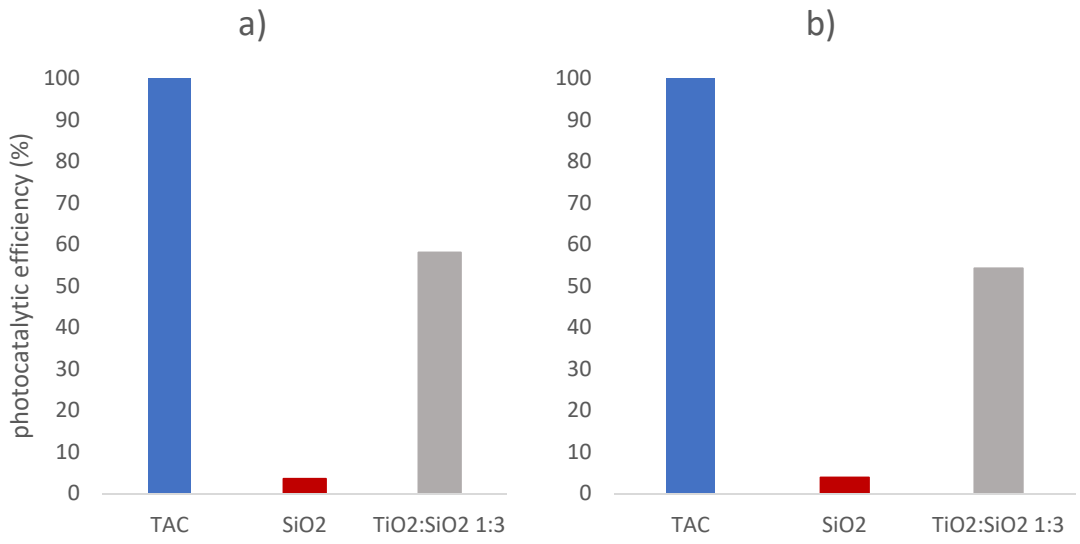

Figure 2.18. Photocatalytic efficiency of TAC, SiO_2 and TiO_2:SiO_2 1:3 sample at 120 min of photocatalytic experiment under (a) UV light (b) visible light.

Comparing the TAC and TiO_2:SiO_2 1:3 sample, the benchmark material (TAC) showed a greater photocatalytic efficiency, both under UV and visible light. This was also confirmed by the kinetic constants degradation in Fig. 2.23a, in fact the kinetic constant (k) of TiO_2:SiO_2 1:3 was about one order of magnitude smaller than that of TAC. Unfortunately, it appears that the presence of silica did not improve the photocatalytic performance of TiO_2, as expected. However, normalizing the data for the amount of active phase (TiO_2), we found that the presence of silica had improved the photocatalytic performance of TiO_2,

as shown by TOF data (Fig. 2.19). We hypothesized that the silica coating on TiO_2 NPs increased the production of active species (•OH) due to the ability of the silica layer to hinder the recombination of radicals but limited oxidative stress in cells[58]. This founding confirmed that the our SSbD strategy consists of introducing of SiO_2 in TiO_2 allows to reduce the use of the active phase in photocatalysts with actually enhancement of the photocatalytic activity without any significant deterioration of its biological impact.

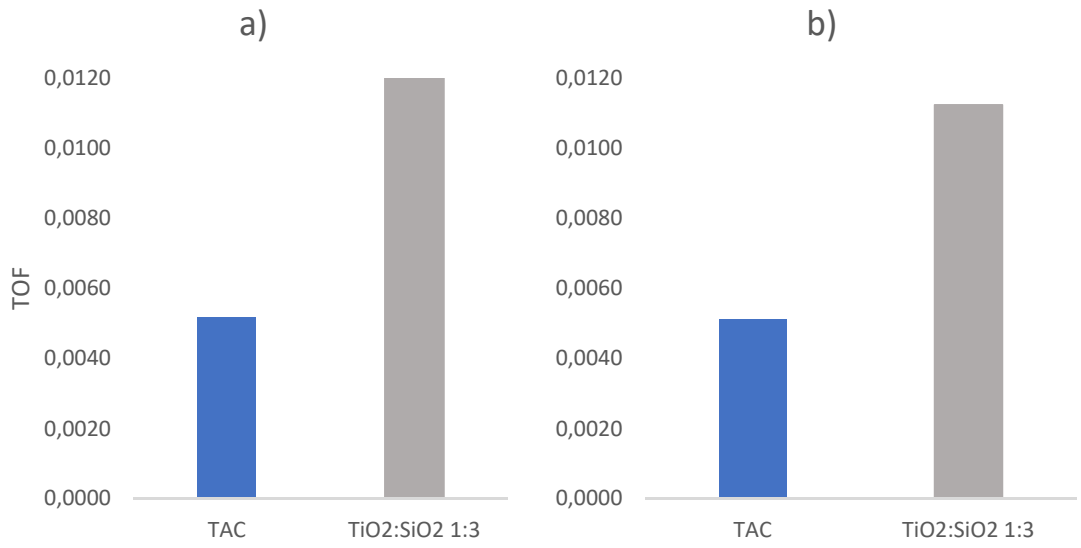

Figure 2.19. TOF value at 120 min of photocatalytic experiment: under (a) UV light (b) visible light.

Comparing TGO with its benchmark material (TiO_2 DT51 – US), we found that the introduction of GO contributed positively in the photocatalytic performance. In fact, under both lights, TGO showed higher photocatalytic efficiency (Fig. 2.20), also confirmed by the kinetic constants (Fig. 2.22), under UV irradiation the kinetic constant of TGO is an order of magnitude higher than the benchmark material TiO_2 DT51 – US. This was further confirmed by TOF values (Fig. 2.21). The presence of GO allowed to adsorb on its surface organic contaminants that spread to the interphase with TiO_2 and were more easily accessible by the radicals that are formed with the activation of TiO_2[59]. GO was also reported to act as a scavenger of electrons and increases their transfer rate. Therefore a minimum concentration (16 wt%) of GO was able to increase the photocatalytic activity and inhibit the hole / electron recombination[45]. GO could in turn be reduced under UV radiation and also produce radicals capable of degrading pollutants[26].

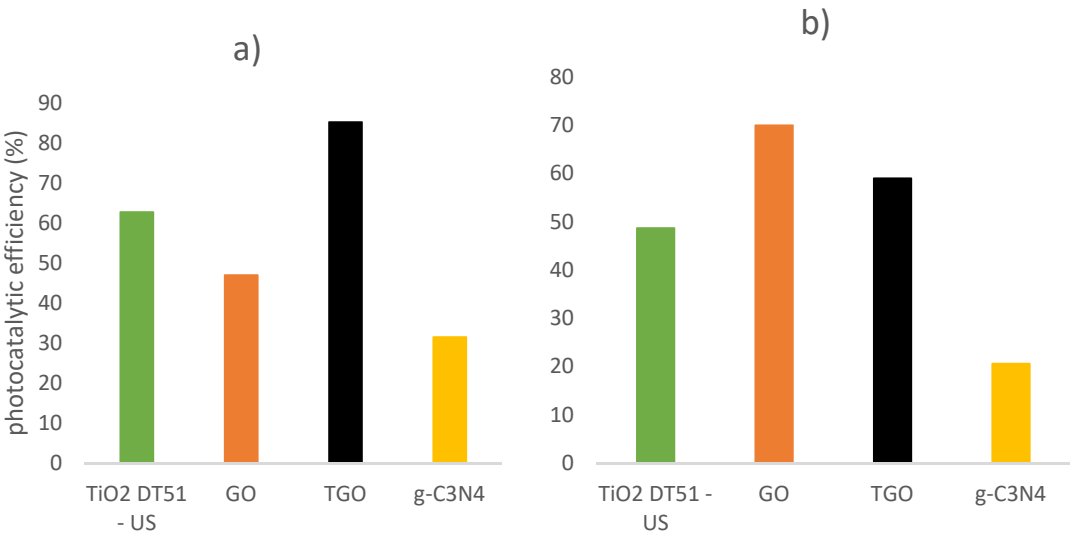

Figure 2.20. Photocatalytic efficiency of TiO_2 DT51 - US, GO, TGO and g-C_3N_4 sample after 120 of photocatalytic test under (a) UV light (b) visible light. The high catalytic efficiency of the GO is the high absorption rate that invalidates the result.

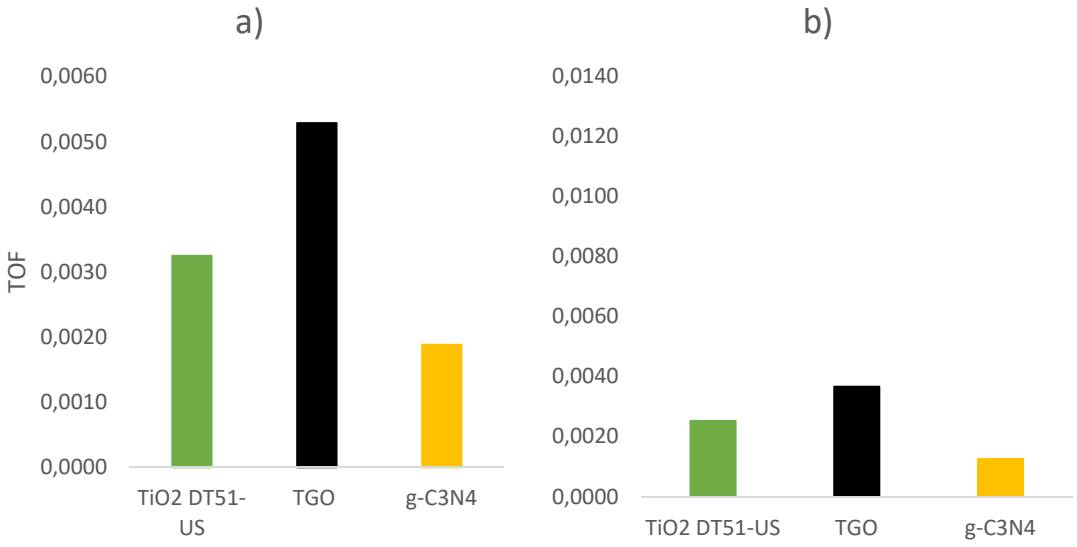

Figure 2.21. TOF value at 120 min of photocatalytic experiment under (a) UV light (b) visible light.

From literature[41,52,60] the g-C_3N_4 sample was a promising photocatalyst, especially under visible light. Unfortunately, the data on g-C_3N_4 contradicted this. As reported by efficiency and kinetic constants results (Fig. 2.20 and Fig. 2.22, respectively), both under visible light and under UV light, the sample g-C_3N_4 showed the lowest photocatalytic performance. Comparing our results with literature[42,61,62], our experimental conditions were stricter. In fact, usually 0.5 g / L of catalysis was used, but we worked at

a concentration of five times lower. Furthermore, the pollutant concentration was much lower than the 7ppm concentration used in this study. Further investigation will help to understand the potentialities of g-C_3N_4 as photocatalyst. A promising alternative could be the coupling of g-$C_3N_4$with TiO_2. It is expected that the coupling of TiO_2 with g-C_3N_4 can improve the recombination of the electron - hole pair, expand the photo - response range and promote oxidation and reduction processes[63].

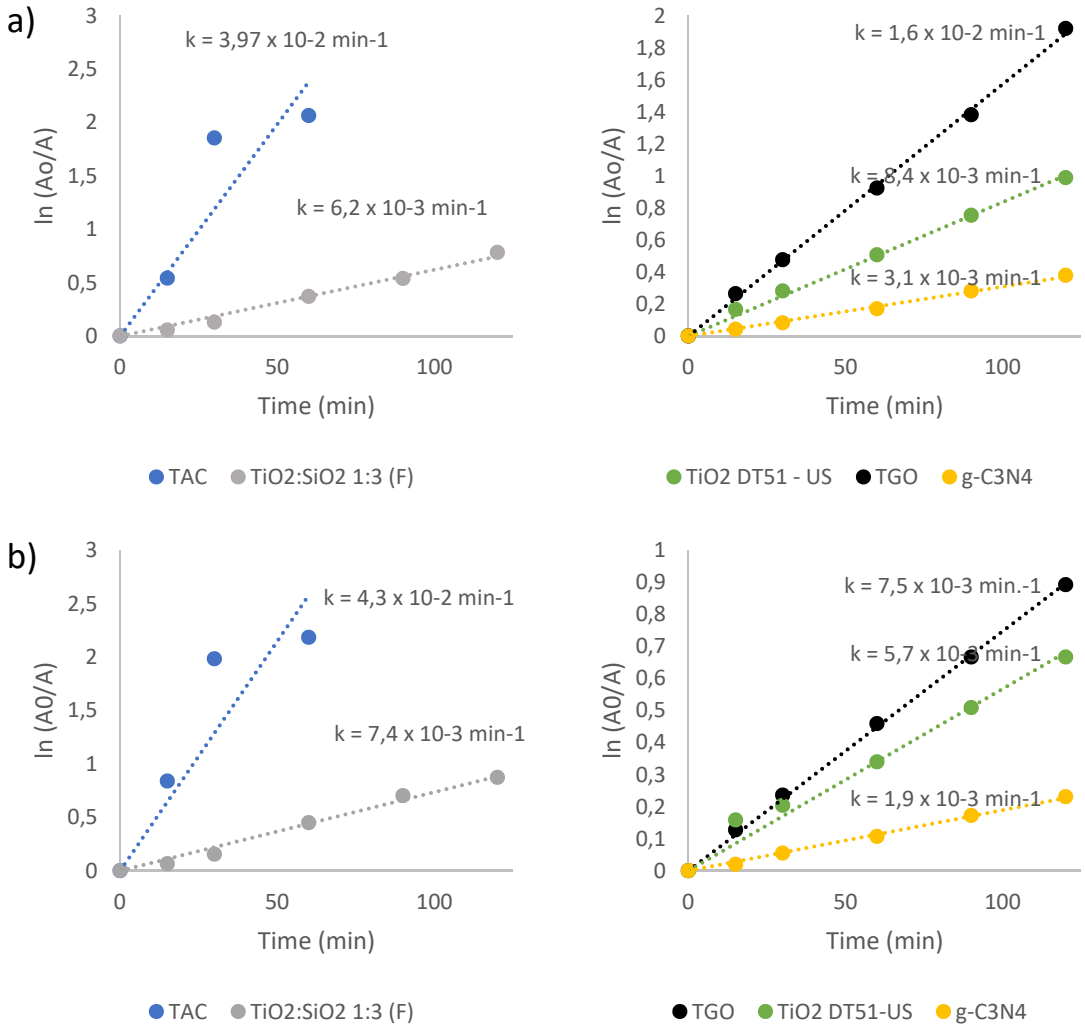

Figure 2.22. Kinetics degradation under (a) UV light and (b) visible light.

There were no significant differences in the results between irradiation with UV light and irradiation with sunlight. The UV - A component of the light sources used were comparable, in fact they are 60 W / m^2 for the UV light and 40 W / m^2 for the solar simulator. This means that even if lower, the UV component in the solar spectrum was

sufficient to activate the photocatalysts, moreover when the RhB dye is irradiated with visible light it behaves as a photosensitiser[64], therefore it is able to pass to an excited state and interact with the neighbour molecules, increased degradation. From this perspective, the proposed TiO_2 - based photocatalysts, TAC, TiO_2:SiO_2 1:3 and TGO, do not require expensive and time - consuming treatments to be activated under visible or sunlight lightweight, with consequent benefits from a safety, environmental and economic point of view[65].

COD is an essential parameter in the field of water treatment and their decontamination. It represents the quantity of oxygen useful for the disinfection of a water (coming from metropolis or from the houses of big cities, from rainwater, sewers or public pits). It is evident that this data is used to ensure better monitoring of the water purification performance. These essential criteria offer an immediate view of the quality of water treatment and purification. COD values for the four photocatalysts, irradiated by the UV and visible light sources were reported in Table 2.5. Current legislation in Italy defines waters that can be discharged into the sewage systems COD < 5000 mg O_2 / L while it is possible to release them on surfaces with COD < 160 mg O_2 / L[66]. Waters with greater COD must undergo special purification treatments[67].

Table 2.5. COD values.

Sample	**Light**	**Time (min)**	**COD (mg O_2 / L)**
RhB	n.a.	0	561
Tap water	n.a.	0	101
Deionized water	n.a.	0	115
TAC	visible	60	84
TiO_2:SiO_2 1:3	visible	120	158
TGO	visible	120	138
g-C_3N_4	visible	120	208
TAC	UV	60	174
TiO_2:SiO_2 1:3	UV	120	166

TGO	UV	120	139
g-C_3N_4	UV	120	126

In order to use the photocatalysts studied in urban water purification plants, the maximum limit coincides with COD = 160 mg O_2 / L. In our case, the starting point (7 ppm RhB solution, before light irradiation) has a COD = 561 mg O_2 / L. At the end of the photocatalytic tests, both UV and visible light sources, the COD values of "wastewater" fell below the threshold limit (160 mg O_2 / L). TAC and TiO_2:SiO_2 1:3 under UV light were exceptions, but the data are very close to the limit. The only sample away from the limit was the g-C_3N_4 under visible irradiation light which showed the lowest efficiencies.

2.3.3. Functional, Sustainability and Cost profile

UV light

The multi - criteria analysis allows to make a ranking of the goodness of the photocatalysts considering functionality (photocatalytic efficiency), environmental sustainability and cost (control function). First of all, the cost function was taken in account and it represents the control function (where 100% means the maximum value obtained of cost efficiency), therefore it was the function that determines the zones of environmental or functional efficiency (the two dependent variables). Areas with efficiency > 60% are considered acceptable. Fig. 2.23 shows the performance field relating to economic efficiency taking in account the cost for the production of materials, which considers the preparation of the composites and the US process for the TiO_2 DT51 - US sample (as reported in the materials and methods section 2.2.6.). The results reported in Fig. 2.23 point out that TGO and TiO_2 DT51 - US samples were not acceptable showing an economic efficiency zone < 60%. This because the two samples required 1h of US process and oven drying, steps that imply high energy consumption and consequent high cost. On the other hand, TAC, TiO_2:SiO_2 1:3 and g-C_3N_4 required minimal preparation.

The three solutions related to the hierarchy of performance functions allowing to identify the three scenarios (Table 2.6): 1) dominance of environmental sustainability performance, 2) fair relevance and 3) dominance of functionality performance.

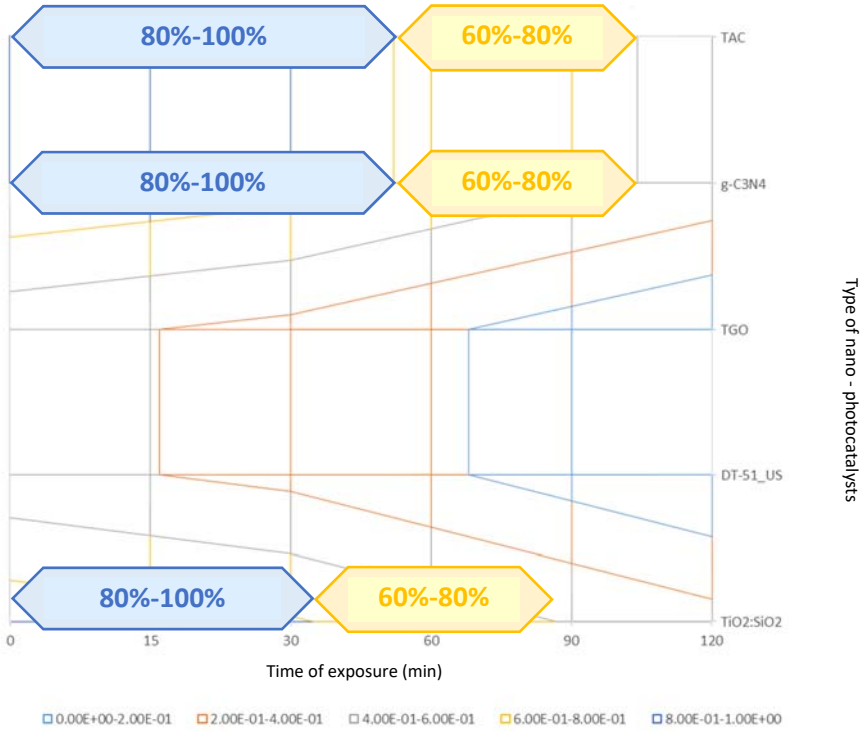

Figure 2.23. Performance space relating to ECONOMIC EFFICIENCY: control function for domain restriction.

Table 2.6. Division of weights to performance in the three scenarios.

Weight	Functional performance	Environmental performance
1) Environmental dominance	30%	70%
2) Fair relevance	50%	50%
3) Functionality domanance	70%	30%

1) <u>Dominance of environmental sustainability performance</u>

In this case of the dominance for environmental sustainability performance, the control function (cost) determined a restriction of the decision - making space (Fig. 2.24), in which we can see that the TAC material had medium (yellow – 60 - 80%) and maximum (blue – 80 - 100%) efficiency for all irradiation times. While the materials g-C_3N_4 and TiO_2: SiO_2 1:3 showed a medium efficiency under 60 minutes of irradiation. It was not possible to accept the choice of the TGO nanomaterial used at the maximum irradiation times.

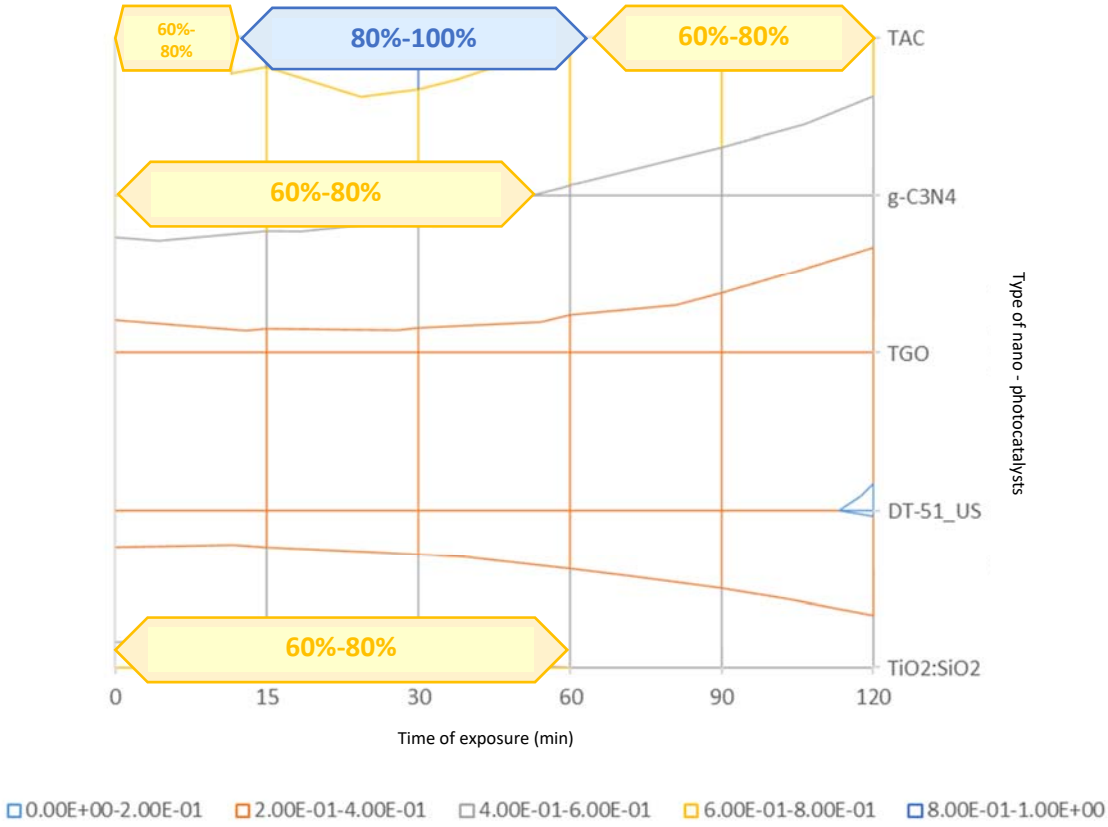

Figure 2.24. Decision - making space and partition of the optimization domain as a function of the multicriteria performance response (weights 30% functional, 70% environmental).

Despite the functional performance were in the 80% - 100% range, the cost factor resulted unacceptable (grey - 40% - 60% of the maximum level of economic efficiency). The production of TGO is uneconomical for a photocatalyst with discreet functional performance.

2) Fair relevance

In the second scenario (Fig. 2.25), the economic control function limited the range of acceptable case studies to only the TAC material with an efficiency of 80-100% for irradiation times between 15 and 90 min.

When the functional component was considered more (respect the previous scenarios), the g-C_3N_4 material has lost its efficiency due to its low photocatalytic efficiency (as shown in Fig. 2.20a) while the TGO, despite not having reached acceptable levels, has increased the percentage of cost efficiency because it had a good photocatalytic efficiency (Fig. 2.20a).

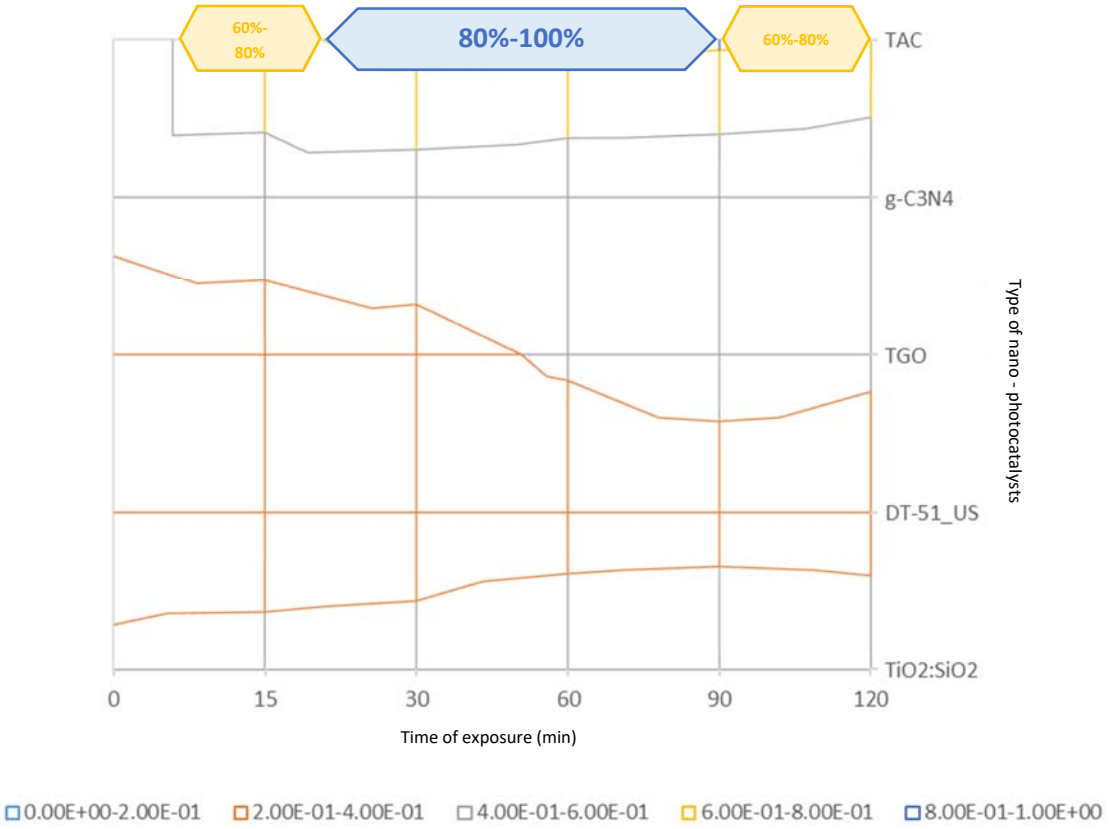

Figure 2.25. Decision - making space and partition of the optimization domain as a function of the multicriteria performance response (weights 50% functional, 50% environmental).

3) Dominance of functionality performance

In the scenario in which the functional performance was dominant, the control cost function has imposed a restriction on the TAC nanomaterial only, which can be considered as acceptable and responding to the simultaneous maximization of the functional – environmental and economic performance indicators. Due to the highest photocatalytic efficiency shown by TAC sample reacheing even 100% (Fig. 2.18), it resulted the most promising photocatalyst. Although the TGO has increased (respect the previous scenarios) its efficiency but the initial cost contribution for the preparation phase made it disadvantageous.

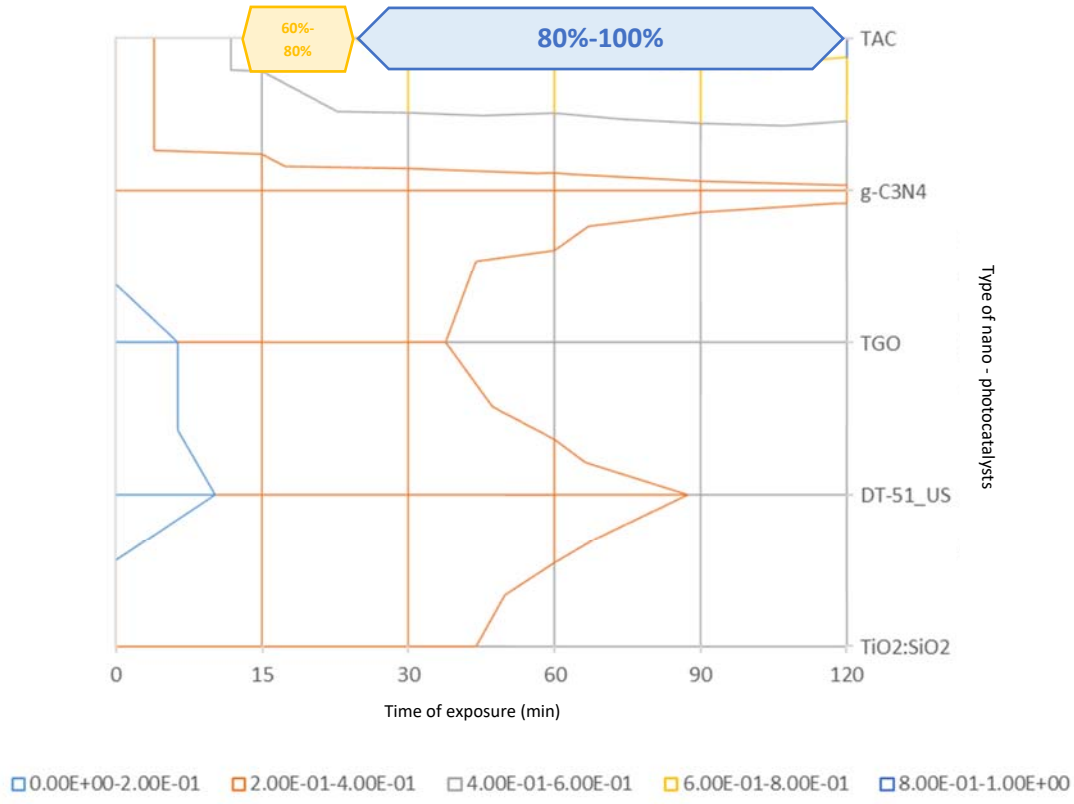

Figure 2.26. Decision - making space and partition of the optimization domain as a function of the multicriteria performance response (weights 70% functional, 30% environmental).

It is important to underline that the environmental and functional coordinates have been assessed in relation to the economic impact that essentially derives from the energy input in the preparation phase of the nanomaterials in a "gate to gate" perspective. Energy inputs for the synthesis of nanomaterials available in their final form or as semi - finished products were not considered, as they concern processes prior to those studied in this sustainable innovation study. This has led to a worse classification of composite materials, as TGO in our case study, which required preparation such as US process and oven drying.

Visible light

The Fig. 2.27 reports the cost control function in the case of irradiation with visible light through solar simulator. The economic efficiency performance range (minimum cost of the solution) as seen for the UV irradiation solution with the effect of reducing the acceptance range towards shorter irradiation values.

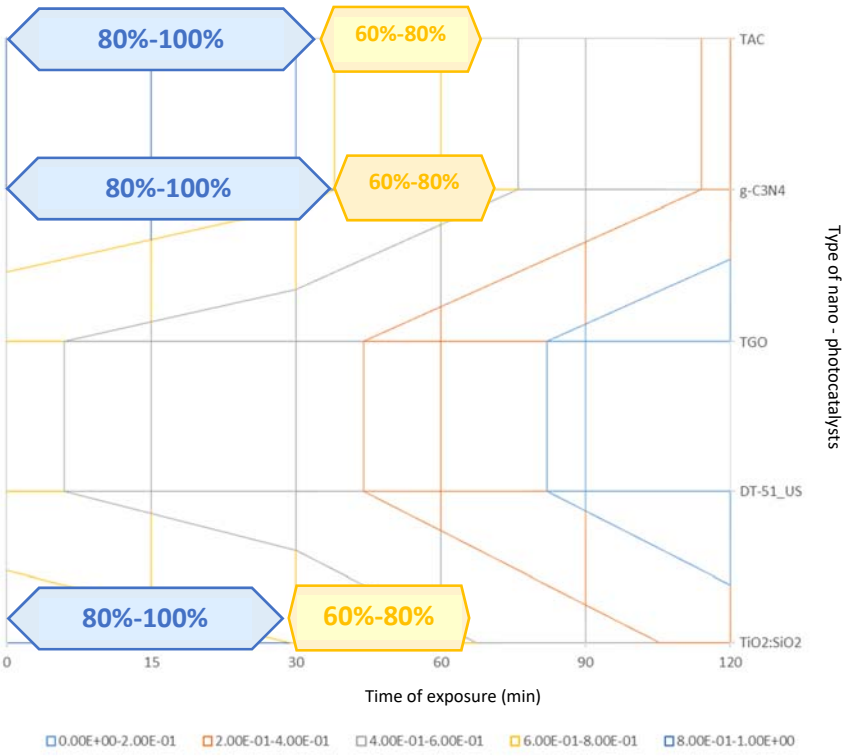

Figure 2.27. Performance space relating to ECONOMIC EFFICIENCY: control function for domain restriction.

1) Dominance of environmental sustainability performance

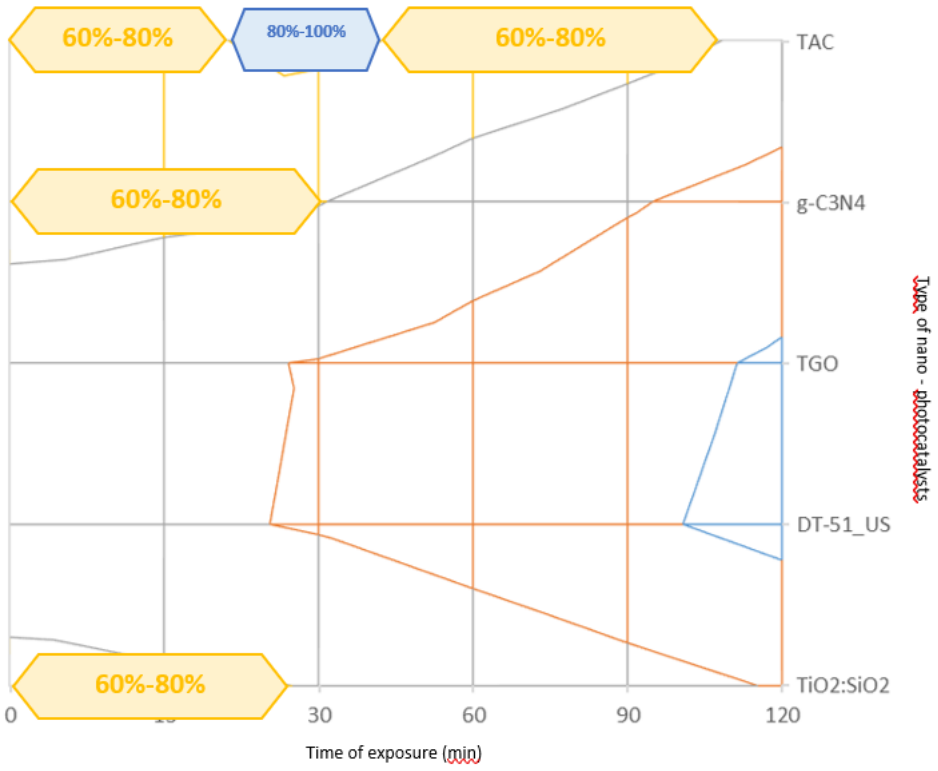

Figure 2.28. Decision - making space and partition of the optimization domain as a function of the multicriteria performance response (weights 30% functional, 70% environmental).

The control function relating to the economic trend determined the restriction of the decision - making sphere (Fig. 2.28).

The performance values in the range 80% - 100% of the maximum value were obtained for the TAC material in the irradiation range at 15 - 60 min. The acceptance of performance levels between 60% and 80% of the maximum value has extended the choice also to materials g-C_3N_4 and TiO_2:SiO_2 1:3 for lower irradiation ranges compared to TAC material. Also, in this

case for the materials TGO and TiO_2 DT51 - US the costs for the preparations made these materials disadvantageous.

2) Fair relevance

In the scenario where the weights are equally distributed for functionality and environmental sustainability, the control function has reduced the range of acceptable cases to the only TAC material irradiated by visible light with an efficiency in the 60 - 80% range for 15 - 120 min irradiation times. Compared to the previous case, where the sustainability component weighed more, the g-C_3N_4 material loses efficiency because it shows a very low photocatalytic activity (Fig. 2.20b). On the contrary, the materials TGO and TiO_2:SiO_2 1:3 have acquired efficiency because they have shown a high photocatalytic efficiency (Fig. 2.20b and 2.18b, respectively). Same trend seen in the case of UV irradiation, this confirms that the differences between UV and visible light irradiation are minimal, matching the criteria of environmental sustainability.

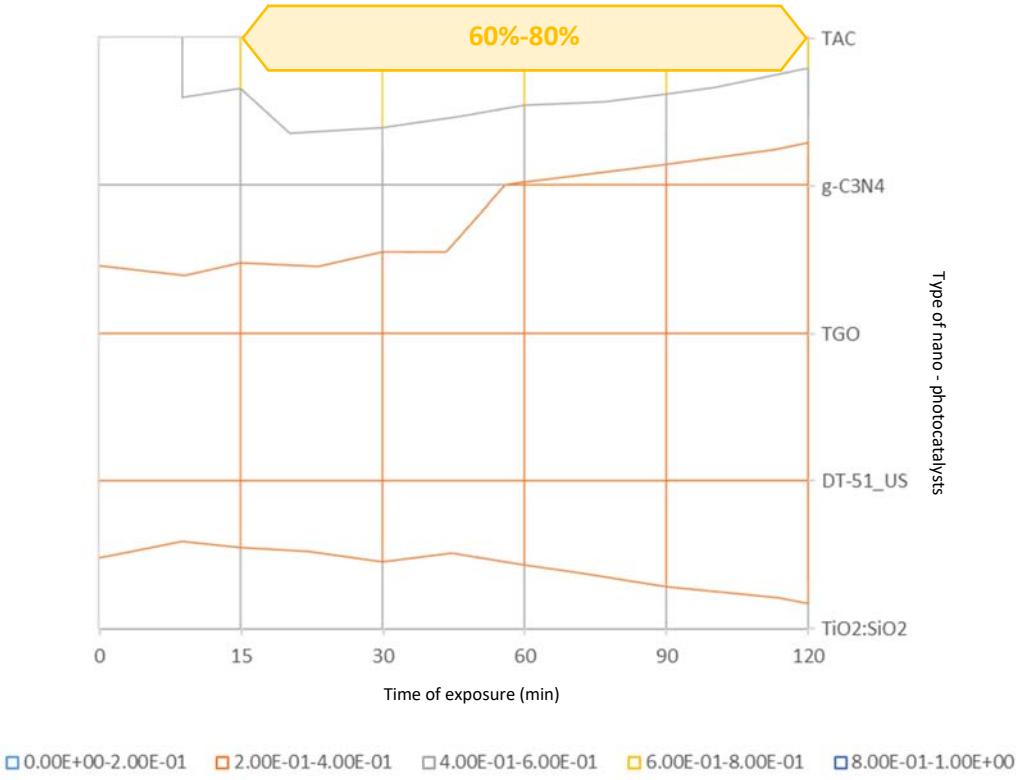

Figure 2.29. Decision - making space and partition of the optimization domain as a function of the multicriteria performance response (weights 50% functional, 50% environmental).

3) <u>Dominance of performance functionality</u>

In the scenario in which the functional performance is dominant, the control function has imposed a restriction on only the TAC nanomaterial in the radiation range 15 - 75min with an economic efficiency in the 60% - 80% range only (Fig. 2.30). It can be considered as acceptable and responsive to the simultaneous maximization of functional-environmental and economic performance indicators.

Again, it is important to point out that energy inputs for the synthesis of nanomaterials available in their final form or as semi-finished products were not considered and this disadvantaged composite materials that may require preparation.

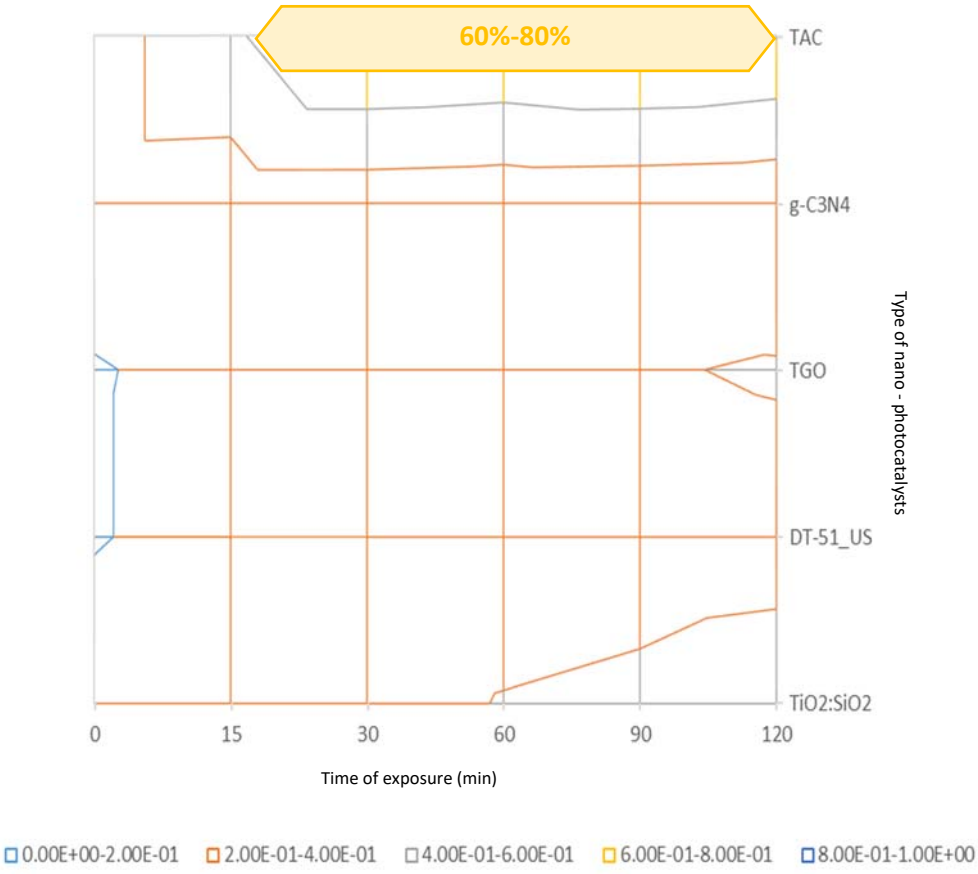

Figure 2.30. Decision - making space and partition of the optimization domain as a function of the multicriteria performance response (weights 70% functional, 30% environmental).

2.4. Conclusion

In this thesis work, an innovative method was exploited to compare the photocatalysts, involving the calculation of the photocatalytic efficiency, the normalization for the quantity of active sites with the TOF parameter, the control of the reduction of COD and finally a profile of environmental and cost sustainability. Based on cost criteria, the use of composite photocatalysts is not recommended, promoting single phase and unmodified materials as commercial sample. However, if we consider environmental sustainability as the predominant factor, from a Green deal perspective, the TiO_2:SiO_2 1:3 composite irradiated with both UV and visible light also obtained a very good score. Moreover, the TiO_2:SiO_2 1:3 composite is the most promising considering both TOF and COD parameters. Regarding the carbon-based materials, an optimization of production process is necessary. In fact, to make TGO a sustainable material the reduction of costs and the environmental impacts are needed deriving from its production process. As regards g-

C_3N_4, the optimization of condition (i.e. concentration) and a possible coupling with TiO_2 could lead to advantages from both cost and sustainability point of view, becoming a good candidate as photocatalysts.

Reference

1. Basis, L.; Background, G. Ftu_2.5.4. **2021**, 1–5.
2. Qu, X.; Alvarez, P.J.J.; Li, Q. Applications of nanotechnology in water and wastewater treatment. *Water Res.* **2013**, *47*, 3931–3946, doi:10.1016/j.watres.2012.09.058.
3. Saravanan, N.; Eric, R. *Photocatalysts*; ISBN 9783540228608.
4. Levchuk, I.; Sillanpää, M. *Titanium dioxide-based nanomaterials for photocatalytic water treatment*; Elsevier Inc., 2020; ISBN 9780128192269.
5. Fraiese, A.; Naddeo, V.; Uyguner-Demirel, C.S.; Prado, M.; Cesaro, A.; Zarra, T.; Liu, H.; Belgiorno, V.; Ballesteros, F. Removal of emerging contaminants in wastewater by sonolysis, photocatalysis and ozonation. *Glob. Nest J.* **2019**, *21*, 98–105, doi:10.30955/gnj.002625.
6. Ahammad, S. Z.; Gomes, J.; Sreekrishnan, T.R. Wastewater treatment forproductionofH2S-free biogas. *J. Chem. Technol. Biotechnol.* **2008**, *83*, 1163–1169, doi:10.1002/jctb.
7. Trevisan, V. Sviluppo di materiali a base di TiO2 per l'abbattimento di inquinanti. **2011**, 1–172.
8. Molinari, R.; Argurio, P.; Szymański, K.; Darowna, D.; Mozia, S. *Photocatalytic membrane reactors for wastewater treatment*; 2020; ISBN 9780128168240.
9. Nosaka, Y.; Nosaka, A.Y. Generation and Detection of Reactive Oxygen Species in Photocatalysis. *Chem. Rev.* **2017**, *117*, 11302–11336, doi:10.1021/acs.chemrev.7b00161.
10. Kunduru, K.R.; Nazarkovsky, M.; Farah, S.; Pawar, R.P.; Basu, A.; Domb, A.J. *Nanotechnology for water purification: applications of nanotechnology methods in wastewater treatment*; 2017; ISBN 9780128043004.
11. Qu, X.; Brame, J.; Li, Q.; Alvarez, P.J.J. Nanotechnology for a safe and sustainable water supply: Enabling integrated water treatment and reuse. *Acc. Chem. Res.* **2013**, *46*, 834–843, doi:10.1021/ar300029v.
12. Anwer, H.; Mahmood, A.; Lee, J.; Kim, K.H.; Park, J.W.; Yip, A.C.K. Photocatalysts for degradation of dyes in industrial effluents: Opportunities and challenges. *Nano Res.* **2019**, *12*, 955–972, doi:10.1007/s12274-019-2287-0.
13. Li, X.; Liu, Y.; Yang, P.; Shi, Y. Visible light-driven photocatalysis of W, N co-doped TiO2. *Particuology* **2013**, *11*, 732–736, doi:10.1016/j.partic.2012.06.018.
14. Yoon, T.P.; Ischay, M.A.; Du, J. Visible light photocatalysis as a greener approach to photochemical synthesis. *Nat. Chem.* **2010**, *2*, 527–532, doi:10.1038/nchem.687.
15. Melchionna, M.; Fornasiero, P. Updates on the Roadmap for Photocatalysis. *ACS Catal.* **2020**, *10*, 5493–5501, doi:10.1021/acscatal.0c01204.
16. Rehman, S.; Ullah, R.; Butt, A.M.; Gohar, N.D. Strategies of making TiO2 and ZnO visible light active. *J. Hazard. Mater.* **2009**, *170*, 560–569, doi:10.1016/j.jhazmat.2009.05.064.

17. Kovalevskiy, N.; Selishchev, D.; Svintsitskiy, D.; Selishcheva, S.; Berezin, A.; Kozlov, D. Synergistic effect of polychromatic radiation on visible light activity of N-doped TiO2 photocatalyst. *Catal. Commun.* **2020**, *134*, doi:10.1016/j.catcom.2019.105841.
18. Helmy, E.T.; Abouellef, E.M.; Soliman, U.A.; Pan, J.H. Novel green synthesis of S-doped TiO2 nanoparticles using Malva parviflora plant extract and their photocatalytic, antimicrobial and antioxidant activities under sunlight illumination. *Chemosphere* **2021**, *271*, 129524, doi:10.1016/j.chemosphere.2020.129524.
19. Xu, T.; Song, C.; Liu, Y.; Han, G. Band structures of TiO2 doped with N, C and B. *J. Zhejiang Univ. Sci. B* **2006**, *7*, 299–303, doi:10.1631/jzus.2006.b0299.
20. Ismael, M. Enhanced photocatalytic hydrogen production and degradation of organic pollutants from Fe (III) doped TiO2 nanoparticles. *J. Environ. Chem. Eng.* **2020**, *8*, 103676, doi:10.1016/j.jece.2020.103676.
21. Chen, A.; Chen, W.F.; Majidi, T.; Pudadera, B.; Atanacio, A.; Manohar, M.; Sheppard, L.R.; Liu, R.; Sorrell, C.C.; Koshy, P. Mo-doped, Cr-Doped, and Mo–Cr codoped TiO2 thin-film photocatalysts by comparative sol-gel spin coating and ion implantation. *Int. J. Hydrogen Energy* **2021**, *46*, 12961–12980, doi:10.1016/j.ijhydene.2021.01.136.
22. Ran, H.; Fan, J.; Zhang, X.; Mao, J.; Shao, G. Enhanced performances of dye-sensitized solar cells based on Au-TiO 2 and Ag-TiO 2 plasmonic hybrid nanocomposites. *Appl. Surf. Sci.* **2018**, *430*, 415–423, doi:10.1016/j.apsusc.2017.07.107.
23. Chen, F.; Zhao, J.; Hidaka, H. Highly selective deethylation of Rhodamine B: Adsorption and photooxidation pathways of the dye on the TiO2/SiO2 composite photocatalyst. *Int. J. Photoenergy* **2003**, *5*, 209–217, doi:10.1155/S1110662X03000345.
24. Lee, S.Y.; Park, S.J. TiO2 photocatalyst for water treatment applications. *J. Ind. Eng. Chem.* **2013**, *19*, 1761–1769, doi:10.1016/j.jiec.2013.07.012.
25. Pan, X.; Zhao, Y.; Liu, S.; Korzeniewski, C.L.; Wang, S.; Fan, Z. Comparing graphene-TiO 2 nanowire and graphene-TiO 2 nanoparticle composite photocatalysts. *ACS Appl. Mater. Interfaces* **2012**, *4*, 3944–3950, doi:10.1021/am300772t.
26. Adly, M.S.; El-Dafrawy, S.M.; El-Hakam, S.A. Application of nanostructured graphene oxide/titanium dioxide composites for photocatalytic degradation of rhodamine B and acid green 25 dyes. *J. Mater. Res. Technol.* **2019**, *8*, 5610–5622, doi:10.1016/j.jmrt.2019.09.029.
27. Varenne, F.; Hillaireau, H.; Bataille, J.; Smadja, C.; Barratt, G.; Vauthier, C. Application of validated protocols to characterize size and zeta potential of dispersed materials using light scattering methods. *Colloids Surfaces A Physicochem. Eng. Asp.* **2019**, *560*, 418–425, doi:10.1016/j.colsurfa.2018.09.006.
28. Lolli, A.; Blosi, M.; Ortelli, S.; Costa, A.L.; Zanoni, I.; Bonincontro, D.; Carella, F.; Albonetti, S. Innovative synthesis of nanostructured composite materials by a spray-freeze drying process: Efficient catalysts and photocatalysts preparation. *Catal. Today* **2019**, *334*, 193–202, doi:10.1016/j.cattod.2018.11.022.
29. Ortelli, S.; Costa, A.L. Nanoencapsulation techniques as a “safer by (molecular) design” tool. *Nano-Structures and Nano-Objects* **2018**, *13*, 155–162, doi:10.1016/j.nanoso.2016.03.006.
30. Pennetta, A.; Di Masi, S.; Piras, F.; Lü, X.; Li, J.; De Benedetto, G.E.; Mele, G. Tio2@lipophilic porphyrin composites: New insights into tuning the photoreduction of cr(vi) to cr(iii) in aqueous phase. *J. Compos. Sci.* **2020**, *4*, doi:10.3390/jcs4020082.
31. Bickerstaffe, S. The science of 4×4. *Automot. Eng.* **2006**, *31*, 37.

32. Qian, W.; Zhaoqun, W.; Xuanfeng, K.; Xiaodan, G.; Gi, X. A facile strategy for controlling the self-assembly of nanocomposite particles based on colloidal steric stabilization theory. *Langmuir* **2008**, *24*, 7778–7784, doi:10.1021/la800532q.
33. Giraud, F.; Couble, J.; Geantet, C.; Guilhaume, N.; Loridant, S.; Gros, S.; Porcheron, L.; Kanniche, M.; Bianchi, D. Experimental Microkinetic Approach of De-NO x by NH3 on V2O5/WO3/TiO2 Catalysts. 5. Impacts of the NH3-H2O Coadsorption on the Coverage of Sulfated TiO2-Based Solids. *J. Phys. Chem. C* **2018**, *122*, 24619–24633, doi:10.1021/acs.jpcc.8b05846.
34. Hu, X.; Yu, Y.; Wang, Y.; Zhou, J.; Song, L. Separating nano graphene oxide from the residual strong-acid filtrate of the modified Hummers method with alkaline solution. *Appl. Surf. Sci.* **2015**, *329*, 83–86, doi:10.1016/j.apsusc.2014.12.110.
35. Marberger, A.; Ferri, D.; Rentsch, D.; Krumeich, F.; Elsener, M.; Kröcher, O. Effect of SiO2 on co-impregnated V2O5/WO3/TiO2 catalysts for the selective catalytic reduction of NO with NH3. *Catal. Today* **2019**, *320*, 123–132, doi:10.1016/j.cattod.2017.11.037.
36. Žerjav, G.; Arshad, M.S.; Djinović, P.; Zavašnik, J.; Pintar, A. Electron trapping energy states of TiO2–WO3 composites and their influence on photocatalytic degradation of bisphenol A. *Appl. Catal. B Environ.* **2017**, *209*, 273–284, doi:10.1016/j.apcatb.2017.02.059.
37. Lambert, T.N.; Chavez, C.A.; Hernandez-sanchez, B.; Lu, P.; Bell, N.S.; Ambrosini, A.; Friedman, T.; Boyle, T.J.; Wheeler, D.R.; Huber, D.L. Synthesis and Characterization of Titania - Graphene Nanocomposites. **2009**, 19812–19823.
38. Ortelli, S.; Malucelli, G.; Blosi, M.; Zanoni, I.; Costa, A.L. NanoTiO 2 @DNA complex: a novel eco, durable, fire retardant design strategy for cotton textiles. *J. Colloid Interface Sci.* **2019**, *546*, 174–183, doi:10.1016/j.jcis.2019.03.055.
39. Ortelli, S.; Poland, C.A.; Baldi, G.; Costa, A.L. Silica matrix encapsulation as a strategy to control ROS production while preserving photoreactivity in nano-TiO2. *Environ. Sci. Nano* **2016**, *3*, 602–610, doi:10.1039/c6en00009f.
40. Ge, L. Synthesis and photocatalytic performance of novel metal-free g-C 3N4 photocatalysts. *Mater. Lett.* **2011**, *65*, 2652–2654, doi:10.1016/j.matlet.2011.05.069.
41. Wen, J.; Xie, J.; Chen, X.; Li, X. A review on g-C 3 N 4 -based photocatalysts. *Appl. Surf. Sci.* **2017**, *391*, 72–123, doi:10.1016/j.apsusc.2016.07.030.
42. Pattnaik, S.P.; Behera, A.; Martha, S.; Acharya, R.; Parida, K. Facile synthesis of exfoliated graphitic carbon nitride for photocatalytic degradation of ciprofloxacin under solar irradiation. *J. Mater. Sci.* **2019**, *54*, 5726–5742, doi:10.1007/s10853-018-03266-x.
43. Panwar, K.; Jassal, M.; Agrawal, A.K. In situ synthesis of Ag-SiO2Janus particles with epoxy functionality for textile applications. *Particuology* **2015**, *19*, 107–112, doi:10.1016/j.partic.2014.06.007.
44. Mohammadi, M.; Sedighi, M.; Alimohammadi, V. Modeling and optimization of Nitrate and total Iron removal from wastewater by TiO 2 /SiO 2 nanocomposites. *Int. J. Nano Dimens* **2019**, *10*, 195–208.
45. Purkayastha, M.D.; Sil, S.; Singh, N.; Ray, P.P.; Darbha, G.K.; Bhattacharyya, S.; Mallick, A.I.; Majumder, T.P. Sonochemical synthesis of nanospherical TiO2 within graphene oxide nanosheets and its application as a photocatalyst and a Schottky diode. *FlatChem* **2020**, *22*, 100180, doi:10.1016/j.flatc.2020.100180.
46. Ye, C.; Wang, R.; Wang, H.; Jiang, F. The high photocatalytic efficiency and stability of LaNiO3/g-C3N4 heterojunction nanocomposites for photocatalytic water splitting to hydrogen. *BMC Chem.* **2020**, *14*, doi:10.1186/s13065-020-00719-w.

47. Goyal, A.; Rumaiz, A.K.; Miao, Y.; Hazra, S.; Ni, C.; Shah, S.I. Synthesis and characterization of TiO[sub 2]–Ge nanocomposites. *J. Vac. Sci. Technol. B Microelectron. Nanom. Struct.* **2008**, *26*, 1315, doi:10.1116/1.2939262.
48. Medri, V.; Servadei, F.; Bendoni, R.; Natali Murri, A.; Vaccari, A.; Landi, E. Nano-to-macroporous TiO 2 (anatase) by cold sintering process. *J. Eur. Ceram. Soc.* **2019**, *39*, 2453–2462, doi:10.1016/j.jeurceramsoc.2019.02.047.
49. Darzi, S.J.; Mahjoub, A.R.; Nilchi, A.R.; Garmarodi, S.R. HEAT TREATMENT EFFECTS ON NON-THERMAL SOL-GEL DRIVED. **2011**, *8*, 20–26.
50. Kumar, P.; Sharma, A.; Karn, R.K.; Pandiyan, S.K. Synthesis of TiO 2 Nanoparticles by Sol-gel Method and Their Characterization Synthesis of TiO 2 Nanoparticles by Sol-gel Method and Their Characterization. *J. Basic Appl. Eng. Res.* **2014**, *1*, 1–5.
51. Hussein, A.; Sarkar, S.; Oh, D.; Lee, K.; Kim, B. Epoxy/p-phenylenediamine functionalized graphene oxide composites and evaluation of their fracture toughness and tensile properties. *J. Appl. Polym. Sci.* **2016**, *133*, doi:10.1002/app.43821.
52. Cui, S.; Xie, B.; Li, R.; Pei, J.; Tian, Y.; Zhang, J.; Xing, X. g-C3N4/CeO2 binary composite prepared and its application in automobile exhaust degradation. *Materials (Basel).* **2020**, *13*, doi:10.3390/ma13061274.
53. Zhu, L.; Lu, Q.; Lv, L.; Wang, Y.; Hu, Y.; Deng, Z.; Lou, Z.; Hou, Y.; Teng, F. Ligand-free rutile and anatase TiO2 nanocrystals as electron extraction layers for high performance inverted polymer solar cells. *RSC Adv.* **2017**, *7*, 20084–20092, doi:10.1039/c7ra00134g.
54. Costa, A.L.; Ortelli, S.; Blosi, M.; Albonetti, S.; Vaccari, A.; Dondi, M. TiO2 based photocatalytic coatings: From nanostructure to functional properties. *Chem. Eng. J.* **2013**, *225*, 880–886, doi:10.1016/j.cej.2013.04.037.
55. Mahardiani, L.; Ashadi, A.; Saputro, S.; Indriyanti, N.Y.; Taufiq, M. The removal of organic pollutant from aqueous solution by modified activated carbon surface. *Moroccan J. Chem.* **2020**, *8*, 936–942, doi:10.48317/IMIST.PRSM/morjchem-v8i4.21728.
56. Friedmann, D.; Mendive, C.; Bahnemann, D. TiO2 for water treatment: Parameters affecting the kinetics and mechanisms of photocatalysis. *Appl. Catal. B Environ.* **2010**, *99*, 398–406, doi:10.1016/j.apcatb.2010.05.014.
57. Montanhera, M.A.; Pereira, É.A.; Spada, E.R.; Paula, F.R. Influência do percentual de fase anatase/rutilo na eficiência fotocatalítica do TiO2 sintetizado quimicamente. *22º CBECiMat - Congr. Bras. Eng. e Ciência dos Mater. Natal, RN, Bras.* **2016**, 9.
58. Ortelli, S.; Costa, A.L.; Matteucci, P.; Miller, M.R.; Blosi, M.; Gardini, D.; Tofail, S.A.M.; Tran, L.; Tonelli, D.; Poland, C.A. Silica modification of titania nanoparticles enhances photocatalytic production of reactive oxygen species without increasing toxicity potential in vitro. *RSC Adv.* **2018**, *8*, 40369–40377, doi:10.1039/C8RA07374K.
59. Štengl, V.; Bakardjieva, S.; Grygar, T.M.; Bludská, J.; Kormunda, M. TiO2-graphene oxide nanocomposite as advanced photocatalytic materials. *Chem. Cent. J.* **2013**, *7*, 1–12, doi:10.1186/1752-153X-7-41.
60. Liang, J.; Yang, X.; Wang, Y.; He, P.; Fu, H.; Zhao, Y.; Zou, Q.; An, X. A review on g-C3N4incorporated with organics for enhanced photocatalytic water splitting. *J. Mater. Chem. A* **2021**, *9*, 12898–12922, doi:10.1039/d1ta00890k.
61. Fu, J.; Yu, J.; Jiang, C.; Cheng, B. g-C3N4-Based Heterostructured Photocatalysts. *Adv. Energy Mater.* **2018**, *8*, 1–31, doi:10.1002/aenm.201701503.
62. Bai, X.; Wang, L.; Zong, R.; Zhu, Y. Photocatalytic activity enhanced via g-C3N4 nanoplates to nanorods. *J. Phys. Chem. C* **2013**, *117*, 9952–9961, doi:10.1021/jp402062d.

63. Kobkeatthawin, T.; Trakulmututa, J.; Amornsakchai, T.; Kajitvichyanukul, P.; Smith, S.M. Identification of Active Species in Photodegradation of Aqueous Imidacloprid over g-C3N4/TiO2 Nanocomposites. *Catalysts* **2022**, *12*, 1–16, doi:10.3390/catal12020120.
64. Sundararajan, M.; Sailaja, V.; John Kennedy, L.; Judith Vijaya, J. Photocatalytic degradation of rhodamine B under visible light using nanostructured zinc doped cobalt ferrite: Kinetics and mechanism. *Ceram. Int.* **2017**, *43*, 540–548, doi:10.1016/j.ceramint.2016.09.191.
65. Chong, M.N.; Jin, B.; Chow, C.W.K.; Saint, C. Recent developments in photocatalytic water treatment technology: A review. *Water Res.* **2010**, *44*, 2997–3027, doi:10.1016/j.watres.2010.02.039.
66. Mantovi, P.; Marmiroli, M.; Maestri, E.; Tagliavini, S.; Piccinini, S.; Marmiroli, N. Application of a horizontal subsurface flow constructed wetland on treatment of dairy parlor wastewater. *Bioresour. Technol.* **2003**, *88*, 85–94, doi:10.1016/S0960-8524(02)00291-2.
67. Barbier, J.; Delanöe, F.; Jabouille, F.; Duprez, D.; Blanchard, G.; Isnard, P. Total oxidation of acetic acid in aqueous solutions over noble metal catalysts. *J. Catal.* **1998**, *177*, 378–385, doi:10.1006/jcat.1998.2113.

Chapter 3: semi -pilot plant study for the photodegradation of water pollutants – SOLUTION 2

3.1. Introduction

The scale - up of a process is an integral part of innovation and is the basis for the success and failure of a process. The scale - up of a process is defined as the set of considerations and actions necessary to recreate laboratory data at an industrial level. It is not an automatic transition because factors such as machinery materials, larger volumes, mass transfers, heat transfers, etc. come into play. The fundamental steps for the creation of a new material have been defined by the European community through the TRL codes (Technology Readiness Levels), which define the technological maturity of the product. During the TRL1 phase the technological principles are observed, at TRL2 a technological concept is formulated. TRL3 and TRL4 include proof of concept developed and laboratory validation of the product. TRL5 and TRL6 serve to validate and demonstrate the technology in an industrial environment. TRL7 foresee the demonstration of a system prototype in the operating environment. TRL8 and TRL9 are used to complete and test the complete system in the operating environment[1].

Despite the huge effort spent to develop and characterize novel nano-photocatalysts, which are especially active under solar light, knowledge gaps still persist for their full - scale application, starting from the reactor design and scale-up and the evaluation of the photocatalytic efficiency in pre - pilot scenarios[2,3]. One of the main objectives addressed by more recent studies is to extend the use of TiO_2 - based photocatalysts to solar (visible) light for the application in areas without electricity or as a sustainable solution to avoid the use of bio - hazardous and costly UV light[4–7]. Nevertheless, the majority of works are carried out on a laboratory scale, and the introduction of other materials into TiO_2 dramatically increases the complexity of the photocatalyst preparation and cost, and the modification with heavy metals or harmful organics could even improve the degree of environment pollution[8,9]. Furthermore, the scale - up of nano - TiO_2 - based photocatalytic technology in water purification systems poses a problem: the recovery of nanoparticles. When studying a method of purification from pollutants, on the one hand it is necessary to ensure the removal of the pollutant itself, on the other hand it is essential to verify that no new pollutants are introduced or generated. If the nanoparticles were left free in the water, they would be able to degrade the pollutants present but if not controlled they could reach living beings and manage an acute or

chronic toxic component. To avoid further treatments (introducing further costs and time) the best strategy is to immobilize the photocatalysts on a support.

Considering the real application in large - scale plants for water purification, a heterogeneous photocatalysis process is necessary involving the immobilization of nano-photocatalysts on different support. This presents an important advantage: the elimination of any type of post - purification treatments that usually involve sophisticate separation processes to separate dispersed nanomaterials. In heterogeneous photocatalysis the choose of the support represents a crucial aspect. We identified the fabrics as ideal supports due to their availability in large quantities, low cost, great affinity with TiO_2 NPs and they are easily adaptable to any geometry.

Moreover, the fabrics functionalized with NPs show a high resistance to washing in the washing machine[4,10], thus eliminating any type of post - treatment.

Finally, again to limit costs, it would be good if the photocatalysts were regenerable in order to always reuse the same support functionalized with nanoparticles and minimize waste and costs.

This work was focused on the semi - pilot plant optimization. We selected two NMs tested at lab - scale (TAC and TiO_2:SiO_2 1:3) which were immobilized on surface fabric supports that were integrated in a semi - pilot plant scale (6 L capacity) reactor, using Rhodamine B (RhB) as a reaction model[20]. We investigated the photocatalytic efficiency of TiO_2 – based coating, when irradiated by both UV and visible light - emitting diode (LED) lights, and identified the best design options, comparing photocatalyst and supports properties, process parameters, and type of irradiation.

3.2. Materials & Methods

3.2.1. Materials

TiO_2 nanosol (NAMA41, 6 wt%), called TAC and SiO_2 nanosol 40 wt% (Ludox® HS - 40) were purchased from Colorobbia (Sovigliana, Vinci (FI), Italy) and Grace Davison (USA), respectively. Rhodamine B (dye content ≈ 95%) target dye, ion exchanger Dowex® 1 × X8

basic anion exchanger resin and ion exchanger Dowex® 50 W × 4 acidic cation exchanger resin were purchased from Sigma Aldrich (Milano, Italy).

3.2.2. TiO_2 - based Nanosuspensions

Acid TiO_2 nanosol (TAC, pH 1.5) was used to prepare two TiO_2 - based nanosuspensions: TACR and TiO_2:SiO_2 1:3 suspensions. TACR was obtained diluting TAC at the 3 wt% concentration with distilled water (DI) water and treated with ion exchanger Dowex® 1 × X8 basic anion exchanger resin in order to increase the pH from 1.5 to 4. This increase in pH is necessary in order to avoid fabric damage caused by acidity, and the residual by the synthesis of original TiO_2 can reduce the photocatalytic activity[21]. TiO_2:SiO_2 (ratio 1:3) 3 wt% was prepared by the heterocoagulation method. SiO_2 nanosol 40 wt% (Ludox® HS - 40) was diluted at the concentration 3 wt% with DI water and treated with ion exchange Dowex® 50 W × 4 acidic cationic exchanger resin in order to decrease the pH from 10 to 4 (SiO_2-R). TiO_2 suspension (TACR) was dropped into SiO_2-R suspension. The TiO_2:SiO_2 1:3 sample was obtained through an electrostatic interaction between negatively charged silica nanoparticles and positively charged titania nanoparticles. The electrostatic interactions between SiO_2 and TiO_2 surfaces are promoted by mixing the sols in well - defined ratios and by ball milling for 24 h with zirconia spheres (diameter 5 mm) as grinding media.

3.2.3. Ceramized Fabric

The coated fabrics was obtained via the dip – pad - curing method. The fabric was pretreated by washing in an ultrasonic bath for 15 min in DI water and dried in an oven at 100 °C. Then, the fabric was dipped in a 10 mL of TiO_2 - based suspension for 5 min, squeezed in two rolls to eliminate the excess of suspension (pad stage), dried in an oven at 100 °C, and finally cured at 130 °C for 10 min in order to fix the NPs to the fabric. A single impregnation was carried out achieving the final dry add - on value (AO%), which is defined as the percent amount of the finishing agent added to the fabric with respect to the initial weight of the latter, i.e.,

$$AO\% = \frac{W_f - W_i}{W_i} * 100$$

where w_i and w_f are the weights of the fabric before and after the dip – pad - curing process, respectively.

We tested four fabrics different in color, weight, and structure described in Table 3.1.

Table 3.1. Fabrics used as supports for nano - TiO_2 - based coatings.

Code	Images	Composition	g / m^2
SP		65% cotton 35% polyester	450
SC		65% cotton 35% polyester	500
SM		Not available	640
C	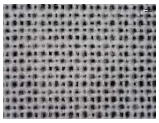	100% cotton	100

3.2.4. Semi - Pilot Plant and Irradiation Source

The photocatalytic tests were carried out in a 6 L semi - pilot plant[22], as schematized in Fig. 3.1. The semi - pilot plant was designed and built by RAFT s.r.l., Montelupo Fiorentino (Italy). It hosts two plastic windows for supporting ceramized fabrics (14.8 × 11.4 cm; 100 cm^2 fabric exposed area for each support), and on the top, there are three holes for UV or visible light lamps. The homogeneity of water flow was ensured through a peristaltic pump, and the feed bath was thermostated by a chiller (Julabo, F12). The LED strip lights were provided by the Wiva Group (Italy). The visible LED light is characterized by a wide emission spectrum (Figure 3.2a) with a main peak at wavelength = 452 nm and a second peak at wavelength = 569 nm. The UV LED light has a very narrow emission spectrum with λ_{max} = 384 nm (Figure 3.2b). The irradiance was calculated placing a radiometric UV probe (UV - A 315–400 nm) on the fabric surface in order to evaluate the UV component irradiance of the two light - emitting sources that resulted in 4.3 × 10^{-3} W / m^2 for visible light and 150 W / m^2 for UV light.

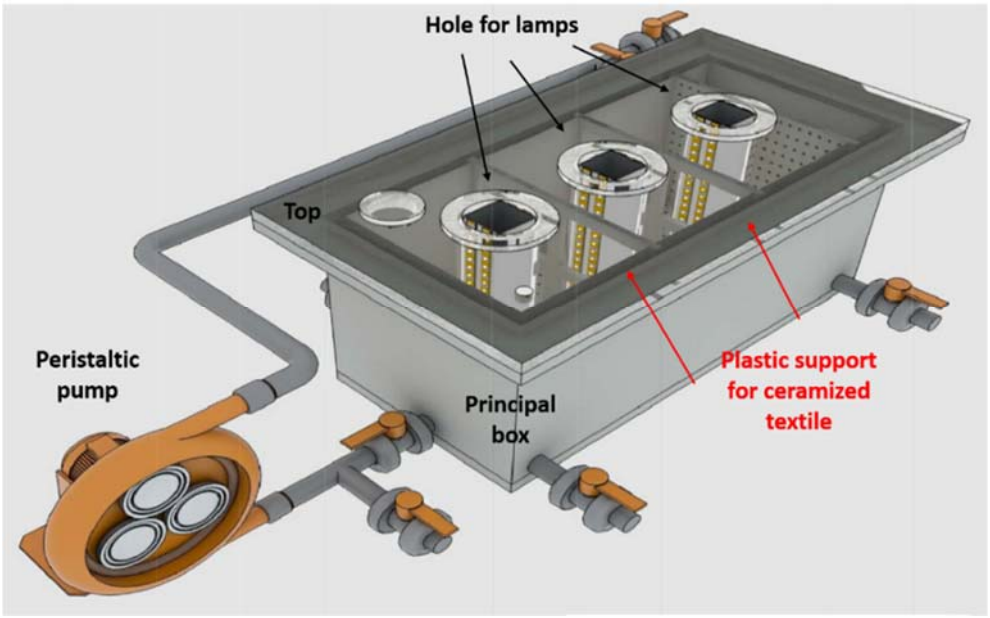

Figure 3.1. Schematized representation of a 6 L semi - pilot plant.

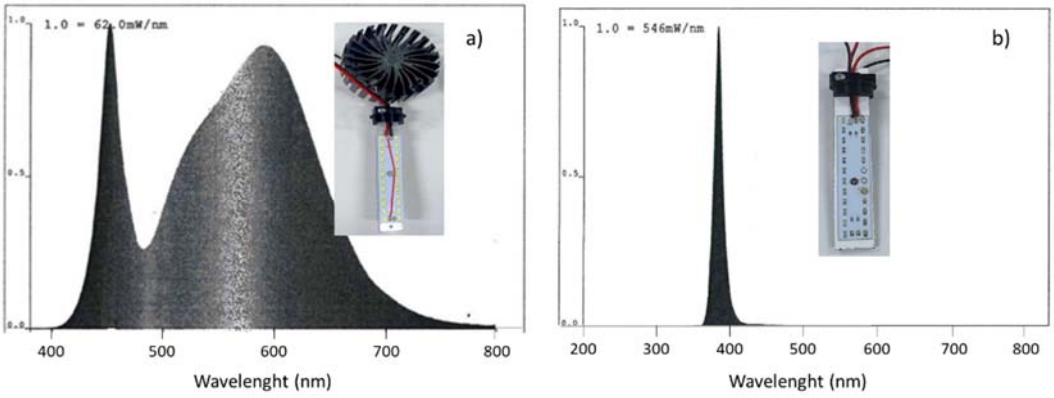

Figure 3.2. Emission spectrum of (a) visible LED light and (b) UV LED light, including photographs of the corresponding LED strips, mounting an air - cooling fan.

3.2.5. Characterization

3.2.5.1. Characterization on Fabrics

The untreated fabrics were morphologically observed by optical microscope using a Hirox 3D digital microscope, RH200 with a magnitude of lens ×35 and ×50. Specifically, we observed the fabric weave, thickness, and color of a single fiber.

The untreated / treated fabrics were observed also using the Field Emission Scanning Electron Microscope (FESEM ZEISS Sigma HV). All samples were gold - coated (thickness = 5 nm) (Spatter Quorum Q150T ES) to increase the conductivity and obtain well - defined images.

The hydrophilicity of untreated and TACR - treated fabrics was evaluated by contact angle analyses. The measurements were carried out using a KRUSS DSA 30 S instrument, a 20 µL drop was deposited by sessile drop deposition method at room temperature (25 °C), and a tangent - fitting method was used for the angle contact measurements.

3.2.5.2. Rhodamine B Degradation Tests

The photodegradation tests were carried out using Rhodamine B (RhB) as a model of organic trace pollutant. RhB is a synthetic dye that is commonly use in water remediation due to the easy detection of small concentrations by UV - Vis absorption analysis using a single beam spectrophotometer Hach Lange, DR3900. RhB imparts a deep magenta hue to its water solutions and displays a well - defined absorbance peak at 554 nm. In our experiment, we used 3.5 mg / L RhB concentration. The lamp was switched on outside the plant 30 min before starting the test in order to stabilize the power of emission; simultaneously, the ceramized textile was put into RhB solution to reach the adsorption–desorption equilibrium. In order to evaluate the degradation kinetics, an aliquot of 3 mL was withdrawn and analyzed every 20 min (A_x) through UV - Vis analysis in the range of 350–700 nm to a final reaction time of 100 min. The A_x was measured in correspondence to the maximum of the absorbance peak detected, considering the shift of the initial absorbance peak of RhB. Before starting the degradation tests, after 30 min of absorption, the initial absorbance (A_0) was determined. The photocatalytic efficiency was calculated at t = 100 min. It indicates the ratio between the amount of reagent consumed and the amount of reagent initially present in the reaction environment, and it was determined by the following formula:

$$Photocatalytic\ efficiency\ (\%) = \left(1 - \frac{A_x}{A_0}\right) * 100$$

where A_x is the peak value at time t and A_0 is the peak value at time 0. In order to facilitate the comparison between the different photocatalysts, normalizing for the amount of catalyst and the time of exposure, the turnover frequency (*TOF*) parameter was calculated. The *TOF* parameter was calculated by following equation:

$$TOF = \frac{(\frac{mol\ of\ product}{t\ (s)})}{mol\ of\ catalyst}$$

where

mol of product is calculated as the initial concentration of reagent per efficiency reached at the time s

mol of catalyst are the moles of the catalyst deposited on the exposure area of fabric calculated by the AO% parameter.

3.3. Result & Discussion

3.3.1. Characterization of Fabrics

A basic morphological characterization of fabrics, used as support for obtaining nano - TiO_2 - coated photocatalysts, was carried out by optical microscope (Fig. 3.3).

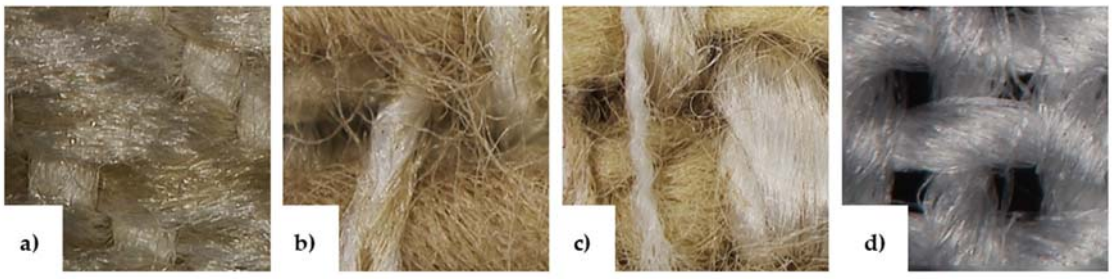

Figure 3.3. Optical microscopy images of untreated fabrics: (a) SP; (b) SC; (c) SM; (d) C.

The images (Fig. 3.3) show the differences of color, warp, and weft of the target fabrics. SP, SC, and SM fabrics are characterized by very intertwined fibers, whilst the weave of the C fabric is more regular and expanded than other fabrics. This can explain the significant differences in the absorption of the TiO_2 - based nanosuspensions (TACR and TiO_2:SiO_2 1:3), as demonstrated by the add - on percentage (AO%) reported in Table 3.2.

In fact, the fabric C being characterized by a large weave and low weight (Table 3.1) adsorbs half the amount adsorbed by the other fabrics.

SEM analysis showed the changes in surface morphology induced by the presence of TiO_2 nanoparticles confirming the formation of a homogeneous nano - TiO_2 coating on the fabric's surface. Unlike the smooth texture of the uncoated fibre (Fig. 3.4a), the fibres in the TACR - coated fabric showed a certain surface roughness due to the thin layer of TiO_2 adhering to the textile substrate (Fig. 3.4b).

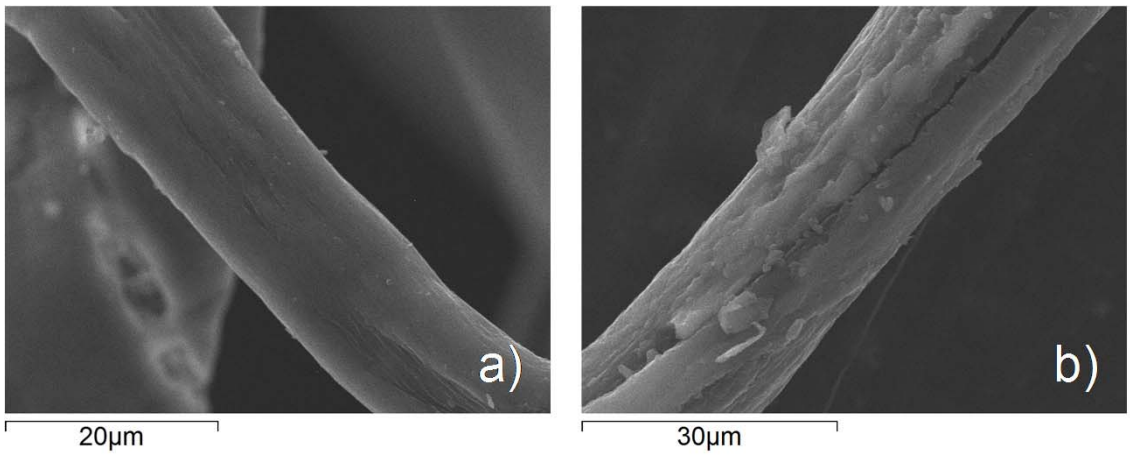

Figure 3.4. SEM image (a) untreated fabric (b) TACR treated fabric.

Table 3.2. AO% parameters calculated.

Fabric	**AO% (TACR)**	**AO% (TiO_2:SiO_2 1:3)**
SP	5.9	8
SC	8.4	n.a.
SM	6.2	n.a.
C	3.8	3

n.a. not available.

In order to evaluate the hydrophilicity of fabrics and estimate the adsorption capacity of the textile supports, before and after the TiO_2 treatment (TACR), contact angle measurements were performed. The results are reported in Table 3.3.

Table 3.3. Contact angle measurements on untreated and TACR coated fabrics.

Fabric	**Untreated**	**Coated**

SP	121 ± 1	121 ± 3
SC	113 ± 1	n.d.
SM	n.d.	n.d.
C	n.d.	122 ± 4

n.d. not determined.

In general, all samples show hydrophilic properties, and no significant differences between untreated and treated fabrics are found. Specifically, the SM fabric exhibits very high hydrophilic behavior both on untreated and treated samples. In fact, the water drop is absorbed so quickly that during the contact angle measurements, the values are not detectable. This also occurs for untreated C and treated SC fabrics. In the case of SC fabric, an increase in hydrophilicity induced by TiO_2 treatment is found. Otherwise, a decrease in hydrophilicity induced by TiO_2 treatment was found in the C sample fabric. In any case, no clear correlation between the variation of hydrophilicity between different samples and the photocatalytic efficiency was found, as the results discussed in the following paragraphs show.

3.3.2. Optimization of Photocatalytic Process

3.3.2.1. Effect of TiO_2 - Based Coatings Composition

Using SP as the target fabric, we evaluated the photocatalytic efficiency of TACR and TiO_2:SiO_2 1:3 coatings under both UV and visible light irradiation. Very low differences were observed between TiO_2 and TiO_2:SiO_2 1:3 compositions. This result (Table 3.4) confirms the different mechanism occurring when the photodegradation of TiO_2 is tested at a liquid and gas state. In fact, in a previous study[23], using NO_x abatement ($DeNO_x$) as the experimental model, we found that the presence of SiO_2 significantly improved the efficiency of the photocatalyst.

Table 3.4. Comparison between different TiO_2 - based photocatalysts. Tests carried out with SP fabrics under UV and visible light.

Irradiation Light	Coating	Photocatalytic Efficiency %
Visible	TACR	49

UV	TiO_2:SiO_2 1:3	51
	TACR	64
	TiO_2:SiO_2 1:3	60

The RhB photodegradation of the two photocatalysts over time is represented in Fig. 3.5, showing a progressive decrease in the absorbance of the RhB peak at 554 nm. Moreover, for both photocatalysts, a blue - shift of the λ_{max} was detected. This is associated to a de-ethylation of RhB molecules, which agrees with the hypothesized RhB degradation mechanism (Fig. 3.6)[24], in the presence of supported photocatalysts. The assessment of photocatalytic efficiency was done by considering the maximum of the absorbance peaks, allowing an estimation of the overall reactivity, because we referred to the capacity of the catalyst to photodegrade the dye and its by - products. The higher shift detected in the case of the TiO_2:SiO_2 1:3 photocatalyst can be attributed to a complete conversion of the N, N, N', N' - tetraethylated rhodamine molecule (λ_{max} = 554 nm) to de-ethylated rhodamine (λ_{max} = 498 nm), as a consequence of the attack of oxidative radicals against N - ethyl group[23], which was not achieved in the case of TACR. This was further confirmed by Chen et al.[25] that showed different absorption mechanisms and consequently different degradation mechanisms using TiO_2 or the TiO_2:SiO_2 1:3 composite. In fact, they declare that in the case of RhB absorption on TiO_2:SiO_2 1:3, the chromophore is absorbed by the photocatalyst through the diethylamino groups while in the case of TiO_2, it is absorbed through the carboxyl groups. This difference results in an attack of the chromophore ring and its cleavage in the RhB - TiO_2 case, while in the RhB - TiO_2:SiO_2 1:3 case, the auxochromic groups are attacked and produce the de-ethylation of the alkylamine group. Moreover, they found that the blue-shift phenomenon due to the RhB de-ethylation is more evident under visible light than UV, which is because the UV radiation directly excites the TiO_2, while under visible light, it is the RhB absorbed on the surface of the photocatalyst to subsequently produce the active oxygen species.

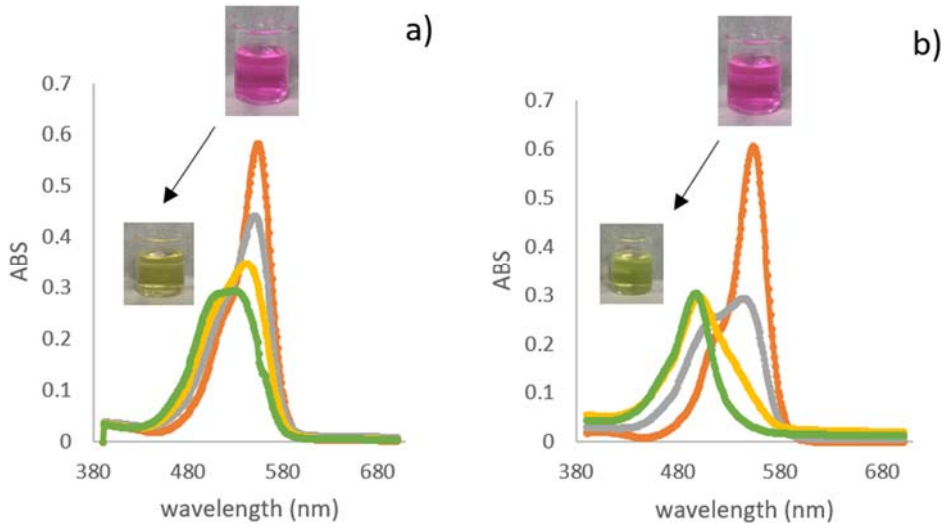

Figure 3.5. Absorbance of RhB solutions after irradiation under visible light at 0 min (orange), 40 min (gray), 80 min (yellow), and 100 min (green). Time 0: λmax 554 nm; time 100: λmax 527 nm for TACR and 498 nm for TiO_2:SiO_2 1:3.

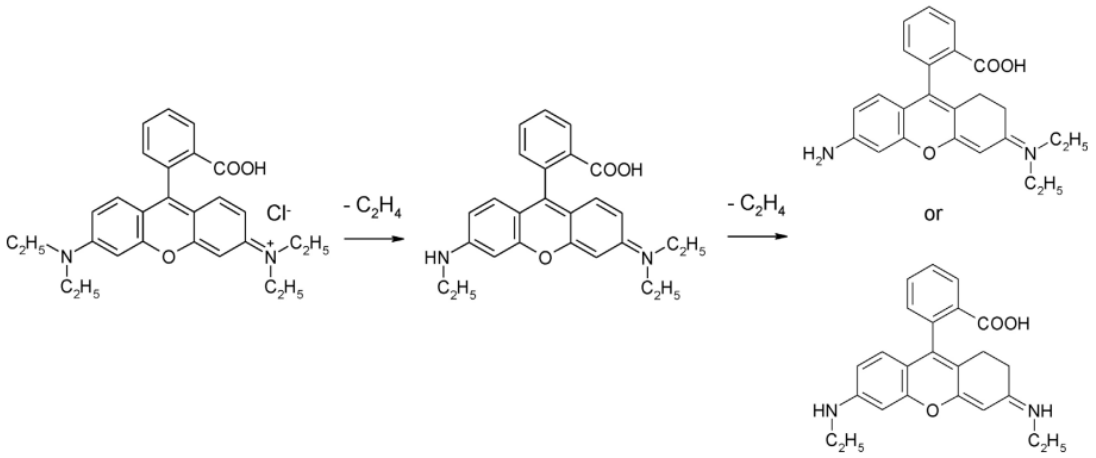

Figure 3.6. De-ethylation proposed mechanism of RhB by TiO_2-based nanoparticles immobilized on fabric[24].

3.3.2.2. Effect of Temperature

The dependence of photocatalytic performance on temperature has been widely investigated in the literature, and it is still under debate, with increasing temperature promoting phenomena such as the desorption of adsorbed reactants and the rate of recombination of photogenerated electron / hole pairs that are detrimental for the photocatalysis[26,27]. Otherwise, it is well known that the temperature influences the reaction kinetics, enhancing the activation energy and so speeding the photodegradation process[28,29]. Photodegradation tests using SP fabrics coated with TiO_2:SiO_2 1:3, under both UV and visible light sources, were compared at three working temperatures: 15 °C,

25 °C (room temperature), and 38 °C. The results are shown in Table 3.5. Under UV LED irradiation, the photocatalytic activity decreases by increasing the temperature, whilst in the case of visible LED, no significant trend was observed. The dependence of photodegradation efficiency by temperature is the result of synergetic (increase in activation energy, increase in charge transfer kinetic) and detrimental effects (the recombination of charge carriers and the altered adsorption equilibrium of reactants such as dye molecules, water, and oxygen)[26,28–30]. Therefore, in this case, the best compromise is working at room temperature, matching environmental and economic requirements[31].

Table 3.5. Effect of temperature. Tests carried out with TiO_2:SiO_2 1:3 - coated SP samples, under both UV and visible LEDs.

Irradiation	Temperature °C	Photocatalytic Efficiency %
Visible	15	55
	25	51
	38	57
UV	15	63
	25	60
	38	59

3.3.2.3. Effect of Fabric Substrate

In order to investigate the effect of fabric substrates vs. type of irradiation (UV and visible light sources), we carried out photocatalytic tests with TACR - coated fabrics, and the results are reported in Table 3.6.

Table 3.6. Effect of fabric substrates. Tests carried out with TACR at T = 25 °C, under both UV and visible light sources.

Fabric	Photocatalytic Efficiency %	
	UV LED	Visible LED
SP	49	64
SC	64	54
SM	56	59

C	53	63

Overall samples showed a comparable photodegradation efficiency despite the type of fabrics used and the type of irradiation source. Nevertheless, the fabric composition and structure seem to affect the efficiency; the SP sample is even more reactive under a visible source. The reactivity shown by the samples irradiated by visible LED was surprising, considering that the TACR crystalline phase, corresponding to anatase with 16% of brookite[21], has a band - gap, previously measured of 3.1 eV, that restricts its use only to the ultra - violet range of light. Considering the UV light fraction intensity measured on the fabric surface—UV LED (48.5 W / m^2) and visible LED (4.3×10^{-3} W / m^2), it is evident that in the case of a visible lamp, the few photons achieving the fabric surface have enough energy to activate the catalyst, and they are responsible for the photodegradation reactivity, which is comparable with that obtained irradiating the samples with UV LED, with a UV irradiation intensity that is five orders of magnitude higher. This result is quite unexpected because even if it is reported that a few photons of energy (i.e., as low as 1×10^{-2} W / m^2) can induce the photo - generation of electron–hole pairs[32], high intensities (400–1000 W / m^2) are needed to achieve a high photocatalytic reaction rate, particularly in water disinfection treatment[33]. The really low intensity of ultraviolet radiation (UVR) needed to activate our photocatalysts encourages their use and activation under solar irradiation; considering that the UV light portion of the yearly average solar irradiance at sea level, on a clear day, is about a few units W / m^2, we can reasonably estimate that the UVR intensity of the sun is in large excess of the amount needed to activate our photocatalysts. From this perspective, the proposed TiO_2 - based photocatalysts do not require costly and time - consuming doping treatments to be activated under visible LED or solar light, with consequent benefits from safety, environmental, and economic points of view[32].

In order to better compare the photocatalytic ability of coated fabrics and select the most suitable fabric support, we calculated the TOF parameter (Table 3.7). The results show that the C fabric presents the highest photoactivity, both under UV and visible LEDs. Considering the natural source of cotton (100% biodegradable), its high availability at low cost and the shown photo - induced reactivity under visible LED, which is one order of magnitude higher than the other photocatalyst, also irradiated by UV light, it is evident

that the cotton photocatalyst under visible LED becomes the best choice, matching the criteria of sustainability and safety.

Table 2.7. TOF parameter calculated at time 100 min. Tests carried out with TACR at T = 25 °C, under both UV and visible light sources.

Fabric	UV LED	Visible LED
SP	7.5×10^{-5}	9.8×10^{-5}
SC	8.9×10^{-5}	7.5×10^{-5}
SM	8.6×10^{-5}	8.8×10^{-5}
C	1.02×10^{-3}	8.7×10^{-4}

3.3.2.4. Process Scalability

The treated fabrics were integrated and tested in the LED - based semi - pilot photocatalytic reactor of Fig. 3.7a. Fig. 3.7b shows the pilot reactor based upon the best design options identified performing tests with the semi - pilot reactor. The performances obtained with the pilot plant and the evaluation about the scalability of the semi-pilot plant are the objective of a future study.

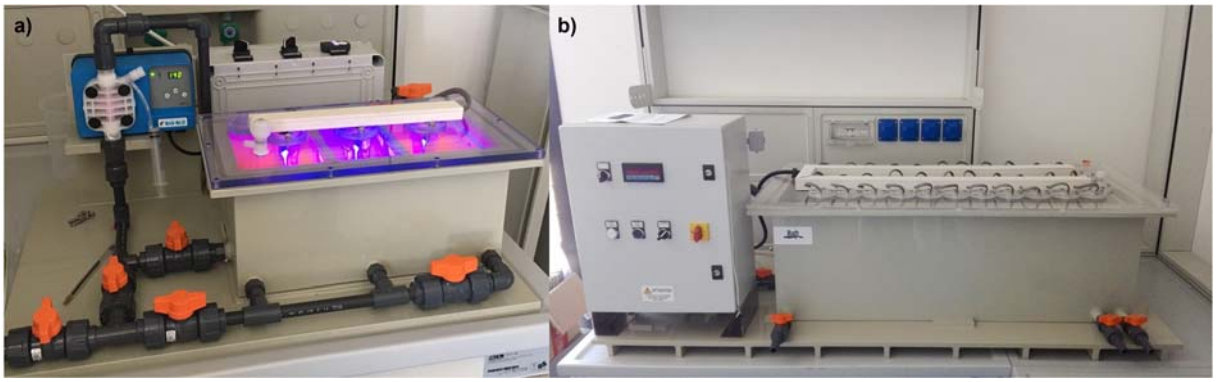

Figure 3.7. (a) LED - based semi - pilot photocatalytic reactor tested (6L), used in this study; (b) Up-scaled reactor (100L) built upon the best design options in the present study.

3.4. Conclusion

In response to the still persisting knowledge gaps for the full - scale application of nano-photocatalysts in water / wastewater purification systems, we immobilized TiO_2 - based nanoparticles as the coating of fabrics, obtaining large available, low cost, highly flexible

photocatalysts that allow an easy implementation in many different geometry water treatment reactors and the easy recovery and regeneration of photocatalysts. We implemented the obtained photocatalytic fabrics in a 6L capacity semi - pilot plant and evaluated the degradation of RhB dye, which was used as a probe molecule, simulating the water pollution. We adopted a multi - variables optimization approach to look for the photoreactor operating parameters that mostly affected the photocatalytic performance and identified the best design option also in response to safety and sustainable criteria. We found that the 100% biodegradable cotton fabric irradiated by visible LED is the best candidate, because it showed a TOF higher than all the other samples, which was irradiated by both UV and visible light sources. The really low intensity of UV radiation - activating fabrics under visible LED expands the applicability of the technology to solar light, since the measured intensity of the UV radiation component, in visible LED, is much lower than the solar yearly average one. The findings from the multi - variable optimization study were translated into updated recommendations for the design and the technical application of these efficient and low - cost TiO_2 - based photocatalysts, which are suitable for developing a range of technologies aimed at environmental protection. The good results obtained encouraged the scale - up of the 6 L semi - pilot plant up to the 100 L pilot plant that has been built, even if the evaluation of photocatalytic performances is still under investigation.

Reference

1. Appendice, B.B. Definizione Technology Readiness Level - TRL. **2020**, 6–7.
2. Khodadadian, F.; de Boer, M.W.; Poursaeidesfahani, A.; van Ommen, J.R.; Stankiewicz, A.I.; Lakerveld, R. Design, characterization and model validation of a LED-based photocatalytic reactor for gas phase applications. *Chem. Eng. J.* **2018**, *333*, 456–466, doi:10.1016/j.cej.2017.09.108.
3. Li, R.; Li, T.; Zhou, Q. *Impact of titanium dioxide (TiO2) modification on its application to pollution treatment—a review*; 2020; Vol. 10; ISBN 2223501117.
4. Costa, A.L.; Ortelli, S.; Blosi, M.; Albonetti, S.; Vaccari, A.; Dondi, M. TiO2 based photocatalytic coatings: From nanostructure to functional properties. *Chem. Eng. J.* **2013**, *225*, 880–886, doi:10.1016/j.cej.2013.04.037.
5. Mahanta, U.; Khandelwal, M.; Suresh Deshpande, A. TiO2@SiO2 nanoparticles for methylene blue removal and photocatalytic degradation under natural sunlight and low-power UV light. *Appl. Surf. Sci.* **2021**, *576*, 151745, doi:10.1016/j.apsusc.2021.151745.
6. Basavarajappa, P.S.; Patil, S.B.; Ganganagappa, N.; Reddy, K.R.; Raghu, A. V.; Reddy, C.V. Recent progress in metal-doped TiO2, non-metal doped/codoped TiO2 and

TiO2 nanostructured hybrids for enhanced photocatalysis. *Int. J. Hydrogen Energy* **2020**, *45*, 7764–7778, doi:10.1016/j.ijhydene.2019.07.241.
7. Dong, X.; Xu, J.; Kong, C.; Zeng, X.; Wang, J.; Zhao, Y.; Zhang, W. Synthesis of β-FeOOH/TiO2/SiO2 by melting phase separation-hydrothermal method to improve photocatalytic performance. *Ceram. Int.* **2021**, *47*, 32303–32309, doi:10.1016/j.ceramint.2021.08.125.
8. Factories, H.; Study, A.C.; Plant, P.; Joseane, J.; Mesa, M.; Sebasti, J.; Gonz, W.; Rojas, H. Murcia Mesa, J.J.; Hernández Niño, J.S.; González, W.; Rojas, H.; Hidalgo, M.C.; Navío, J.A. Photocatalytic Treatment of Stained Wastewater Coming from Handicraft Factories. A Case Study at the Pilot Plant Level. Water 2021, 13, 2705. https://doi.org/10.3. *Water* **2021**.
9. Sciscenko, I.; Mestre, S.; Climent, J.; Valero, F.; Escudero-Oñate, C.; Oller, I.; Arques, A. Magnetic photocatalyst for wastewater tertiary treatment at pilot plant scale: Disinfection and enrofloxacin abatement. *Water (Switzerland)* **2021**, *13*, 1–12, doi:10.3390/w13030329.
10. Ortelli, S.; Malucelli, G.; Blosi, M.; Zanoni, I.; Costa, A.L. NanoTiO 2 @DNA complex: a novel eco, durable, fire retardant design strategy for cotton textiles. *J. Colloid Interface Sci.* **2019**, *546*, 174–183, doi:10.1016/j.jcis.2019.03.055.
11. Cernuto, G.; Rusconi, F.; Colonna, G.M.; Tecnologia, A.; Co, I.; Stazione, D. NANOTECNOLOGIE PER L ' INDUSTRIA TESSILE. 52–57.
12. Bae, G.Y.; Min, B.G.; Jeong, Y.G.; Lee, S.C.; Jang, J.H.; Koo, G.H. Journal of Colloid and Interface Science Superhydrophobicity of cotton fabrics treated with silica nanoparticles and water-repellent agent. *J. Colloid Interface Sci.* **2009**, *337*, 170–175, doi:10.1016/j.jcis.2009.04.066.
13. Li, C. SCIENCE AND Improving the antistatic ability of polypropylene fibers by inner antistatic agent filled with carbon nanotubes. **2004**, *c*, 2089–2096, doi:10.1016/j.compscitech.2004.03.010.
14. Ortelli, S.; Malucelli, G.; Cuttica, F.; Blosi, M.; Zanoni, I.; Luisa, A. Coatings made of proteins adsorbed on TiO 2 nanoparticles : a new flame retardant approach for cotton fabrics. *Cellulose* **2018**, *25*, 2739–2749, doi:10.1007/s10570-018-1745-z.
15. Xiaomeng, Y.; Jianwen, H.O.U.; Yuan, T.; Jingya, Z.; Qiangqiang, S.U.N. Antibacterial surfaces : Strategies and applications. **2022**.
16. Oliva, J. Science of the Total Environment Photocatalytic materials immobilized on recycled supports and their role in the degradation of water contaminants : A timely review. *Sci. Total Environ.* **2022**, *807*, 150820, doi:10.1016/j.scitotenv.2021.150820.
17. Yang, Y.; Guo, Z.; Li, Y.; Qing, Y.; Wang, W. Multifunctional superhydrophobic self-cleaning cotton fabrics with oil-water separation and dye degradation via thiol-ene click reaction. *Sep. Purif. Technol.* **2022**, *282*, 120123, doi:10.1016/j.seppur.2021.120123.
18. Rao, P.; Dhar, M.; Advances, R.; Aspects, A.; Studies, I.C.; Science, S.; All, E.S.B. V No Title. **1998**, *113*, 329–335.
19. Varesano, A.; Vineis, C.; Tonetti, C.; Omar, D.; Ramírez, S.; Mazzuchetti, G.; Ortelli, S.; Blosi, M.; Costa, A.L. Multifunctional Hybrid Nanocomposite Nanofibers Produced by Colloid Electrospinning from Water Solutions. **2015**, 41–48.
20. Faccani, L.; Ortelli, S.; Blosi, M.; Costa, A.L. Ceramized fabrics and their integration in a semi-pilot plant for the photodegradation of water pollutants. *Catalysts* **2021**,

11, doi:10.3390/catal11111418.
21. Ortelli, S.; Costa, A.L.; Dondi, M. TiO2 nanosols applied directly on textiles using different purification treatments. *Materials (Basel).* **2015**, *8*, 7988–7996, doi:10.3390/ma8115437.
22. Tolio, T.; Copani, G.; Terkaj, W. *Factories of the future: The Italian flagship initiative*; Springer International Publishing, 2019; ISBN 9783319943589.
23. Ortelli, S.; Poland, C.A.; Baldi, G.; Costa, A.L. Silica matrix encapsulation as a strategy to control ROS production while preserving photoreactivity in nano-TiO2. *Environ. Sci. Nano* **2016**, *3*, 602–610, doi:10.1039/c6en00009f.
24. Ortelli, S.; Blosi, M.; Albonetti, S.; Vaccari, A.; Dondi, M.; Costa, A.L. TiO2based nano-photocatalysis immobilized on cellulose substrates. *J. Photochem. Photobiol. A Chem.* **2014**, *276*, 58–64, doi:10.1016/j.jphotochem.2013.11.013.
25. Chen, F.; Zhao, J.; Hidaka, H. Highly selective deethylation of Rhodamine B: Adsorption and photooxidation pathways of the dye on the TiO2/SiO2 composite photocatalyst. *Int. J. Photoenergy* **2003**, *5*, 209–217, doi:10.1155/S1110662X03000345.
26. Meng, Y.; Xia, S.; Pan, G.; Xue, J.; Jiang, J.; Ni, Z. Preparation and photocatalytic activity of composite metal oxides derived from Salen-Cu(II) intercalated layered double hydroxides. *Korean J. Chem. Eng.* **2017**, *34*, 2331–2341, doi:10.1007/s11814-017-0135-9.
27. Meng, F.; Liu, Y.; Wang, J.; Tan, X.; Sun, H.; Liu, S.; Wang, S. Temperature dependent photocatalysis of g-C3N4, TiO2 and ZnO: Differences in photoactive mechanism. *J. Colloid Interface Sci.* **2018**, *532*, 321–330, doi:10.1016/j.jcis.2018.07.131.
28. Barakat, N.A.M.; Kanjwal, M.A.; Chronakis, I.S.; Kim, H.Y. Influence of temperature on the photodegradation process using Ag-doped TiO2 nanostructures: Negative impact with the nanofibers. *J. Mol. Catal. A Chem.* **2013**, *366*, 333–340, doi:10.1016/j.molcata.2012.10.012.
29. Chen, Y.W.; Hsu, Y.H. Effects of reaction temperature on the photocatalytic activity of TiO2 with Pd and Cu cocatalysts. *Catalysts* **2021**, *11*, doi:10.3390/catal11080966.
30. Liu, B.; Zhao, X.; Parkin, I.P.; Nakata, K. *Charge carrier transfer in photocatalysis*; 2020; Vol. 31; ISBN 9780081028902.
31. Alisawi, H.A.O. Performance of wastewater treatment during variable temperature. *Appl. Water Sci.* **2020**, *10*, 1–6, doi:10.1007/s13201-020-1171-x.
32. Chong, M.N.; Jin, B.; Chow, C.W.K.; Saint, C. Recent developments in photocatalytic water treatment technology: A review. *Water Res.* **2010**, *44*, 2997–3027, doi:10.1016/j.watres.2010.02.039.
33. Rincón, A.G.; Pulgarin, C. Photocatalytical inactivation of E. coli: Effect of (continuous-intermittent) light intensity and of (suspended-fixed) TiO 2 concentration. *Appl. Catal. B Environ.* **2003**, *44*, 263–284, doi:10.1016/S0926-3373(03)00076-6.

Chapter 4: Experimental evaluation of the reactivity of nano-photocatalysts and assessment of their potential (eco-) toxicity – SOLUTION 3

4.1. Introduction

This chapter focuses on two fundamental aspects of the development of photocatalysts for water purification:

1- the conditions that maximise the photocatalytic production of radicals that will oxidise organic pollutants,
2- the definition of the safety profile of the nano-photocatalysts, in order to assess ecological risks arising from their emission into aqueous environment.

The growing and rapid production of nanomaterials has inevitably increased the exposure of human and eco - system to these materials. Therefore, it is essential to prevent potential hazardous effects while not restricting their functionality[1]. Due to their small size, nano-photocatalysts can potentially damage cells or organisms by activating mechanisms driven by the generation of reactive oxygen species (ROS), that is, the same extremely reactive species that are used for the mineralization of organic pollutants. Nano-photocatalysts, in fact, can produce peroxides (H_2O_2), superoxide ($\bullet O_2^-$), hydroxyl radicals ($\bullet$OH - ROS more reactive), singlet oxygen ($^1O_2$)) also through mechanisms other than the photochemical ones. The excess of these species in a cell is defined as Oxidative Stress, a condition that can lead to the death of the cells, and the ability of a toxicant to induce oxidative stress is defined as oxidative power. From a practical point of view, analysing the acellular ability of a nanomaterial to consume antioxidant (e.g., glutathione, cysteine) or to generate ROS may provide information about the reactivity once they penetrate into cells. Many factors, however, concur in the oxidative power of nanomaterials, and machine learning methodologies may become effective strategies to extract useful information about the oxidative potential of nanoparticles from massive datasets[2]. The majority of the available predictive tools are focused on in vitro endpoints to predict cellular viability in diverse organisms[3,4]. To our knowledge, there is neither an explicit mechanistic interpretation nor a predictive model specific to oxidative stress., in this thesis, we developed a machine learning model that that identifies the characteristics of the nanoparticles, and of exposure, that correlate with the experimental consumption of antioxidant and the generation of ROS, this type of information is crucial for supporting safety – by - design actions for the nano - based photocatalyst.

4.1.1. Generation of ROS

The efficiency of the photoinduced degradation of organic pollutants varies depending on the types of semiconductors (photocatalysts) used and on the operative conditions. Since ROS are primary intermediates of photocatalytic oxidation , the identification, quantification and kinetics of ROS production are important factors of the photodegradation mechanisms and their analysis enables the design of efficient solutions [5].

In a common set - up, nano-photocatalysts are suspended in water, where, by irradiation, radicals can be formed (Fig. 4.1); when a water molecule comes into contact with a nanoparticle excited by the light it can be oxidized to H_2O_2 or •OH. Conversely, an O_2 molecule can be reduced to $•O_2^-$. In a subsequent step, the dimerization of the •OH to H_2O_2 or the disproportionation of the $•O_2^-$ to H_2O_2 can occur. $•O_2^-$ can also oxidize to $^1O_2$. The radicals can then interact multiple times with the pollutants, which can be mineralized to CO_2 and H_2O[6]. Different methods used to detect radicals in water differ in selectivity, sensitivity and fast time resolution[11]. Radical half - life ranges from a minimum of nanoseconds (in most cases) to a few seconds, these life - times lead to concentrations that range from pico- to micromolar. Due to these two factors, direct methods for the detection of radicals in water are in most cases impossible, with the exception of the methods for H_2O_2 which has the longest half-life[12].

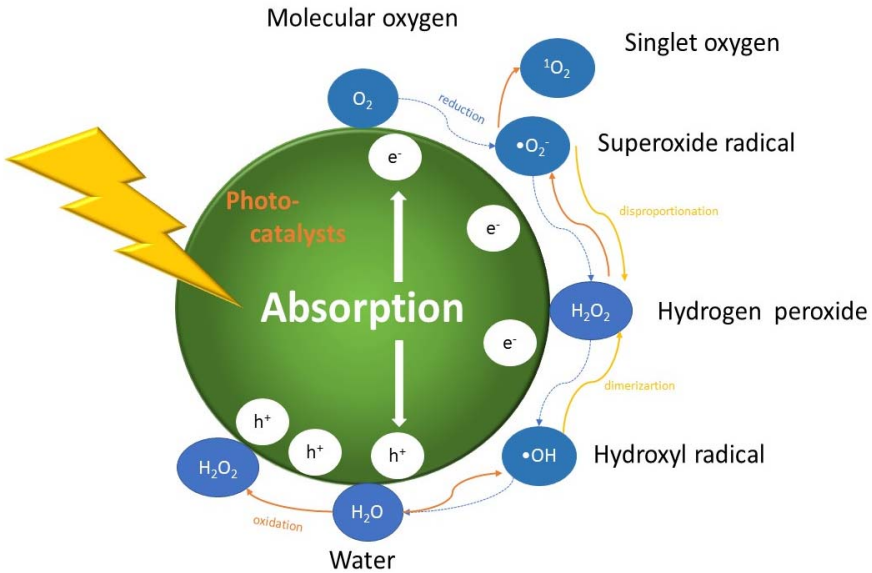

Figure 4.1. ROS generated in the photocatalytic reduction and oxidation steps of oxygen and water.

For my Ph.D. thesis, I used a fast, simple method, which does not require particular expensive chemical probes to provide information on •OH production. Among the most commonly used indirect methods, we find: Electron Paramagnetic Resonance – (EPR) of adducts formed between a probe molecule (i.e., spin trap) and a radical[13], Colorimetric assays, Chemiluminescence assays[14], Fluorescence emission[15,16].

All these methods, suitably calibrated, can be selective for a specific radical. On the other hand, they all have the disadvantage of requiring very expensive equipment, which, in turn, requires specialized and skilled users.

4.1.2. Quantification of the Oxidative power

One the objectives of this thesis is the evaluation of the oxidative power of nanoparticles. Upon cellular uptake, nanoparticles can induce oxidative stress by a number of mechanisms, which include the catalytic production of radicals (e.g., through the Fenton mechanism), or consumption of antioxidants[17].

The term Oxidative Stress indicates the set of alterations that lead to an excess of oxidizing agents in cells. Oxidizing species and free radicals play very important physiological roles, such as defence against bacteria, transmission of biochemical signals between cells, blood pressure control etc... It is only their excess, generally referred to one or more classes of oxidants, that is implicated in oxidative stress, now considered to be associated with over one hundred human pathologies[18,19].This excess, in fact, may result in metabolic alteration, damage and cell death. Any disturbances in normal redox state due to the production of peroxides and free radicals can have toxic effects that damage several components of the cell, including proteins, lipids and DNA.

ROS can also interfere with intracellular signalling mechanisms and in the regulation of gene expression. in a normal state, antioxidants can neutralize ROS. When ROS exceed antioxidant defences, a cascade of effects may follow:

1- Cell proliferation is initially activated and the concentration of "free" intracellular Ca^{2+} increases. As oxidative stress progresses, transition metal ions are released which catalyse free radical reactions. Some metals bind to DNA making it a target for hydroxyl radicals. It also increases the release of Ca^{2+} which is kept low in the

case of normal cells. At this point the cell increases its protective defences and tries to repair the damage to the DNA (anti - oxidant defence).

2- Inflammation stage: at this level the cells are subjected to the cytokine storm activated by the immune system that tries to defeat the cause of advanced oxidative stress. Under normal conditions, the cell is able to regulate this mechanism but when previous damage is present the production of cytokines is not stopped and this leads the cells to self - injure.

3- Cytotoxicity: the cell is no longer able to protect itself and dies; the cell membrane breaks; the released metal ions and toxins increase the lesions to neighbouring cells, causing them to die quickly in a cascade. Effects are to some extent cell - type specific, being influenced by parameters such as the presence of a given cell surface receptor and signal transduction mechanisms, as well as levels of antioxidant defence[20–22].

For this thesis, I evaluated the intrinsic ability of nanoparticles to produce radical and to consume antioxidant by simple, yet accurate methods for the acellular study of these mechanisms. Results of this screening may be used in ranking the potential toxicity of nanoparticles and inform the design of safe systems for photocatalytic purification of water[23].

Depletion of antioxidant was evaluated as consumption of Glutathione (GSH) and Cysteine (Cys) induced by a nanoparticle in a acellular environment[24]:

- GSH / GSSG (Fig. 4.2a): GSH is a low – molecular - weight, water - soluble natural tripeptide. It is composed of three amino acids units (glutamic acid, cysteine and glycine) with a high ability to neutralize oxidants through the thiol group (-SH) present in cysteine terminal, which, upon oxidation, dimerizes by forming a -SS- bond and according to the reaction (1).

-

$$2\ G - SH + ROOH \rightarrow GSSG + ROH + H_2O \qquad (1)$$

Its antioxidant function is restored by a NADPH - dependent enzyme. The relationship between the oxidized and the reduced form is a dynamic equilibrium that provides information on the state of tissues and cells[19,25].

- Cysteine / cystine (Fig. 4.2b) is an amino acid. Two distinct thiol groups in an oxidizing environment can bind, giving rise to a disulphide bridge (cystine) (as in the case of GSH) and then to the tertiary or quaternary structures of proteins. Cysteine deficiency leads to weakness, decreased muscle mass, atrophy, liver damage, skin lesions and much more[19].

-

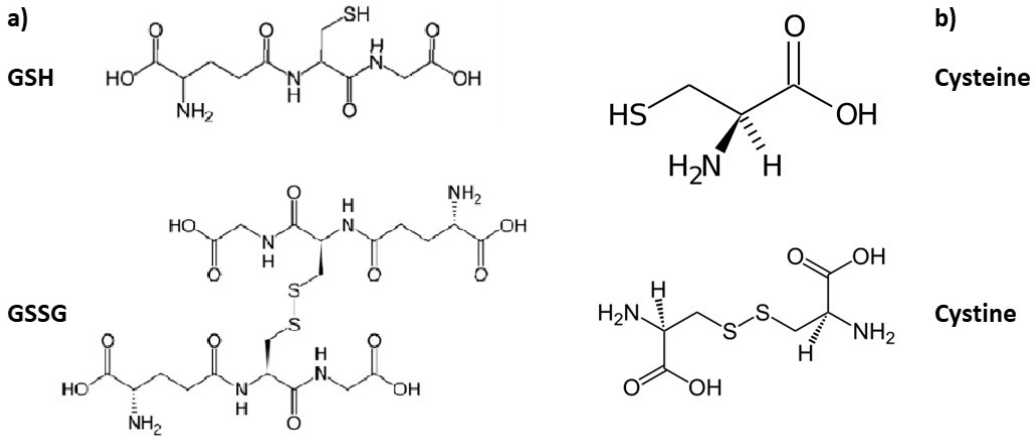

Figure 4.28. a) Structures of GSH and of GSSH b) Structures of Cysteine and of cystine.

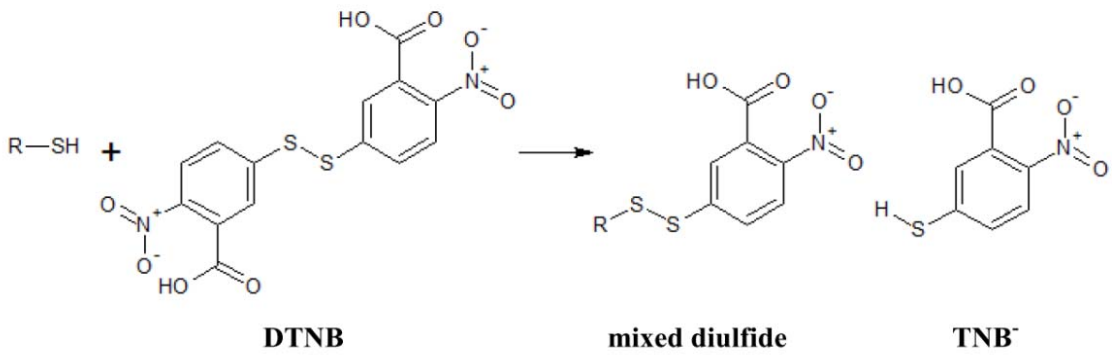

Figure 4.3. Mechanism of the Ellman assay.

In the testing protocol I used, the unconsumed portions of these two substances are detected using the Ellman assay, a colorimetric method which is based on the reaction between Ellman's reagent (DTNB) and a thiol group (-SH) which leads to formation of a mixed disulphide and the anion TNB_2^- which absorbs at 412 nm. The reaction mechanism is shown in Fig. 4.3.

The ability of the photocatalysts to generate •OH radicals was evaluated by incubation with N, N – dimethyl - 4 - nitrosoaniline (RNO – $C_8H_{10}N_2O$) followed by irradiation with UV radiation (the same conditions as in the photocatalysis experiment – chapter 2); the formation of adducts of RNO and •OH can be followed spectrophotometrically: the degree of discoloration of the RNO provide a measure of the tendency of the photocatalyst to produce •OH[7]. RNO in the solid state appears as a soft green powder, when put into solution it becomes straw yellow in colour at low concentrations and brown in high concentrations. When the RNO is attacked by a hydroxyl radical, the N = O double bond is destabilized with consequent formation of the N - OH bond and the loss of the yellow colour (Fig. 4.4[8])[9,10].

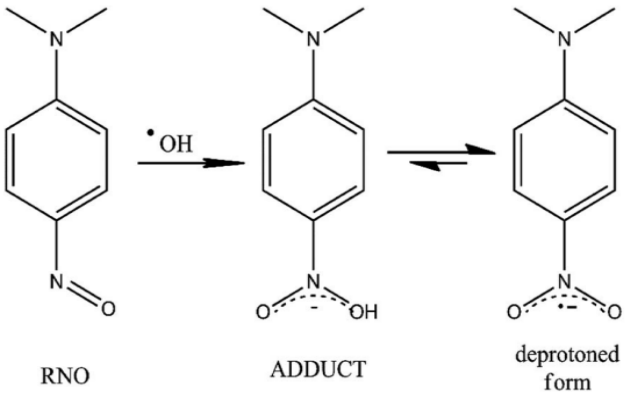

Figure 4.4. The oxidation of p-nitrosodimethylaniline by the hydroxyl radical.

4.2. Material & Methods

4.2.1. Materials

Phosphate buffer solution (PBS) powder, glutathione (GSH) (pharmaceutical secondary standard), L - Cysteine (Cys) ≥ 98%, N, N – Dimethyl – 4 - nitrosoaniline (RNO), 5,5' – Dithio-bis - (2 - nitrobenzoic Acid) (Ellman reagent) 99%, ethylenediaminetetraacetic acid (EDTA) anhydrous ≥ 98%, hydrogen peroxide (H_2O_2) solution 30% (w / w) in water were purchased from Sigma Aldrich (Italy).

4.2.2. Antioxidant (GSH, Cys) and •OH generation (RNO depletion) tests

Preparation of solutions and suspensions

A suspension for TAC and TiO_2:SiO_2 2 mM was prepared diluting the stock suspension (6 wt% and 3 wt% respectively) in PBS 0.01M. TGO and g-C_3N_4 suspension 2 mM was

prepared mixing powder and PBS 0.01M. The suspension underwent 15 minutes of ultrasonic bath to promote the dispersion of nanoparticles.

The solutions in PBS 0.01M of GSH 1.1 mM, Cys 1.1 mM, RNO 40 µM were prepared. The final concentration of GSH and Cys during the test was 0.1 mM. To determine the GSH / Cys / RNO concentrations, we recorded absorbance at different concentrations; we used these values to construct a calibration curve (Fig. 4.5, 4.6, and 4.7 respectively). The measurements were carried out in triplicate. To check if the mixing method could consume some of the initial amounts of probe - molecule, we have quantified the response for GSH / Cys / RNO at three different times (0, 1, 3h) for manual stirring, bath (Elmasonic S-30H) or ultrasonic probe (Bandelin sonoplus). Three aliquots of the same initial solution of GSH / Cys / RNO were subjected to manual stirring, 5 minutes in an ultrasonic bath and the to 5 minutes of ultrasound probe. We measured the absorbance of the resulting solution after the mixing.

Ellman reagent required a different solvent for a good solubilization of the compound: we prepared a 0.15 mM of Ellman reagent in PBS 0.1 M + 1 mM of EDTA.

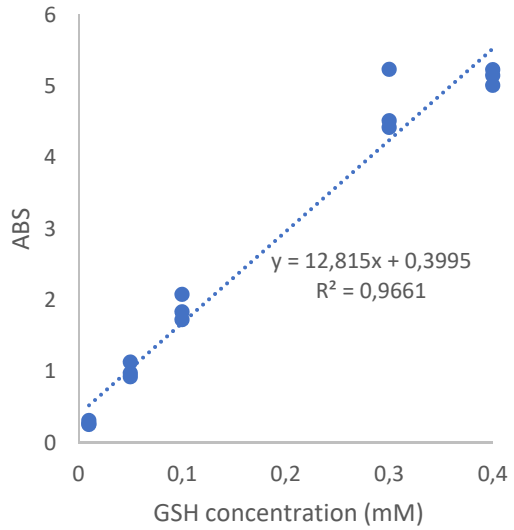

Figure 4.5. GSH calibration curve

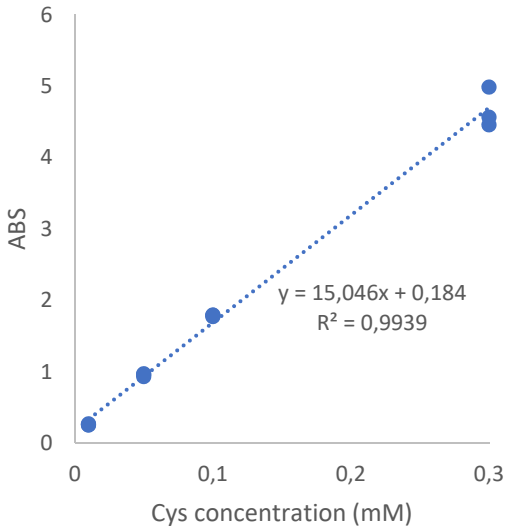

Figure 4.6. Cys calibration curve

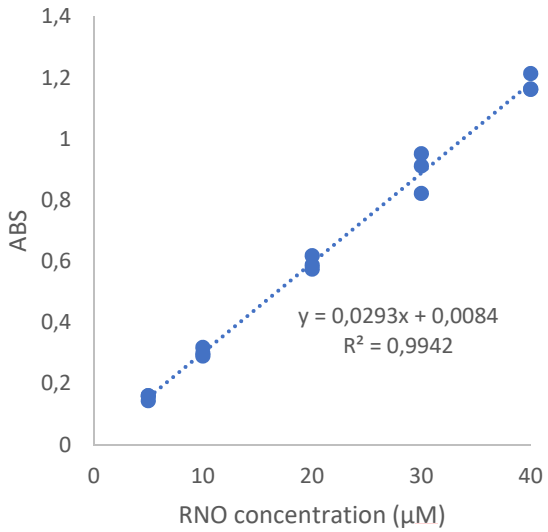

Figure 4.7. RNO calibration curve

Incubation & measurements of absorbances

Two scenarios were evaluated: 1) Dark condition and 2) UV irradiation.

1) Dark conditions mimic exposure in the environment: 5 mL of 2mM nano – suspensions were put inside a plastic test tube, to which we added 0.5 mL of GSH or Cys 1.1 mM (final concentration 0.1 mM), or, for the •OH generation test, RNO 40 µM, RNO 40 µM + H_2O_2 30% 5 µl; the vials were covered and maintained in the dark. At different times, 1, 4, 24, 48 h, the samples were filtered (PES – 0.22µm) to eliminate photocatalysts, before measuring absorbance with a beam spectrophotometer Hach Lange, DR3900. For each combination of time, photocatalysts and probe - molecule, 3 sample were analysed and the results reported as average of these three - independent measurement of absorbance.

   2) UV light irradiation: 5 mL of nano – suspension 2mM were put inside a plastic test tube, to which we added 0.5 mL of GSH or Cys 1.1 mM (final concentration 0.1 mM) or RNO 40 µM, RNO 40 µM + H_2O_2 30% 5 µl; the vials were put under UV lamp (OSRAM ultra - vitalux 300 W lamp - emission spectra are reported in Chapter 2), irradiance of UV-A: 60 W / m^2. At different times, 15, 30, 60, 90 and 120 minutes, the sample was filtered (PES – 0.22µm) in order to eliminate photocatalysts, and

absorbance measured with a single beam spectrophotometer Hach Lange, DR3900.

4.2.3. Building a theoretical model for the prediction of the Oxidative potential of the nano-photocatalysts

The purpose of predictive models is to provide preliminary information on the behaviour of nanomaterials easily and quickly without having to conduct tests that require a lot of time, a lot of experience and sometimes the use of cells. For my thesis work, I used experimental data obtained for the depletion of antioxidants and for the generation of •OH to train a machine learning algorithm that could provide estimation of oxidative potential for untested nanoparticles. The final model allows us to identify which physico - chemical characteristics of the material and / or the experimental conditions most influence the oxidative power of the nanomaterials.

As a predictive tool, we used a supervised linear decision tree in Python (version 3.8.0) and a classification algorithm[26]. In summary, the linear tree algorithm divides the data sets into groups and subgroups (rectangles in Fig. 4.17), each characterized by a minimum of variance; the process ends when further splitting does not lead to lower variances (green oval in Fig. 4.17). The algorithm divides the data set into "nodes" which correspond to the decision point (i.e. division) according to a rule, and leaves, which correspond to the final groups. The algorithm defines (i.e. learns) decision rules, nodes, and leaves from the dataset (i.e., training set) through a multiple linear regression approach. Once the groups, subgroups (i.e. leaves) and decision rules (in correspondence of Nodes) have been established, it will be possible to predict the oxidative power of an untested nanoparticle whose data does not belong to the training set.

Fig. 4.8 shows the concept underlying the model. In particular, the results of the chemical - physical characterizations of the materials, and the conditions and results of the tests with GSH / Cys / RNO. The model validates itself according to the data from which it has learned and returns the characteristics or conditions that weighed more on the amounts of probes molecules consumed.

To build the Tree model, we created a dataset comprising of 522 rows, where each row was a sequence of the exposure conditions, experimental characteristics and the physico

- chemical properties. No missing values are recorded to the final input features. Molecular weight as a feature was not considered since this information on g-C_3N_4 is not available due to the potential presence of impurities. Each row in the datasets represents one element of the experiment, meaning one replica of a specific assay targeting the capacity of the materials to consume the molecule of interest (RNO, GSH, Cys, and RNO + H_2O_2). Since some inputs are expressed into categorical variables (in words), a so called *"hot encoding"* was performed in order to transform them into numerical features, understandable by the model.

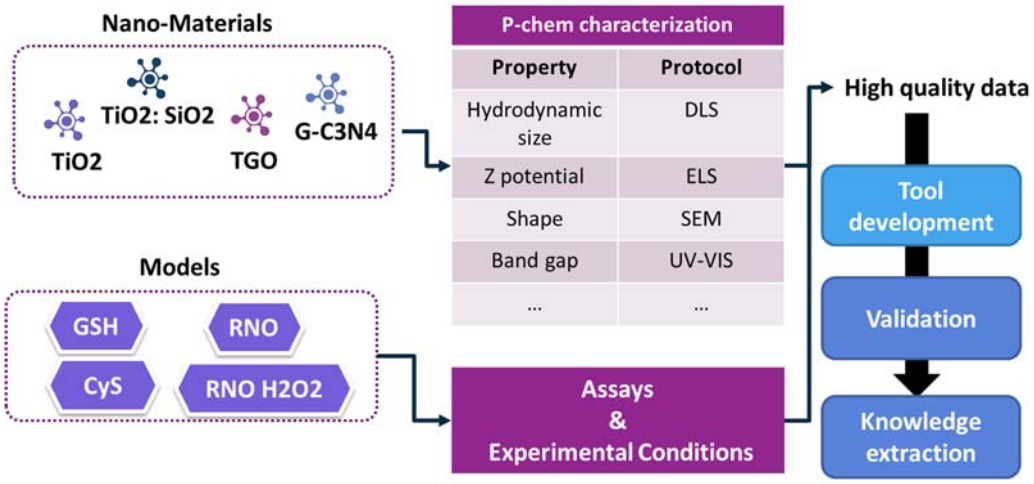

Figure 4.8. Roadmap towards model development and information extraction for SSbD purposes.

4.3. Results & Discussion

4.3.1. Analysis of potential Effects of Dispersing method on the depletion of GSH, Cys, and RNO

As a preliminary test, we checked the dispersing method could induce some artefact in the experimental data. The consumption of GHS, Cys, and RNO after 0, 1h, 3h were measured after ultra sound sonication, ultrasound bath, and manual mixing. Results are plotted in Fig. 4.9.

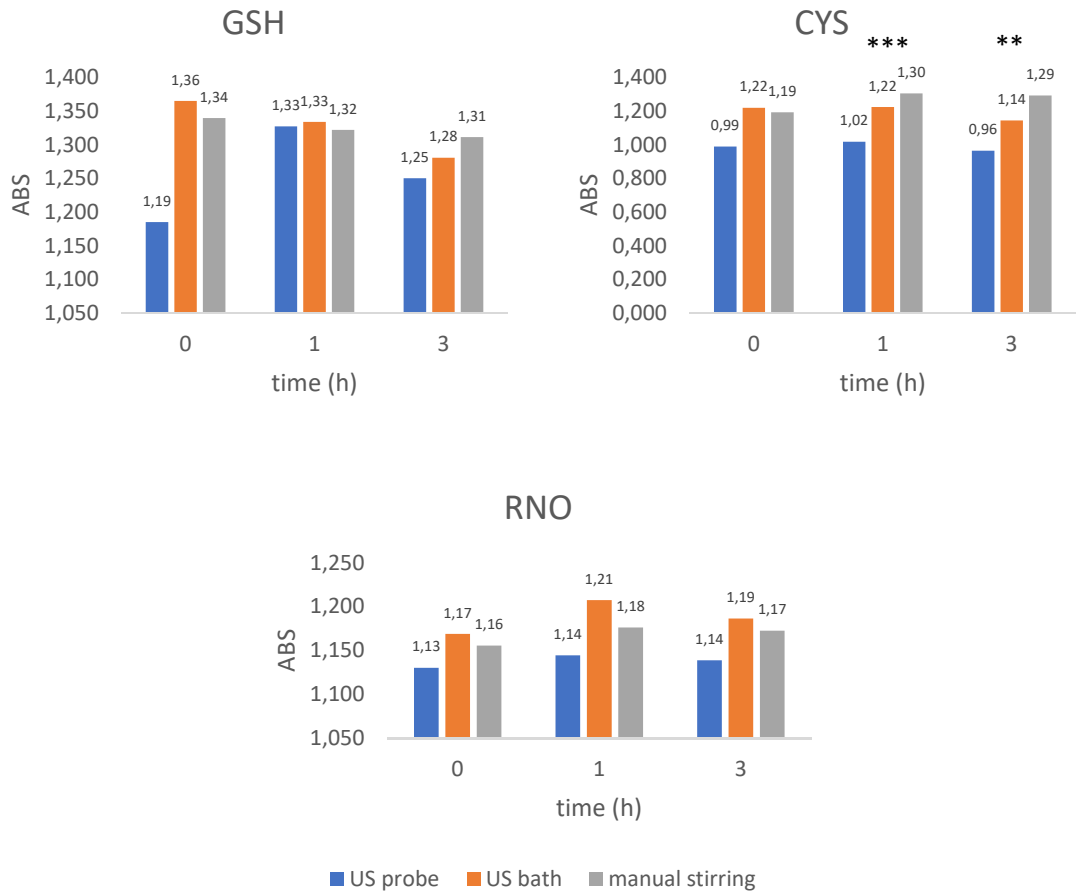

*Figure 4.9. Bar graph of GSH / Cys / RNO subjected at different dispersing method: US probe, US bath and manual stirring. The results are the average of three independent measure at 0, 1 and 3 hours. Ultra Sonic Probe = US probe, Ultra Sonic Bath = US bath. P - value obtained by one - way ANOVA test, ** p-value < 0.01 *** p-value < 0.001.*

As it can be seen, the samples subjected to US probes showed a lower absorbance than the other dispersion methods. This outcome should be expected when considering that a US probe is able to generate strong energies that can destroy the molecules[27,28]; they can also generate ROS[29] capable of degrading the molecules. From the statistical analysis (one - way ANOVA), only the data at 1h and 3h were significant for the Cys, which reveal that the US probe compromises the molecule. For these reasons and for practical work reasons, manual stirring was chosen as the dispersion method.

4.3.2. Detection of •OH radical

Dark condition:

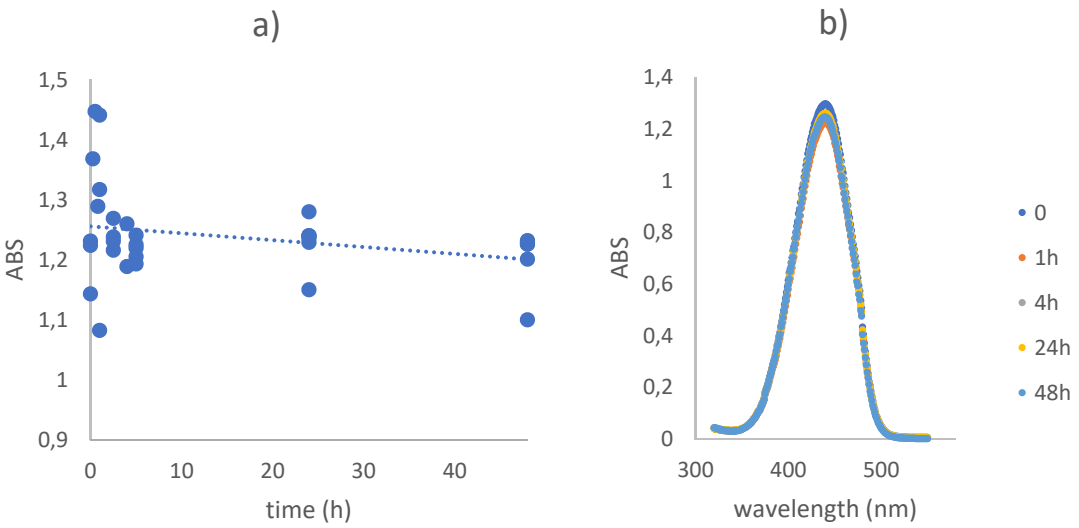

Figure 4.10. (a) Absorbance vs. time (h) of the spontaneous consumption of RNO in air (b) RNO absorbance spectra at different time.

A preliminary check of the stability of RNO in the experimental condition used to test the photocatalyst revealed a high stability of the probe - molecule[30]. The results showed that only 4.2% (calculated from tendency line in Fig. 4.10a) of RNO was spontaneously consumed in 48h, confirmed by Fig. 4.10b. The molecule was stable[31] and the values from this study were used as controls for subsequent calculations. Results of this test were used as base - line for the analysis of the photocatalysts.

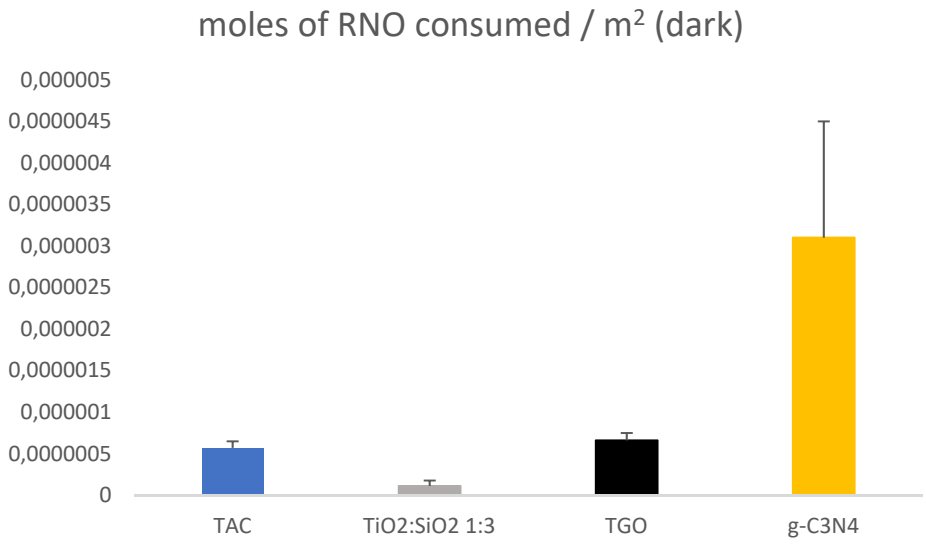

Figure 4.11. Moles of RNO consumed by nano-photocatalysts particles in DARK condition after 48h. The results are the average of three indipendet measurement.

Fig. 4.11 shows the RNO moles consumed per m^2 of nano-photocatalysts, in dark condition.

To explain the unexpected high consumption of RNO by g-C_3N_4, we hypothesised that a significant portion of RNO was removed through adsorption in dark condition. In principle, nanoparticles could remove a detectable portion of RNO from the solution through surface adsorption due to their high specific surface, high porosity and active surface[32], especially carbon - based nanoparticles[33]. This reduction was obviously not determined by the production of •OH. The low, yet detectable, consumption of RNO at the TGO sample, which although it has a carbonaceous part does not show the same behaviour as GO, may be due to adsorption at the TiO_2 nanoparticles that surround it (as can be seen from Fig. 2.8 in the chapter "Development of nano-photocatalysts used in AOPs for removing (bio-) organic pollutants"). TAC and TiO_2:SiO_2 1:3 samples have a lower absorption capacity than carbon - based materials, and, in particular the TiO_2:SiO_2 1:3 sample after heterocoagulation may have less free adsorbing surface available.

Effects of Irradiation with UV:

In photocatalysis, the degradation of pollutants can take place through the formation of ROS deriving from the oxidation of water, or by direct oxidation[34], which occurs when the pollutant molecule is adsorbed on the surface of the catalyst and is degraded by the free charges on the surface of the nanoparticle of the photocatalyst. Direct oxidation is the most likely route in cases where the active species is TiO_2. In fact, as it can be seen from the graphs in Fig. 4.12 the TAC, TiO_2:SiO_2 1:3 and TGO samples show the highest photocatalytic efficiency but the lowest tendency to produce •OH radicals. These results can be explained by the ability of anatase form of TiO_2 to generate holes (positive charges) on the surface that have enough energy to oxidize organic pollutants[35]. Production of radical less energetic than •OH, however, cannot be excluded altogether, because RNO is not able to detect them.

The band - gaps of nanostructures are crucial for their photocatalytic applications. The g-C_3N_4 has a band gap of ~ 2.7 eV, corresponding to an optical wavelength of 460 nm, which makes it active under visible light.

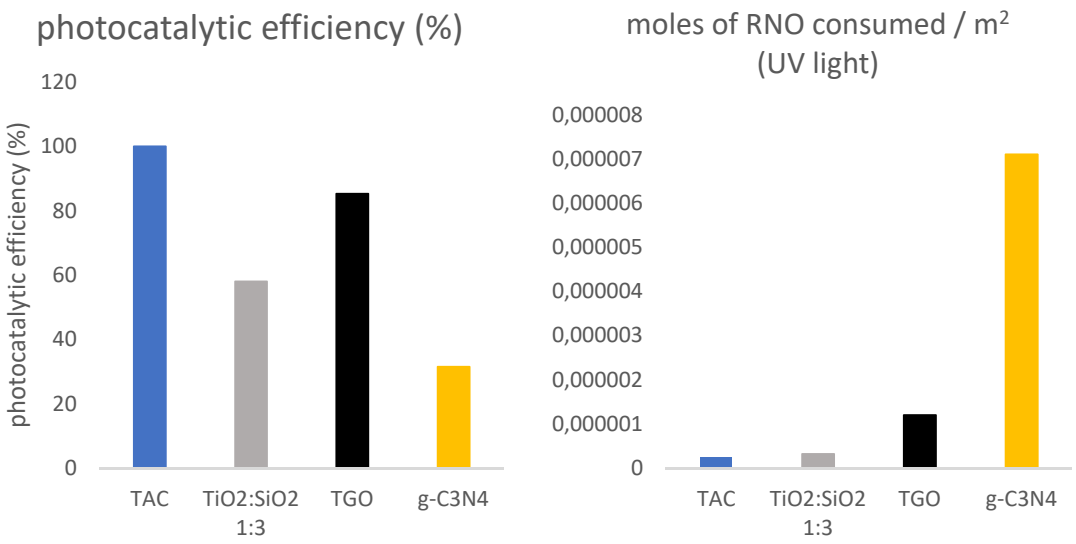

Figure 4.12. Comparison between photocatalytic efficiency (%) and production of •OH radicals by RNO method. Time experiment 2h under UV light.

But more importantly than the band gap extension, the position of the conduction band of g-C_3N_4 matches the energies of several compounds that can then be reduced upon irradiation (Fig. 4.13). The conduction band of g-C_3N_4 (- 1.3 eV), for example, is more negative than the TiO_2 - based semiconductors (- 0.5 eV).

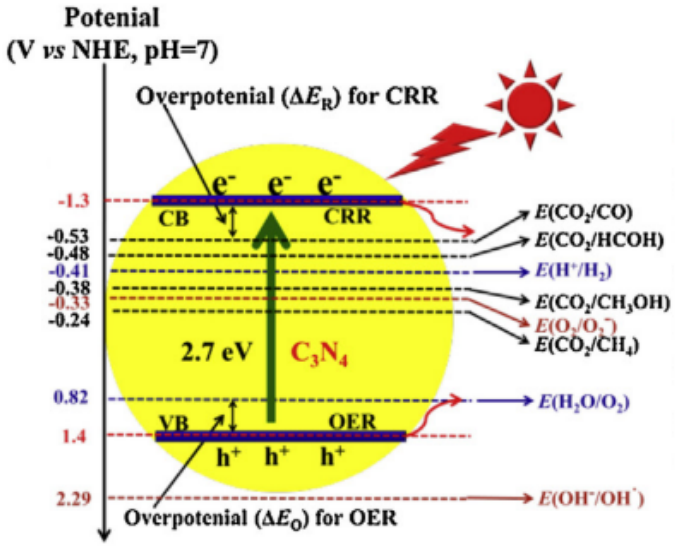

Figure 4.13. The redox potentials of the relevant reactions with respect to the estimated position of the g-C_3N_4 band edges[36].

Furthermore, the CB of g-C_3N_4 is more negative than the redox potential of the H_2 / H^+ pair and the O_2 / O_2^- pair. This means that the e^- photogenerated by irradiation of g-C_3N_4 have a great thermodynamic driving force to reduce O_2 (to $\bullet O_2^-$ and after to •OH) and consequently to from electron - holes (h^+) that can oxidize H_2O and generate •OH radicals[36]. At neutral pH, due to the different redox potentials, the reduction of O_2 is favoured and the hole / e^- recombination is so fast that the RhB is not attacked by radicals and therefore there is no degradation[37]. This is why g-C_3N_4 also exhibits very low photocatalytic efficiency under UV light but despite high tendency to •OH production.

4.3.3. Acellular Assessment of Oxidation Power

Dark condition:

As performed with RNO, a spontaneous oxidation study was conducted with the aim of evaluating the stability of the GSH / Cys molecule in aqueous solution in contact with air. Probe molecules are subjected to oxidation when in contact with atmospheric O_2 [30]. In fact, we observed that respectively 40% and 34% of moles of GSH and Cys were spontaneously consumed in 48h (data calculated by tendency line in Fig. 4.14a). The molecules are indeed partially consumed (i.e., oxidized) (considerable lowering of the peak at 410 nm in Fig. 4.14b) and the values from this study were used as base - line for subsequent calculations so as to eliminate spontaneous consumption.

a)

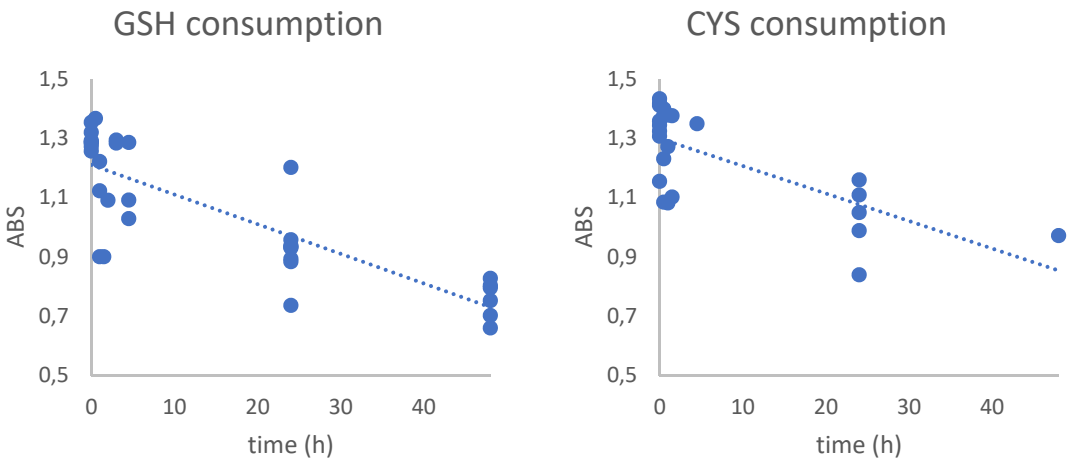

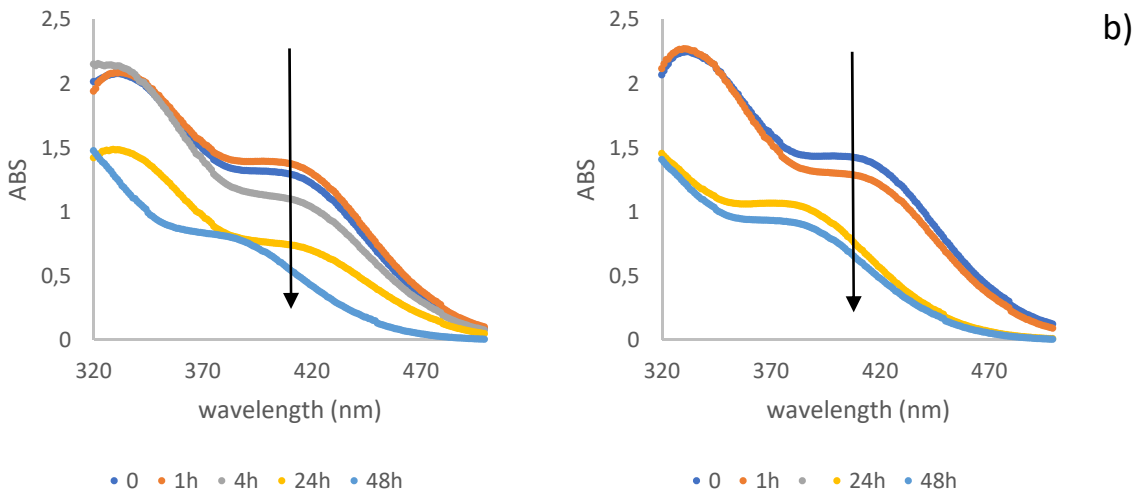

Figure 4.14. (a) GSH / Cys absorbance vs. time of exposure. (b) GSH / Cys absorbance spectra vs. wavelength for time of exposure.

Fig. 4.15 shows the GSH and Cys moles consumed by nano – photocatalysts in dark condition. It is possible to note that in the case of GSH only TGO and TiO_2:SiO_2 1:3 materials consume substantial amounts of GSH, while for the Cys, only TAC and TGO exhibit a measurable activity.

The TGO - based composite has a part of GO which was synthesized by the modified Hummer method[38]. This method uses strong acids, hydrochloric and sulfuric, and potassium permanganate. Despite the final washes portions of manganese heptoxide – Mn_2O_7 remain and it was known that this was an unstable and unsafe molecule[39].

The TAC sample resulted more capable of consuming Cys, due to smaller molecule than GSH, so more of it could be adsorbed on the surface of TiO_2 nanoparticles. When SiO_2 comes into play in the TiO_2:SiO_2 1:3 composite, the trend is reversed; in fact, we see a greater consumption of GSH compared to Cys, contrary to what can be seen in the literature, where the inclusion of Silica increases the photo - efficiency but decreases the toxicity and the production of ROS[40]. A possible explanation is based on the mechanism by which SiO_2 oxidizes GSH, which involves a catalytic mechanism (with ROS as intermediaries), while for Cys a phenomenon of direct surface oxidation would occur[35]. Therefore, with the introduction of SiO_2 in the composite, there is more formation of •OH radicals (as can be seen from the Fig. 4.12), and since GSH is more efficient than Cys in neutralizing radicals, we observe a higher consumption of GSH[41].

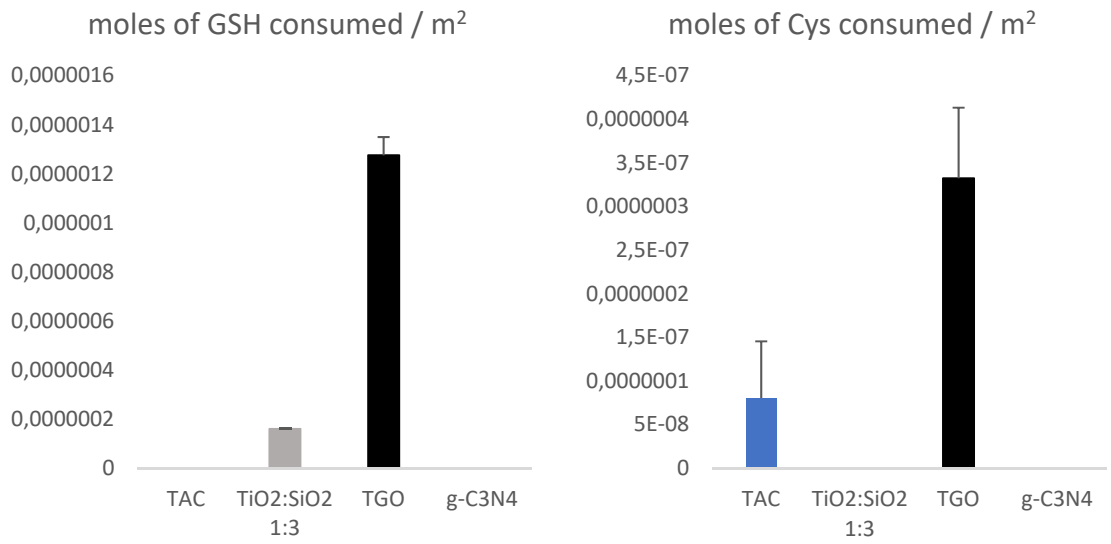

Figure 4.15. Moles of GSH / Cys consumed by nano-photocatalysts particles in DARK condition. Time experiment 48h. The results are the average of three independent measurement.

UV light irradiation:

Fig. 4.16 shows the ability of the photocatalyst to consume either GSH, or Cys when irradiated with UV light. We observe that g-C_3N_4 is the most active compound, almost one order of magnitude more active than the others.

g-C_3N_4 tends to produce a large quantity of •OH radicals, with the consequence of considerable consumption of anti - oxidant GSH and Cys. TAC and TiO_2:SiO_2 1:3 show no ability to oxidize GSH, but show little ability to consume Cys. the two molecules, in fact, have different redox potentials (GSH: -260 mV / Cys: -160 mV)[42]. The TGO shows the same degree of oxidation of the two molecules as in dark conditions.

Oxidative power of nanoparticles - predictive model:

The experimental results described in the previous sections provided data to compile a global dataset made of 522 rows. This dataset included information on physico - chemical properties of nano-photocatalysts, exposure and experimental conditions and outcomes of the consumption of probe molecules for the oxidative power. These data were utilized to build a “linear tree”, a machine learning algorithm that could predict the concentration of the “RNO, GSH, Cys, and RNO + H_2O_2” not consumed (mole) from physico - chemical background information.

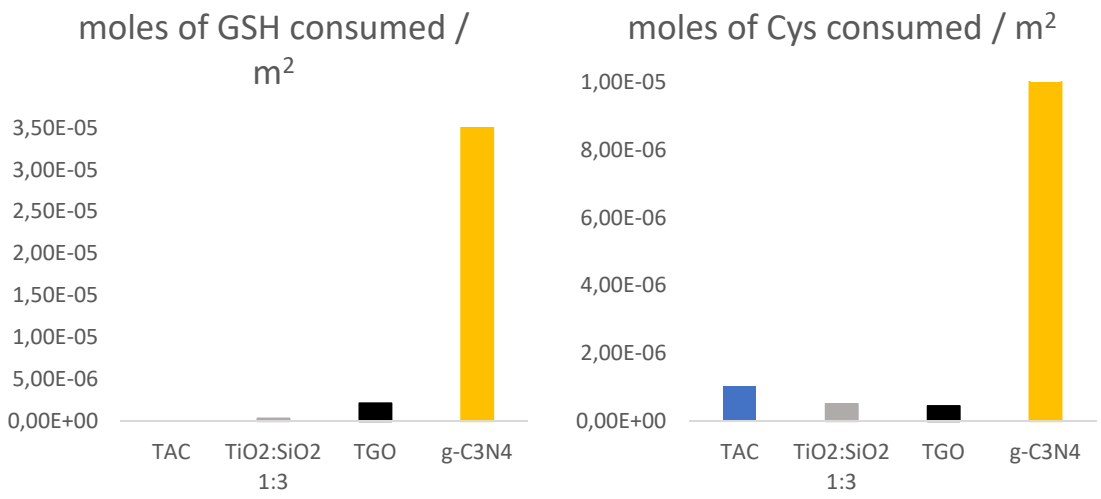

Figure 4.16. Moles of GSH / Cys consumed by nano-photocatalysts particles in UV light condition. Time experiment 2h.

The input variables of the tree are listed in Table 4.1. The features that are outcome related were not included in the training dataset due to high collinearity (Pearson correlation results not shown).

Table 4.1. Dataset input features, their type, min max values or labels (one hot encoded) and a description.

Input category	Input feature	Type	Min-Max or labels & Metric	Meta-data description
Physico - chemical properties	Material	Categorical	TAC, TGO, TiO_2:SiO_2, g-C_3N_4	
	Surface Area	Numeric	11.07- 388.42 (m^2 / g)	
	Hydrodynamic Size	Numeric	27 - > 6000 (nm)	
	Z - potential	Numeric	-22 – 38 (mV)	
	pH Suspension	Numeric	1.5 – 5.5	
	pH isoelectric point	Numeric	2.2 – 7.7	
	Shape / morphology	Categorical	Spherical, Cuboid	
	Band Gap	Numeric	2.7 – 3.2 (eV)	
Exposure conditions	Conditions	Categorical	Dark, Light (UV)	
	Sample surface area	Numeric	0.01 – 0.39 (m^2)	*This feature is calculated from BET and the mg in order to see how much m^2 is in the sample*
	Incubation time	Numeric	0-25 – 48 (h)	
	Intermediate Volume	Numeric	5.2 – 5.5 (mL)	*Indicates the volume of the "model" such as GSH and Cys*

	Model intermediate volume	Numeric	0.04 – 0.1 (mM)	*Volume of GSH and Cys*
	Model Initial volume	Numeric	2.08E-07 – 5.5E-07 (mM)	
	Final volume	Numeric	5.2 – 6 (mL)	*Final volume of the solution*
	Ellman reagent concentration	Numeric	0 – 0.15 (mM)	
Experimental characteristics	Model	Categorical	Cys, GSH, RNO, RNO+H_2O_2	
	Control ABS	Numeric	0 – 1.88	*Control absorbance*
	Peak ABS	Numeric	412 – 440 (nm)	*Peak evaluation*
	Control concentration	Numeric	0 – 2.61E-04 (mole)	
	Spontaneous consumption	Numeric	-37E-05 – 8.12E-05 (mole)	
Outcome related variables	Model consumed per mg of nano	Numeric	-5.5E-05 – 2.4E-04 (mole)	
	Model consumed per mole of nano	Numeric	-5.5– 24 (mole)	
	Model consumed per m2 of nano	Numeric	-5E-03 – 8.6E-03 (mole)	
	Absorbance of model consumed	Numeric	0 – 1.68 (mole)	
Outcome	Model not consumed final	Numeric	0 – 2.95E-04 (mole)	

We used the RidgeClassifier from sklearn as linear estimator to build the tree structure shown in Fig. 4.17.

Each leaf in Fig. 4.17 represents the result of a pruning process which was applied in each explored path of the structure. When there is no significant information gain from partitioning the data, the training process ends (ellipses in in Fig. 4.17). Each leaf contains a fitted linear model that predicts all the samples that meet the given set of criteria (*decision rules – light blue in Fig. 4.17*). The combination of all of the rules make up the tree structure. For each node, it was possible to extract the set of the decision rules (i.e., conditions) that lead to each leave. Importantly, Fig. 4.18 - 4.19 - 4.20 indicate the importance of each the variable in establishing the decision rule at each node.

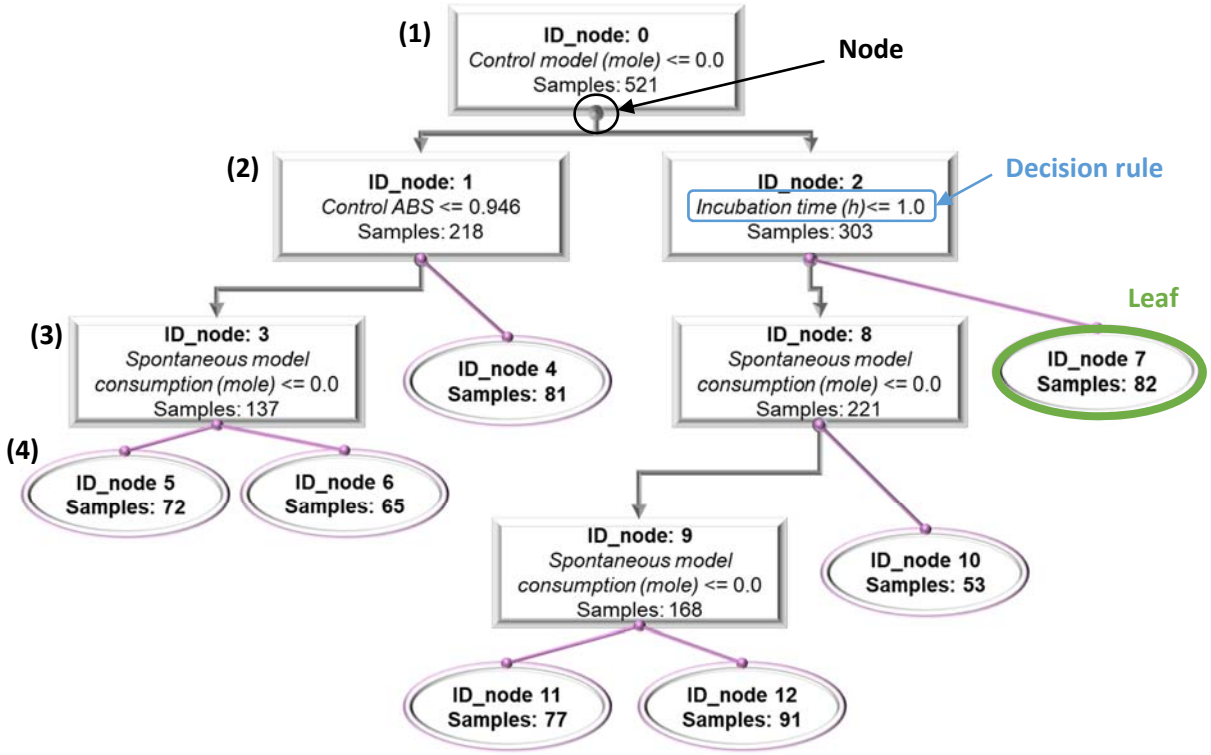

Figure 4.17. The tree structure. The round shapes represent the leaves. Where samples, the designed cases of experiment.

For example, to get to leaf ID_node 5 (Fig. 4.18, top), the model divided the 521 samples according to the decision rule 'Control model (mole) <= 0.0' (1), if the rule is respected the sample is inserted in the group ID_node: 1 (2). The model now looks for correlations between the set of 218 samples and divides them according to the rule 'Control ABS <= 0.946', also in this case if the sample respects the rule, then it is inserted in the group ID_node: 3 (3). The model looks for correlations among the 137 samples and generates the rule 'spontaneous model consumption (mole) <= 0.0'. If the sample complies with the rule it is inserted in the leaf ID_node 5. In this case the model generates a leaf because it does not find condition (or decision rules) to split the 72 samples further. For ID_node 5, was evident that the characteristics (input of model) that have most influenced these decision rules were the characteristics highlighted in Fig. 4.18, that is the GSH model, the Cys model and the absorbance of the controls.

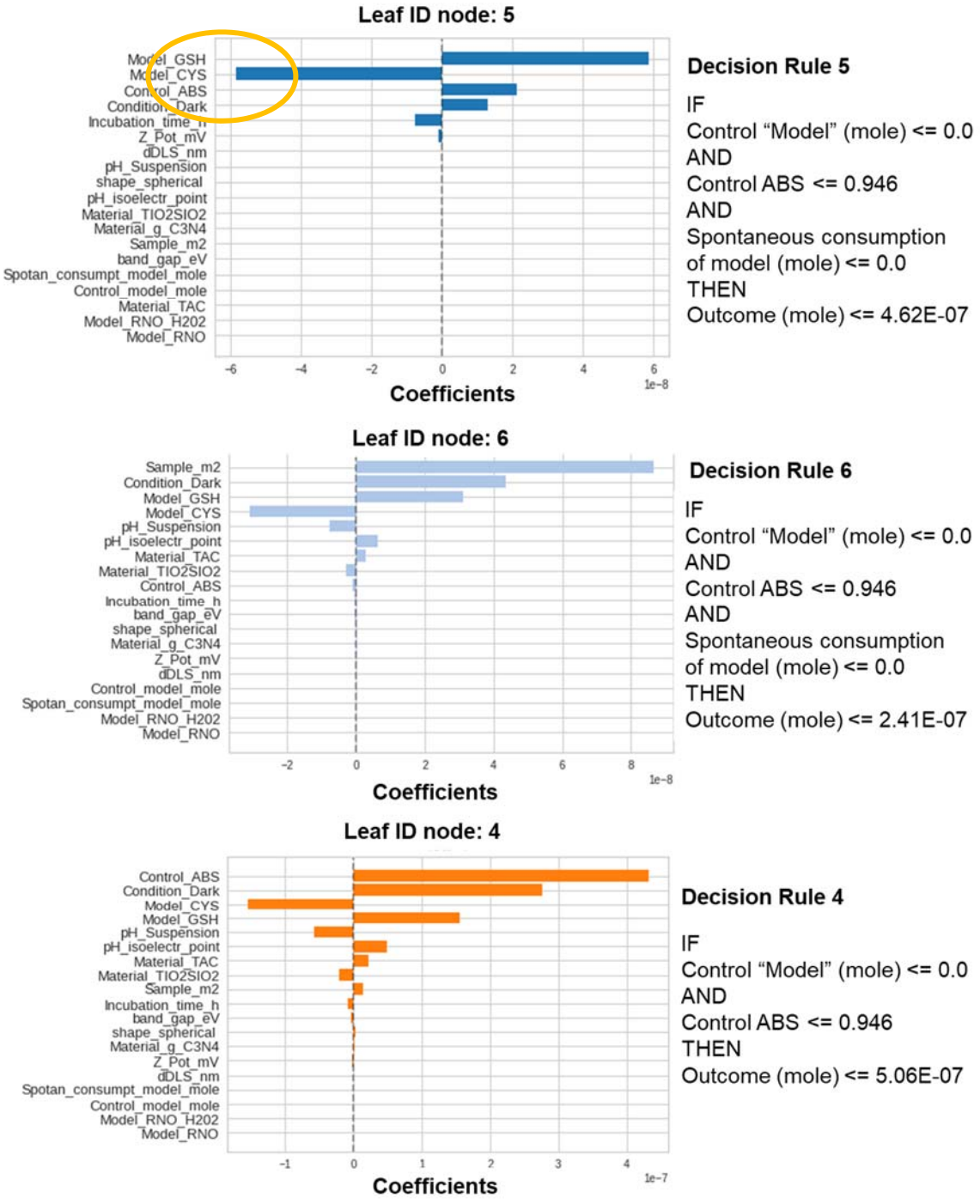

Figure 4.18. Coefficients on the left. Decision rule of leaves 5, 6 and 4 on the right.

So, in leaves node 5, 6 and 4, the type of model (GSH and Cys) tested has significant impact in determining the outcome (moles of models not consumed (Outcome (mole)) <= 5.06E-07). The *absorbance of the control* appears in the top of the decision rule in leaf 4 and *sample surface (m^2)* appears to be the most influential in this decision rule 6. The *dark* conditions together with the *incubation time* are important features in leaf 5. pH (of the

suspension and the pH of the isoelectric point) with the nanomaterials' type have an effect in predicting the outcome in leaf 6 and 4. From the physico - chemical properties, zeta potential appeared to have a slight impact. Removing the features that relate to the experiment, zeta potential and size are the top two features that can determine the outcome.

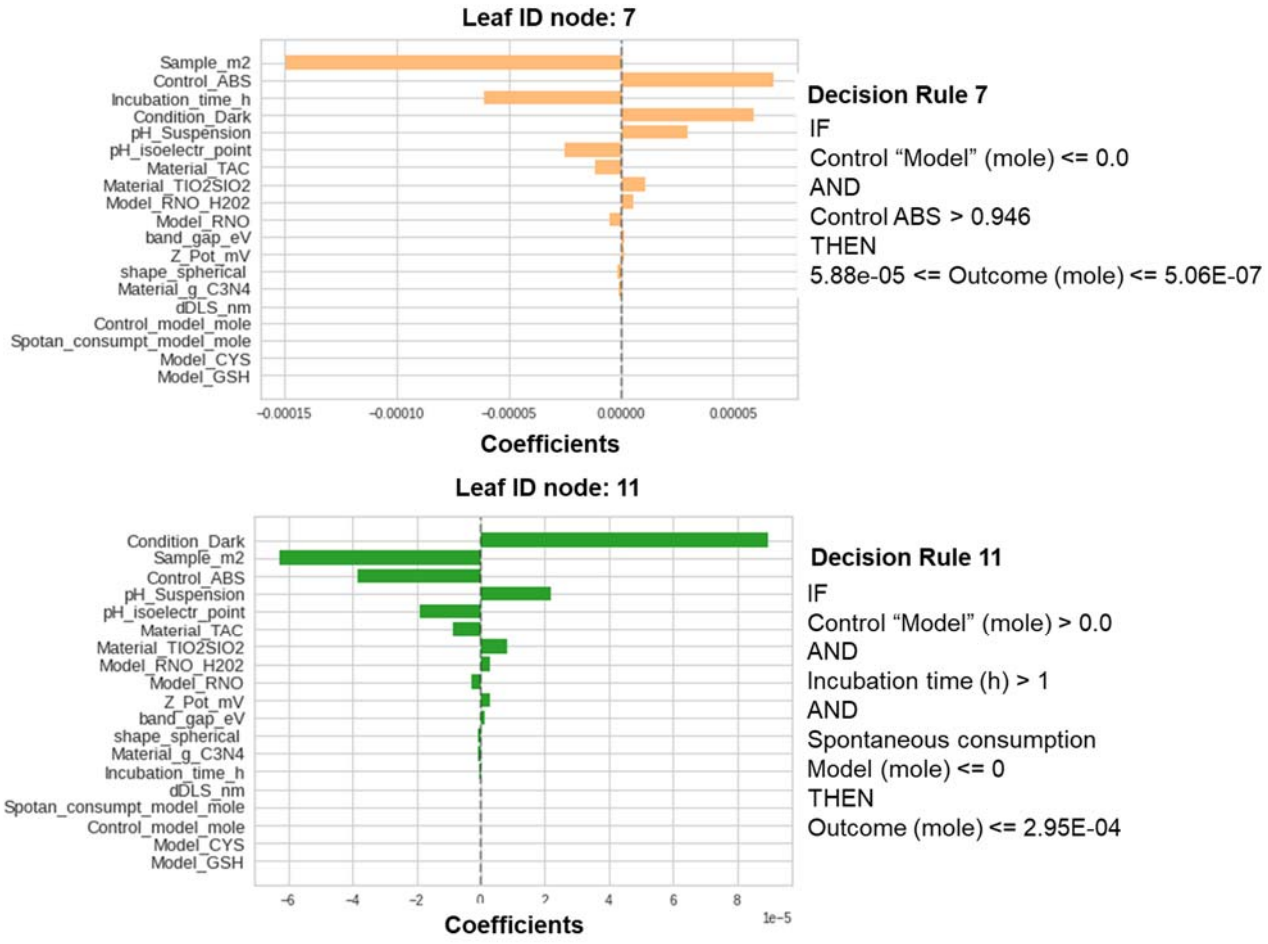

Figure 4.19. Coefficients on the left. Decision rule of leaf 7 and 11 on the right.

In leaf nodes 7 and 11, contrary to the previous nodes, the model (GSH / Cys / RNO) does not have significant impact towards the outcome. *Dark* conditions, Ph (of the suspension and the pH of the isoelectric point) with the nanomaterials' type have significant impact in determining the decision rule for the outcome (moles of models not consumed) value between 5.88e-05 <= model's (mole) <= 5.06E-07. The incubation time appears to have strong influence in leaf 7 and zeta potential in leaf 11. From physico - chemichal properties, zeta potential and band gap appear as important.

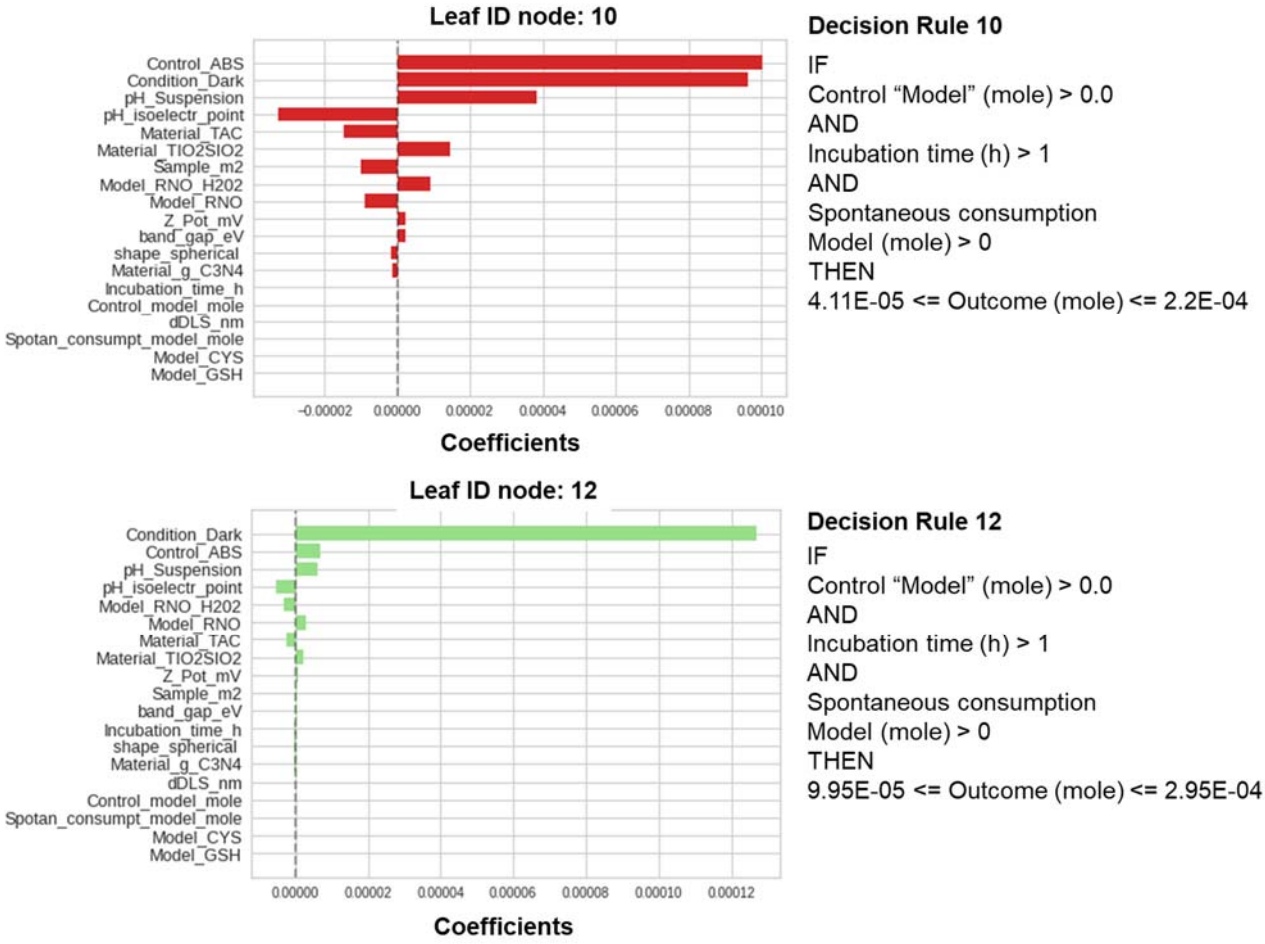

Figure 4.20. Coefficients on the left. Decision rule of leaves 10 & 12 on the right.

In leaf nodes 12 - 10, model type (RNO / RNO + H_2O_2) *dark* conditions, pH (of the suspension and the pH of the isoelectric point) with the nanomaterials' type have significant impact in determining the decision rule for the outcome (moles of models not consumed) value between 4.11E-05 <= model's (mole) <= 2.95E-04.

At the end of the process we can indicate which parameters are most influential on the moles of probe consumed / m^2 of nano-photocatalysts. The zeta potential, pH parameters and light conditions appeared to be the most influential.

The model was finally validated via internal validation showing the following performance metrics: R^2: 0.9604, mean squared error (MSE): 4.055E-10, mean absolute error (MAE): 1.026E-05 and Mean absolute percentage error (MAPE): 0.2662.

4.4. Conclusion

During this study two paths were followed:

1- the evaluation of the tendency to form •OH radicals which allows to take the steps to understand the reaction mechanisms of the developed photocatalysts and to understand how to maximize the production of •OH.
2- The evaluation of the ability of photocatalysts to induce oxidative stress, evaluating the consumption of the biological molecules most involved in the defence of cells from antioxidants.

The methods developed a rapid scan of the materials and requires special materials or tools or experience.

From the results we can conclude that the TiO_2 materials are effective, they are capable of photodegrading the pollutants with ways other than the production of radicals. While the organic alternative g-C_3N_4, although it produces many •OH, and is also harmful, does not show a great photocatalytic activity.

Regarding the predictive model of oxidative stress induced by nano-photocatalysts, we can say that further investigations are necessary:

- A classification of the oxidative potential based on regulations and numeric results from experiments would be essential to classify nanomaterials easy into safe, no safe, intermediate.
- High quality data are needed in the field of nanotechnology to advance their safety while maximizing their functionality, in our case photocatalytic efficiency.

In any case, the analysis of the whole data set provided important information about the parameters that tune the photocatalytic process relevant to both the degradation of organic pollutants and to the assessment of their risks for human health and for the environment.

Reference

1. Furxhi, I.; Perucca, M.; Blosi, M.; Lopez de Ipiña, J.; Oliveira, J.; Murphy, F.; Costa, A.L. ASINA Project: Towards a Methodological Data-Driven Sustainable and Safe-by-Design Approach for the Development of Nanomaterials. *Front. Bioeng. Biotechnol.* **2022**, *9*, 1–8, doi:10.3389/fbioe.2021.805096.
2. Furxhi, I.; Murphy, F.; Mullins, M.; Arvanitis, A.; Poland, C.A. Practices and trends of machine learning application in nanotoxicology. *Nanomaterials* **2020**, *10*, 1–32, doi:10.3390/nano10010116.
3. Furxhi, I. Health and environmental safety of nanomaterials: O Data, Where Art Thou? *NanoImpact* **2022**, *25*, 100378, doi:10.1016/j.impact.2021.100378.
4. Furxhi, I.; Murphy, F.; Mullins, M.; Arvanitis, A.; Poland, C.A. Nanotoxicology data for in silico tools: a literature review. *Nanotoxicology* **2020**, *14*, 612–637, doi:10.1080/17435390.2020.1729439.
5. Ma, H.Y.; Zhao, L.; Guo, L.H.; Zhang, H.; Chen, F.J.; Yu, W.C. Roles of reactive oxygen species (ROS) in the photocatalytic degradation of pentachlorophenol and its main toxic intermediates by TiO2/UV. *J. Hazard. Mater.* **2019**, *369*, 719–726, doi:10.1016/j.jhazmat.2019.02.080.
6. Nosaka, Y.; Nosaka, A.Y. Generation and Detection of Reactive Oxygen Species in Photocatalysis. *Chem. Rev.* **2017**, *117*, 11302–11336, doi:10.1021/acs.chemrev.7b00161.
7. Niu, X.; Yan, W.; Zhao, H.; Yang, J. Synthesis of Nb doped TiO 2 nanotube/reduced graphene oxide heterostructure photocatalyst with high visible light photocatalytic activity. *Appl. Surf. Sci.* **2018**, *440*, 804–813, doi:10.1016/j.apsusc.2018.01.069.
8. Simonsen, M.E.; Muff, J.; Bennedsen, L.R.; Kowalski, K.P.; Søgaard, E.G. Photocatalytic bleaching of p-nitrosodimethylaniline and a comparison to the performance of other AOP technologies. *J. Photochem. Photobiol. A Chem.* **2010**, *216*, 244–249, doi:10.1016/j.jphotochem.2010.07.008.
9. Daussmann, T.; Aivasidis, A.; Wandrey, C. Purification and characterization of an alcohol : N , iV-dimethyl-4-nitrosoaniline oxidoreductase from the methanogen Methanosarcina barkeri DSM 804 strain Fusaro. **1997**, *896*, 889–896.
10. Santos, E.L.; Silva, D.R.; Mart, C.A.; Vieira, E.; Quiroz, M.A. RSC Advances Cathodic hydrogen production by simultaneous dichlorophenoxyacetate aqueous solutions using. **2020**, 37695–37706, doi:10.1039/d0ra03955a.
11. Fernández-Castro, P.; Vallejo, M.; San Román, M.F.; Ortiz, I. Insight on the fundamentals of advanced oxidation processes: Role and review of the determination methods of reactive oxygen species. *J. Chem. Technol. Biotechnol.* **2015**, *90*, 796–820, doi:10.1002/jctb.4634.
12. Burns, J.M.; Cooper, W.J.; Ferry, J.L.; King, D.W.; DiMento, B.P.; McNeill, K.; Miller, C.J.; Miller, W.L.; Peake, B.M.; Rusak, S.A.; et al. Methods for reactive oxygen species (ROS) detection in aqueous environments. *Aquat. Sci.* **2012**, *74*, 683–734, doi:10.1007/s00027-012-0251-x.
13. Zhao, H.; Chen, X.; Li, X.; Shen, C.; Qu, B.; Gao, J.; Chen, J.; Quan, X. Photoinduced formation of reactive oxygen species and electrons from metal oxide-silica nanocomposite: An EPR spin-trapping study. *Appl. Surf. Sci.* **2017**, *416*, 281–287, doi:10.1016/j.apsusc.2017.04.088.
14. Luo, Y.; Peng, R.; Cui, Q.; Niu, P.; Li, L. Internal Chemiluminescence Light-Driven Photocatalysis. *ACS Appl. Mater. Interfaces* **2021**, *13*, 60471–60477,

doi:10.1021/acsami.1c19833.
15. Ishibashi, K.I.; Fujishima, A.; Watanabe, T.; Hashimoto, K. Detection of active oxidative species in TiO2 photocatalysis using the fluorescence technique. *Electrochem. commun.* **2000**, *2*, 207–210, doi:10.1016/S1388-2481(00)00006-0.
16. Gomes, A.; Fernandes, E.; Lima, J.L.F.C. Fluorescence probes used for detection of reactive oxygen species. *J. Biochem. Biophys. Methods* **2005**, *65*, 45–80, doi:10.1016/j.jbbm.2005.10.003.
17. Tee, J.K.; Ong, C.N.; Bay, B.H.; Ho, H.K.; Leong, D.T. Oxidative stress by inorganic nanoparticles. *Wiley Interdiscip. Rev. Nanomedicine Nanobiotechnology* **2016**, *8*, 414–438, doi:10.1002/wnan.1374.
18. Picardo, M.; Dell'Anna, M.L. Oxidative stress. *Vitiligo* **2010**, 231–237, doi:10.1007/978-3-540-69361-1_27.
19. Liebert, M.A.; Jones, D.P. Clinical Measures of the Balance. **2006**, *8*.
20. Pruchniak, M.P.; Araźna, M.; Demkc, U. Biochemistry of oxidative stress. *Adv. Exp. Med. Biol.* **2016**, *878*, 9–19, doi:10.1007/5584_2015_161.
21. Meng, H.; Xia, T.; George, S.; Nel, A.E.; Pisoschi, A.M.; Pop, A.; Picardo, M.; Dell'Anna, M.L.; Liebert, M.A.; Jones, D.P.; et al. Oxidative stress. *J. Altern. Complement. Med.* **2011**, *8*, 55–74, doi:10.1007/5584_2015_161.
22. Ni, M.; Leung, M.K.H.; Leung, D.Y.C.; Sumathy, K. A review and recent developments in photocatalytic water-splitting using TiO2 for hydrogen production. *Renew. Sustain. Energy Rev.* **2007**, *11*, 401–425, doi:10.1016/j.rser.2005.01.009.
23. Meng, H.; Xia, T.; George, S.; Nel, A.E. A predictive toxicological paradigm for the safety assessment of nanomaterials. *ACS Nano* **2009**, *3*, 1620–1627, doi:10.1021/nn9005973.
24. Banerjee, R. Redox outside the box: Linking extracellular redox remodeling with intracellular redox metabolism. *J. Biol. Chem.* **2012**, *287*, 4397–4402, doi:10.1074/jbc.R111.287995.
25. Finaud, J.; Biologie, L. art%3A10.2165%2F00007256-200636040-00004.pdf. **2006**, *36*, 327–358.
26. Nie, F.; Zhu, W.; Li, X. Decision Tree SVM: An extension of linear SVM for non-linear classification. *Neurocomputing* **2020**, *401*, 153–159, doi:10.1016/j.neucom.2019.10.051.
27. Taurozzi, J.S.; Hackley, V.A.; Wiesner, M.R. Ultrasonic dispersion of nanoparticles for environmental, health and safety assessment issues and recommendations. *Nanotoxicology* **2011**, *5*, 711–729, doi:10.3109/17435390.2010.528846.
28. Mikheev, I. V.; Pirogova, M.O.; Usoltseva, L.O.; Uzhel, A.S.; Bolotnik, T.A.; Kareev, I.E.; Bubnov, V.P.; Lukonina, N.S.; Volkov, D.S.; Goryunkov, A.A.; et al. Green and rapid preparation of long-term stable aqueous dispersions of fullerenes and endohedral fullerenes: The pros and cons of an ultrasonic probe. *Ultrason. Sonochem.* **2021**, *73*, 105533, doi:10.1016/j.ultsonch.2021.105533.
29. Giuntini, F.; Foglietta, F.; Marucco, A.M.; Troia, A.; Dezhkunov, N. V.; Pozzoli, A.; Durando, G.; Fenoglio, I.; Serpe, L.; Canaparo, R. Insight into ultrasound-mediated reactive oxygen species generation by various metal-porphyrin complexes. *Free Radic. Biol. Med.* **2018**, *121*, 190–201, doi:10.1016/j.freeradbiomed.2018.05.002.
30. Taube, H. Mechanisms of Oxidation with Oxygen.
31. Ling, Y.; Mills, C.; Weber, R.; Yang, L.; Zhang, Y. NMR , IR / Raman , and Structural Properties in HNO and RNO (R) Alkyl and Aryl) Metalloporphyrins with Implication

for the HNO - Myoglobin Complex. **2010**, 1583–1591.
32. Kumari, P.; Alam, M.; Siddiqi, W.A. Usage of nanoparticles as adsorbents for waste water treatment : An emerging trend. *Sustain. Mater. Technol.* **2019**, *22*, e00128, doi:10.1016/j.susmat.2019.e00128.
33. Santoso, E.; Ediati, R.; Kusumawati, Y.; Bahruji, H.; Sulistiono, D.O.; Prasetyoko, D. Review on recent advances of carbon based adsorbent for methylene blue removal from waste water. *Mater. Today Chem.* **2020**, *16*, 100233, doi:10.1016/j.mtchem.2019.100233.
34. Guo, Q.; Zhou, C.; Ma, Z.; Yang, X. Fundamentals of TiO 2 Photocatalysis : Concepts , Mechanisms , and Challenges. **2019**, *1901997*, 1–26, doi:10.1002/adma.201901997.
35. Schneider, J.; Matsuoka, M.; Takeuchi, M.; Zhang, J.; Horiuchi, Y.; Anpo, M.; Bahnemann, D.W. Understanding TiO 2 Photocatalysis : Mechanisms and Materials. **2014**.
36. Wen, J.; Xie, J.; Chen, X.; Li, X. A review on g-C 3 N 4 -based photocatalysts. *Appl. Surf. Sci.* **2017**, *391*, 72–123, doi:10.1016/j.apsusc.2016.07.030.
37. Fang, S.; Lv, K.; Li, Q.; Ye, H.; Du, D.; Li, M. Effect of acid on the photocatalytic degradation of rhodamine B over g-C 3 N 4. *Appl. Surf. Sci.* **2015**, *358*, 336–342, doi:10.1016/j.apsusc.2015.07.179.
38. Adly, M.S.; El-Dafrawy, S.M.; El-Hakam, S.A. Application of nanostructured graphene oxide/titanium dioxide composites for photocatalytic degradation of rhodamine B and acid green 25 dyes. *J. Mater. Res. Technol.* **2019**, *8*, 5610–5622, doi:10.1016/j.jmrt.2019.09.029.
39. Lakhe, P.; Kulhanek, D.L.; Zhao, X.; Papadaki, M.I.; Majumder, M.; Green, M.J. Graphene Oxide Synthesis : Reaction Calorimetry and Safety. **2020**, doi:10.1021/acs.iecr.0c00644.
40. Ortelli, S.; Poland, C.A.; Baldi, G.; Costa, A.L. Silica matrix encapsulation as a strategy to control ROS production while preserving photoreactivity in nano-TiO2. *Environ. Sci. Nano* **2016**, *3*, 602–610, doi:10.1039/c6en00009f.
41. Cysteine, R.O.F. REACTION OF CYSTEINE AND GLUTATHIONE (GSH) AT THE FRESHLY FRACTURED QUARTZ SURFACE : A POSSIBLE ROLE IN SILICA-RELATED. **2003**, *35*, 752–762, doi:10.1016/S0891-5849(03)00398-8.
42. Go, Y.; Jones, D.P. Free Radical Biology & Medicine Cysteine / cystine redox signaling in cardiovascular disease. *Free Radic. Biol. Med.* **2011**, *50*, 495–509, doi:10.1016/j.freeradbiomed.2010.11.029.

Chapter 5:

Identification and characterization of new class of pollutants: micro – nano plastics (MNPs) – SOLUTION 4

5.1. Introduction

5.1.1. Definition

Micro – nano plastics (MNPs) can be defined as piece of plastic with size < 100 nm (nano), from 1 μm to 1 mm (micro)[1] but some authors[2–4] indicates as maximum size 5 mm.

Real MNPs can be divided into two categories:

- primary[5]: are plastics that are manufactured in a microscopic or nanometric size for particular industrial or domestic (especially cosmetic field) applications.
- secondary[6]: are fragments derived from the breakdown or abrasion of larger plastic debris. Over time, plastic debris can be reduced by physical, biological and chemical processes. Exposure to sunlight can result in photo - degradation because ultraviolet (UV) radiation causes oxidation of the polymer matrix and subsequent fragmentation. Microplastics may also originate from abrasion, wave - action and turbulence.

5.1.2. Reasons of concern

Micro – nano plastics (MNPs) are more present in the world, are a new class of pollutants both in aquatic and terrestrial environment (ocean, lake and river, street, soil) and have a potential to affect fauna and biota[7]. The presence of MNPs change the life circle because it is mistaken by animals for food, causing inflammation and the death, in some cases. It also changes the physico - chemical characteristics of water and sediment or beaches[2,8].
For animals: In marine organisms, ingestion of microplastic may cause choking, internal or external wounds, ulcerating sores, blocked digestive tracts, false sense of satiation, impaired feeding capacity, starvation, debilitation, limited predator avoidance or death. Some experiment shown that fibres of plastic can form filament balls in the stomach[9]. MNPs can cause an inflammatory response in tissues and reduce membrane stability in cells of the digestive system are also translocated into the circulatory system[1,10,11].
For humans: MPs in freshwater may transfer effects to terrestrial system, as many freshwater organisms are prey to terrestrial insect, amphibians, reptiles and birds. So, MNPs can transfer from water to terrestrial environment, causing possible damage also for human. The impact of MNPs on human are not well documented. Also, in food area,

there isn't restriction and are unknown the consequences of MPs presence[10]. Abiotic sea products are a source of food for humans and there is a possibility that the presence of MNPs in the sea could lead to the contamination of sea products and potential transfer to humans, one of such products is sea salt[12]. Synthetic fibre are also found in beer, honey and sugar[13].

5.1.3. Source of primary MNPs

Principal sources of MNPs in environment are shown in Fig. 5.1. Primary MNPs can enter in aquatic environment directly or indirectly via domestic or industrial drainage system[14]. Coastal tourism, recreational and commercial fishing, marine vessels and marine - industries are all sources of plastic. For example, debris of fishing gear such as the plastic monofilament line and nylon netting can sink and tangle marine biota (phenomenon called 'ghost fishing')[15].

Figure 5.1. Sources of MPs in the aquatic environment.

- Domestic sources: in exfoliating hand cleansers and facial scrubs but also in tooth paste, deodorant and bubble bath lotions there are small pellets used for abrasives function. For example, was reported presence of polyethylene, polystyrene and

polypropylene in cosmetic product. These plastics can vary in size, composition and shape typically irregular[10,15,16].

- Industrial sources: can be small pellets used as abrasives in some industrial process[17] or another source of MNPs are granules and small resin pellets as raw material to product packaging materials. These can escape during transport from industry.

In addiction synthetic clothes, medicine as a vector and other similar sources input MNPs in environment. MNPs come from by water used for washing clothes in textile industry and fibres (primary MNPs) are subjected to degradation and become secondary MNPs[7,14].

5.1.4. Environmental distribution on MNPs

When MNPs are in aquatic environment can be mixed (also transport in large distance because MNPs are low density) from storm sewers, wind and currents and therefore can be degraded and reduce size becoming more dangerous[18]. For example, oceanographic modelling indicates that a large portion of floating debris reaching the ocean will accumulate in gyres, the centre of vast anti - cyclonic, subtropical ocean currents. Plastic consists of many different polymers and, depending on their composition, density and shape, can be buoyant, neutrally - buoyant or sink[10]. So, even in calm weather condition MNPs are present in each part of aquatic environment with heterogeneous distribution[19], in other world if we divided the water in columns is possible to find different polymeric debris in each compartment (Fig. 5.2):

1. Surface: here is more likely to find low-density plastic such as polypropylene and polyethylene[15]. Also, polystyrene pellets (1 - 2 mm) was found on the sea surface. [10, 20] It is known that the densities of debris decrease, but the quantities of the fragments increase 18% over the time. One research group[17] developed a theoretical model that indicates that the MPs obtain from surface tows are dependent on wind speed. Also, closed basins are threatened by MNPs pollution. In surface water many fish live, including the plankton. One study[21] report that there is a large plastic to plankton ratio. Type of plastic more common in plankton is polystyrene.

2. Middle: high - density plastic can be found because debris with large - surface area or due to tidal fronts can remain in suspension[15]. There are a most of MNPs that were retained near a seamount, as well as reef fish[17].
3. Sediment: more present high - density plastic, including polyvinylchloride, polyester and polyamide. These are present in largest quantities in benthos (ecologic category to which all organism that live in contact with seabed)[15]. High - density plastic in seabed come back in surface with storm. Some pellets found are translucent and 2-5 mm in size and related to accidental spillages at the major ports. Many of pellets showed deterioration due to weathering[17,22].

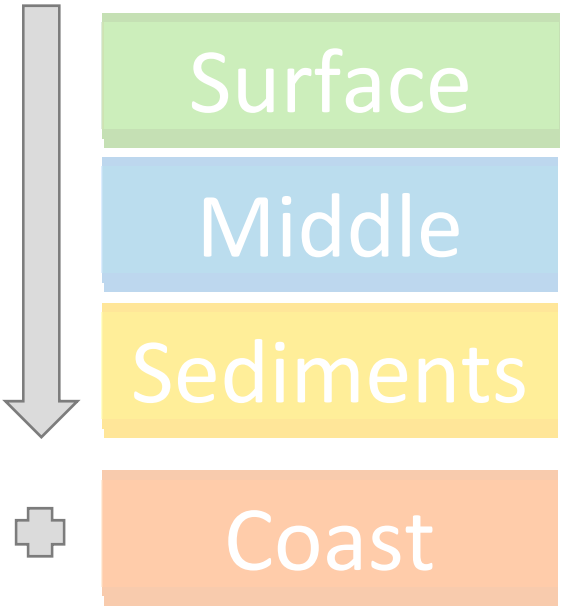

Figure 5.2. Parts of aquatic columns.

4. Coast: coastlines receive plastic litter from both terrestrial and marine sources. Much of the pellets were yellow or brown in colours due to photo - oxidation by sunlight. The present of plastic debris increase the permeability of the sediment and decrease heat absorbance of these. Consequently, there are affect in marine biota. For example, lower maximal temperatures might affect sex - determination in turtle eggs, reduction in the number of females. The sediments cores from sandy beaches revealed that MNPs deposition tripled over the last 20 years. By analysis sediments from different beaches, most often observed polymers in the form of fibres[15,17,23].

After storm, the type of MPs that can be found in different part of water column can be mixed. Moreover, the MNPs concentration were 5 times higher before a strong wind event than after the event.

5.1.5. MNPs as a carrier of harmful species

Plastics are typically considered biochemically inert, some time there are additives in formulation of plastic to improve their performance, functionality and ageing property (i.e. plasticizer, flame retardants or light and heat stabilizers). In addiction MNPs are able to adsorb chemical compounds by environment. MNPs have a large surface area to volume ratio than macro - plastics and are more susceptible to contamination by a few pollutants. Plastics are highly hydrophobic materials, the chemical pollutants are concentrated in and onto their surfaces, and MNPs act as reservoirs / carries of toxically chemicals. So, MPs can absorb a numerous of waterborne - pollutants, including heavy metals, chemicals, persistent organic pollutants (POPs) and hydrophobic organic contaminants (HOCs). Typically, these chemicals are abundant in surface microlayer where low - density plastics are accumulate and these are bio - accumulative and toxic[15]. One research group[17] showed that the black pellets exhibited higher concentrations of polychlorinated biphenyls (PCBs) than aged pellets, possibly because they have higher adsorption rates. Another group[7] has shown that organic compounds and metals were accumulate on PE plastic pellets. The porous level of several plastic is one factor for chemical adsorption, so PE adsorbed more than PP and PVC[10]. One group[3] studied the role of plastic as a carrier of hydrophobic organic chemicals (HOCs) and the kinetics of release and adsorption[24]. Affinity of HOCs for plastic is high. Another phenomenon can be microbial films that rapidly develop on submerged plastic and change their properties[10]. In addition the microbial film growth can determine the sedimentation of MNPs[15]. Plastic not only have the potential to transport contaminants, but they can also increase their environmental persistence.

5.1.6. MNPs in WWTPs

Recently, more MNPs studies are performed in waste water treatment plants (WWTPs)[25], and the results are discordant because some authors found a lot of MNPs in the WWTPs effluent[2], in contrast other authors found that the second and tertiary treatment process are able to reduce significantly MNPs pollutants[26]. The major challenge in this study is sampling and characterization the MNPs. So, a new method to do this was developed by Ziajahromi research group[27], they combined a new device for

sampling with multiple mesh screens, organic matter digestion with hydrogen peroxide and FT-IR spectroscopy to identify non - plastic particles. The efficiency of sampling and characterization method is from 92% to 99% based on size mesh. The most frequently detected MNPs were PET fibres and irregular shape PE particles. Three different WWTPs were tested with different type of treatment (A) only primary treatment (B) primary and secondary treatments (C) primary, secondary, tertiary and reverse osmosis. And the results shown that in (C) plant, after the last treatment the MNPs particles per litre is very low (< 10 size range 25 - 100 µm < 20 size range 100 - 190 µm).

In conclusion, there are many aspects of MNPs currently not investigated[30] and the scientific community is dedicating itself more and more to this emerging class of pollutants (Fig. 5.3).

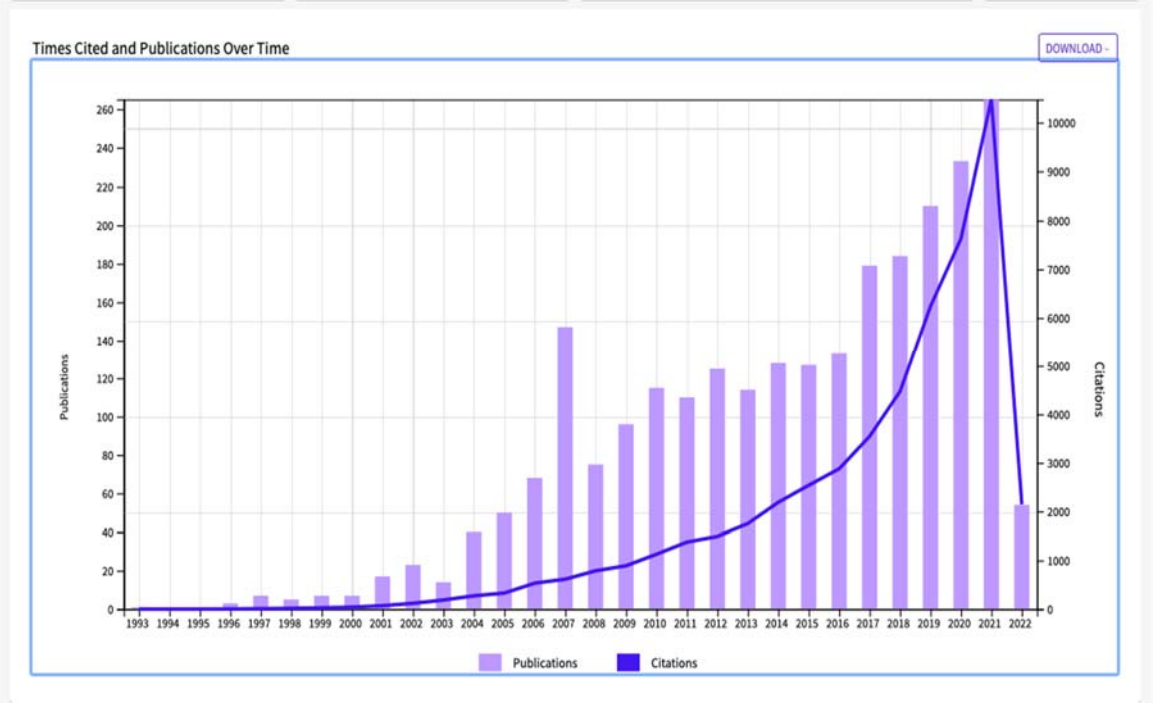

Figure 5.3. publication and citation of MNPs as pollutant. 2537 result from Web of Science Core Collection for: micro nano plastics.

The assessment and control of MNPs impact on human health and environment is a challenging goal that scientific community begins to face. The first challenge is the characterisation of physico-chemical identity of MNPs, that passes through the definition of robust protocols for the preparation and collection of simulated and real

samples[31,32]. The second challenge is the risk assessment with the characterisation of MNPs hazard and exposure, that needs measurement and testing methods appropriate and capable of producing scientifically solid data[33]. Finally, the management of MNPs potential risk requires the optimisation of water purification methods able to treat also plastic nanoparticles (NPs) that so far been rarely addressed[34].

So, during my thesis I contributed to the basic characterization of most relevant MPs, as polyethylene (PE), polyurethane (PU) and polyethylene terephthalate (PET), in order to define their physico - chemical identity (morphology, surface chemistry) and to the study of dispersibility to identify suitable protocols for their characterisation in water - based media, finally I studied the colloidal properties of MPs in real matrices such as river and sea water.

5.2. Material & Methods

5.2.1. Materials

Table 5.1 shows all the MPs tested during the thesis with the information (size, shape, presence of additives) declared by the supplier. The samples LDPE – CP and PU were examined in a internal study. The other samples and characterisation were performed within the European PlastcsFate project.

Table 5.1. MPs investigated during the thesis.

Material	CODE	Supplier	Declared size (µm)	Declared shape	Primary / secondary	additives
Low-density polyethylene	LDPE - CP	Cospheric LLC (Santa Barbara, CA, USA)	10 - 150	spherical	primary	30%
	LDPE - PF	BAM (Germany)	< 75	spherical	primary	n.a.
	HDPE – PF - P	Clariant (Italy)	5	n.a.	primary	n.a.

High – density polyethylene	HDPE – PF - S	BAM (Germany)	60	irregular	Secondary – Cryo milled	No
Ultra – high-molecular weight polyethylene	UHMWPE – PF - C	BAM (Germany)	145	Cloud	primary	n.a.
	UHMWPE – PF - P	BAM (Germany)	57	Potato	primary	n.a.
	UHMWPE – PF - PC	BAM (Germany)	22	Popcorn	primary	n.a.
Polyurethane	PU	Lamberti (Italy)	5 - 8	Spherical	primary	n.a.
Polyethylene terephthalate	PET – PF - L	BAM (Germany)	44	Irregular	Secondary – Cryo milled	No
	PET – PF - M	BAM (Germany)	70	Irregular	Secondary – Cryo milled	No
	PET – PF - H	BAM (Germany)	130	irregular	Secondary – Cryo milled	No

Dispersing system: Bovin Serum Albumin (BSA), heat shock fraction, pH 7, ≥ 98%. Polysorbate Tween® 60 were purchased by Sigma Aldrich (Italy). Sodium Surfactin (SS) was purchased by Ambrosia Lab.

The environmental matrices were chosen from the reference matrices used in the eco - toxicological studies. It is about:

5. Egg Water (EW), sea simulant fluid. It is obtained from dilution of “instant oceans salt” purchased by TermoFisher Scientific Inc. (Canada). Theorical composition (mg / L): 18.2 Na^{+}; 0.630 K^{+}; 2.17 Mg^{2+}; 0.646 Ca^{2+}; 0.0285 Sr^{2+}; 0.0111 Al^{3+}; 31.7 Cl^{-}; 1.26 SO_4^{2-} [35].

6. Elendt M7 (M7), river simulant fluid. The following salts were dissolved in DI water (mg / L): 0.715 H_3BO_3; 0.0901 $MnCl_2 \cdot 4H_2O$; 0.0765 LiCl; 0.0178 RbCl; 0.0380 $SrCl_2 \cdot 6H_2O$; 0.00400 NaBr; 0.0158 $Na_2MoO_4 \cdot 2H_2O$; 0.0168 $CuCl_2 \cdot 2H_2O$; 0.0130 $ZnCl_2$; 0.0100 $CoCl_2 \cdot 2H_2O$; 0.00325 KI; 0.000219 Na_2SeO_3; 0.0000575 NH_4VO_3; 1.25 $Na_2EDTA \cdot 2H_2O$; 0.498 $FeSO_4 \cdot 7H_2O$; 2940 $CaCl_2 \cdot 2H_2O$; 1230 $MgSO_4 \cdot 7H_2O$; 5.80 KCl; 64.8 $NaHCO_3$; 10.0 $Na_2SiO_2 \cdot 9H_2O$; 0.274 $NaNO_3$; 0.143 KH_2PO_4; 0.184 K_2HPO_4[36].

5.2.2. Stock suspension stability

Dispersing agents were tested in order to prepare a stock suspension useful for further dilution and characterisation under the testing exposure conditions:

1. Water.
2. Water + EtOH pre - wetting (0.4 mL / 1 mg powder).
3. Bovine Serum Albumin (BSA) (powder dissolved in DI water at 0.25 mg / mL concentration): prepared following Nanogenotox protocol[37]. BSA is a protein derived from cows. BSA has numerous biochemical applications, it is a small, stable and moderately non - reactive protein. BSA is used for its ability to boost signal in tests, its lack of effect in many biochemical reactions, and its low cost, as large quantities can be readily purified from bovine blood, a by - product of the livestock industry. It is a very popular molecule in the field of nanoparticles because it is biocompatible and does not interfere with in vitro toxicology studies, it also has a remarkable dispersing property, preventing the aggregation of the nanoparticles.
4. Polysorbate Tween® 60 (powder dissolved in DI water at 0.25 mg / mL concentration): Polysorbates (Fig. 5.4) are a class of emulsifiers used in some pharmaceutical products and in food preparation. They are often used in cosmetics to solubilize essential oils in water - based products. Polysorbates are oily liquids derived from ethoxylated sorbitan (a derivative of sorbitol) esterified with fatty acids. The number following is related to the type of fatty acid associated with the polyoxymethylene sorbitan part of the molecule (60 = monostearate).

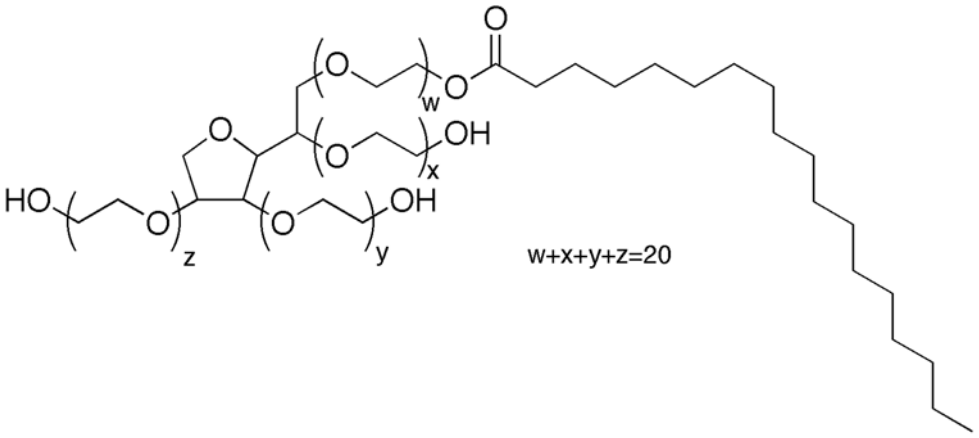

Figure 5.4. structure of polysorbate.

5. Sodium Surfactin (SS) (powder dissolved in DI water at 0.25 mg / mL concentration): Sodium Surfactin is a bio - surfactant, belonging to the group of Lipopeptides (LPs), mainly from *Bacillus sp.* Different isoforms of surfactin (Fig. 5.5) occur naturally, but overall its amphiphilic structure makes it a very good surfactant with a (CMC) in water (23 mg / L) and approximately two orders of magnitude less than the majority of other surfactants. Due to the recognized bioactivity (anti - microbial, anti - cancer) various investigators examined the cytotoxic effects of surfactin[38].

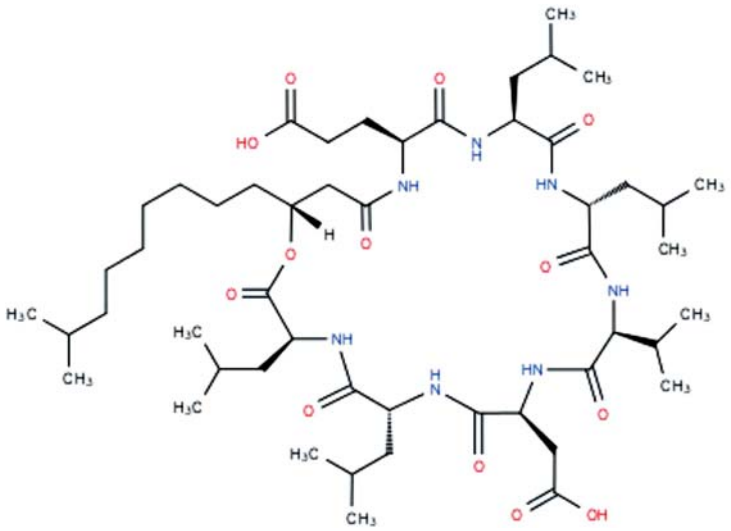

Figure 5.5. chemical structure of Surfactin.

We evaluated the degree of dispersion of the sample HDPE – PF - P the 5 different dispersion systems. Then we extended the study to the samples: LDPE – PF; HDPE – PF – S; UHMWPE – PF – C; UHMWPE – PF – P; UHMWPE – PF – PC; PET – PF – L; PET – PF – M

and PET – PF – H in the media SS and BSA. The MP dispersions were prepared adding the powder of sample (LDPE – CP and PU at 2560 ppm; other samples at 5000 ppm) in the dispersant system (previously prepared). The dispersions were subjected to sonicator bath treatment (15 min) + 1 min Vortex before using.

To evaluate the degree of stability, photos were taken at different time (0, 5 min, 30 min, 60 min, 24h, 48h) in order to visually distinguish which MPs remain in suspension, settle or float.

5.2.3. Physico - chemical characterization

Morphology, shape and dimension

The morphology and shape of MPs was investigated by optical microscope (Hirox 3D digital microscope, RH200). The dispersions were dropped on a glass slide and dryed in an oven at 80 °C for 15 minutes. The size dimension was evaluated by software ImageJ, over a count of more than 100 particles for each sample. Investigated samples: LDPE – PF; HDPE – PF – P; HDPE – PF – S; UHMWPE – PF – C; UHMWPE – PF – P; UHMWPE – PF – PC; PET – PF – L; PET – PF – M and PET – PF – H.

For LDPE – CP and PU samples the morphology and dimensions were analysed using the Scanning Electron Microscope (ZEISS Sigma HV). The powders were attached onto an aluminium holder using carbon tape. All samples were gold - coated (thickness = 5 nm) (Spatter Quorum Q150T ES) to increase the conductivity and obtain well - defined images. The images were analysed with ImageJ software, calculating the diameter of at least 500 sample MPs; for the statistical analysis of results, a 95% confidence interval was chosen.

Fourier Transform Infrared Spectroscopy – Attenuated Total reflectance (FTIR-ATR)

The surface chemistry of powders was assessed by ATR-FTIR analysis (Nicolet iS5 spectrometer, Thermo Fisher Scientific Inc. - Waltham, MA, USA) Powders were previously dried in an oven at 110 °C for 15 minutes in order to remove traces of residual water, were subjected to. For the analysis it was set a wave number range between 400 and 4000 cm^{-1} and was used the ATR (iD7 model) as an accessory. Subsequently, in the obtained spectra were identify the positions of the peaks using the OMNIC software and, by comparison

with the data in the literature, the possible vibrational transitions responsible for the peak. the chemical structure of the polymer.

Electrophoretic Light scattering (ELS)

Zeta potential of MPs dispersion (5000 ppm) was measured by Zetasizer instrument (Malvern Instruments, Zetasizer Nano - ZS, Malvern, UK) based on the electrophoretic light scattering (ELS) techniques. The zeta potential was measured on 700 µL of the sample at 25 °C, setting the measurement time, the attenuator position, and the applied voltage to automatic. After a 2 min temperature equilibration step, the samples were measured three times, and the data were obtained by averaging the three measurements. The data of zeta potential (mV) are derived by electrophoretic mobility using Smoluchowski's formula. The reliability of the measurements was controlled by check the phase plot graph. The same instrument coupled with an automating titrating system was used to measure zeta potential vs. pH (sample: HDPE – PF – P; UHMWPE – PF – PC; LDPE – PF; PET – PF – L suspended in dispersing system and DI water) to identify the pH at which the zeta potential sets to zero, namely the isoelectric point ($pH_{i.e.p.}$). The titrants used were 0.1M KOH solution and 0.1M HCl solution.

5.2.4. Exposure tests in environmental media

The MPs were dispersed in the environmental matrices for different times and at different concentrations. In particular, suspensions at 100, 500 and 1000 mg / L were prepared, with times of exposure of 1 hour, 24 hours and 240 hours. The selected concentrations are in agree with real samples investigated by Ferraz[39] that found an average content of microplastics for river water equal to 330.2 particles / L, with size between 200 and 1000 µm. The times of exposure have been chosen in order to have a comparison between three possible scenarios: two in the short term (1 and 24 hours) and one in the long term (240 hours). Once prepared, the suspensions were incubated at 20 °C under dynamic conditions inside an oscillating bath (SB 35, ArgoLAB) coupled to a chiller (F12, Julab) for the time set, simulating the average temperature and the currents to which MPs are subjected in seas and rivers. Following the exposure described above, the suspensions at 100 and 1000 mg / L have undergone titration (Z - potential vs. pH).

5.3. Results & Discussion

5.3.1. Stock suspension stability

The preparation of stable stock suspension is crucial for investigating colloidal properties such as particle size distribution, shape, aggregation / agglomeration, surface charge, etc. This in turn ultimately influences the interaction of the particles with the test media and the outcome of various in vitro and in vivo experiments, in order to evaluate the potential hazard of suspended phases. The stock suspension preparation protocol described above (Materials and methods) was established by evaluating the colloidal stability as the ability of the dispersed phases to remain suspended over the time of the experiment or during the use. In Fig. 5.6 is possible to see the HDPE – PF – P sample dispersed into five different dispersant systems, from left: water + EtOH, Tween® 60, SS, BSA and water at time 0.

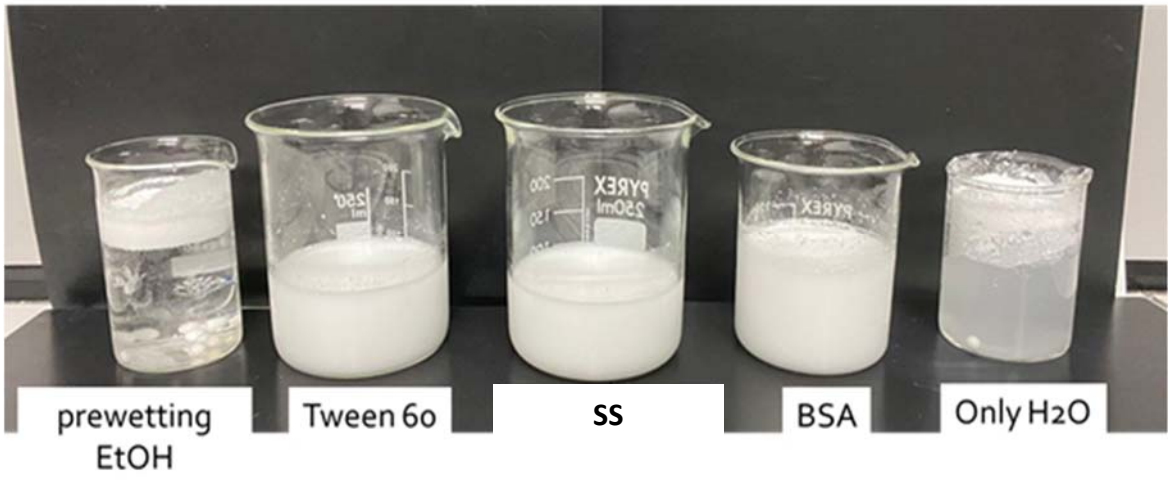

Figure 5.6. HDPE -PF - P sample (5000 ppm) dispersed in different dispersant system (0.25 mg/ml). Time 0.

Samples dispersed in water and water + EtOH floated immediately because PE has a lower density than water (ρ = 0,94 - 0,965 g / cm^3), while in the presence of dispersants (BSA, Tween® 60 and SS) the suspension resulted visually homogeneous, especially for SS dispersant.

We repeated the dispersion tests vs time (results not shown) in order to have an idea of stability in more long time and we found that for 24h the suspension of HDPE – PF – P with dispersants (BSA and SS) resulted stable. We decided to apply the same protocol to all sample dispersed in SS (Fig. 5.7) and BSA (Fig. 5.8).

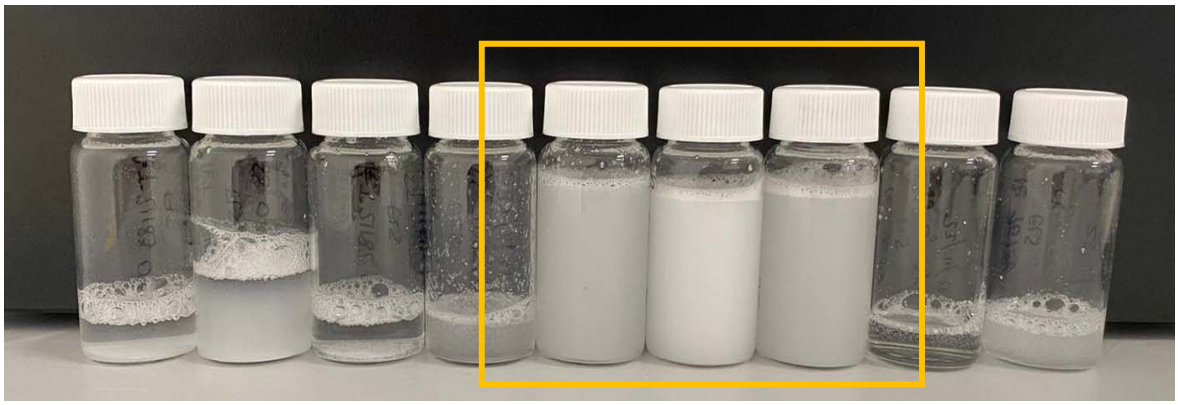

Figure 5.7. from left: PET – PF – M; PET – PF – L; PET – PF – H; HDPE – PF – S; LDPE – PF; HDPE -PF – P; UHMWPE – PF – PC; UHMWPE – PF – C; HDPE – PF – P 5 mg / mL in SS dispersant. Time 0.

From visual observation it can be noted that only PE in yellow rectangle samples show a good degree of dispersion without gentle shaking the samples. PE is the plastic with the lower density among those investigated and the concentration of the dispersing media is sufficient to keep the MPs in dispersion at least for the time of the measurements.

Figure 5.8. sample 5mg / mL is BSA dispersant. Time 0.

The visual observation of samples dispersed in BSA showed how the most plastic stocks immediately tend to settle on the bottom (PET samples), due to the higher density compared to water (density of 1.38 g / cm^3) or float on top (PE samples) of the vials. Only HDPE - PF - P samples show a good degree of dispersion over time (48 h).

5.3.2. Physico - chemical characterization

Morphology, shape and dimension

The SEM and optical images for all samples are reported in Table 5.2. In general, it is possible to confirm the information received from the supplier of the MPs. For the samples (LDPE - CP and PU) observed at SEM it was also possible to appreciate the surface

which appears rough in both. This could be an important aspect of the potential dangerous absorption of pollutants or chemicals on the surface of the MPs, referred to in the introduction (section “MNPs as a carrier of harmful species “).

For HDPE – PF – S and UHMWPE – PF – PC it was not possible to calculate the size distribution due to the irregular shape of MPs.

The PET samples appeared well dispersed, with an irregular shape, as reported by supplier. We detected in all samples a variety of fragments with different shape and size, probably produced during the cryo - milling process. The small differences in size dimension can be associated to the low number of particles analyzed by the software and the sampling procedure.

Table 5.2. SEM, optical image and size distribution for analysed sample.

CODE	**Declared size (µm) shape**	**Size shape (from image)**	**Image**	**Size distribution (frequency vs. diameter (µm)**
LDPE - CP	10 - 150 spherical	70 Spherical	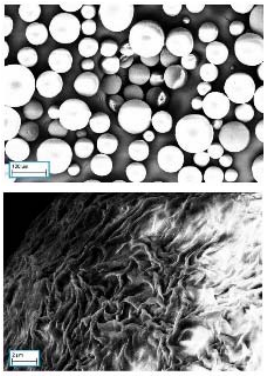 Wrinkled surface	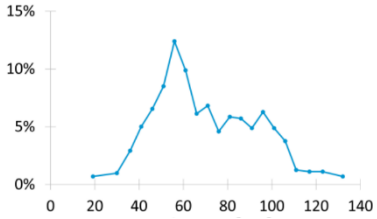
LDPE - PF	< 75 spherical	22 spherical	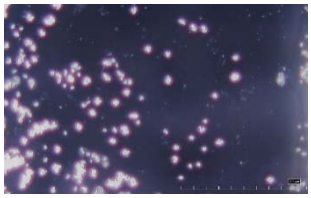	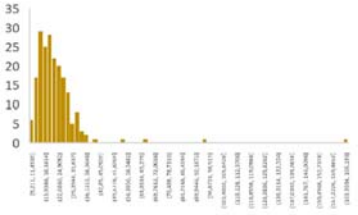

HDPE – PF - P	5 n.a.	4.7 round	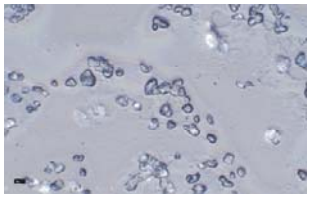	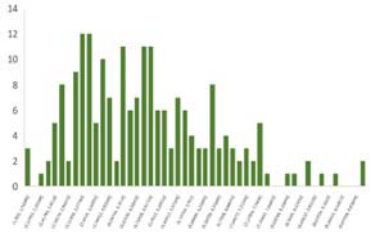
HDPE – PF - S	60 irregular	irregular		n.a.
UHMWPE – PF - C	145 cloud	82 cloud	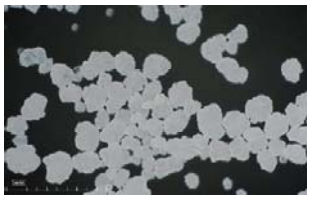	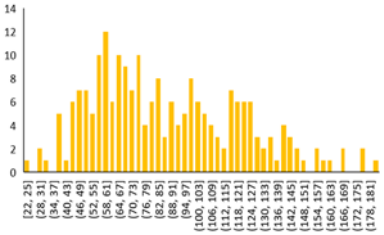
UHMWPE – PF - P	57 potato	52 potato	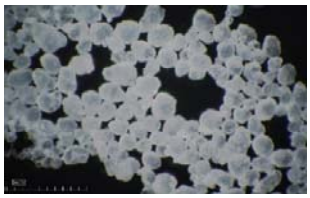	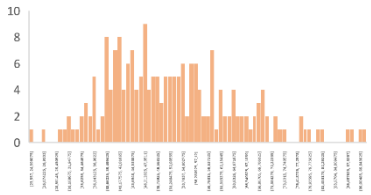
UHMWPE – PF - PC	22 popcorn	Irregular	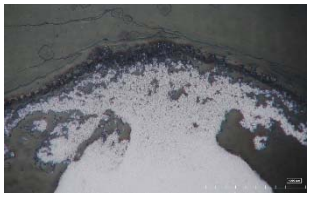	n.a.

PU	5 - 8 spherical	6 spherical	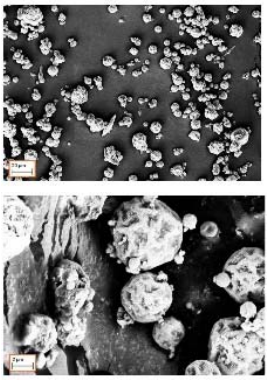 Gnarled and irregular surface	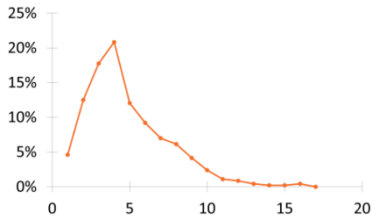
PET – PF - L	44 irregular	35 irregular	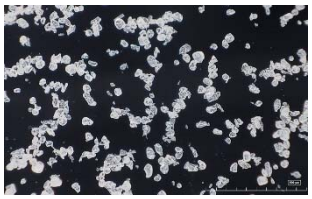	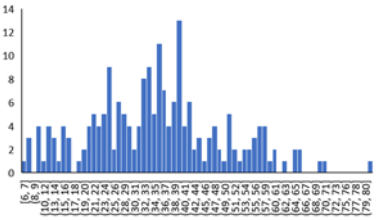
PET – PF - M	70	55 irregular	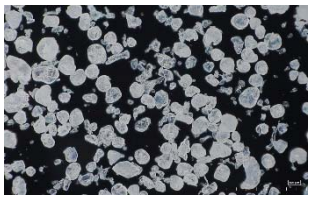	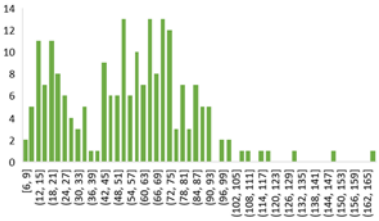
PET – PF - H	130	126 irregular	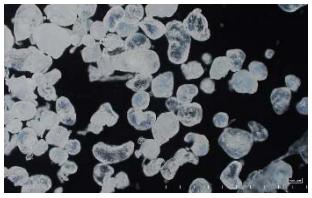	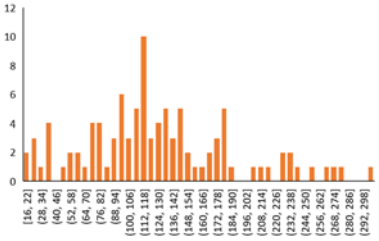

FTIR-ATR

The AT-IR spectrum of LDPE - CP sample of Fig. 5.9 (blue), shows the typical peaks of PE (Fig. 5.11). The peaks at 2914 and 2847 cm^{-1} are attributed to the stretching of the C - H bond; while those at 1472 and 1462 cm^{-1} are attributed to the bending of $– CH_2$ and $– CH_3$. In the AT-IR spectrum of the PU MP shown in Fig. 5.9 (orange), the peak at 3340 cm^{-1} can be attributed to the stretching of the N - H bond, typical of the urethane group. The series of peaks between 2867 and 2969 cm^{-1} is attributed to the stretching of the C - H bond of the methyl group, probably due to an alkyl chain. Finally, the peaks at 1720, 1633 and 1556 cm^{-1} can be attributed respectively to the stretching of the C = O bond, to the stretching of the C - N bond and to the bending of the N - H bond[41].

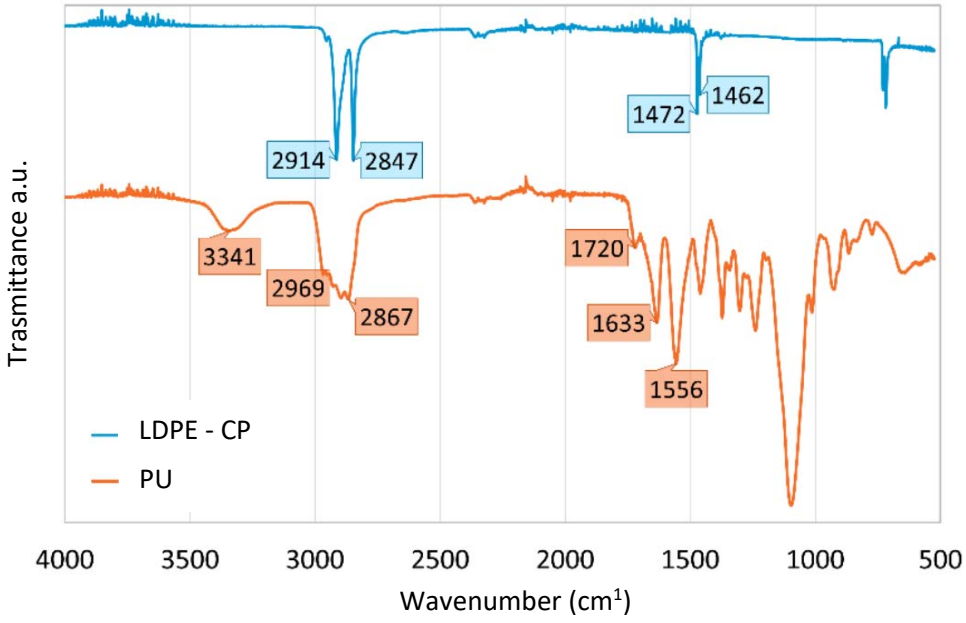

Figure 5.9. AT-IR spectra of LDPE - CP (blue) and PU (orange) samples.

In Fig. 5.10 are reported the AT-IR spectra of all PE samples (excluding LDPE – CP, shown above). Comparing the measured spectra with reference spectrum of PE reported in Fig. 5.11[42], we observed a perfect matching of the characteristic picks of $-CH_3$ and $-CH_2$ stretching at ca. 2900 cm^{-1}, $-CH_3$ bending at 1300 cm^{-1} and $-CH_2$ vibration at 700 cm^{-1}. No significative differences were observed between primary PE particles (HDPE – PF – P) and secondary (HDPE – PF – S) one or between LDPE, HDPE and HUMWPE particles.

In Fig. 5.12, we reported the AT-IR spectra of secondary PET particles. Checking the picks with one reported as reference in Fig. 5.13[43], we didn't observe any differences in terms

of spectra and vibration associated. So, it is possible to see a strong intensity peak of stretching C = O bound at 1711 cm^{-1}, while at 1407, 870 and 721 cm^{-1} there are a medium intensity peaks regarding C = C, =C – H and C- H bonds stretching vibration respectively. C – H shown a stretching vibration at 1339 cm^{-1} and the ester bond C – O shown three strong stretching vibration at 1239. 1091 and 1015 cm^{-1}[44].

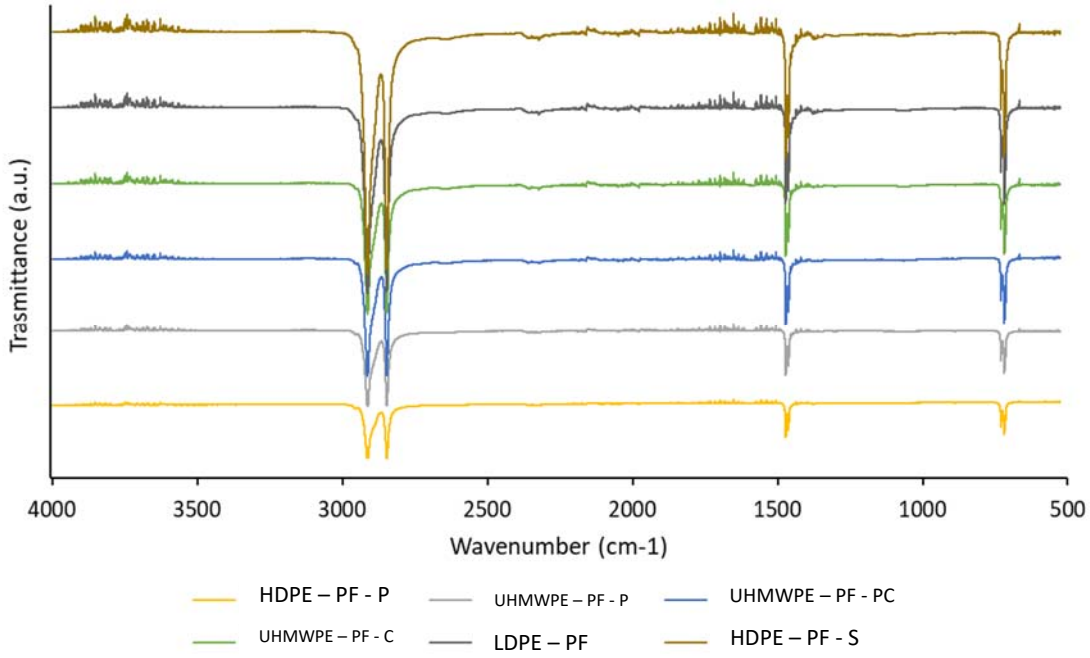

Figure 5.10. AT-IR spectra of PE samples.

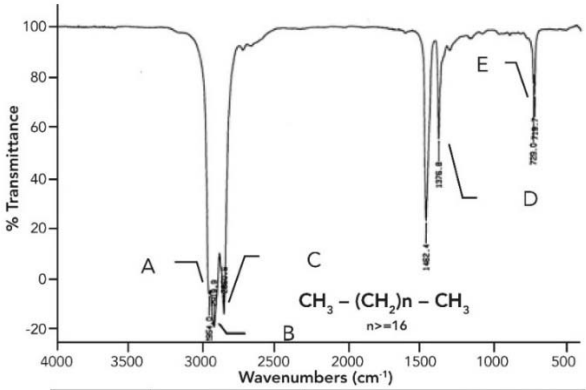

A	2954	CH_3 Asymmetric stretch
B	2920	CH_2 Asymmetric stretch
C	2860	CH_2 Symmetric stretch
D	1377	CH_3 Umbrella bending mode
E	729, 720	Split CH_2 rocking vibration

Figure 5.11. Reference spectrum of PE and relative main picks[42].

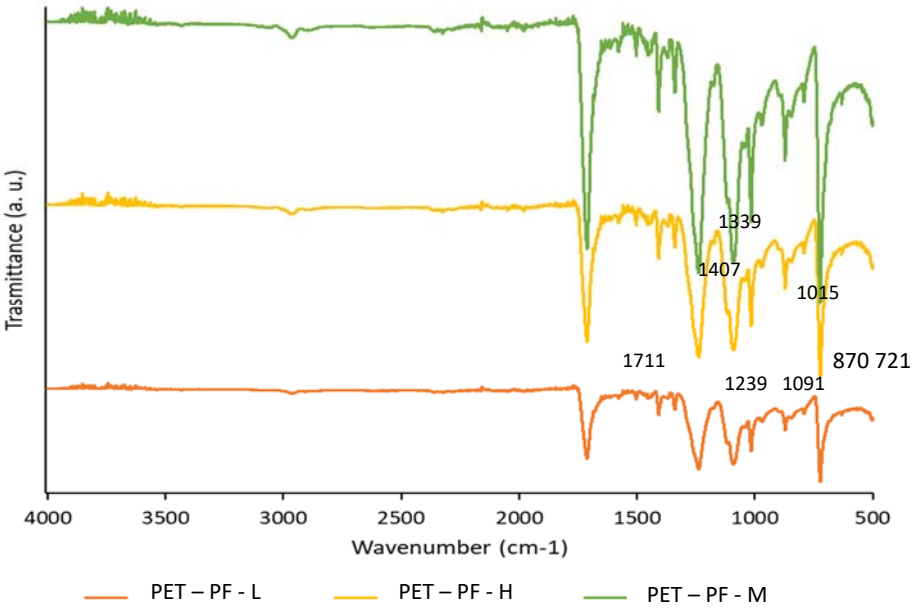

Figure 5.12. AT-IR spectra of secondary PET samples.

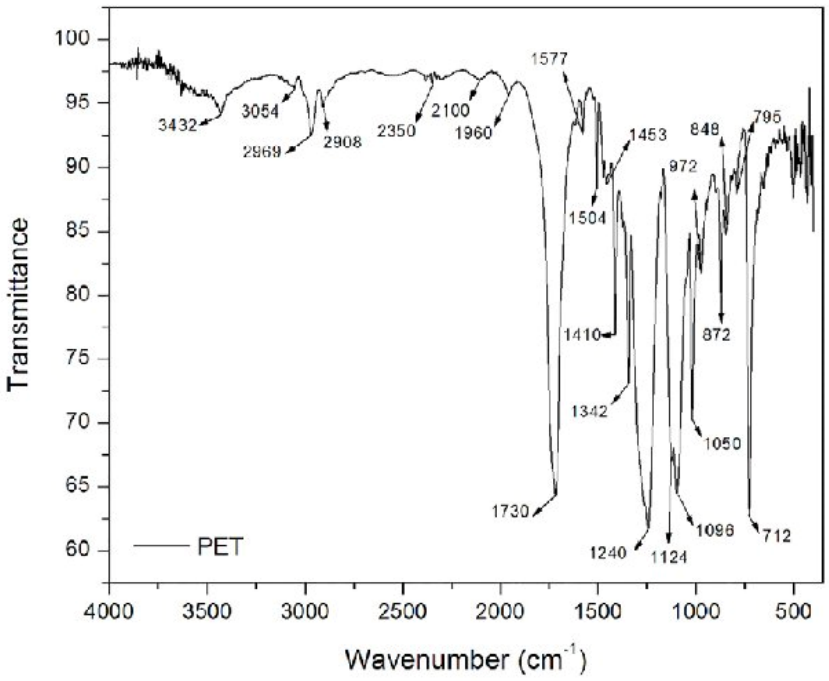

Figure 5.13. reference spectrum of PET[43].

Zeta potential (ELS)

In Fig. 5.14 the Z – pot vs pH titration curves for the samples LDPE – CP and PU are shown. The first showed the characteristic reverse sigmoid shape with $pH_{i.e.p.}$ = 3.8. A colloidal system is considered stable when | Z - pot | > 35 mV, the system is considered metastable when 15 mV <| Z - pot | <35 mV[45]. Therefore, in the case of the LDPE - CP sample we can say that the system is stable up to pH 5 and becomes metastable from pH 5 to values <3.5. The presence of additives (30% of the composition, information from the supplier) is confirmed by the negative Z – pot shown up to 3.8 that cannot be justified by the acidity of PE polymer surface that is characterized by an alkyl chain, highly hydrophobic.

The PU sample showed a more flattened curve and is not classifiable as stable. Thanks to the polarity of the urethane group, the PU showed a greater affinity with water [46] and a negative charge in an higher range of pH, most likely due, also in this case by the presence of additives coming from the formation of foam.

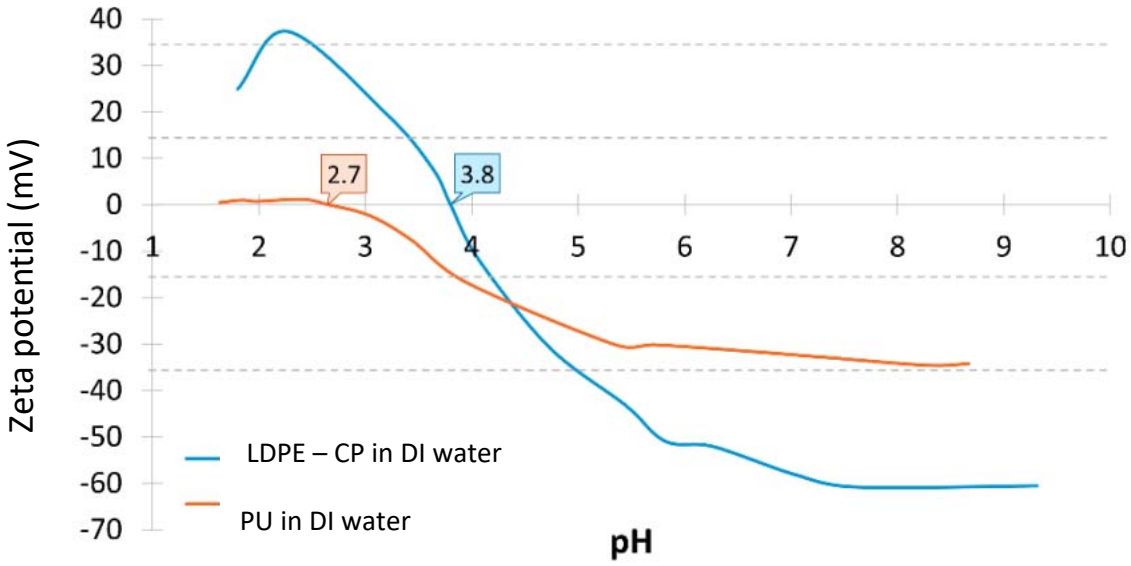

Figure 5.14. Z - potential vs pH for LDPE - CP (blue) and PU (orange) sample.

The zeta potential values of the MPs investigated in the two dispersing systems BSA and SS 0.025 wt% are reported in Table 5.3. It is possible to notice how the MPs have very high negative zeta potential. Polymers are generally neutral but, the presence of additives used during the synthesis can change their surface charge [47]. As well the presence of BSA and SS adsorbed on the surface justified the negative zeta - potential found.

Table 5.3. zeta potential of micro plastics 0.5 wt% in BSA and SS dispersant 0.025 wt%.

CODE	BSA 0.025 wt%		SS 0.025 wt%	
	Z – pot (mV) ± std	pH	Z – pot (mV) ± std	pH
SS			-45 ± 2	7
BSA	-19 ± 2	6.8		
LDPE - PF	-41 ± 10	7.7	-85.4 ± 5	7.4
HDPE – PF - P	-59.4 ± 1	7.7	-66 ± 2	7
HDPE – PF - S	0	7.8	-75.4 ± 3	8
UHMWPE – PF - C	-13 ± 4	7.3	-37 ± 5	8
UHMWPE – PF - P	-48.5 ± 4	7.1	-87 ± 6	7.6
UHMWPE – PF - PC	-57 ± 3	7	-106 ± 4	7.8
PET – PF - L	-56 ± 9	7.8	-60 ± 20	8
PET – PF - M	-43 ± 9	7.9	-68 ± 12	7.8
PET – PF - H	-55 ± 6	7.9	-53.6 ± 10	8

The high affinity of the MPs[48] for surrounding chemicals was also confirmed by observing the Z -Pot titration curves of the MPs in the presence of intentionally added dispersing agents: BSA and SS. In fact, from Fig. 5.15 - 5.16 it is possible to see how the MPs dispersed in the medium replicate the titration curve of the dispersant itself. This happens for both PE and PET in both BSA and SS media.

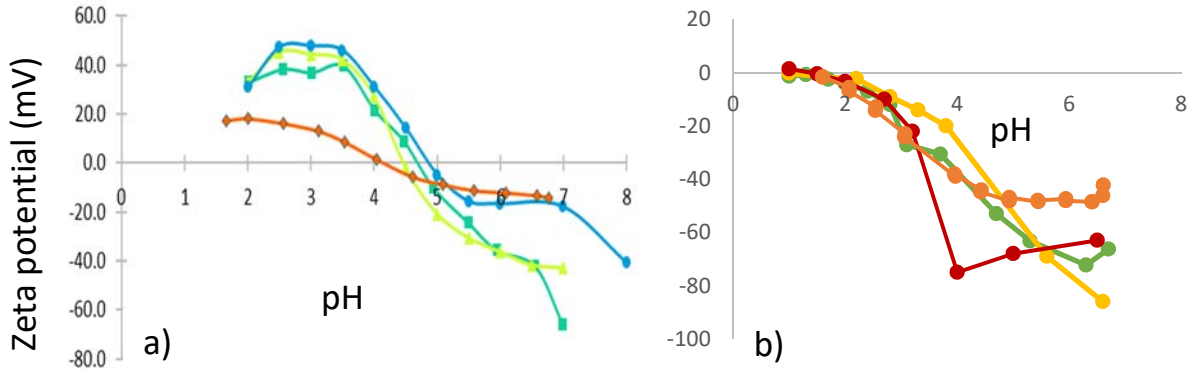

Figure 5.15. ZP – pH curves of different PE sample (a) In BSA (orange) (UHMWPE – PF – PC in green, HDPE – PF – P yellow and LDPE – PF in blue). (b) In SS (orange) (HDPE – PF – P in green, LDPE – PF in yellow and UHMWPE – PF – PC in red).

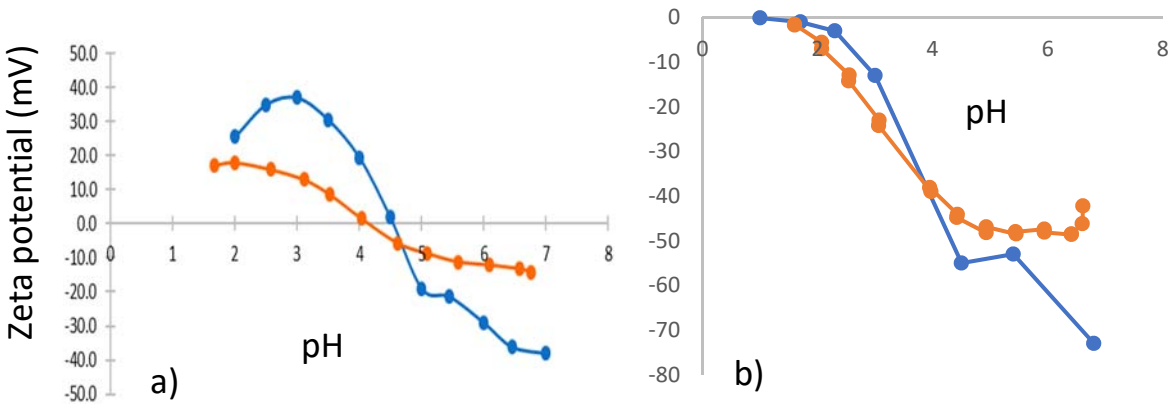

Figure 5.16. ZP – pH curves of PET – PF - L sample (blue) (a) In BSA (orange) (b) in SS (orange).

As can be observed both for PE and PET samples, the $pH_{i.e.p.}$ and the shape of the titration curves tend to replicate those of the dispersing system. This means, that based on the dispersant chosen the MPs show different colloidal behaviours that can also reflect on the toxicity of the MPs both for the environment and for the human being.

5.3.3. Exposure condition in simulant fluids

The properties of LDPE - CP and PU samples (ELS, titration) and (SEM morphology) were investigated after exposure to river (M7) and sea water (Egg water) simulating media.

LDPE – CP

Figure 5.17 shows the Z - potential vs. pH for 100 and 1000 mg / L samples of LDPE – CP in Egg water, M7 and for comparison in distilled water, at different exposure times (1h, 24h and 240h). The dispersion of LDPE - CP in Egg water (Fig. 5.17 a), showed a shift of the

$pH_{i.e.p.}$ to lower pH values, for both concentrations and at all times. In the sample at 1000 mg / L, the $pH_{i.e.p.}$ shifted from a pH value of 3.3, to 2.9 and finally to 2.2 after 1, 24 and 240 hours of exposure respectively; while for the sample at 100 mg / L, the $pH_{i.e.p.}$ value shifted from 3.0 to 2.9 and didin't achieved the $pH_{i.e.p}$ after 240 hours, falls below the considered range. This trend suggests a progressive adsorption in the double layer of bivalent anions from the medium, which contribute to lowering the $pH_{i.e.p}$. Furthermore, for all samples, the reverse sigmoid is more flattened, the absolute value of zeta – potential tend to 0 mV throughout the pH range considered. This is attributable to the adsorption of monovalent anions in the electrical double layer. Finally, it is possible notice a difference in behaviour between the 100 and 1000 mg / L concentrations, in fact if in the first case the system is unstable throughout the pH range investigated, in the second it results metastable up to about pH 4.5. This difference could be due to the fact that the higher concentration of MPs in the sample at 1000 mg / L makes the amount of salts present in the medium less effective in destabilizing a single microsphere.

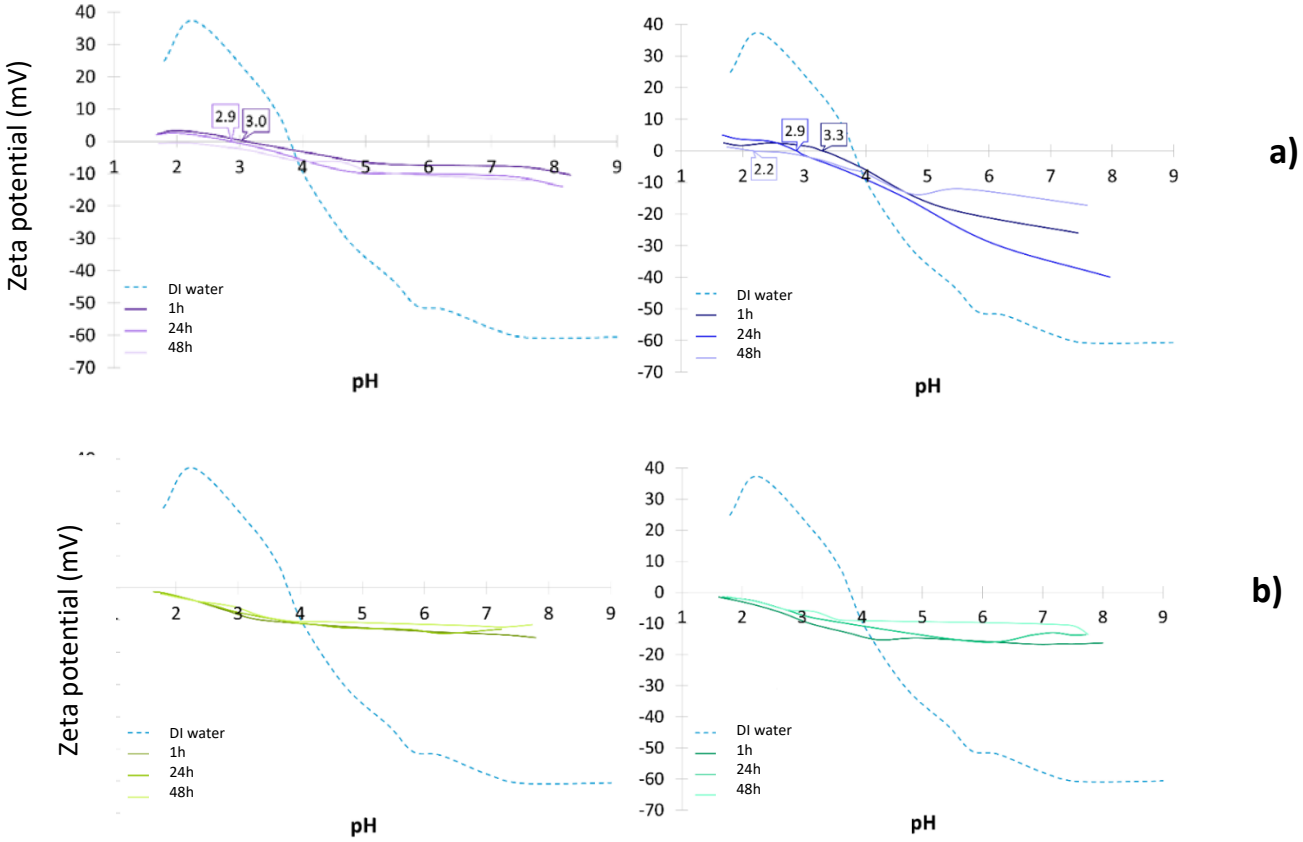

Figure 5.17. LPDE - CP sample (a) in Egg water (purple) 100 - 1000 ppm (b) in M7 (green) 100 - 1000 ppm. The dashed curve in each graph refers to the sample in DI water.

Figure 5.17b shows the zeta potential vs. pH for 100 and 1000 mg / L samples for LDPE - CP in M7 at different exposure times. From the comparison between the curve for LDPE – CP in DI water and those in M7, you immediately notice a crushing of the latter to values of z - pot higher than -15 mV, values such that the system is unstable, and a lowering the $pH_{i.e.p.}$ value below the investigated pH range ($pH_{i.e.p.} < 1.5$) for all samples and all exposure times. The strong destabilization of the system caused by M7 is from look for the presence of high amounts of salts in the medium, containing both anions and mono and bivalent, which contribute respectively to the flattening of the curve and to the displacement of the IEP. In this case, there are no significant differences for the different concentrations. On the contrary, as the exposure time varies, it is possible to notice as, after 240 hours, zeta potential values tend to approach 0 mV in the pH range between 4.5 and 8.0. This suggests that it takes time for the system to reach equilibrium.

The images of LDPE - CP exposed for 240 hours in the two media are shown in Figure 5.18a and 5.18b; while the dimensional distribution is shown in Figure 5.18c. From the point of view dimensional it is possible to observe an increase in the average size of the MPs; while observing the size distribution, two different populations are jet present, but the larger population increases in importance with respect to the pristine material. The increase in the size of the MPs could be due to swelling of the material caused by the permanence in the water, however a possible loss of the smaller fraction when handling the sample, resulting in modification the relative importance of the two populations. From the morphological point of view, we observe changes in the shape and appearance of the MPs, even if it is possible note the presence of some broken MPs, with an average of 12% for the sample exposed in Egg water and 8% for the sample exposed in M7. However, it has been verified by means of blank proof that this event is due to the manipulation of the MPs from part of the operator and not exposure to the vehicle.

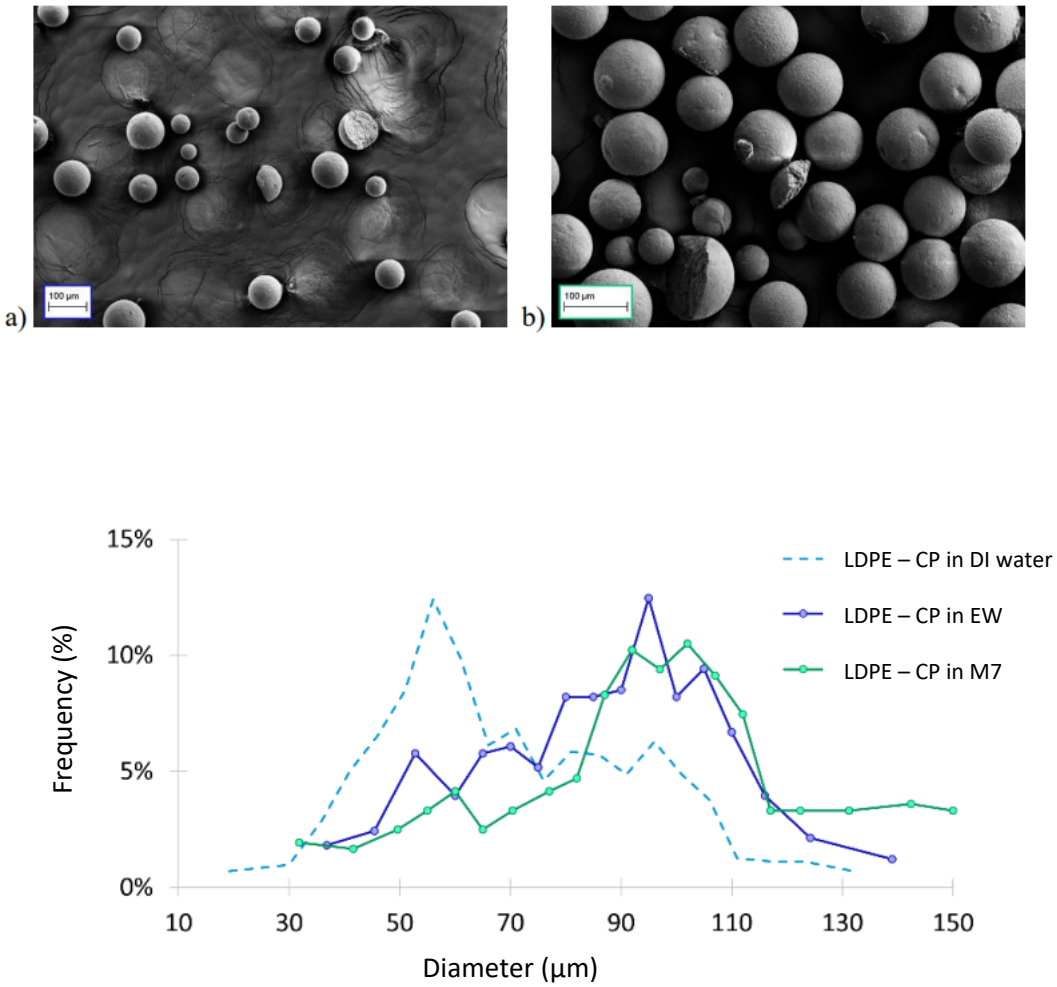

Figure 5.18. SEM image of LPDE - CP (a) in egg water (b) in M7 after exposure. (c) size distribution.

PU

Figure 5.19 shows the Z - potential vs. pH for 100 and 1000 mg / L samples of PU in Egg water, M7 and for comparison in distilled water, at different exposure times (1h, 24h and 240h). The dispersion of PU in Egg water there is a slight "flattening" of the curve (of about 5 mV) for pH < 4, for both concentrations and at all times. This crushing, of lesser entity than that measured for LDPE, it could be due to a lower interference of the monovalent anions with the electrical double layer of the PU MPs. As for the $pH_{i.e.p.}$: in the sample at 1000 mg / L, the value goes from 2.9 to 2.8 and finally at 1.9 respectively after 1, 24 and 240 hours of exposure; in the sample at 100 mg / L, the pH value instead goes from 2.4 to 2.1 in short exposure (1 and 24 hours), while it decreases below the considered range after 240 hours. Considering that the $pH_{i.e.p.}$ value of the PU in DI water is equal to 2.7, it

is evident that, regardless of the concentration of the MPs, some time is required for the divalent ions contained in the medium migrate inside the double electrical layer, leading to decrease in $pH_{i.e.p.}$

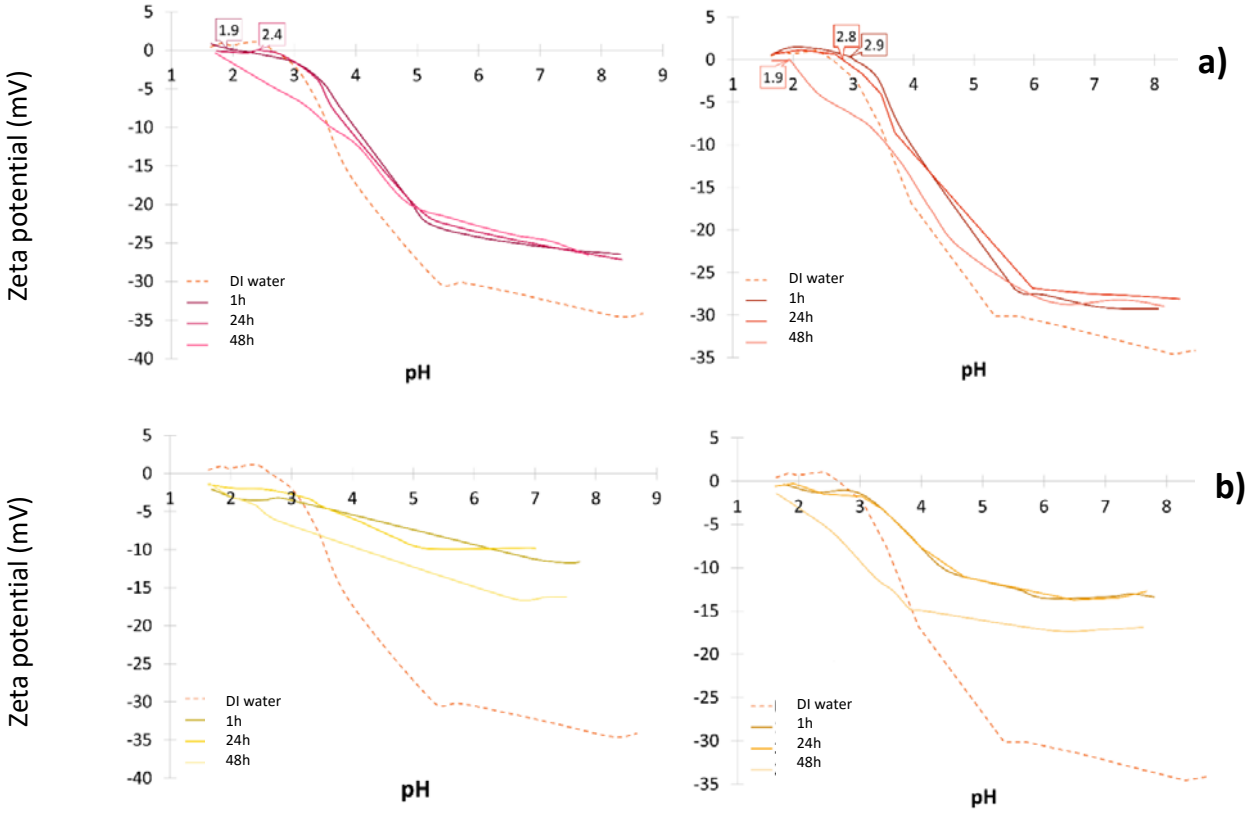

Figure 5.19. PU sample (a) in Egg water (red) 100 - 1000 ppm (b) in M7 (yellow) 100 - 1000 ppm. The dashed curve in each graph refers to the sample in DI water.

Figure 5.19b shows the zeta potential vs. sample pH of PU in M7. Similarly, to what was found for LDPE - CP in M7, a significant crushing of the inverse sigmoid throughout the pH range considered, compared to that relating to the PU dispersed in DI water. Furthermore, by dispersing the PU in M7, compared to the Egg water, the destabilization of the system is probably much more marked due to a higher concentration of salts in the medium. This is also confirmed by the $pH_{i.e.p}$ values which, for all samples and at all times, result in pH values lower than range considered ($pH_{i.e.p} < 1.5$). Considering the changes over time, an increase in the absolute value of the zeta potential passing from an exposure of 1 and 24 hours to 240 hours. This suggests that, over time, the system reaches an equilibrium that increases its stability.

Regarding the PU MPs, the SEM images of the sample exposed to the two media are shown in Figure 5.20a and 5.20b. Comparing the exposed MPs with those as they are not evident morphological modifications of the surface, but it is possible to notice a greater one aggregation of the material. This is probably due to the method of retrieving the MPs at the end of the exposure period. In fact, during the collection of MPs from the filter paper, the formation of agglomerates, not present, was noted in the suspension before filtration. From the dimensional point of view, we note an increase in average size equal to about 2 µm for both the sample exposed in Egg water and the one shown in M7; this trend is confirmed by the shift of the size distribution observable in Figure 5.20c. In this case, such behaviour is almost certainly due to a swelling phenomenon, favoured by nature of the material, more hygroscopic than LDPE - CP.

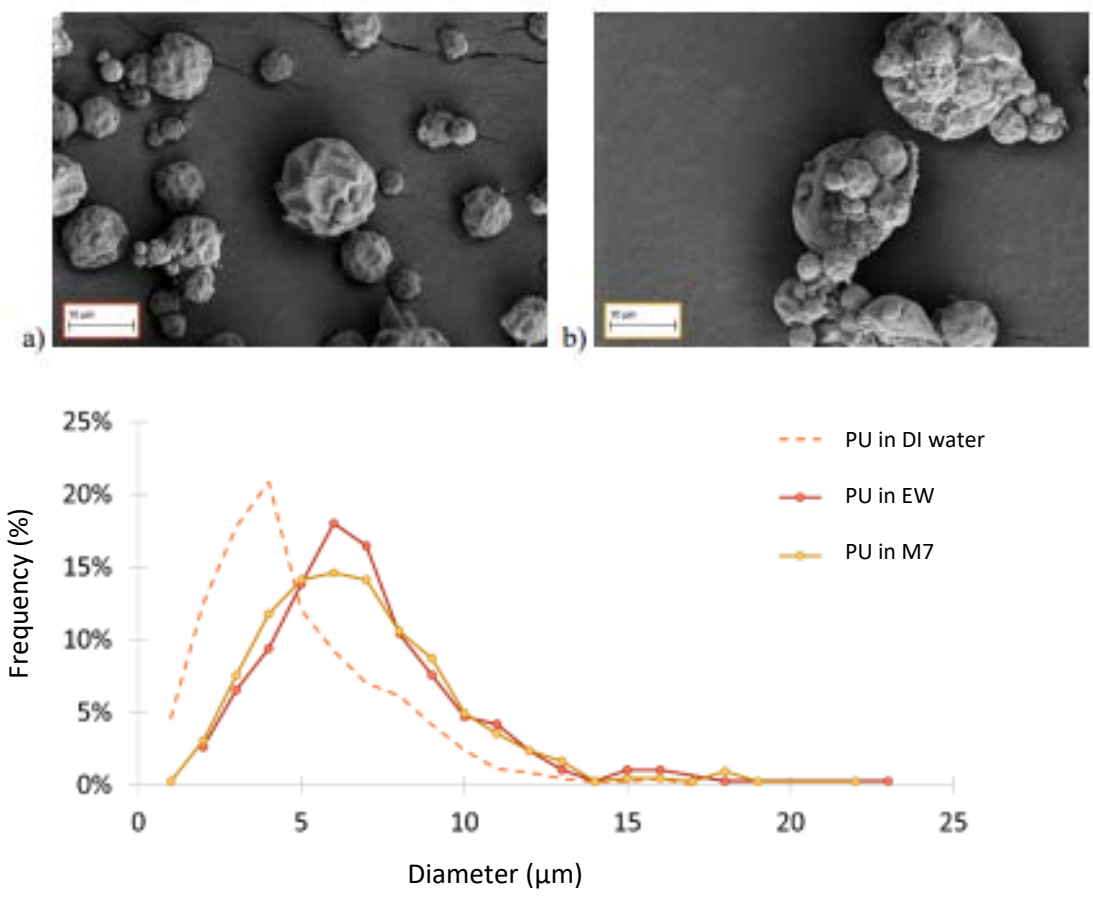

Figure 5.20. SEM image of PU (a) in Egg water (b) in M7 after exposure. (c) size distribution.

5.4. Conclusion

Microplastics are currently one of the emerging complex pollutants of more important, however, information on them is still lacking in the literature behaviour under simulated or real exposure conditions. The data collected from this study aimed at evaluating the variation of the zeta potential and of the adsorption phenomena after incubation in environmental media, combined with other physico - chemical characterizations of base provide vital information that will help support the studies (eco-) toxicological and to fill the knowledge gap on these aspects.

The activity focused on the study of the dispersion method, dimensional and surface characterization, colloidal behaviour of microplastics, such as PE, PET and PU considered emerging environmental pollutants.

It was possible to identify two dispersing systems: BSA and SS, which allowed the PE suspensions to be stable for at least 24h. Further studies are needed for PET suspensions.

The Z – potential vs pH titration in environmental matrices made it possible to identify some trends in the behaviour of microplastics, in particular related ones to the concentration of ions in the media in general, it has been observed that an increase in salt concentration led to a greater destabilization of the colloidal system, as evidenced by the titration curves obtained in the Elendt M7 medium compared to those measured in Egg water and DI water. It was also possible to make hypothesis on surface chemistry, revealing the presence of additives adsorbed on plastic surfaces.

Reference

1. Claessens, M.; Meester, S. De; Landuyt, L. Van; Clerck, K. De; Janssen, C.R. Occurrence and distribution of microplastics in marine sediments along the Belgian coast. *Mar. Pollut. Bull.* **2011**, *62*, 2199–2204, doi:10.1016/j.marpolbul.2011.06.030.
2. Talvitie, J.; Mikola, A.; Setälä, O.; Heinonen, M.; Koistinen, A. How well is microlitter purified from wastewater? – A detailed study on the stepwise removal of microlitter in a tertiary level wastewater treatment plant. *Water Res.* **2017**, *109*, 164–172, doi:10.1016/j.watres.2016.11.046.
3. Koelmans, A.A.; Bakir, A.; Burton, G.A.; Janssen, C.R. Microplastic as a Vector for Chemicals in the Aquatic Environment: Critical Review and Model-Supported Reinterpretation of Empirical Studies. *Environ. Sci. Technol.* **2016**, *50*, 3315–3326,

doi:10.1021/acs.est.5b06069.
4. JRC Microplastics - Focus on Food and Health. *Eur. Union, Jt. Res. Cent.* **2017**, 2.
5. Mitrano, D.M.; Wohlleben, W. Microplastic regulation should be more precise to incentivize both innovation and environmental safety. *Nat. Commun.* **2020**, *11*, 1–12, doi:10.1038/s41467-020-19069-1.
6. Rillig, M.C. W © 2012. **2012**, 6453–6454.
7. Eerkes-Medrano, D.; Thompson, R.C.; Aldridge, D.C. Microplastics in freshwater systems: A review of the emerging threats, identification of knowledge gaps and prioritisation of research needs. *Water Res.* **2015**, *75*, 63–82, doi:10.1016/j.watres.2015.02.012.
8. Wu, W.M.; Yang, J.; Criddle, C.S. Microplastics pollution and reduction strategies. *Front. Environ. Sci. Eng.* **2017**, *11*, 1–4, doi:10.1007/s11783-017-0897-7.
9. Wang, W.; Yuan, W.; Xu, E.G.; Li, L.; Zhang, H.; Yang, Y. Uptake, translocation, and biological impacts of micro(nano)plastics in terrestrial plants: Progress and prospects. *Environ. Res.* **2022**, *203*, 111867, doi:10.1016/j.envres.2021.111867.
10. Auta, H.S.; Emenike, C.U.; Fauziah, S.H. Distribution and importance of microplastics in the marine environmentA review of the sources, fate, effects, and potential solutions. *Environ. Int.* **2017**, *102*, 165–176, doi:10.1016/j.envint.2017.02.013.
11. Chen, G.; Li, Y.; Liu, S.; Junaid, M.; Wang, J. Effects of micro(nano)plastics on higher plants and the rhizosphere environment. *Sci. Total Environ.* **2022**, *807*, 150841, doi:10.1016/j.scitotenv.2021.150841.
12. Rainieri, S.; Barranco, A. Microplastics, a food safety issue? *Trends Food Sci. Technol.* **2019**, *84*, 55–57, doi:10.1016/j.tifs.2018.12.009.
13. De-la-Torre, G.E. Microplastics: an emerging threat to food security and human health. *J. Food Sci. Technol.* **2020**, *57*, 1601–1608, doi:10.1007/s13197-019-04138-1.
14. Revel, M.; Châtel, A.; Mouneyrac, C. Micro(nano)plastics: A threat to human health? *Curr. Opin. Environ. Sci. Heal.* **2018**, *1*, 17–23, doi:10.1016/j.coesh.2017.10.003.
15. Cole, M.; Lindeque, P.; Halsband, C.; Galloway, T.S. Microplastics as contaminants in the marine environment: A review. *Mar. Pollut. Bull.* **2011**, *62*, 2588–2597, doi:10.1016/j.marpolbul.2011.09.025.
16. Zhang, Y.; Li, Y.; Su, F.; Peng, L.; Liu, D. The life cycle of micro-nano plastics in domestic sewage. *Sci. Total Environ.* **2022**, *802*, 149658, doi:10.1016/j.scitotenv.2021.149658.
17. Ivar Do Sul, J.A.; Costa, M.F. The present and future of microplastic pollution in the marine environment. *Environ. Pollut.* **2014**, *185*, 352–364, doi:10.1016/j.envpol.2013.10.036.
18. Stark, M. *Letter to the Editor Regarding "are We Speaking the Same Language? Recommendations for a Definition and Categorization Framework for Plastic Debris";* 2019; Vol. 53; ISBN 9783319165097.
19. Ajith, N.; Arumugam, S.; Parthasarathy, S.; Manupoori, S.; Janakiraman, S. Global distribution of microplastics and its impact on marine environment—a review. *Environ. Sci. Pollut. Res.* **2020**, *27*, 25970–25986, doi:10.1007/s11356-020-09015-5.
20. Faure, F.; Corbaz, M.; Baecher, H.; De Alencastro, L.F. Pollution due to plastics and

microplastics in lake Geneva and in the Mediterranean sea. *Arch. des Sci.* **2012**, *65*, 157–164, doi:10.5169/seals-738358.
21. Eriksen, M.; Mason, S.; Wilson, S.; Box, C.; Zellers, A.; Edwards, W.; Farley, H.; Amato, S. Microplastic pollution in the surface waters of the Laurentian Great Lakes. *Mar. Pollut. Bull.* **2013**, *77*, 177–182, doi:10.1016/j.marpolbul.2013.10.007.
22. Van Cauwenberghe, L.; Vanreusel, A.; Mees, J.; Janssen, C.R. Microplastic pollution in deep-sea sediments. *Environ. Pollut.* **2013**, *182*, 495–499, doi:10.1016/j.envpol.2013.08.013.
23. Hurley, R.R.; Nizzetto, L. Fate and occurrence of micro(nano)plastics in soils: Knowledge gaps and possible risks. *Curr. Opin. Environ. Sci. Heal.* **2018**, *1*, 6–11, doi:10.1016/j.coesh.2017.10.006.
24. Shen, M.; Zhu, Y.; Zhang, Y.; Zeng, G.; Wen, X.; Yi, H.; Ye, S.; Ren, X.; Song, B. Micro(nano)plastics: Unignorable vectors for organisms. *Mar. Pollut. Bull.* **2019**, *139*, 328–331, doi:10.1016/j.marpolbul.2019.01.004.
25. Bandini, F.; Taskin, E.; Bellotti, G.; Vaccari, F.; Misci, C.; Guerrieri, M.C.; Cocconcelli, P.S.; Puglisi, E. The treatment of the organic fraction of municipal solid waste (OFMSW) as a possible source of micro- and nano-plastics and bioplastics in agroecosystems: a review. *Chem. Biol. Technol. Agric.* **2022**, *9*, 1–17, doi:10.1186/s40538-021-00269-w.
26. Carr, S.A.; Liu, J.; Tesoro, A.G. Transport and fate of microplastic particles in wastewater treatment plants. *Water Res.* **2016**, *91*, 174–182, doi:10.1016/j.watres.2016.01.002.
27. Ziajahromi, S.; Neale, P.A.; Rintoul, L.; Leusch, F.D.L. Wastewater treatment plants as a pathway for microplastics: Development of a new approach to sample wastewater-based microplastics. *Water Res.* **2017**, *112*, 93–99, doi:10.1016/j.watres.2017.01.042.
28. Wang, Z.; Lin, T.; Chen, W. Occurrence and removal of microplastics in an advanced drinking water treatment plant (ADWTP). *Sci. Total Environ.* **2020**, *700*, doi:10.1016/j.scitotenv.2019.134520.
29. Talvitie, J.; Mikola, A.; Koistinen, A.; Setälä, O. Solutions to microplastic pollution – Removal of microplastics from wastewater effluent with advanced wastewater treatment technologies. *Water Res.* **2017**, *123*, 401–407, doi:10.1016/j.watres.2017.07.005.
30. Uddin, S.; Fowler, S.W.; Habibi, N.; Behbehani, M. Micro-Nano Plastic in the Aquatic Environment: Methodological Problems and Challenges. *Animals* **2022**, *12*, 1–18, doi:10.3390/ani12030297.
31. Pinto da Costa, J.; Reis, V.; Paço, A.; Costa, M.; Duarte, A.C.; Rocha-Santos, T. Micro(nano)plastics – Analytical challenges towards risk evaluation. *TrAC - Trends Anal. Chem.* **2019**, *111*, 173–184, doi:10.1016/j.trac.2018.12.013.
32. Renner, G.; Schmidt, T.C.; Schram, J. Analytical methodologies for monitoring micro(nano)plastics: Which are fit for purpose? *Curr. Opin. Environ. Sci. Heal.* **2018**, *1*, 55–61, doi:10.1016/j.coesh.2017.11.001.
33. De Ruijter, V.N.; Redondo-Hasselerharm, P.E.; Gouin, T.; Koelmans, A.A. Quality Criteria for Microplastic Effect Studies in the Context of Risk Assessment: A Critical Review. *Environ. Sci. Technol.* **2020**, *54*, 11692–11705, doi:10.1021/acs.est.0c03057.
34. Mattsson, K.; Jocic, S.; Doverbratt, I.; Hansson, L.A. *Nanoplastics in the aquatic*

environment; Elsevier Inc., 2018; ISBN 9780128137475.
35. Taylor, P.; Wen, J. Food Additives &# x26 ; Contaminants : Part B : Surveillance Elemental composition of commercial sea cucumbers (holothurians). 37–41, doi:10.1080/19393210.2010.520340.
36. Samel, A.; Ziegenfuss, M.; Goulden, C.E.; Banks, S.; Baer, K.N. Culturing and Bioassay Testing of Daphnia magna Using Elendt M4 , Elendt M7 , and COMBO Media. **1999**, *110*, 103–110.
37. Hartmann, N.B.; Jensen, K.A.; Baun, A.; Rasmussen, K.; Rauscher, H.; Tantra, R.; Cupi, D.; Gilliland, D.; Pianella, F.; Riego Sintes, J.M. Techniques and Protocols for Dispersing Nanoparticle Powders in Aqueous Media - Is there a Rationale for Harmonization? *J. Toxicol. Environ. Heal. - Part B Crit. Rev.* **2015**, *18*, 299–326, doi:10.1080/10937404.2015.1074969.
38. Santana, V.; Santos, V.; Silveira, E.; Pereira, B.B. Toxicity and applications of surfactin for health and environmental biotechnology. *J. Toxicol. Environ. Heal. Part B* **2019**, *00*, 1–18, doi:10.1080/10937404.2018.1564712.
39. Ferraz, M.; Bauer, A.L.; Valiati, V.H. Microplastic Concentrations in Raw and Drinking Water in the Sinos River , Southern Brazil. **2020**, 1–10.
40. Arechabala, B.; Coiffard, C.; Rivalland, P.; Coiffard, L.J.M. Comparison of Cytotoxicity of Various Surfactants Tested on Normal Human Fibroblast Cultures using the Neutral Red Test , MTT Assay and LDH Release. **1999**, *165*, 163–165.
41. Jiao, L.; Xiao, H.; Wang, Q.; Sun, J. Thermal degradation characteristics of rigid polyurethane foam and the volatile products analysis with TG-FTIR-MS Thermal degradation characteristics of rigid polyurethane foam and the volatile products analysis with TG-FTIR-MS. *Polym. Degrad. Stab.* **2013**, *98*, 2687–2696, doi:10.1016/j.polymdegradstab.2013.09.032.
42. Smith, B.C. The Infrared Spectra of Polymers II : Polyethylene. 1–7.
43. Vermelha, P.; Janeiro, R. De Processing and Characterization of PET Composites Reinforced With Geopolymer Concrete Waste. **2017**, *20*, 411–420.
44. Al, B.; Mahmoud, G.; Strehlow, B.; Mohr, E. Development of thrombus-resistant and cell compatible crimped polyethylene terephthalate cardiovascular grafts using surface co- immobilized heparin and collagen Development of thrombus-resistant and cell compatible crimped polyethylene terephthalate cardiovascular grafts using surface co-immobilized heparin and collagen. *Mater. Sci. Eng. C* **2017**, *43*, 538–546, doi:10.1016/j.msec.2014.07.059.
45. Zetasizer.
46. Republic, F. a -Olefinsulfonates. **2012**, doi:10.1002/14356007.a25.
47. Kirby, B.J.; Jr, E.F.H. Review Zeta potential of microfluidic substrates : 2 . Data for polymers. **2004**, 203–213, doi:10.1002/elps.200305755.
48. Tourinho, P.S.; Ko, V.; Loureiro, S.; Gestel, C.A.M. Van Partitioning of chemical contaminants to microplastics : Sorption mechanisms , environmental distribution and effects on toxicity and. **2019**, *252*, 1246–1256, doi:10.1016/j.envpol.2019.06.030.

Chapter 6:

Conclusion

Nanotechnologies have been used in this thesis work to meet the needs in the field of water purification from pollutants. In particular we proposed four key point of innovation:

1- Developing and testing nano-photocatalysts towards a SSbD application:
   TiO_2 - based and carbon - based photocatalysts have been developed, as a green alternative to be employed in advanced oxidation processes (AOPs). The functionality (in terms of photocatalytic efficiency, TOF and COD) of nano-photocatalysts was assessed by following the degradation of RhB, under UV and simulated solar light. The functionality has been combined with cost and environmental sustainability profiles, in terms of energy spent for the production and use of the nano-photocatalysts. It was possible to find which material together with which type and irradiation time allows to maximize functionality, keeping costs low and having little impact on the environment in terms of kg CO_2 – eq / kWh. It was noted from the results that the commercial TAC material, being ready to use and having shown a good photocatalytic efficiency, turned out to be the optimal choice. When the weight of environmental sustainability component prevailed, the TiO_2:SiO_2 composite showed excellent performance, also thanks to the fact that it uses a lower quantity of active species (TiO_2) while maintaining a high efficiency. As next steps, the comparison of performance attributes will be extended to further life - cycle stages, as the synthesis and deposition process steps, in order to evaluate further design options and verify if catalysts such as TGO that are disadvantaged from the point of view of energy consumption at the use phase can improve their overall efficiency, considering the good photocatalytic reactivity shown.

2- Scale - up photoreactors for nano–photocatalysts integration supported by fabrics:
   Two TiO_2 - based nano-photocatalysts (TAC and TiO_2:SiO_2) were deposited on fabric substrates by dip - pad curing process and integrated in a semi - pilot 6 litres plant, designed to simulate a system suitable for wastewater treatment, in real application. it was possible to find the best strategy for the scale - up of the photocatalysis process. In particular the 100% cotton fabric support, the TiO_2:SiO_2

coating and a working temperature of 25 °C are the optimal design options. The comparison of the reactivity of nano-photoatalysts active under UV light (TiO_2-based) under different source of irradiation did not show significant differences, allowing the use of the developed system also under solar light and visible LED irradiation. This result is most likely explained by the UV component present in the simulating solar light used in lab - scale tests of solution 1) and to the photosensitizing effect of orange RhB that acts as a photosensitizer, providing charge carriers capable of degrading the molecules, when irradiated by visible LED light as in solution 2. The results obtained expand the technology to visible light with the advantage to be cheaper, easily available and exploitable, making it very advantageous both from the point of view of costs and of the applicability, matching. the rules of the Green deal, to obtain climate neutrality. As next step we will expand optimisation functions tested in solution 1) to the pre - pilot plant variables, supporting a further scale - up in industrial plants.

3- Development of experimental model, predictive of the functionality of nano–photocatalysts and their eco - toxic potential:

Different experimental models were applied to the investigated systems at the aim to predict their performance attributes, including the photodegradation (discoloration) of RhB dye, the capacity to produce OH• radicals (RNO model) and the oxidative potential against cell natural antioxidant defences (GSH / CyS model). TiO_2 - based materials and also the TGO composite showed very good photocatalytic efficiency most likely driven by the direct oxidation of the photo-induced positive holes on the surface. On the contrary the organic material g-C_3N_4, produced many OH• despite to the low photocatalytic efficiency confirming a fast recombination of the charge carriers that did not allow the photo-degradation of target pollutant. A machine learning tool was implemented to understand which physico - chemical characteristics and / or exposure conditions had the greatest influence on the oxidative power and the tendency to produce OH• of the nano-photocatalysts. As next steps, we will improve the predictive capacity of the investigated models, by extending dataset also to no-oxidative conditions (performing tests under inert atmosphere) and by correlating the results with

cellular models in order to identify scores of potential hazards linked to the acellular tests developed.

4- Identification and characterization of new class of pollutants: MNPs

Micro plastics, such as PE, PET and PU considered emerging environmental pollutants were characterised in terms of physico - chemical properties and colloidal behaviour. The investigation of their dispersibility, in different environmental relevant media and using biomimetic or bio - sourced dispersants such as bovine serum albumin (BSA) and sodium surfactin (SS) was exploited in the European project Plasticsfate at the aim to identify a common dispersion protocol through different characterisation partners in order to improve samples reproducibility and allow their assessment in biological matrices. As next steps we will further investigate the dispersibility in biological relevant fluids in order to support dosimetry studies and provide a right estimation of the amount of micro plastics pollutant that come in touch with biological targets.